



HAL
open science

Characterization and modeling of microstructure evolution of cable insulation system under high continuous electric field

Raphaël Guffond

► **To cite this version:**

Raphaël Guffond. Characterization and modeling of microstructure evolution of cable insulation system under high continuous electric field. Physics [physics]. Sorbonne Université, 2018. English. NNT: 2018SORUS039 . tel-02121074

HAL Id: tel-02121074

<https://theses.hal.science/tel-02121074v1>

Submitted on 6 May 2019

HAL is a multi-disciplinary open access archive for the deposit and dissemination of scientific research documents, whether they are published or not. The documents may come from teaching and research institutions in France or abroad, or from public or private research centers.

L'archive ouverte pluridisciplinaire **HAL**, est destinée au dépôt et à la diffusion de documents scientifiques de niveau recherche, publiés ou non, émanant des établissements d'enseignement et de recherche français ou étrangers, des laboratoires publics ou privés.

**THÈSE DE DOCTORAT DE
SORBONNE UNIVERSITÉ**

École doctorale : Sciences Mécaniques, Acoustique, Électronique et Robotique de Paris

réalisée au

Laboratoire de Physique et d'Étude des Matériaux

présentée par

Raphaël Guffond

pour obtenir le grade de

DOCTEUR DE SORBONNE UNIVERSITÉ

ayant pour titre

**Characterization and modeling of microstructure
evolution of cable insulation system under high
continuous electric field**

soutenue le 6 mars 2018
devant le jury composé de

Lionel Flandin, Professeur à l'Université Savoie Mont Blanc	Rapporteur
Petru Notingher, Professeur à l'Université de Montpellier	Rapporteur
Séverine Le Roy, Chargée de Recherches à l'Université Paul Sabatier	Examinatrice
Hamid Kokabi, Professeur à Sorbonne Université	Examinateur
Anthony Combessis, Docteur Ingénieur R&D, Nexans	Encadrant
Stéphane Holé, Professeur à Sorbonne Université	Directeur

Remerciements

Ce travail de thèse s'est déroulé au sein du laboratoire de physique et d'étude des matériaux à l'école supérieure de physique et chimie industrielle de Paris en collaboration avec le centre de recherche de Nexans à Lyon. La particularité de cette thèse est que l'ensemble de mon travail a principalement eu lieu au sein du centre de Nexans. Je tiens ainsi tout d'abord à remercier Arnaud Allais (directeur du NRC), sans qui cette thèse n'aurait pas eu lieu, de m'avoir accueilli au sein du centre de recherche tout en accordant une énorme attention à mon travail. Je tiens aussi à remercier Gérard Bacquet pour avoir fortement contribué, à l'élaboration et à l'avancée du projet de recherche en lien avec mon travail. Je tiens aussi à exprimer ma reconnaissance envers Gabriele Perego pour l'intérêt porté à mon travail.

Mes plus profonde reconnaissances sont adressés à Anthony Combessis, mon co-encadrant de thèse, et à Stéphane Holé, mon directeur. Je remercie Anthony d'avoir été présent tout au long de ma thèse pour m'avoir aidé à avancer dans mon travail. Il m'a transmis tout son savoir scientifique et sa rigueur et m'a apporté un énorme soutien à la fois scientifique et moral. J'ai vraiment apprécié qu'il ait mis tout ses effort pour m'amener à la réussite et à me préparer à mon futur métier de docteur ingénieur R&D. Je remercie Stéphane pour sa disponibilité, ses conseils, son transfert de connaissances et son soutien tout au long de ma thèse. C'est grâce à Stéphane et Anthony que j'ai pu acquérir une certaine expertise dans le domaine en lien avec mon sujet de travail et je leur en serait pour cela éternellement reconnaissant.

Je souhaite aussi remercier chaleureusement messieurs Lioniel Flandin, professeur à l'université Joseph Fourier, et Petru Nothinger, professeur à l'université de Montpellier, d'avoir accepté d'être rapporteur de ma thèse. Je souhaite aussi remercier madame Severine Le Roy d'avoir accepté d'examiner mon travail. J'adresse aussi de très vifs remerciement à monsieur Hamid Kokabi pour sa présence lors de mon comité de suivi de thèse à mi-parcours et pour avoir accepté d'être examinateur à ma soutenance.

Au sein du centre de recherche de Nexans, Je souhaiterai remercier Dimitri Charrier et Jihane Sahyoun pour leur bienveillance, leur gentillesse et nos échanges de savoir très fructueux et Adrien Charmettant, pour sa bonne humeur, sa capacité à me mettre scientifiquement au défi et ses précieux conseils en terme de modélisation.

Je souhaite aussi remercier Cécile Gasnier pour sa bonne humeur quotidienne, son accueil chaleureux et son aide administrative précieuse.

Je remercie aussi vivement Melek Maugin, technicienne sans pareille, qui a été toujours là dans les moments les plus compliqués de ma thèse en m'apportant un énorme soutien moral. Je n'oublie pas non plus Basile Salamé, Christelle Mazel, Jean-michel Marty, Daphné Merle et Patrick Fornage pour la richesses de nos échanges.

Je souhaite ensuite remercier les thésards et anciens thésards du groupe Instrumentation, pour avoir rendu mes passages au sein du LPEM très agréable.

Enfin, je souhaite remercier mes parents pour leur soutien infailible tout au long de cette thèse et leurs encouragements.

Contents

Introduction	11
1 State of the Art	15
1.1 Context	15
1.1.1 HVDC cable manufacturing	15
1.1.2 HVDC cable system testing	16
1.1.3 HVDC cable lifetime modeling	16
1.2 Electrical properties and related methods	17
1.2.1 Conductivity	18
1.2.2 Space Charge (SC)	19
1.3 Charge transport and aging modeling	21
1.3.1 Analytical model for charge transport	21
1.3.1.1 Space Charge Limited Current (SCLC)	21
1.3.1.2 Poole-Frenkel [1]	24
1.3.1.3 Variable Range Hopping (VRH)	24
1.3.2 Analytical model for charge injection	25
1.3.2.1 Fowler-Nordheim injection	26
1.3.2.2 Schottky injection [2]	26
1.3.2.3 Interface effect	27
1.3.3 Breakdown physical process	28
1.3.3.1 Electrical breakdown	28
1.3.3.2 Mechanical breakdown	29
1.3.3.3 Thermal runaway	30
1.3.4 Aging phenomenology and modeling	30
1.3.4.1 Dakin, inverse power and Eyring models (1948)	31
1.3.4.2 Crine model	31

1.3.4.3	DMM (Dissaldo/Montanari/Mazanti) model	31
1.3.4.4	Lewis electromechanical model	32
1.3.4.5	Summary	32
1.4	Physical heterogeneity effect	33
1.4.1	Description and formation	33
1.4.1.1	Description	33
1.4.1.2	Formation	34
1.4.2	Behavior under temperature and electric field	36
1.4.2.1	Annealing effect	36
1.4.2.2	Relaxation processes	36
1.4.2.3	Behavior under electric field	38
1.4.3	Effect on electrical properties: model and experiment	38
1.4.3.1	Charge transport model in specific heterogeneous semicrystalline polymeric structure	39
1.4.3.2	Effect on conductivity and space charge	42
1.5	Chemical heterogeneities	44
1.5.1	Charge transport model in polymeric structures with chemical residues	44
1.5.2	Behavior under temperature and electric field	45
1.5.2.1	Behavior under temperature	45
1.5.2.2	Behavior under electric field	46
1.5.3	Peroxide decomposition products (PDP)	47
1.5.3.1	Formation	47
1.5.3.2	Diffusion properties	48
1.5.3.3	Effect on space charge and conductivity	48
1.5.4	Antioxidants	50
1.5.4.1	Formation	50
1.5.4.2	Effect on space charge and conductivity	50
1.5.5	Water content	51
1.5.5.1	Formation	51
1.5.5.2	Diffusion properties	51
1.5.5.3	Effect on space charge and conductivity	52
1.5.6	Oxidation	52
1.5.6.1	Formation	52
1.5.6.2	Effect on space charge and conductivity	53

2	Experimental approach	55
2.1	Materials	55
2.1.1	PE-based material	55
2.1.2	PP-based material	56
2.1.3	PET-based material	57
2.2	Physical and chemical characterization	57
2.2.1	Morphological analysis	57
2.2.1.1	Differential scanning calorimetry (DSC) method	57
2.2.1.2	Analysis on material <i>models</i>	58
2.2.1.3	Crystallinity variation with temperature	59
2.2.2	Chemical composition	61
2.2.2.1	Methods	61
2.2.2.2	Results	63
2.3	Dielectric spectroscopy measurement	65
2.3.1	Setup description	65
2.3.2	Morphological impact on permittivity	66
2.3.3	Glass transition and crystalline phase influence on conductivity	69
2.4	Current density measurement	70
2.4.1	Setup description	70
2.4.2	Test procedures	70
2.4.3	Crystallinity impact on conductivity	72
2.4.4	PDP influence on conduction	73
2.4.5	Interface effect	75
2.5	Space charge measurement	76
2.5.1	Setup description	76
2.5.1.1	Stimulus and measurement systems	76
2.5.1.2	Reduction of waves reflections	76
2.5.1.3	Signal resolution	78
2.5.1.4	Data processing	79
2.5.2	Test procedures	80
2.5.3	Glass transition influence on space charge	81
2.5.4	Crystallinity impact on space charge	82
2.5.5	PDP influence on space charge	83

3	Genetic model description	87
3.1	Electrical properties output	88
3.1.1	Electric field	89
3.1.2	Charge density	90
3.1.3	Permittivity and temperature	91
3.2	Development of evolution laws	92
3.2.1	Charge injection	92
3.2.2	Charge transport	92
3.2.3	Charge extraction	93
3.2.4	Charge trapping and detrapping	94
3.3	Evolution of the system over time	94
3.3.1	System evolution from evolution laws	94
3.3.2	Current density calculation	95
3.3.3	Step time calculation	96
3.4	Simulation results	97
3.4.1	Leakage current and space charge measurements	97
3.4.2	Current density dependency with electric history: space charge effect	98
3.4.3	Electrical properties dependency with electric field: SCLC	99
4	Genetic evolution of semi-crystalline polymer	103
4.1	Heterogeneous semicrystalline structure simulation	103
4.1.1	Distribution of random spherulites in the model	103
4.1.2	Distribution of random lamellae related to spherulite	105
4.1.3	Algorithm for crystalline fraction calculation	107
4.1.4	Local permittivity calculation from local crystalline fraction	109
4.2	Evolution laws development	111
4.2.1	Charge injection and transport	111
4.2.2	Charge trapping	114
4.2.3	Microstructure modification with temperature: annealing	116
4.3	Criticality of model parameters	116
4.3.1	Parameters for charge transport and injection	117
4.3.2	Parameters for charge trapping	120
4.4	Comparison with experiments	123
4.4.1	Current density behavior	123

4.4.2	Space charge profile	125
4.4.3	Dependency with crystallinity	129
4.4.4	Glass transition temperature	129
5	Genetic evolution of undegassed insulation system	133
5.1	PDP distribution simulation	133
5.1.1	Distribution in the polymer	134
5.1.2	Impact on local permittivity	135
5.1.3	Influence of degassing time	136
5.2	Evolution law development	137
5.2.1	Genetic behavior of ACP	137
5.2.1.1	Diffusion of ACP from concentration gradient	137
5.2.1.2	Impact on electrical properties: deep traps for electrons	137
5.2.2	Genetic behavior of α CA	139
5.2.2.1	Diffusion of α CA from concentration gradient	139
5.2.2.2	Impact on electrical properties: ionic transport	140
5.2.3	Effect of macroscopic interfaces	142
5.3	Criticality of model parameters	144
5.3.1	Parameters for α CA genetic behavior	144
5.3.2	Parameters for ACP genetic behavior	147
5.4	Comparison with experiment	148
5.4.1	Impact of PDP in space charge distribution of XLPE	148
5.4.1.1	Effect of α CA	148
5.4.1.2	Effect of ACP	151
5.4.2	Impact of PDP in current density of XLPE	152
5.4.2.1	Degassing time	152
5.4.3	Interface effect	155
5.5	Summary	156
	Conclusion	157
	Bibliography	161

Introduction

For electrical power transmission, High Voltage Alternating Current (HVAC) technologies have been the standard for more than a century. However, for long distances, AC power transmission suffers from considerable power losses. It requires the use of so-called *power factor correction* (PFC) equipments, which increase in turn the capital expenditure of such power lines. In the same time, the constant growth in worldwide energy needs combined with the absolute necessity of rebalancing the energy mix with increased fraction of renewable energies (wind, solar, wave and tidal,...) advocate for very long distance lines, or *energy highways*. Although HVDC terminal stations are more expensive due to the power electronics required to achieve AC-DC conversion, the absence of reactive power from capacitive effects makes the line cost per km more competitive. Moreover most DC technologies require the use of 2 cables instead of 3 in AC. Thus, from a critical distance, the total cost of DC lines becomes lower than for AC lines, as illustrated in Figure 1.

Besides the economical standpoint, the main uses of HVDC lines concern the interconnexion of asynchronous grids, the energy transmission of foreign renewable energy fields (e.g. offshore windfarms) to the consumption places and the subsea interconnexions.

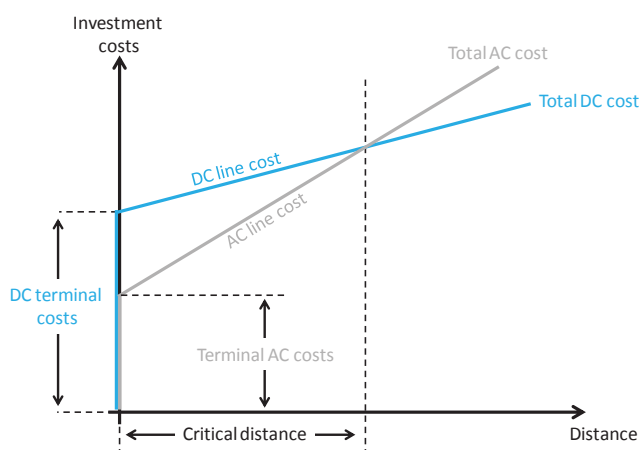


Figure 1: Investment cost in HVDC and HVAC as a function of transmission line distance. Adapted from [3].

Among the existing technologies for power cable insulation, synthetic insulation has become the most popular. Based on crosslinked polyethylene (XLPE), synthetic insulation combines advantages of attractive raw material and process costs, low weight, appropriate electrical and thermomechanical properties. Moreover, once installed, XLPE land and subsea cables are main-

tenance free. Moreover XLPE, is already well recognized in HVAC applications for its very good reliability over long eras.

For DC applications, the *exponential* dependence of electrical resistivity of the polymer to temperature and DC electric field may however lead to unexpected features [4, 5, 6, 7]. During use, a temperature gradient is set across the cable insulation, caused by heating from Joule losses originating from the current flow in the conductor. From this temperature gradient, a conductivity variation by several orders of magnitude may be expected, yielding electric field distributions far different from the predicted Laplacian distribution. Furthermore, under DC electric field, polymeric insulations show propensity to accumulate charges through injection or by internal generation processes. From these so-called *space charge* accumulations, electrical field distortion may be produced throughout the insulation thickness. Under these conditions, an insulation system may suffer from chemical, physical, and electrical aging after long-standing operation under voltage leading to premature failure.

Electrical properties of insulation system under HVDC are directly related to its heterogeneities. At macroscopic scale, the insulation system of extruded power cables is constituted by three concentric layers of macroscopical homogeneous polymer-based materials, one insulation layer between two semiconductive layers, deposited on the conductor surface by co-extrusion (see Figure 2). This insulation system reveals however heterogeneities at several scales located at the interfaces between layers, and within the bulks of each layer. As a semi-crystalline polymer, XLPE presents obviously an heterogeneous morphological structure. Moreover its formulation with other polymers, fillers or adjuvants and its chemical crosslinking, achieved in catenary vulcanization (CV) lines, also induces chemical heterogeneities [8]. Semiconductive layers are made of XLPE filled with large amounts of carbon black and show similar physical and chemical heterogeneities. The quality of the interfaces between the semiconductive layers, called semi-cons, and insulation strongly impact as well the conductivity and space charge in the resulting insulation systems [9].

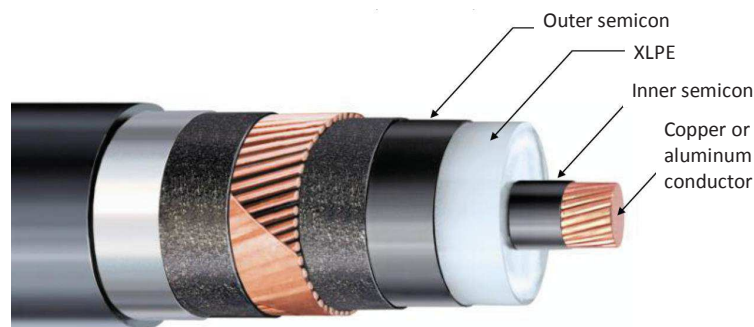


Figure 2: Main components of a power cable.

Power cables are designed, manufactured and installed with the aim of lasting for decades. It thus appears of great concern to well identify, understand and control the aging mechanisms in order to predict as accurately as possible the insulation durability. A large number of models have been proposed for the electro-thermal ageing process: insulation failure was first associated with macroscopic causes, rather than to microstructure [10]. From electrical engineering view point,

insulating polymers were indeed first considered as invariant solid systems, which constituted an invalid statement for polyolefins used at temperatures well above glass transition. Models were then developed to take into account the heterogeneous structure of polyethylene and the related charge transport process. The transport models consider the polymer as a large gap imperfect semiconductor containing authorized states between conduction and valence bands introducing the concept of *space charge* [11]. Unfortunately, such models focus on the electrical description and do not manage the microstructure evolution of the material with time, temperature and electric field, which are driving forces for conduction mechanisms.

Since recently, some works are looking more carefully at the microstructure contribution to insulation damage. Jones *et al.* describe the formation of microvoids in semicrystalline polymer when submitted to electrical stress [12]. Other authors consider in their models the presence of heterogeneities by introducing distribution of trap states at different energy levels. However no model in the literature integrates the complete set of chemical and physical heterogeneities composing the insulation microstructure. Yet related interactions and coupling between these heterogeneities are likely to be present in polymer insulation.

In this context, this work aims at developing a new model able to simulate the modifications over time of the microstructure in insulation polymers submitted to electric field and temperature as well as the related impacts on electrical properties and durability. The two main objectives of this study are *i*) to model electrical properties of polymer by taking into account all the influencing heterogeneities (physical and chemical) and *ii*) to highlight the impact of the microstructure evolution over time on electrical properties. To do so, a new model approach is used based on Markov chains model and genetic evolution [13]. Markov model is a stochastic model where system is composed of a states distribution changing with time. At a given time, the distribution evolves (mutates) into a new state distribution based only on the distribution of the previous state. The main advantage of this model compared to others is that simulation is based on local interaction calculation and not on global criteria.

In the present study, a state distribution is used to describe the heterogeneities in crosslinked semi-crystalline polymer. Each state represents a local microstructure of the insulation. From this microstructure distribution, polymer electrical properties, such as space charge, local permittivity or current density, are simulated for a given set of electric field and temperature. The random distribution follows the inhomogeneous structure of the semi-crystalline polymers including chemical residues.

Furthermore, when stressed under electric field and temperature, microstructure of polymers changes. The strength of the developed model is that this feature is taken into account by modifying the state distribution over time according to evolution laws. From the simulated microstructure evolution results electrical property changes over time at both transient and steady states.

The main challenge of this work is to find the appropriate evolution laws, which have to be accurate enough to correctly describe the material behavior and simple enough to allow fast calculation. To define these laws, a dual approach, experimental and numerical, is used. In particular, the experimental work aims at obtaining quantitative correlations between the polymer heterogeneities and electrical properties.

In order to have an independent control of morphological and chemical heterogeneities in polymers, electrical measurements are performed on polymeric material called material *models*, which are chosen in order to dissociate the different microstructure effects. From electrical property variations of the material *models versus* electric field, temperature and time, a qualitative and quantitative impact of the related heterogeneity is obtained. The genetic algorithm is then developed by establishing the most accurate evolution law to describe both the influence of this heterogeneity on polymer electrical properties and its evolution over time.

This manuscript consists of five chapters.

In the first chapter, a literature review describes the main heterogeneities found in the dielectric layer and identifies their contribution to space charge and conductivity. Then, aging models from the literature are presented and discussed.

The second chapter presents the experimental study where electrical properties of material *models* are studied. Firstly material *models* used to assess the respective contributions of polymer heterogeneities on electrical properties are detailed. Specific manufacturing processes are developed to precisely control the microstructure modifications. In the second part of this chapter, physical, chemical and electrical characterization methods are described and the associated experimental results are presented.

The third chapter describes the core of the genetic model developed under MatLab. At first, a overview description of the state matrix, the evolution laws and the explicit calculation method is presented. Then, an exhaustive list of the heterogeneities present in each state is presented. Physical laws for charge injection, extraction and trapping are finally implemented. The resulting *core model* is implemented to validate the range of the first simulation results.

The fourth chapter focuses on the contribution of the polymer microstructure (*i.e.* crystalline organizations and macromolecules relaxations) to the charge transport and trapping. Evolution laws are developed to simulate the semi-crystalline structure influence on polymer electrical properties. These laws are based on experimental results obtained on material *models*.

The fifth chapter sets the evolution laws associated to the chemical heterogeneities in crosslinked industrial polyethylene and the presence of semicon layers. Evolution laws are developed to simulate the influence of these chemical heterogeneities and this interface on polymer electrical properties. These laws are based on experimental results obtained in this study or published in the literature.

To conclude, strengths and further development perspectives of this model are discussed.

Chapter 1

State of the Art

1.1 Context

1.1.1 HVDC cable manufacturing

Since late 1970's, extruded synthetic cables are progressively replacing paper-insulated lead covered cables in the cables business [14]. The main advantages of extruded insulation cables compared to oil or mass impregnated lapped paper cables are low material cost, low weight, easier manufacture and easier repair [14].

Extruded power cables are produced in a seamless continuous process. The insulation system composed of a dielectric layer surrounded by two semiconductive layers is coextruded on the outer surface of a metallic conductor, made of stranded copper or aluminum wires. The cable insulation system is immediately further crosslinked in a tubular vulcanization line by the radical decomposition of peroxide, achieved under elevated temperature and pressure conditions [14]. After cooling, the produced cables are submitted to a degassing step where harmful chemicals (*e.g.* methane) resulting from peroxide decomposition are desorbed.

The cable conductor is intended to transport the current. It is thus made of metals selected as a compromise between high conductivity, mechanical properties and acceptable price. The electric fields is transported through dielectric layer. In extruded power cables, the dielectric generally consists of crosslinked ethylene homopolymer or copolymer, the standard being low density crosslinked polyethylene (XLPE). The polymer is formulated with peroxides (generally dicumyl peroxide in HVDC applications) for chemical crosslinking, and antioxydants to delay radical degradation and thermal-oxydation.

The third components of the electric system are the semiconductive layers. These are crosslinked ethylene copolymers filled with carbon black in necessary volume fraction so that electrical percolation is achieved [15, 16, 17]. The role of semicons is to generate smoothest and most perfect interfaces with the dielectric so that the electric field within the dielectric is almost perfectly defined in the radial direction [14]. The inner semicon is placed between the conductor and the dielectric and put at the high potential, the outer semicons is connected to the low potential (ground).

Depending on the application, other layers are added to the cable design such as swelling tapes, screen wires, aluminum laminate and covering sheath. Moreover, subsea cables usually include an

extruded lead sheath as water barrier and armoring wires providing further mechanical protection [18].

1.1.2 HVDC cable system testing

Today's Operating voltage of XLPE based HVDC cables is ± 320 kV [19] and next generation of cables from ± 400 kV to ± 1100 kV are currently produced and being installed [20]. The applied Voltage yields to an electric field gradient sustained by the cable insulation with average electrical stress from 20 kV/mm to 40 kV/mm. In addition, thermal gradient from 50°C to 70°C is present in the insulation of power cable under load condition. Under these high electrical and thermal stresses, cables are designed to last tenths of year. CIGRE recommends a series of tests to submit on cable systems to guarantee their performance such as prequalification and type tests [21]. Possible configuration of test objects in a test loop is shown in Figure 1.1.

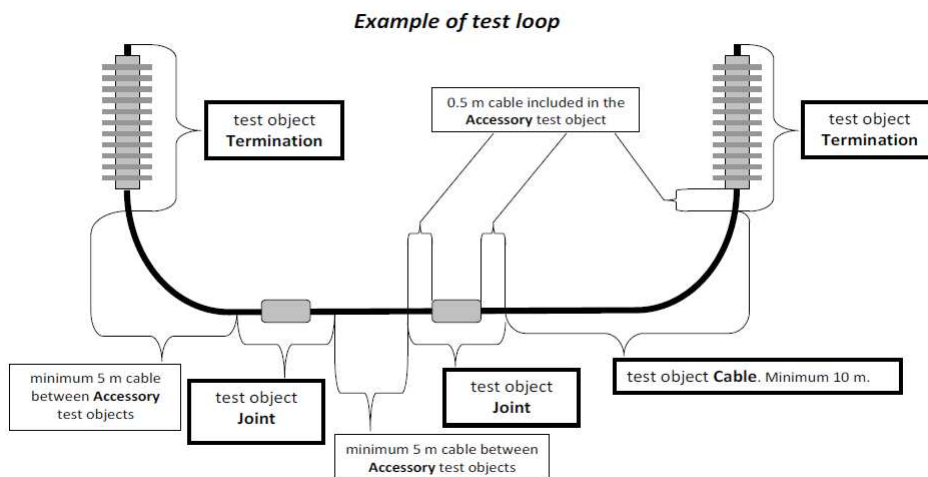


Figure 1.1: Example of test loop recommended by CIGRE [21].

1.1.3 HVDC cable lifetime modeling

From new polymer selection to full size cable, several levels of technological readiness have to be fulfilled. Reliable simulations of the electrical behavior of insulation systems are of great interest to decrease the development costs and time-to-market. Indeed simulation reduces both test time and prototyping costs by allowing *ab initio* selection of material candidates and then ease the scale-up from lab samples to marketable solution.

Electrical properties, such as leakage current or electric field distribution, must be predicted both in HVDC insulation system at steady and transient states. To do so, multiphysics models are used to correlate electrical properties of insulation with material properties. Along the years, the main approach used to simulate electrical properties of insulation use space-dependent simulations like Finite Element Method (FEM) or Finite-difference time-domain method (FDTD) [22, 23]. However, insulation systems are composed of materials of very heterogeneous structures at several scales making very the model development from these approaches a challenge. Furthermore these models are specific to a given material and do not deal with the general

case. Moreover, with the space-dependent structure of this model, local defects can not take into account.

With genetic algorithm, position does not matter since statistically all situations will occur. Genetic algorithms simulate the interaction between neighboring states constituting the insulation system. From this interaction, insulation system and its electrical properties evolve over time under electric field and temperature. All heterogeneities of polymer insulation can be easily implemented and added to this model. Finally evolution of polymer microstructure under stress can be simulated simultaneously to its electrical properties variation.

To develop this model, it is necessary to determine what causes the material to change its microstructure, and therefore its electrical properties, as a function of the stress.

In the next section, a review of the main insulation electrical properties and their related measurement method is done. Physical process behind electric charge transport is then presented followed by breakdown and aging models with their advantages and limits. Finally a focus is made on the physical and chemical microstructure of polymer, its evolution under electric field, temperature and time and its effect on dielectric electrical properties, such as space charge and conductivity.

1.2 Electrical properties and related methods

Regardless their intrinsic resistivity, all polymers submitted to high electric fields allow electrical conduction. The charge transport across the polymer results in a measurable current density called *leakage current density* that can be expressed, by neglecting the diffusion current, as:

$$\vec{J}_{leakage} = \vec{J}_d + \vec{J}_c = \frac{d(\varepsilon\vec{E})}{dt} + \sigma\vec{E} \quad (1.2.1)$$

with ε [F/m] the material permittivity, E [V] the electric field, and σ [S/m] the material conductivity. The first term J_d , called displacement current, is due to the electric field variation over time and the second term J_c , called conduction current, is due to the flow of charges under the applied electric field. Leakage current of high resistivity materials can be measured by the method presented in section 1.2.1. However due to their nature, their affinity with their environment and the applied electric field, tremendous variations in the mobility can be observed from one charge carrier to another [23]. Some are very mobile and contribute to the conduction processes. Some others are stuck and can be considered as trapped at the interface or in the bulk of the dielectric. These charges, called *space charge*, do not contribute to the conduction current but induce instead local variations in the electric field. These local differences in the electrical stress were identified in the literature as a major precursor to the ageing and breakdown of HVDC insulation [24]. Indeed, the trapped charges interact with the applied electric field so that the total electric stress may be increased at some positions and decreased in others. For instance, electric field enhancement can induce huge electric stress on tie chains resulting in the formation of microvoids when too many of crystalline lamellae break [25]. Space charge distributions of insulation materials can be measured using several complementary techniques. Among these techniques, the pulsed electro-acoustic (PEA) method consists in applying a voltage pulse

to a sample polarized between two parallel electrodes. The subsequent Coulomb force generates a slight and rapid dislocation of each charge, which yields to pressure waves proportional to the net charge distribution [26, 27]. The thermal step method (TSM) is another technique that consists in applying a thermal step across the dielectric. The thermal diffusion induces local variation of the permittivity and local dilatation of the tested sample [28]. These variations on charges yield to a measurable current. As for PEA, space charge accumulation is monitored as a function of time and polarization field strength. TSM offers a higher resolution at the interface compared to PEA measurements but it is hardly suitable for the characterization of dynamic processes [28]. This makes PEA and TSM complementary space charge measurement methods both being recommended by CIGRE [29, 28]. Detection of electroluminescence (EL) is an alternative technique used to investigate the onset of space charge formation and subsequent electrical degradation in polymer insulation [30]. This technique provides information regarding charge injection from the interface and charge carriers recombination within the bulk of the material.

1.2.1 Conductivity

Leakage current measurements can be performed in parallel plate configuration by applying a high voltage between two electrodes as sketched in Figure 1.2. The subsequent leakage current is then measured with ammeter or voltmeter in divider bridge configuration. Guard electrodes are commonly used to retrieve all surface currents in order to measure exclusively the bulk leakage current. This technique is well documented in the literature [31] and standards [32]. In parallel plate configuration, the corresponding macroscopic electric field is calculated as V/d , where V [V] is the applied voltage and d [m] the sample thickness. In leakage current measurements, the measured current corresponds to the sum of three currents (Figure 1.3) [33]:

- Conduction current proportional to the applied electric field;
- Charging current that corresponds to the charge of the insulator;
- Polarization or/and diffusion current that corresponds to the charges movement inside insulation.

The experimentally measured leakage current can most of the time be fitted with a decreasing double exponential function. The conduction or DC current is defined as the asymptotic value. Macroscopic insulation conductivity is evaluated as:

$$\sigma(E, T) = \frac{i_{DC}}{U} \times \frac{e}{S} \quad (1.2.2)$$

with U [V] the input voltage, i [A] the output current, e [m] the thickness of the sample and S [m²] the surface of collecting electrode (BV) which has the smaller surface. Despite the measured conductivity is a macroscopic value, the latter can be correlated to a certain extent to the microstructure of the sample under test, making conductivity measurement a sensitive probe of the influence of physical and chemical parameters on electrical properties [31]. The exponential current decay can be related to thermal or electrical process, responsible of microstructure changes [34].

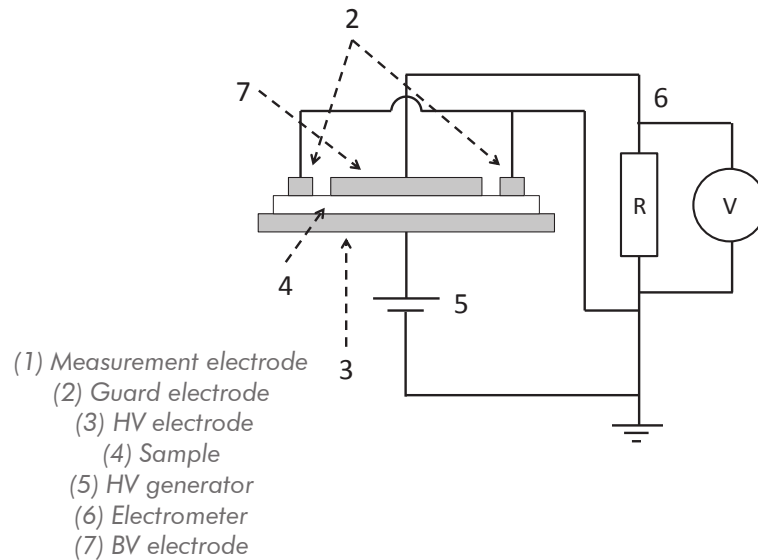
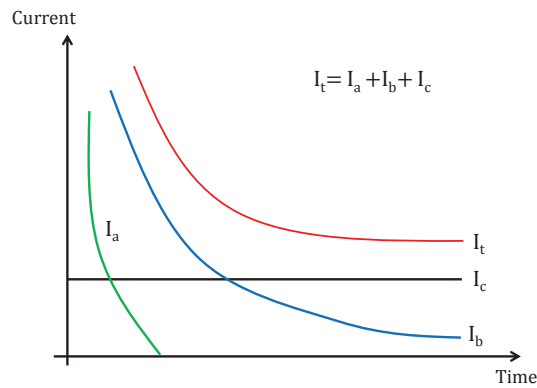


Figure 1.2: Leakage current measurement method on plates.

Figure 1.3: Leakage current I_t decomposition with I_a charging current, I_b polarization current and I_c conduction current. Adapted from [33].

1.2.2 Space Charge (SC)

Space charge is a general term which refers to all charges present inside insulation including [35]:

1. Trapped electric charges or charges with very low mobility. Such charges can be measured using space charge measurement techniques. These charges are considered as extrinsic and can either accumulated at the interface or being trapped within the bulk or near the opposite electrode. In the first case, trapped charges have the same polarity as the neighboring electrode, this space charge is called homocharge. In the other case, the trapped charges have an opposite polarity to the neighboring electrode, this space charge is called heterocharge.
2. Ionic trapped, or mobile charges. These charges may also be present and accumulate if the applied electric field is high enough to cause ionization of impurities. Positive ions will migrate towards the negative electrode and negative ions will migrate towards the positive electrode under the influence of the applied electronic field. As ions cannot penetrate into the metal contact, heterocharge are formed.

Several measurement methods of space charge distribution in solid insulating materials are based on acoustic propagation through materials. The two most commonly used methods to measure space charge distribution are the pressure wave propagation (PWP) method and pulsed electro acoustic (PEA) method [36, 37]. The principle of the pulsed electro-acoustic (PEA) method, developed in 1987 [38], for space charge characterization is shown in Figure 1.4.

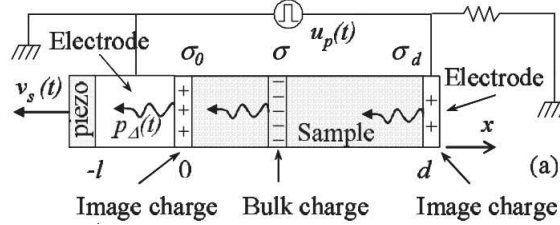


Figure 1.4: Schematic of the basic PEA space charge measurement system [39].

A dielectric sample containing a given charge density $\rho(x)$ is polarized under a steady DC voltage. A voltage pulse (or step) is additionally applied periodically. The subsequent electric field variation ΔE induces a variation of the electrostatic force within the sample under test, yielding to the generation of mechanic waves [40]. This electrostatic force is expressed as:

$$\vec{f} = \rho \Delta \vec{E} - \left[\frac{1}{2} \vec{E} \Delta \vec{E} \vec{\nabla}(\varepsilon) + \frac{1}{2} (\Delta E)^2 \vec{\nabla}(\varepsilon) \right] + \left[\vec{\nabla}(a \vec{E} \Delta \vec{E}) + \frac{1}{2} \vec{\nabla}(a E^2) \right] \quad (1.2.3)$$

In equation (1.2.3), the first term describes the Coulombic force which is the force acting on charges. The second and third terms describe the force density applied to induced dipoles that is the force necessary to align the dipoles among the electric field. The two last terms correct the electrostrictive effect resulting from the slight permittivity change due to the material deformation. In steady state, electrostatic and elastic forces compensate each other. The charges in the dielectric are at equilibrium and $\vec{f} = \vec{0}$ (Figure 1.5).

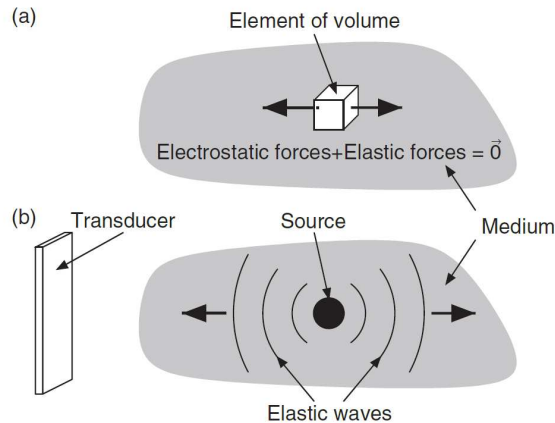


Figure 1.5: Variation of electrostatic force induces elastic force modification resulting in the generation of elastic waves [41].

In space charge measurements by PEA, voltage pulses yield a transient change of the elastic force, resulting in the generation of elastic waves which amplitudes are proportional to the net

charge distribution in the sample under test. In other words, the generated mechanical waves are an image of the distribution and the density of space charge in the sample under test.

Acoustic waves are further collected and converted into an exploitable electric signal using a piezoelectric transducer placed at the sample output. The output signal amplitude is proportional to the space charge amount. The time delay is related to the distance of the charges from the sensor, thus revealing the position of charges within the tested sample. Space charge accumulation is finally probed as a function of time, polarization field strength and temperature.

The described electro-mechanical phenomena is a very fast process (establishment and recovery) that allows for applying voltage pulses at frequencies of 100 Hz or higher. This makes it possible the characterization of dynamic processes such as (di)electrophoresis of polar and ionic species [42].

1.3 Charge transport and aging modeling

Under a critical value of the electric field, insulating synthetic polymers show Ohmic behavior, that is to say a current density change proportional to the applied electric field. However, when the electric field exceeds a threshold value, current density increases following an exponential or power law with electric field [4, 5, 7, 43, 44].

This threshold value also corresponds to the onset electric field for space charge accumulation within the bulk of the polymer [45]. The threshold value depends on several parameters such as the chemical nature of the insulation [46], the injection work function of the electrodes [47], the electrode-polymer interface roughness [47] as well as the testing environmental conditions. Temperature is indeed a prominent parameter: the higher the temperature, the lower the critical field [48]. In the case of LDPE the onset value for space charge accumulation was measured to be in the range of 10 kV/mm at 30°C [49].

It is generally assumed that conduction in synthetic polymers is a thermally activated process meaning that the current density increases with temperature following an Arrhenius relationship:

$$j \propto \exp\left(\frac{-E_a}{k_B T}\right) \quad (1.3.1)$$

with E_a [eV] the activation energy and k_B [J/K] the Boltzmann's constant (1.38×10^{-23} J/K).

The associated charge transport mechanisms are based on the energy band theory [50]. The polymer is described as a semiconductor with a large band gap of more than 5 eV and localized states acting as traps between the conduction and the valence bands.

1.3.1 Analytical model for charge transport

1.3.1.1 Space Charge Limited Current (SCLC)

In this model, the conduction current density is driven by the flow of mobile charge carriers under an applied electric field. The measured current is given by:

$$\vec{j} = \rho \mu \vec{E} - D \vec{\nabla}(\rho) + \frac{\partial \varepsilon \vec{E}}{\partial t} + \frac{\partial \vec{P}}{\partial t} \quad (1.3.2)$$

with ρ [C/m³] the charge density, μ [V.m²/s¹] the charge carrier mobility, D [m²/s] the diffusion constant and ε [F/m] the permittivity. The first term corresponds to the charge transport under electric field, the second term to diffusion current due to a concentration gradient, the third term to the displacement current and the last term to the polarization current. SCLC aims at describing current at steady state meaning that displacement current and polarization current are not taken into account. Furthermore diffusion current is often considered negligible due to the high value of applied electric field.

At low electric field, space charge is low in the bulk of the dielectric and injected charges have a velocity $\vec{v} = \mu\vec{E}$. Conduction current density coming from this charge transport is given by the Ohm's law:

$$\vec{j}_{conduction} = \rho\vec{v} = \rho\mu\vec{E} \quad (1.3.3)$$

When the electric field is increasing, the number of charges injected is also increasing so as space charge. Above an electric field threshold, space charge becomes high enough to induce electric field modification according to Poisson's relation:

$$div(\vec{E}) = \frac{\rho}{\varepsilon} \quad (1.3.4)$$

In one dimension, combining equation (1.3.3) and equation (1.3.4), the relation between current density and electric field is:

$$E(x) = \sqrt{\frac{2j_x}{\varepsilon\mu}(x + x_0)} \quad (1.3.5)$$

With x_0 [m] an integration constant. In case of Ohmic contact (limit case where local electric field is canceled at the interface by the space charge), this integration constant is equal to zero and using the relation between electric field and applied voltage $E = -\partial V/\partial x$, conduction current density relation with applied voltage at high electric field is [51]:

$$j_{conduction,1D} = \frac{9}{8}\epsilon\mu\frac{V^2}{d^3} \quad (1.3.6)$$

with d [m] the insulation thickness. The transition between the Ohmic current behavior and the high electric field behavior occurs at a transition potential given by:

$$V_{tr} = \frac{8\rho d^2}{9\epsilon} \quad (1.3.7)$$

This relation is true only if there are no charge trapping and no intrinsic charge, which is not the case in real insulation. To take into account charge trapping, the first assumption that can be made is to consider a single trapping level. In this case, the mobile-over-trapped charges ratio is given by:

$$\theta = \frac{n_{conduction}}{n_{trapped}} = \frac{N_{conduction}}{N_{trapped}} \exp\left(\frac{E_c - E_t}{k_B T}\right) \quad (1.3.8)$$

where $N_{conduction}$ [m⁻³] is the density of states in the conduction band, $N_{trapped}$ [m⁻³] is the density of traps, E_c [eV] is the energy of the minimum of conduction band and E_t [eV] is the

energy of the trap level. The obtained current density is:

$$j_{conduction,1D} = \frac{9}{8} \epsilon \mu \theta \frac{V^2}{d^3} \quad (1.3.9)$$

The change of current density with voltage is represented in Figure 1.6.

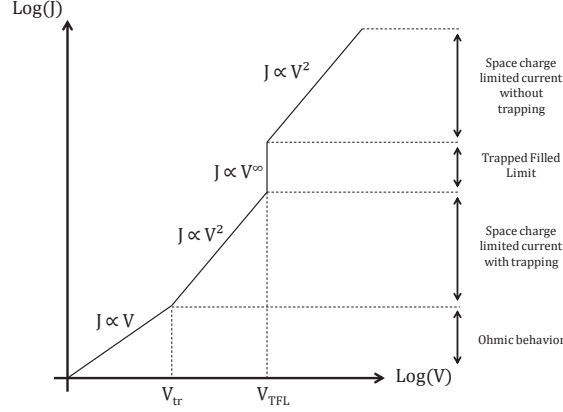


Figure 1.6: Current density *versus* voltage characteristic for a space charge limited current mechanism in case of single trap level.

- when $V < V_{tr}$: No space charge effect on the electric field. Current density follows Ohmic behavior;
- when $V_{tr} < V < V_{TFL}$: Current is limited by space charge with a unique level of trapping and follows equation (1.3.9). Trapping is very efficient and thus the mobile-over-trapped charges ratio is low;
- when $V > V_{TFL}$: This transition is called *trapped field limit* - all traps are full and current is limited by space charge itself instead of charge trapping. Indeed space charge act as electrostatic shield.

The *trapped field limit* obtained from Poisson's equation is given by:

$$V_{TFL} = \frac{qN_{trapped}d^2}{2\epsilon} \quad (1.3.10)$$

The bipolar transport case (electron and hole transport) of this SCLC model was studied by Lampert *et al.* [52]. Similar current density expression as in equation (1.3.6) is obtained but with an effective mobility taking into account mobility of both electrons and holes.

When more than one trap level is attributed to charge trapping, leakage current variation with electric field is no more quadratic. For an exponential distribution of trap levels, the variation of current density with electric field is given by:

$$j_{conduction,1D} \propto \frac{V^{l+1}}{d^{l+2}} \quad (1.3.11)$$

where l is a parameter experimentally obtained from the variation of leakage current *versus* voltage.

SCLC model is widely used in the literature to fit experimental data-sets and explain leakage current behavior against electric field. This model is in particular used to determine the electric field threshold where Ohmic behavior turns to SCLC behavior. Bogeda *et al.* [53] measured a threshold for XLPE and EPR at 10 kV/mm. Dissado *et al.* [45] compared threshold measured in SCLC with the threshold related to space charge accumulation and the threshold related to electroluminescence. The three values were found to coincide. The *trapped field limit* was observed in LDPE for electric field higher than 50 kV/mm [54].

1.3.1.2 Poole-Frenkel [1]

When a charge carrier is trapped, there is a probability of detrapping from this trap to the conduction band which increases with increasing electric field. The required detrapping energy is given by the height of the barrier φ_0 , the applied electric field and the electrostatic field between the carrier which is escaping and a carrier with opposite polarity left in the metal as illustrated in Figure 1.7. The total potential energy is then given by:

$$Ep_{tot} = -\frac{e^2}{4\pi\epsilon r} - eEr + \varphi_0 \quad (1.3.12)$$

with r [m] the distance from the trap. The detrapping energy corresponds to the maximum of this potential energy:

$$Ep_{tot,max} = -\sqrt{\frac{e^3 E}{4\pi\epsilon}} + \varphi_0 \quad (1.3.13)$$

In case of thermally activated hop from trap to conduction band, conductivity is given by:

$$\sigma \propto \exp\left(-\left(-\frac{\beta_{PF}}{k_B T} \sqrt{E} + \varphi_0\right)\right) \quad (1.3.14)$$

with $\beta_{PF} = \sqrt{\frac{e^3}{4\pi\epsilon}}$, the Poole-Frenkel constant.

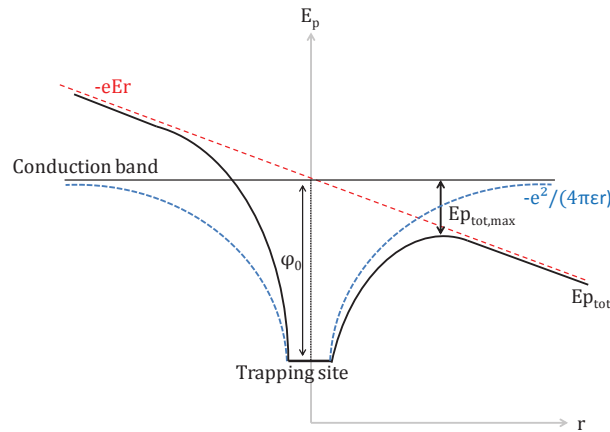


Figure 1.7: Band diagram in the case of the Poole-Frenkel effect.

1.3.1.3 Variable Range Hopping (VRH)

Localized energy states, related to chemical and physical disorder in dielectrics, are present between conduction and valence bands. According to Mott [55], these traps are described as an exponential distribution of energy states. In the VRH model, conduction originates from

charge carrier hopping between localized energy states. Considering an energy diagram with two localized energy states with a spatial distance of ΔR and energy distance of ΔE , the probability of charge transfer between the two sites by thermal activation or tunnel effect is given by:

$$P(\text{thermal}) \propto \exp\left(\frac{-\Delta E}{k_B T}\right) \quad \text{and} \quad P(\text{tunnel}) \propto \exp(-2\alpha \Delta R) \quad (1.3.15)$$

with $\alpha = \sqrt{2mE/\hbar^2}$ [m^{-1}]. Hopping conductivity follows in this case the law: $\log(\sigma) \propto T^{-\frac{1}{4}}$. This relation, observed only at very low temperature (liquid nitrogen temperature), does not take into account the effect of electric field on the energy difference between the two trapping sites.

Variable Range Hopping conduction model taking into account effect of electric field was obtained from the adjustment of ionic conduction model obtained by Mott [51]. With electric field, energy barrier height ΔU is changed according to the electric field direction by the amount $\pm \frac{1}{2}E\Delta x$ (Figure 1.8). By assuming a uniform distribution of localized energy states, conductivity is given by the relation [51]:

$$\sigma \propto \frac{1}{E} \exp\left(\frac{-\Delta U}{k_B T}\right) \sinh\left(\frac{eE\Delta x}{k_B T}\right) \quad (1.3.16)$$

For low electric field, $eE\Delta x \ll k_B T$ and conductivity is simplified to:

$$\sigma \propto \exp\left(\frac{-\Delta U}{k_B T}\right) \frac{e\Delta x}{k_B T} \quad (1.3.17)$$

Conductivity becomes independent of electric field and an Ohmic behavior is obtained as expected at low electric field. For high electric field, $eE\Delta x \gg k_B T$ and conductivity is simplified to:

$$\sigma \propto \frac{1}{E} \exp\left(\frac{-\Delta U}{k_B T}\right) \exp\left(\frac{eE\Delta x}{k_B T}\right) \quad (1.3.18)$$

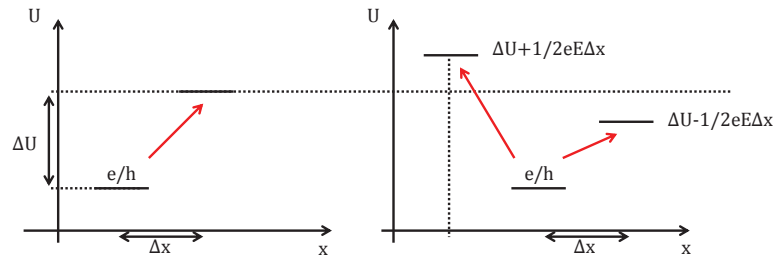


Figure 1.8: Energy diagram for a positive or a negative charge hopping from a site to another, (left) without electric field, (right) in presence of an electric field.

1.3.2 Analytical model for charge injection

Injection of charges from the interfaces is a determining process in the charge generation and transport. Theoretical approaches like Schottky or Folwer-Nordheim describe this injection [7].

1.3.2.1 Fowler-Nordheim injection

The Fowler-Nordheim injection [56] describes the process of a carrier tunnelling through an energetic barrier without hopping as shown in Figure 1.9. By solving Schrodinger equation, probability of crossing an energetic barrier with a width $w = \varphi_0 + E_F - E_p/eE_C$ is given by:

$$P = \exp\left(-\sqrt{\frac{2m}{\hbar^2}} \frac{4}{3} \frac{1}{eE_C} (\varphi_0 + E_F - E_p)^{3/2}\right) \quad (1.3.19)$$

with m [kg] the effective height of charge carrier, E_F [eV] the Fermi energy, E_C [V] the electric field at the cathode and E_p [eV] the potential energy of the charge carrier. Current density is obtained by calculating the velocity and density of charge carriers crossing this energetic barrier:

$$j = -C_1 E^2 \exp(-C_2/E) \quad \text{with} \quad C_1 = e^3/(8\pi h \varphi_0) \quad \text{and} \quad C_2 = 4/3 \sqrt{2m/(e^2 \hbar^2)} \varphi_0^{3/2} \quad (1.3.20)$$

Tunneling effect can occur for an energetic barrier with a maximum width of 50 Å. To this maximum width corresponds a minimum electric field of 200 kV/mm for an energetic barrier of 1 eV.

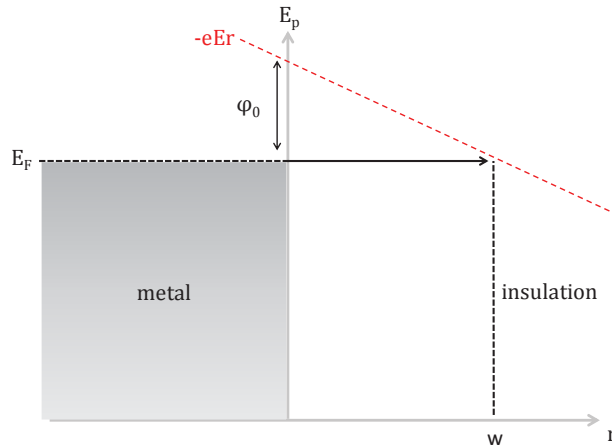


Figure 1.9: Band diagram at the metal/insulation interface with Folwer-Nordheim injection.

1.3.2.2 Schottky injection [2]

At the interface between metal electrode and insulation, Schottky mechanism is similar to Poole-Frenkel effect, except that charge carriers are extracted from the metal as illustrated in Figure 1.10. By considering the height of the injection barrier φ_0 , the electric field at the cathode E_C and the electrostatic field between the carrier which is escaping and a carrier with opposite sign left in the metal, potential energy is given by:

$$E_{p_{tot}} = -\frac{e^2}{4\pi\epsilon r} - eE_C r + \varphi_0 \quad (1.3.21)$$

with r [m] the distance from the trap. The required detrapping energy corresponds to the maximum of this potential energy:

$$E_{p_{tot,max}} = -\sqrt{\frac{e^3 E_C}{4\pi\epsilon}} + \varphi_0 = -\beta_S \sqrt{E_C} + \varphi_0 \quad (1.3.22)$$

From the calculation of the kinetic energy of a charge carrier escaping from metal, and by introducing the Fermi function and the density of state, current density can be expressed as:

$$j_x = AT^2 \exp\left(\frac{\beta_S \sqrt{E_C} - \varphi_0}{k_B T}\right) \quad (1.3.23)$$

with the Richardson's constant $A = 4\pi m k_B^2 e / h^3$ [A/(m.K)²]. To obtain the electric field at the cathode from the applied voltage, space charge at the interface need to be taken into account. E_C is then given by:

$$E_C = \gamma \frac{V}{d} \quad (1.3.24)$$

with V [V] the applied voltage, d [m] the sample thickness and $\gamma < 1$ when homocharges are at the cathode and $\gamma > 1$ when heterocharges are at the cathode. Taylor *et al.* [57] considered that space charge affects the electrostatic field between the carrier which is escaping and a carrier with opposite sign left in the metal. They found an expression of the current density expressed as:

$$j_x = AT^2 \exp\left(\frac{\beta_{TL} E^{\frac{n}{n+1}} - \varphi_0}{k_B T}\right) \quad (1.3.25)$$

with β_{TL} a constant and $n < 1$ when there is space charge effect on interface and $n = 1$ when there is no space charge.

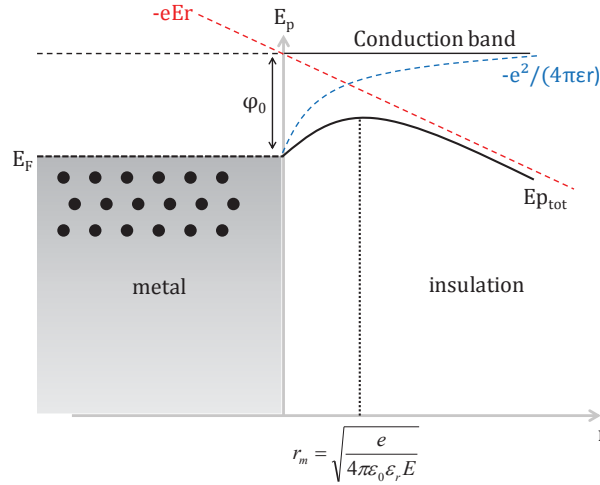


Figure 1.10: Band diagram at the metal/insulation interface with Schottky injection.

1.3.2.3 Interface effect

In the Schottky injection process described in section 1.3.2.2, barrier height for the injection is depending on the metal work function. However, it was shown experimentally that injection is less governed by the metal work function than by localized (or surface) states introduced by rugosity, surface treatment, impurity doping, oxidation surface contamination or adsorbed gas

[58, 59]. For instance roughness difference may lead to strong dispersion in measured leakage current (Figure 1.11) [47, 60]. This interface effect was also seen through space charge measurements with highest injection generally obtained with semiconductive electrodes than metallic electrodes [61, 62]. With semiconductive electrodes, diffusion of the localized states near the interface occurs, most probably due to the distribution of carbon black (CB) particles at the semicon/insulation interface, especially when samples are processed by co-extrusion [9]. These localized states thus enhance injection. According to a simulation made by Xiao *et al.* [63], simulated electric field near the interface was larger for an interface made of CB doped EVA than coated metal, which coincides with larger injection with semiconductive electrodes.

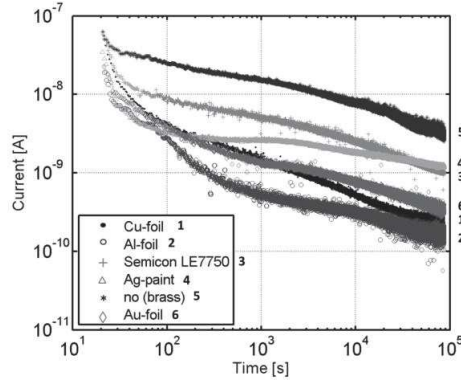


Figure 1.11: Leakage current with various electrode contact [60].

These models are notably used to fit and explain experimental results obtained in conductivity variation measurement and used as a basis to electrical model development.

1.3.3 Breakdown physical process

Electrically and thermally stressed polymer insulation systems see their microstructure change over time, leading to short and/or long term degradations. The former is referred to as breakdown and the latter as ageing phenomena (see Figure 1.12). The three processes responsible for short time degradation are electric breakdown, thermal breakdown and electro mechanical breakdown [24].

1.3.3.1 Electrical breakdown

In the avalanche breakdown mechanism, charge carriers, gaining enough kinetic energy from the electric field, ionize the polymer macromolecules by collisions. Additional carriers are created from the ionization, increasing the collisions probability. This accelerates the structural degradation and creates reaction products such as gases that may damage the solid if the solubility limit is exceeded [24]. The energy released by these charge carriers which is the onset of electrical aging, was observed from optical emission measurements [64]. Several regimes can be considered depending on the kinetic energy of the charge as shown in Figure 1.13 [64]:

1. $E > E_{crit}^{(2)}$: Impact ionization regime with creation of electron-cations pairs ($AB + e_{hot}^- \rightarrow AB^+ + 2e^-$);

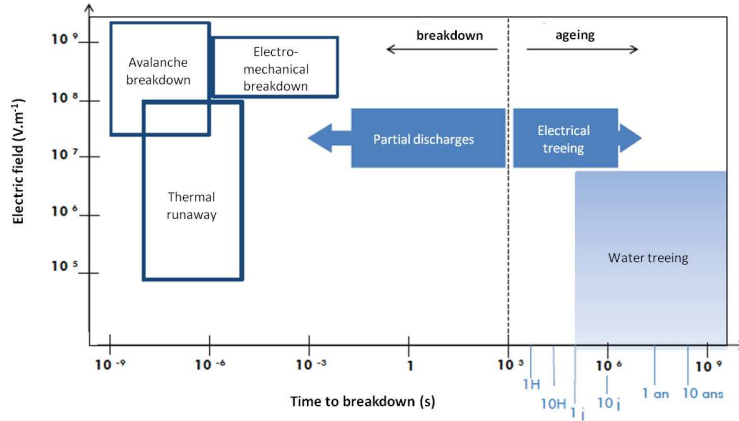


Figure 1.12: Polymer degradation and breakdown mechanisms with the related electric field as a function of time to breakdown. Adapted from [24].

2. $E_{crit}^{(1)} < E < E_{crit}^{(2)}$: Impact excitation regime with creation of an excited state ($AB + e_{hot}^- \rightarrow AB^* + e^-$).

Degradation can be also coming from trapped space charges [65, 66]. In presence of an electric field, a trapped charge may form a quasi-particle called *polaron*. This polaron polarizes the surrounding medium. The permittivity around this charge increases from the vacuum permittivity to a static permittivity as a function of the distance from the trapped charge as illustrated in Figure 1.14. The polarization around a trapped charge increases the local energy. Thus, a large amount of electromechanical energy (2 to 10 eV) is stored in the vicinity of a trapped charge [66]. These charges can be detrapped by high electric field, mechanical stress, rapid temperature increase, or radiation. The internal energy concentrated around a trapped charge is then released, producing either ageing or electric breakdown [66].

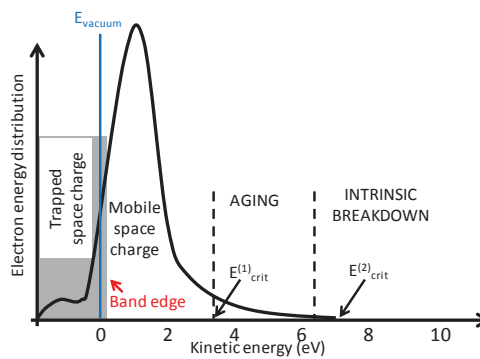


Figure 1.13: Electron energy distribution as a function of electron kinetic energy with $E_{crit}^{(1)}$ the threshold field for impact ionization regime and $E_{crit}^{(2)}$ the threshold field for impact excitation regime. Adapted from [64].

1.3.3.2 Mechanical breakdown

Electro-mechanical breakdown is caused by the decrease in insulation thickness due to electrostatic attraction of the electrodes on both sides of the insulating material. This thickness decrease may be accelerated by the polymer softening due to Joule heating [24].

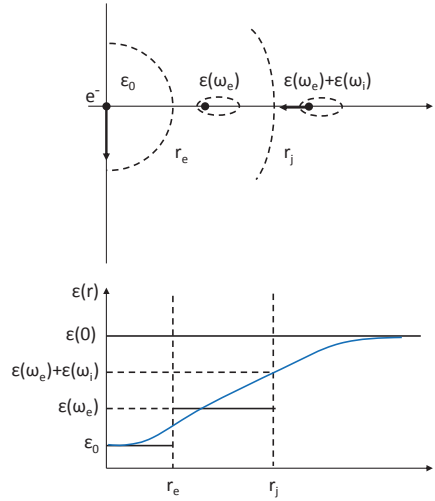


Figure 1.14: Polarisation of the medium around a trapped charge and radial variation of the permittivity. Adapted from [66].

Some measurements reinforced the theory that electrical ageing and breakdown in polymeric solids have essentially mechanical origins [67]. Measurements have demonstrated that applying an electric field to films of polyethylene (PE) and polypropylene (PP) has a marked effect on their viscoelastic properties with a decrease of the elastic storage modulus with increasing electric field [67]. The created stress in presence of an electric field is given by:

$$\Delta\sigma(x) = -\frac{1}{2}\epsilon(x)E^2(x) \quad (1.3.26)$$

Decrease in free volume with aging lowers mobility of macromolecules, and thus decreases charge carriers motion [68].

1.3.3.3 Thermal runaway

Thermal runaway is initiated by a local temperature increase, not dissipated, increasing the local electrical conductivity. This increased electrical conductivity causes more current to flow through the material, increasing the temperature by joule heating. As this process is developing, a thermal runaway can occur in the material [24].

Breakdown strength relative to thermal runaway is below the electronic breakdown strength (100 – 130 kV/mm for XLPE) [69]. Its value is depending on the insulation thickness and the load current [69].

1.3.4 Aging phenomenology and modeling

According to IEC and IEEE standards, aging is defined as: *occurrence of irreversible, deleterious changes in insulating materials or systems which affect their serviceability, i.e their ability to satisfy requested performances* [70]. Ageing refers to as slow degradation processes, which become severe after several years of operation and can root of several failure mechanisms [70]. Along the years, several physical models were developed in the literature to explain ageing process occurring in insulation polymer. In the models proposed for electro-thermal ageing of insulation, material

degradation is initiating and propagating from localized defects [71]. Several ageing causes were assumed: space charge accumulation in the Dissado/Montanari/Mazzanti model [10, 71, 72], high electro-mechanical stress in the Lewis model [25], or high local currents in free volume in the Crine model [73]. It can be noticed that all these models were developed at first to explain AC breakdown process.

1.3.4.1 Dakin, inverse power and Eyring models (1948)

These models were first used to treat thermal ageing or chemical reactions kinetics. They were then adapted for electrical ageing although none does take explicitly into account the effect of space charges on ageing. Dakin's model proposes an electric ageing law based on the Arrhenius law [74]. Eyring's thermodynamic ageing model is based on the equation that describes the kinetics of a chemical reaction *versus* temperature, adapted to take into account the electric field as well. These models do not take into account the complex structure of polymers and do not explain the physical origin of the insulation degradation. However, they are quite simple and still used for the design of insulation systems [75].

1.3.4.2 Crine model

In this model, ageing is described by polymer macromolecules deformation due to electromechanical forces [73]. A threshold electric field is considered for the triggering of macromolecules deformation in the amorphous phase when weak van der Waals bonds are broken, leading to nanocavity formation. Then electronic avalanche occurs after the formation of cavities. Charge carriers ionize the polymer macromolecules after crossing these cavities which enlarge the cavities. The larger the cavities, the higher the kinetic energy of electrons breaking the intramolecular bonds. Strong charge injection occurs only after nanocavity formation, *i.e.* Crine's model considers space charge as a consequence and not as a cause of ageing.

1.3.4.3 DMM (Dissado/Montanari/Mazanti) model

Dissado/Montanari/Mazzanti model considers space charges as the driving force for ageing [10, 71, 72]. In this model, formation rate of defects (called moiety by the authors) into insulation is described with a thermally activated degradation process between two states, *i.e.* un-aged and aged states. An energy barrier represents the transfer between both states during the ageing process.

This degradation is physically triggered by space charge accumulation. Space charge accumulation induces, by polaronic effect, a local storage of electromechanical energy that lowers the energy barrier between the two states. The transfer rate of defects between the two states increases due to space charge accumulation, electric field enhancement and temperature effect (thermal activation). In this model, breakdown is considered to occur when a fraction of moiety has reached the aged states. Space charge accumulation occurs in microscopic morphological defects such as voids located at interfaces between crystalline and amorphous regions. Mechanical stress created by accumulated space charges localized in this void is given by:

$$\sigma = \frac{1}{2}\alpha E^2 \quad (1.3.27)$$

where α [N/V^2] is the electrostriction coefficient. As no macromolecule is present in the cavity, highest stress applied on polymer is present at the interface of this cavity. Due to this stress, a progressive enlargement of this cavity occurs. Then hot electrons are formed and electronic avalanche starts followed by partial discharges and cavity erosion. The main limitation is that this model does not take into account the heterogeneous semi-crystalline structure of PE and the dynamics of macromolecules. Furthermore it considers only two states instead of a distribution of states.

1.3.4.4 Lewis electromechanical model

In this model, polymer degradation comes from electromechanical forces [25, 12]. High electric field stresses polymer macromolecules in the orthogonal direction to the applied electrical field in the amorphous phase. As the stress increases, macromolecules, that connect two adjacent crystalline lamellae, extend between the two lamellae and then pull up from one of the lamellae. These macromolecules fail successively until there is decohesion of the two lamellae and crack formation, as illustrated in Figure 1.15. The crack propagates by breaking all the adjacent polymeric chains to finally form voids. The failure of the material thus corresponds to cavity formations extending under the influence of an electric field. In this model, space charge effect is not considered as a cause of the ageing process.

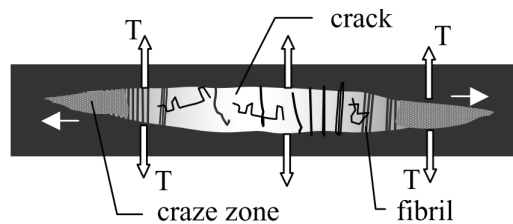


Figure 1.15: Craze and crack development in an inter-lamellar space under tension T [12].

1.3.4.5 Summary

In all the ageing models described above, lifetime depends on an electro-thermal stress. Damage initiates from micro-defects and propagates through the material until breakdown. Ageing is thermally activated and further accelerated by the application of an electric field. For some models, space charges are only a side effect of the ageing, whereas for others, space charges act as a cause of ageing. For all models, even if the applied electric field is not large enough to inject hot electrons, trapped charges store electromechanical and electrostatic energy which may favor degradation reactions by lowering energy barriers. However, each ageing model is based on a single physical concept and their parameters are only related to their mechanisms which cannot always be generalized for all polymeric materials. Thus, these ageing models are not applicable to all polymers. Finally parameters of these model are fixed over time which is not consistent with the polymer micro-structure modification over time.

1.4 Physical heterogeneity effect

In the case of HVDC insulation, the polymer resin commonly used is Low Density Polyethylene (LDPE). This polymer is obtained from polymerization of ethylene monomer at very high pressure (1000 bars) which results in a highly branched PE with a density ranging between 0.91 g/cm^3 and 0.92 g/cm^3 [54]. Contrarily to purely amorphous polymer such as poly(methyl methacrylate) (PMMA), LDPE has a semi-crystalline structure, making it morphologically heterogeneous by nature. Furthermore crosslinking of polyethylene is performed to increase its mechanical resistance at elevated temperatures [76]. Chemical crosslinking of PE is based on the thermal decomposition of a peroxide molecule into radicals. For high voltage applications, dicumyl peroxide (DCP) is the most used peroxide [77]. DCP decomposition in two radicals reacts with PE chains by withdrawing an H^+ and thus starting the crosslinking [76]. This reaction yields to the formation of chemical species that can contribute to conduction increase and trapping [78, 79, 42]. This last point is further discussed in section 1.5.3.1.

This semi-crystalline crosslinked structure induces physical heterogeneities in the polymer. This chapter first aims at defining the changes in heterogeneities that one may expect from electric field and thermal stresses. Secondly, consequences in the electrical properties are described from models and experiments performed in the literature.

1.4.1 Description and formation

1.4.1.1 Description

In semi-crystalline polymers like PE, macromolecules are arranged in spherulites. A spherulite is an organized structure consisting of radial lamellae growing from a nucleation center, and separated from one another by amorphous phase [80]. This is illustrated in Figure 1.16.

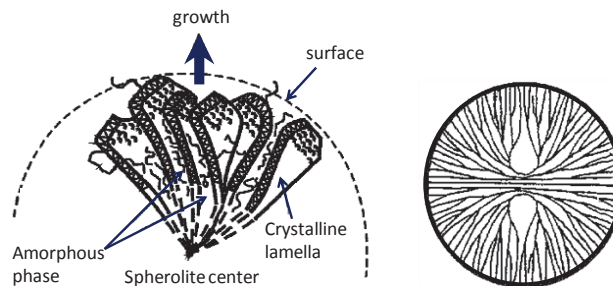


Figure 1.16: Spherulite morphology. Adpated from [81].

During crystallization, spherulites grow until they touch each other or until temperature is too low that growth stops [81]. Lamellae are all-trans PE chains parallel to one another with an orthorhombic crystalline structure [82]. As shown in Figure 1.17, the crystalline lamella thickness is about 20 nm in the PE chain direction (*c*-axis) and 100 nm wide [12, 83]. In this *c*-axis, a strong cohesion is present as this direction corresponds to the PE macromolecules direction with covalent bonds. Whereas in the orthogonal direction (*a*-axis and *b*-axis), cohesion is weaker, achieved by secondary bonds (Van der Walls). Thus, a Young modulus of 240 GPa is measured in the *c*-direction against only 140 GPa in the orthogonal directions [81]. However,

at the macroscopic scale, PE is mechanically isotropic as it contains spherulites with different c -directions. Semi-crystalline structure is characterized by the degree of crystallinity. Two different crystalline fractions are defined [81]: the crystalline fraction in volume defined as:

$$\chi_V = \frac{\text{volume of crystalline phase}}{\text{Total volume}} \quad (1.4.1)$$

and crystalline fraction in weight defined as:

$$\chi_P = \frac{\text{weight of crystalline phase}}{\text{Total weight}} \quad (1.4.2)$$

The distribution in lamellae and spherulite sizes is controlled by the chain structure (molar mass, tacticity defects, comonomer content or chain stiffness) and by crystallization conditions (*e.g.* increased cooling speed yields to smaller spherulites). Furthermore, the melting temperature of polymer lamellar crystals depends on their thickness. The correlation between the thickness of lamellae and their melting temperature was established by Gibbs-Thomson as [84]:

$$T_f = T_{f_0} \left(1 - \frac{2\gamma}{l\Delta H_{f_0}}\right) \quad (1.4.3)$$

where T_{f_0} [K] is the theoretical melting temperature of crystal with infinite size, H_{f_0} [J/m³] is the theoretical melting enthalpy of the 100% crystallized polymer, γ [J/m²] is related to surface energy of lamellar extremity and l [m] is the thickness of lamellae. Wunderlich [85] published the following equation for PE data collected by Illers and Hendus [86]:

$$T_f = 414.2 \left(1 - \frac{0.627}{l}\right) \pm 0.8 \text{ K} \quad (1.4.4)$$

where l is given in nanometer. The distribution in lamellae and spherulite sizes is responsible for the stretched melting temperature range currently observed with polymers. In PE used for cable insulation, the onset temperature for melting is ranging between 30 and 40°C while the melting point (corresponding to the peak maximum in a thermogram) is observed between 90 and 110°C. Amorphous phase consists in a disordered state of macromolecules that can be found between the crystal lamella or between spherulites [87]. In the inter-lamellar space, several conformations exist for the amorphous macromolecules. A continuing chain from the lamellae can take 3 conformations:

- Connecting to an adjacent lamella (tie);
- Returning to the lamella where it comes from (loop);
- Terminating as chain ends (cilia).

Moreover, tie chains play a major role in the mechanical stability of PE [25].

1.4.1.2 Formation

The fraction and morphology of crystalline phase are strongly governed by both cable processing and operating conditions. Crystallization mechanism is decomposed in two mechanisms: nucleation and growth. Both mechanisms require macromolecular mobility. Thus crystallization

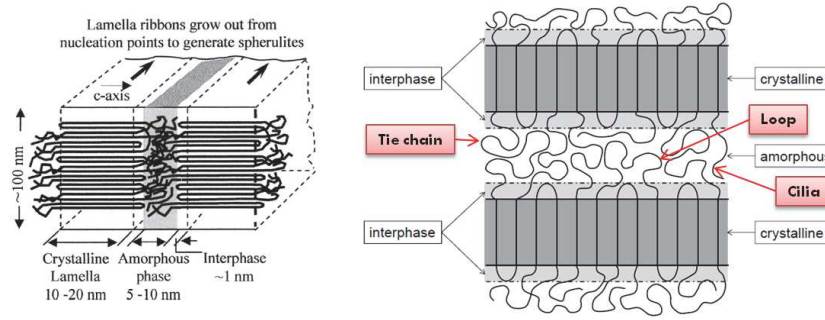


Figure 1.17: Semi-crystalline structure of PE [12].

temperature is obviously between glass transition temperature and melting temperature. The first process, germination, corresponds to the formation of nuclei. However nuclei formation is either triggered by thermal fluctuation in homogeneous polymer in the molten state (homogeneous nucleation) in which case they are assumed to appear sporadically with a linear dependence on time [88]. Nuclei formation can also be triggered by the presence of pre-existing impurities (heterogeneous nucleation) in which case they appear instantaneously at the process start [88]. Nucleation rate is depending on the crystallization temperature: the lower the temperature the higher the nucleation rate [88]. In the second process, crystalline lamellae are growing from the formed nuclei. Growth rate is also depending on crystallization temperature: the higher the temperature the higher the growth rate [89]. Thus, from these two processes, crystallization rate is maximum at a temperature between glass transition and melting temperature [89] as described in Figure 1.18.

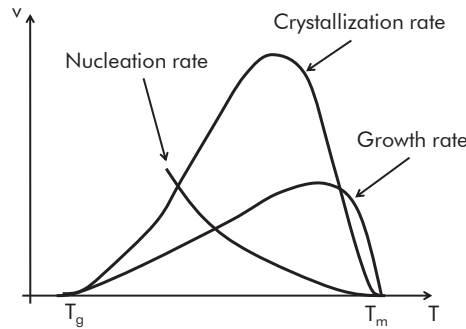


Figure 1.18: Nucleation rate, growth rate and crystallization rate as a function of crystallization temperature.

During crystallization, crystalline fraction increase over time is given by an equation developed by Avrami *et al.* [90]:

$$\chi_C = (1 - \exp(-kt^n)) \quad (1.4.5)$$

with t [s] the time, k [s^{-n}] a constant depending on material properties and n the Avrami constant: an integer having a value between 1 and 4 depending on whether nucleation is isothermal or not, and also on the number of dimensions in which growth occurs.

Several parameters may also affect polymer crystallization. Among them, chain structures such as length of monomer, branching and crosslinks amounts are factors that, when increasing, decrease crystalline fraction [91, 92]. Processing aids such as plasticizers or solvents also decrease

crystallinity by separating macromolecules. Furthermore crystalline fraction is determined by crystallization conditions such as cooling rate [93, 94] (the higher the cooling rate, the lower the crystallinity). However the sensitivity to cooling speed varies with the polymer nature and macromolecules conformation: polyethylene terephthalate (PET) has a crystallinity very sensitive to the cooling speed [95], whereas PE shows only limited sensitivity because of the very fast macromolecules rearrangement [95]. Furthermore, mechanical stress during crystallization may yield anomalous crystalline morphology [96]. For instance, biaxially orientation of polypropylene (BOPP processes) resulting from macromolecules orientation during processing may be observed [97]. Specific semi-crystalline structure can also be found in multilayered systems [98]. Finally, transcrystalline structures may be found at polymer interface with semiconductive or metallic electrodes where the growth of spherulite is hindered laterally [87].

1.4.2 Behavior under temperature and electric field

1.4.2.1 Annealing effect

After crystallization, thermal treatment of polymer at temperatures comprised between glass transition and melting temperature affects their semi-crystalline morphology. Annealing at a temperature below melting temperature results in a recrystallisation of thinnest crystal lamellae into thicker ones. This recrystallization is either due to partial melting of these lamellae or to the diffusion of crystalline defects out from the crystalline phase by an α -relaxation process [99] (see section 1.4.2.2). Indeed, Hestad *et al.* [100] observed a clear influence of thermal history on the morphology change of PE. Differential Scanning Calorimeter (DSC) measurements were performed on virgin XLPE and XLPE after annealing at several temperatures. Despite the authors measured same crystalline fractions from one sample to another, a change in the thermogram profile was observed and ascribed to recrystallisation. For PE, this effect is maximum for an annealing time of 30 min. No further structural change occurred at longer annealing times [99]. For PP annealed at 90°C, a new melt peak appears close to the applied temperature of 90°C [101]. The authors observed a dependency of the maximum melting temperature of this secondary peak to cooling rate [101]. The secondary peak is located at a lower temperature for a higher cooling rate [101]. The change in melting temperature may be responsible for the change in PP mechanical properties with a decrease of tensile strength after thermal treatment [101]. As insulation is submitted to thermal cycles during cable operation, this annealing effect is likely to occur.

1.4.2.2 Relaxation processes

As a function of temperature, macromolecule relaxations in polymer occur both in the crystalline and amorphous phases. These chain dynamics are described by relaxation processes. In the temperature interval between the melting point and 0 K, two or even three processes are commonly observed [102]. Relaxation processes are highly depending on the degree of crystallinity of the polymer [102]. Indeed the amorphous phase, where the relaxation processes take place, is more restrained in polymer with a high degree of crystallinity than with a medium degree of crystallinity [102]. In PE, three relaxation processes are observed with increasing temperature, namely γ -relaxation, β -relaxation and α -relaxation [102].

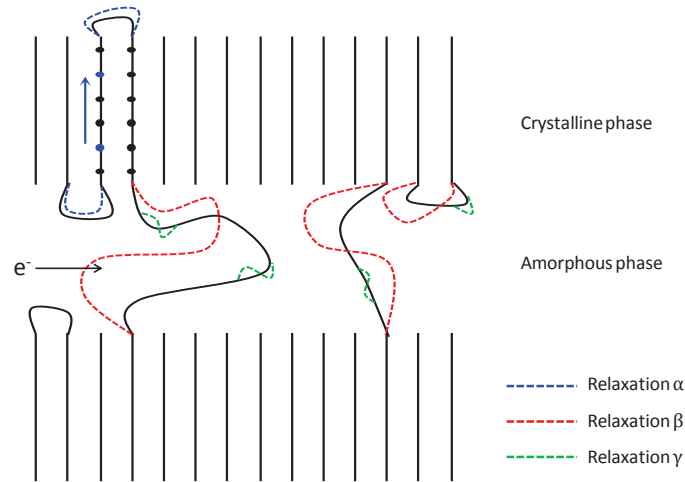


Figure 1.19: Relaxation processes in semicrystalline polymer.

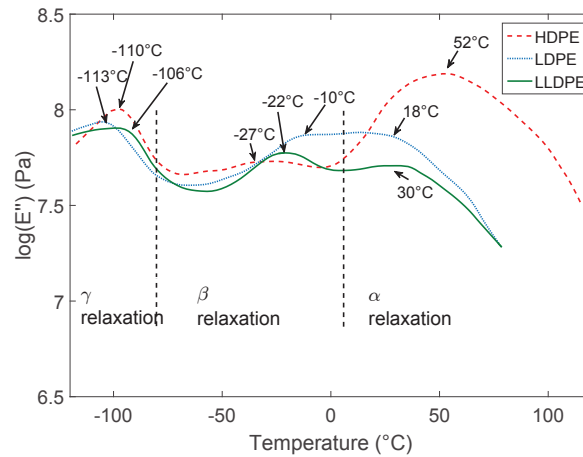


Figure 1.20: Relaxation processes measured with DMA for several PE. Adapted from [103].

At the lowest temperature, γ -process corresponds to local motion within the amorphous phase but also at loose chain ends in crystals [102] as shown in Figure 1.19. It is observed on Dynamic Mechanical Thermal Analysis (DMTA) between -107°C and -120°C (see Figure 1.20) [103]. The intensity of the γ -peak decreases with increasing polymer density indicating their presence in the amorphous phase [103]. Furthermore γ -relaxation temperature increases with the number of carbon atoms between the surfaces of the crystal, *i.e.*, the fold length [102]. γ -process involves local molecular motions of shorter range compared to the β -relaxation [104].

At higher temperature, β -relaxation occurs which corresponds to correlated molecular fluctuations of the chain segments in the amorphous phase and also corresponds to the dynamic glass transition [105]. β -process occurs at relatively low temperature with a maximum of loss modulus between -5°C and -35°C which depends on the nature of PE (see Figure 1.20) [103]. The relaxed amorphous phase modulus is very high (of the order of 100 MPa) due to the constraining influence of the crystals [102] and is decreasing strongly with temperature and increasing with frequency. T_{β} increases with increasing molecular weight and increasing amount and size of branching [95].

At higher temperature, the α -process occurs. It corresponds to movement in the crystalline lamellae [105]. It is the highest temperature process with a maximum of loss modulus, observed by DMTA, between 20°C and 60°C (see Figure 1.20) [103]. α -relaxation amplitude increases with PE density [95] and its related temperature increases with crystal lamellar thickness [95]. The α -peak was thus experimentally ascribed to the crystalline phase. This relaxation process corresponds to translation of macromolecule segments assisted by a chain twisting in the crystalline phase (see Figure 1.19) [105]. This process impacts also the amorphous macromolecules in the inter-lamellar space connected to the crystal. As the lamellar thickness depends on the thermal history of PE, α -relaxation depends highly on thermal history of PE.

All these three processes follow an Arrhenius behavior with an activation energy of around 0.2 eV for γ -process [102], around 0.6 eV for β -process [102] and around 1.2 eV for α -process [102].

1.4.2.3 Behavior under electric field

When electric field is applied to semi-crystalline polymers, electro-mechanical stress is applied to macromolecules. Experimentally, when studying mechanical deformation of semicrystalline polymer as a function of increasing electric field, two variations are observed [12, 106]. Under an electric field threshold, mechanical deformation is increasing linearly with electric field whereas, above this electric field threshold, variation is quadratic. This mechanical electric threshold is very close to the electric threshold value between Ohmic behavior and SCLC behavior in the leakage current measurement of this same material [12, 106] as shown in Figure 1.21. Applying an electric field introduces two different stresses: Maxwell stress and electrostrictive stress [107, 108]. Electrostrictive effect expresses the coupling between the polarization and mechanical response in the material and Maxwell effect is due to the interaction between free charges on the electrodes (Coulomb interaction) and to electrostatic forces that arise from heterogeneities present in the polymer. Strains resulting from both effects are proportional to the square of the applied electric field [109].

α , β and γ relaxation temperatures were shown to coincide with current peaks observed by thermo-stimulated current (TSC) measurements [4] (see section 1.4.3.1). The current peaks associated to charge detrapping, correspond to activation of macromolecular motions at several scales. In Figure 1.22, a temperature increase relative to the peak C_3 and C_4 is shown with increasing electric ageing time [110]. It means that the activation energy of chain motions relative to the α and β processes is increasing under electric field.

1.4.3 Effect on electrical properties: model and experiment

The semi-crystalline structure of polymers plays a major role on electrical properties. Indeed, charge carrier transport depends both on the nature of the charge carrier and on the microstructure of the surrounding media.

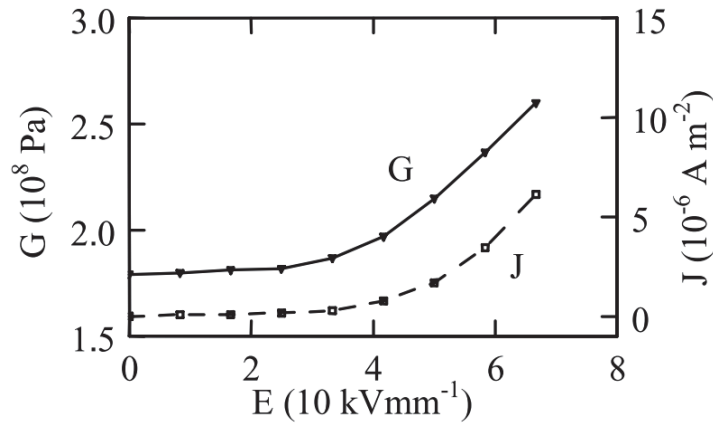


Figure 1.21: Correlation of shear modulus G and current density J for LDPE at room temperature [12].

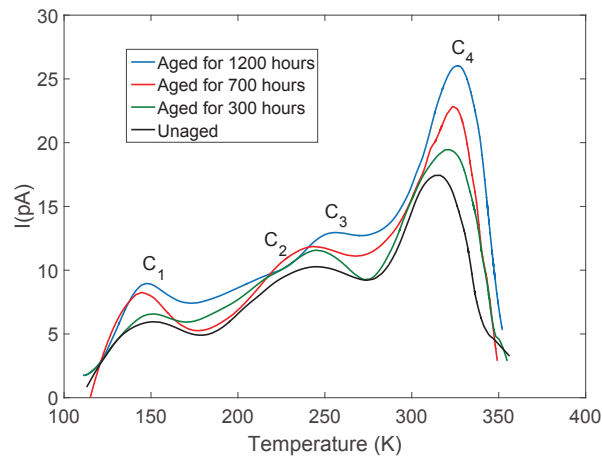


Figure 1.22: Effect of aging time on TSC spectrum in LDPE. Adapted from [110].

1.4.3.1 Charge transport model in specific heterogeneous semicrystalline polymeric structure

Mechanisms governing charge transport, trapping and detrapping are intimately related to the nature of electronic states in dielectric polymers. Figure 1.23 shows the energy diagram of PE. Conduction and valence bands are separated by a band gap larger than 8 eV [111]. Moreover, the energy of the conduction band is 0.4 eV lower in the amorphous phase than in the crystalline one [82]. Consequently, electron conduction is more likely to occur in the amorphous phase. From Density Functional Theory (DFT) electronic calculation, it is shown that injected electrons in PE are mostly transported between the polymer chains by hopping process [112]. For holes, transport occurs along the PE chains with a hopping probability higher in crystalline regions than in amorphous region [113]. However, the electrical behavior of semicrystalline polymers such as polyethylene could not be described properly by using conventional band diagrams, which do not take into account the heterogeneous structure of polymers. To take into account the contribution of heterogeneities, the scientific community introduced localized states between the conduction and the valence bands as illustrated in Figure 1.23 [114, 115].

The localized states in the energy diagram constitute traps for charge carriers. Depending on the energy difference with the conduction band, these traps are considered as *shallow* or *deep* traps. The trapping energy for shallow traps is lower than 1 eV. Hence, the residence time of charge carriers inside the latter is very low (10^{-13} s to 10^{-11} s) [116]. Such traps assist the charge transport. Conversely, the trapping energy ascribed to deep traps covers the energy range of 1 to 3 eV, meaning that once caught the electric charges are very difficult to release [117]. In other words deep traps contribute to local charge accumulation in the insulating media. These traps are either of physical (voids, interfaces, conformational disorder) or chemical (impurities in macromolecules, byproducts, antioxidants, radicals) nature [117].

Macromolecular relaxations also appear as governing parameters [117]. The relaxational origin of physical defects was identified in the literature by correlating Thermo Simulated Current (TSC) and Dynamic Mechanical Analysis (DMA) measurements performed on PE [4]. The temperature coincidence observed by the authors between current peaks, associated to charge detrapping, and maximum of mechanical losses resulting from the activation of local and stretched macromolecular motions, is likely to show that charge traps are formed between macromolecules and that the charge release is assisted by molecular motion related to the relaxation processes as illustrated in Figure 1.24.

Furthermore, some of the physical defect such as nanovoids, also originate from conformational changes in PE chains [66, 118]. Trap depth from conformational disorder in the amorphous regions are between 0.15 eV and 0.3 eV with a trap density of 3.1×10^{20} traps/cm³ [116]. Moreover, the interfacial regions between amorphous and crystalline structures have been demonstrated from DFT to constitute deep electron traps of 1 eV [119].

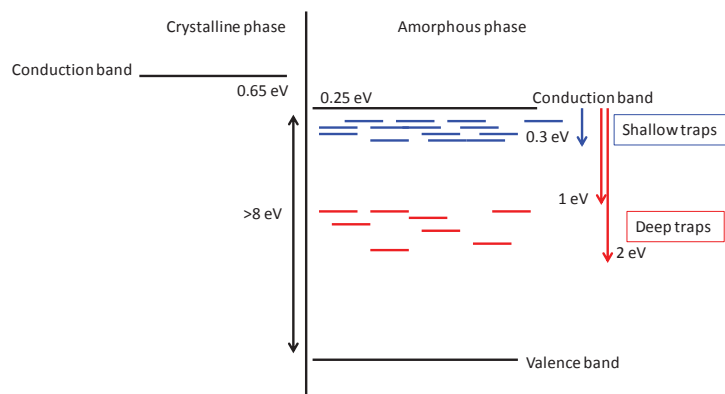


Figure 1.23: Energy diagram of PE.

Based on energetic description, predictive models were developed. Among them, Le Roy *et al.* developed two models of bipolar charge transport in polyethylene [59, 120, 121]. These models were developed to simulate the distribution of electric field and leakage current as a function of stress in a wide range of polymers. DFT results were taken as a basis for these model developments by using the trap energy distribution for holes and electrons. For both models, Schottky bipolar injection (holes and electrons) is considered and there is no extraction barrier. In the first model, shown in Figure 1.25, two energy levels are considered in the band diagram [121]: *i*) A *transport level* where charge carriers are transported with a mobility depending on the electric field, the temperature and taking into account the possible trapping and detrapping in shallow traps. *ii*) A *trapping level* where charge carriers are deeply trapped and where they

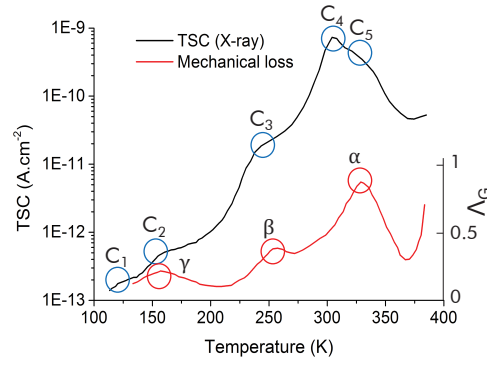


Figure 1.24: Thermo-Simulated Current (TSC) and Dynamic Mechanical Analysis (DMA) as a function of temperature in PE. Adapted from [4].

have a probability to be detrapped. From this model coefficients B_e and B_h have been defined as trapping coefficients for respectively electrons and holes and D_e and D_h as detrapping coefficients for respectively electrons and holes. Charge carrier recombination is also taken into account with 4 recombination coefficients. In the second model, an exponential distribution of trapping levels is considered [23]. Charge transport is in this case described by a hopping mechanism between traps of this exponential distribution.

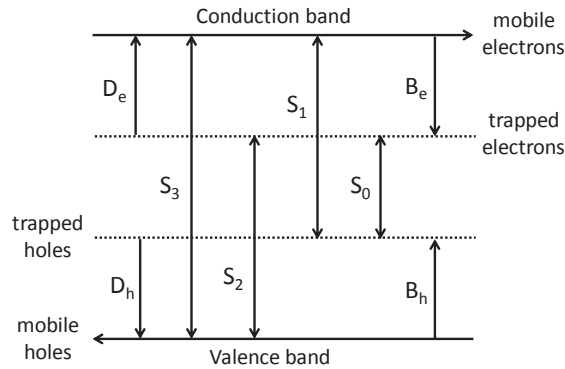


Figure 1.25: Schematic representation of the conduction and trapping coefficients for the first model of Le Roy *et al.* S_1 , S_2 , S_3 and S_4 are recombination coefficients, B_e and B_h are trapping coefficients and D_e and D_h are detrapping coefficients. Adapted from Le Roy *et al* [120].

From these descriptions, space and time dependent equations, such as Gauss equation and the charge conservation law, are solved considering an one-dimensional problem. Boundary Element Method is used to determine the electric field distribution and numerical scheme for the solving of the transport equation [122]. Good prediction results are obtained in LDPE for several geometries (plates and cables) and for several surface states. However these models have some limitations. Firstly, they only consider electronic transport and are not valid anymore in case of ionic contribution which can be a problem in case of undegassed XLPE simulation. Furthermore, simulation of another polymer than PE need a complete recalculation of the set of parameters. Finally they do not take into account polymer microstructure change over time such as annealing or aging.

1.4.3.2 Effect on conductivity and space charge

The amount and morphology of crystallized PE macromolecules impact both charge conduction and trapping [117]. Similarly to gas permeation, crystallites act as barriers to the conduction process and contribute to charge accumulation [117]. Such phenomenon is already described for AC electric field by the Maxwell-Wagner-Sillars polarization. Maxwell-Wagner-Sillars polarization is a polarization process caused by a separation of charges taking place at the boundaries of crystalline-amorphous interface [123].

The crystallinity, considered as a barrier for electron, is likely to impact charge transport and trapping. In leakage current measurement, Ping *et al.* [124] observed for HDPE, in the crystalline range from 50% to 70%, an increase of the current density variation *versus* electric field with crystallinity increase. It means that the higher the crystallinity, the higher the activation energy of charge transport. In space charge measurements, Zhao *et al.* [93] measured space charge in linear low density polyethylene (LLDPE) for several various crystalline fraction χ_c from 50% to 65% at 40°C under 40 kV/mm. No effect of χ_c has been observed on charge injection, but charge packet phenomena were observed with a mobility around $10^{-16} \text{ m}^2/(\text{V s})$ which was decreasing as crystallinity was increasing. They ascribed these results to the higher crystallinity formed at lower cooling rate which act as deep trap for charges [93]. It may also be due to the amorphous/crystalline interface increase with crystallinity, acting as deep trap of 1 eV for electron. It yields to a higher activation energy for detrapping and a decrease of charge packet mobility.

The impact of crystalline/amorphous interface on electrical properties was further demonstrated by comparing conductivity of HDPE with LDPE [54]. Much lower current density and higher charge amount have been measured for HDPE compared to LDPE as shown in Figure 1.26. Furthermore, dielectric measurements performed on both samples showed a higher imaginary permittivity at low frequency for HDPE (see Figure 1.27). These low-frequency peaks are generally associated with interfacial polarization, thus higher peaks indicate larger amount of interface charge. With a larger crystalline/amorphous interface amount, higher deep trapping occurs in HDPE resulting in lower conductivity than for LDPE.

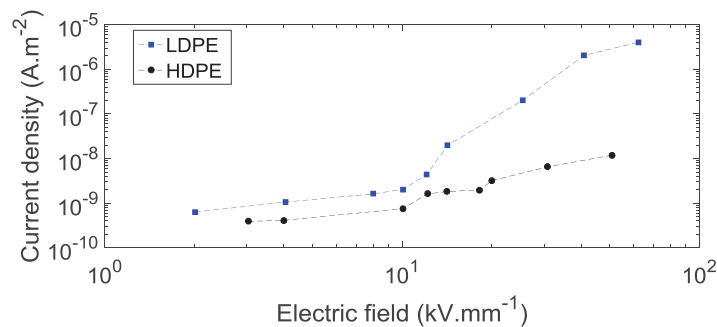


Figure 1.26: Current density DC on log-log plot of LDPE and HDPE as a function of electric field at 25°C. Adapted from [54].

With spherulite diameter increase in HDPE, Kolesov *et al.* [125] observed an electric strength decrease. They ascribed this result to the density decrease of the polymer in the amorphous phase with spherulite size increase [125]. It may also be a hint that the amorphous/crystalline

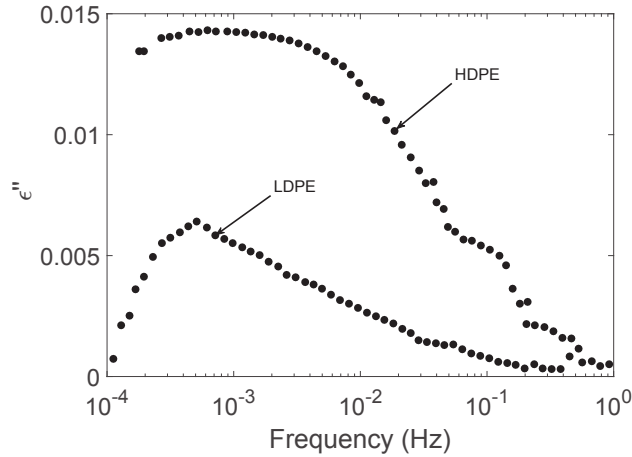


Figure 1.27: Imaginary part of permittivity *versus* frequency for HDPE and LDPE, derived from the Fourier transform of discharging current curves under $E = 14 \text{ kV/mm}$. Adapted from [54].

interface is increasing with spherulite diameter. As this interfacial region act as deep trap for charges, there is an increase of space charge leading to an electric strength decrease.

Chemical crosslinking with peroxides yields the formation of covalent bonds between macromolecules in the molten state. A first consequence is a decrease of the crystalline fraction due to the polymer chain mobility decrease [31, 126]. The second consequence is the presence of crosslinking bonds affecting polymer chain relaxation by limiting movements of PE macromolecules, explaining a lower conductivity in XLPE than in LDPE [127, 128, 129]. Moreover, higher conductivity threshold and higher activation energy was measured in XLPE compared to LDPE [128]

Copolymerisation of polymer have also an effect on conductivity. Nakane *et al.* [130] showed that copolymerisation of PP by 3-3.5% of ethylene enhances its conductivity at 40°C and 50 kV/mm and Li *et al.* [131] observed that space charge of random copolymers of PP with 3.4% of ethylene have a much lower space charge amount than PP. When ethylene is randomly distributed in PP, at each ethylene units along molecular chains, regular arrangement of propylene unit sequence into lamellae is held back stopping the lamella growth. It results in lower spherulite size and lower crystalline lamellae thickness. The authors ascribed the conductivity increase by the presence of small lamellae that act as shallow traps for charges [131]. It may also be a hint to the fact that interfacial amorphous/crystalline region, acting as deep trap, is decreasing explaining the decrease of space charge accumulation and increase in conductivity.

Annealing modifies polymer morphology and thus its electrical properties. Aakre *et al.* [101] studied the influence of annealing on PP conductivity and observed a conductivity decrease after thermal treatment. As seen in section 1.4.2.1, annealing at a temperature below melting temperature results in a recrystallisation of thin crystal lamellae into thicker ones. Thicker lamellae restrain more amorphous regions and thus decrease electron transport. Even if crystalline fraction is similar, materials may have different electrical properties when the shape of their melt peaks is different.

Summary

Physical heterogeneities in semi-crystalline polymer are highly depending on polymer matrix nature, processing and electrical and thermal stresses. These heterogeneities are present at different scales and can affect strongly polymer electrical properties.

1.5 Chemical heterogeneities

The 1st source of chemical heterogeneities is chemical defects from the PE synthesis. In commercial grades of polyethylene homopolymer, the pristine $-\text{[CH}_2\text{-CH}_2\text{]}_n-$ is often chemically modified to better master the synthesis or to confer specific properties. For instance Borealis developed years ago Supercure PE grades containing a low amount of un-saturated functions in order to improve the polymer reactivity to radical crosslinking [132]. In-chain defects such as double bonds, vinyl, carbonyl or hydroxyl groups are randomly present in PE macromolecules [133].

Several chemical species are present in polymer and constitute a second type of chemical heterogeneities. Chemical species come from formulation (antioxidants), crosslinking (crosslinking by-products), aging (oxidation), and conditioning (water). They are rejected during crystallisation into the amorphous region of XLPE and their mobilities are driven both by temperature and electric field. It is well known that these chemicals even in minimum quantities can dramatically affect the electrical properties of insulation material as they affect both charge transport and trapping [12]. Understanding the influence of such chemical heterogeneities on the electrical properties and their transport through the polymer are of essential importance for the simulation of electrical properties and lifetime of XLPE under temperature and electric field.

1.5.1 Charge transport model in polymeric structures with chemical residues

Similarly to physical heterogeneities, chemical defects and impurities introduce localized states into the band gap of PE. Position of the localized states related to the different chemical heterogeneities was obtained using DFT.

In-chain chemical defects such as carbonyl, vinyl, hydroxyl, double bonds and conjugated double bonds generate both deep traps, in the range of 1.0 to 2.3 eV, as well as shallow traps in the range of 0.1 to 0.5 eV [133, 134, 135], as depicted in Figure 1.28. The charge-trapping ability of chemical heterogeneities results either from the chemical structure of the considered heterogeneity, or from subsequent physical distortion of adjacent ethylene groups.

Concerning peroxide decomposition products, cumylalcohol constitutes shallow traps for both holes and electrons, acetophenone constitutes shallow traps for holes and deep traps for electrons and α -methylstyrene constitutes deep traps for both holes and electrons [134, 135], as shown in Figure 1.29. Crosslinking by-products constitute a very interesting case as they are intrinsic deep traps with high mobility. Indeed by-products are prone to migrate under electric field and temperature by diffusion or ionic transport [136, 137, 42].

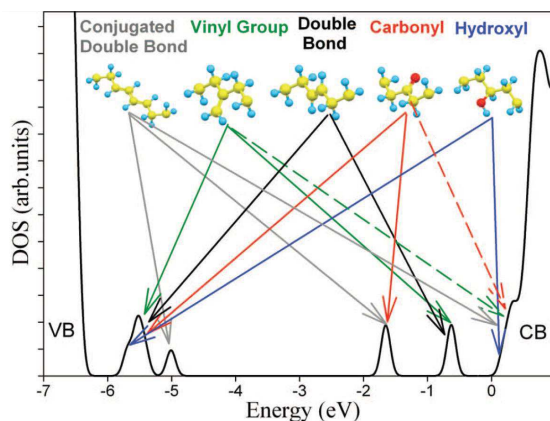
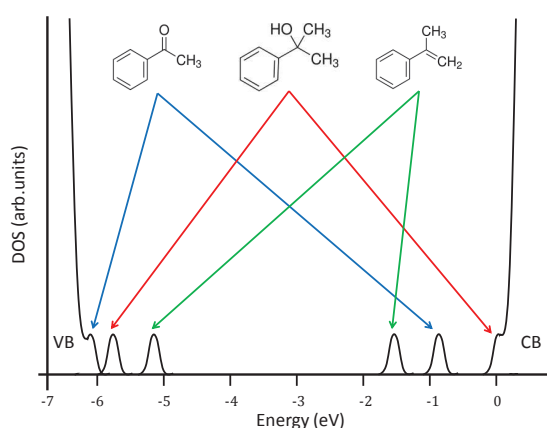


Figure 1.28: Localized states associated to in-chain defects [133].

Figure 1.29: Localized states associated to peroxide decomposition products defects (energy state values obtained from Meunier *et al.*[134] and Teyssedre *et al.*[134, 135]).

1.5.2 Behavior under temperature and electric field

1.5.2.1 Behavior under temperature

Chemical residues are distributed in the free volume of the amorphous phase [138]. Under temperature, diffusion of these impurities occurs through polymer. Diffusion characteristic time depends on the polymer morphology, the concentration of the species, the temperature and the physical and chemical interactions between the diffusing substances and the polymer matrix [139]. Two mathematical models, Fick's law and Arrhenius equation, explain most of the diffusion processes. Fick's first law ascribes the diffusion of species through a polymer matrix due to concentration gradient:

$$F = -D \frac{\partial c}{\partial x} \quad (1.5.1)$$

with F [m^2/s] the rate of mass transfer per unit cross section, c [m^{-3}] the concentration of migrating species, x [m] the direction of diffusion, and D [m^2/s] the diffusion coefficient. The diffusion coefficient follows an Arrhenius law:

$$D = A \exp\left(-\frac{E_A}{RT}\right) \quad (1.5.2)$$

with A [m^2/s] the pre-exponential factor, E_A [J/mol] the activation energy, R the gas constant ($8.314 \text{ J}/(\text{mol}\cdot\text{K})$) and T [K] the temperature. The morphology of polymer play a major role on

the diffusion of species. For instance, for same migrants at same temperature, diffusion constants in LDPE are four times larger than for HDPE due to the barrier effect of the cristallites [139]. Diffusion constant decreases with increasing molecular weight of the species in polyolefins. The molar volume has only a small impact [139, 140]. Furthermore the polymer-migrant interaction strongly influence the diffusion constant [139]. Polar groups and chain branching in migrants considerably decrease the diffusion rate in polyolefins [139]. However, halogenated molecules and molecules containing aromatic rings diffuse much more rapidly than aliphatic molecules of similar molecular weight in polyolefins [139].

1.5.2.2 Behavior under electric field

In presence of electric field, chemical impurities can react in two different ways. They can be ionized generating cations and anions that can further migrate by electrophoresis. Otherwise a partial dipolar alignment in presence of electric field can occur. Ionic dissociation of polar peroxide decomposition products is favoured by temperature [48] and by the presence of water. Electrical conduction in polymers under relatively low electric fields is considered to be ionic and is affected strongly by the microstructure of polymer. The ionic conductivity can be described using an Arrhenius law.

In polymers, ionic transport is related to free volume between macromolecules, more than electronic charges as their size is much higher [141]. Conductivity equation taking into account this free volume was established by Miyamoto *et al.* [142]:

$$\sigma \propto \exp\left(-\gamma \frac{V_f^*}{V_f} - \frac{E_A + W/(2\varepsilon)}{k_B T}\right) \quad (1.5.3)$$

with W [eV] the ionic dissociation energy, ε [F/m] the dielectric constant, V_f [m³] the free volume, V_f^* [m³] the critical free volume, and γ a constant value to correct the overlap of the free volume. Arrhenius plot of ionic conductivity of several polymers have shown a linear variation with a slope change at a given temperature [142]. This temperature corresponds to the glass transition temperature of the polymers. At temperature above the glass transition, global molecular fluctuation of macromolecules occurs in the amorphous phase which results in an increase in the free volume. By taking into account the free volume change in the Arrhenius plot of ionic conductivity, plots are linear with a single slope in all temperature range including the glass transition region. Slope of this linear variation is related to the activation energy and the ionic dissociation energy. When electric field is applied, as for hopping conductivity, energy barrier height $E_A + W/(2\varepsilon)$ is changed according to the electric field direction by the amount $\pm \frac{1}{2} E \Delta x$. Conductivity is then given by the relation [51]:

$$\sigma \propto \frac{1}{E} \times \exp\left(-\gamma \frac{V_f^*}{V_f} - \frac{E_A + W/(2\varepsilon)}{k_B T}\right) \times \sinh\left(\frac{eE\Delta x}{k_B T}\right) \quad (1.5.4)$$

For infinitely diluted solution of ions, mobility of ionic species is related to their diffusion coefficient with the Nernst-Einstein relation:

$$\mu = \frac{qD}{k_B T} \quad (1.5.5)$$

1.5.3 Peroxide decomposition products (PDP)

1.5.3.1 Formation

Crosslinking polyethylene reaction process is triggered by a radical reaction through the thermal decomposition of peroxide agent such as dicumyl peroxide (DCP). This reaction yields chemical impurities such as methane, water, acetophenone, cumylalcohol and α -methylstyrene, as illustrated Figure 1.30. Whereas methane is easily degassed after crosslinking, the other species may remain in cable insulation for dozens of years [143].

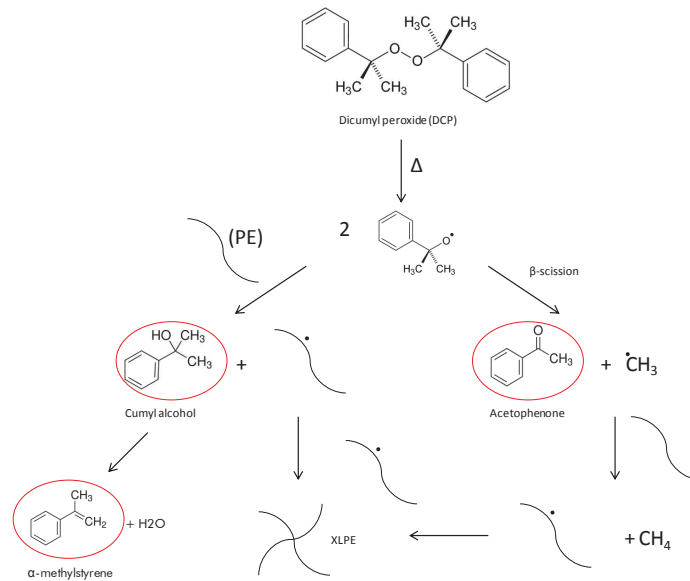


Figure 1.30: Crosslinking reaction of PE with DCP .

The main physical properties of the remaining PDP are presented in Table 1.1. Methane has appreciable solubility in PE, but can form bubbles in the absence of pressure. This is why cable vulcanization is achieved at a high pressure conditions. Each peroxide decomposition product has specific activation energy of formation. Thus the proportion of the different peroxide decomposition products (PDP) is depending on the crosslinking temperature [144] as shown in Figure 1.31.

An increased crosslinking temperature favors β -scission resulting in higher acetophenone and CH_4 contents. Furthermore, crosslinking by-products are also well known in the literature to play a major role in the premature degradation of the insulation by impacting conductivity and space charge behavior [129, 145]. They may also impact the morphology of semi-crystalline polymer if maximum solubility is reached [126].

PDP	acetophenone	α -methylstyrene	α -cumylalcohol
T_{melting}	19-20°C	32-34°C	24°C
T_{boiling}	198°C - 204°C	88°C - 90°C	164°C - 168°C
Permittivity (28°C)	17	5.6	9.7

Table 1.1: Main physical properties of the PDP.

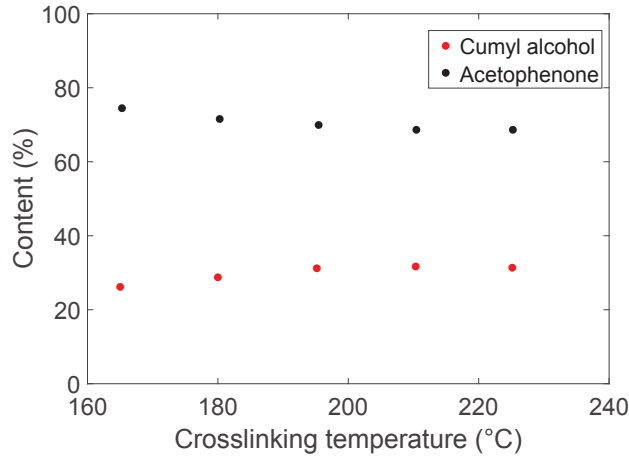


Figure 1.31: Content of Acetophenone and Cumyl alcohol in XLPE as a function of temperature. Adapted from [144].

1.5.3.2 Diffusion properties

Diffusion constant of PDP, measured at different temperature by Sahyoun *et al.* [146], are presented in Table 1.2. The corresponding activation energies are 0.72 eV for acetophenone and cumylalcohol and 0.92 eV for α -methylstyrene. Similar diffusion constant of $8.413 \times 10^{-13} \text{ m}^2/\text{s}$ was measured for acetophenone at room temperature by Wutzler *et al.* [138].

Diffusion constant (m^2/s)	Temperature			
	22°C	50°C	70°C	80°C
Acetophenone	8.66×10^{-13}	1.39×10^{-11}	5.54×10^{-11}	12.80×10^{-11}
α -cumylalcohol	1.52×10^{-13}	0.86×10^{-11}	3.12×10^{-11}	8.17×10^{-11}
α -methylstyrene	14.30×10^{-13}	1.02×10^{-11}	9.42×10^{-11}	15.9×10^{-11}

Table 1.2: Diffusion constant of PDP at different Temperatures [146].

1.5.3.3 Effect on space charge and conductivity

Montanari *et al.* [128] compared the conductivity of XLPE plates before and after thermal treatment (90 h at 50°C). The authors observed a factor 10 decrease in current density after thermal treatment, as shown in Figure 1.32. Thermal treatment both modifies the crystalline structure and removes volatile species such as crosslinking by products. However, the observed conductivity decrease should be attributed to the residue desorption. Indeed a much lower current density variation was observed in LDPE being submitted to the same thermal treatment. Under electric field, PDP can dissociate, act as shallow traps and assist charge transport, or act as deep traps and favor accumulation. Space charge in PE is highly modified with the presence of PDP. At room temperature and under 35 kV/mm, homocharge accumulation is observed in LDPE and fully degassed XLPE, whereas heterocharge is measured in undegassed or partially degassed XLPE [147]. Furthermore heterocharge in XLPE accumulates quickly (<1 h) and a large part of it decays just as quickly whereas homocharges in degassed XLPE accumulate slowly and decay even slowerly (> 24 h) [147].

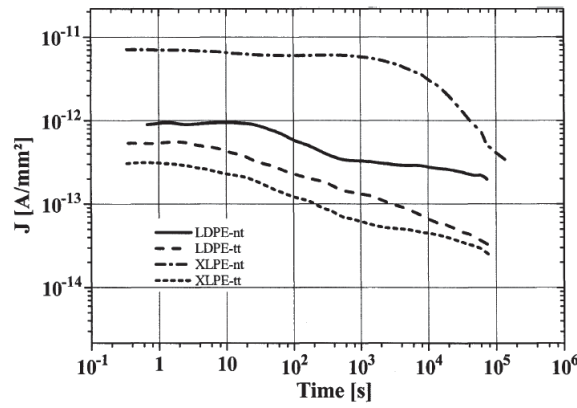


Figure 1.32: Current density at 60 kV/mm and 20°C of LDPE and XLPE, before and after thermal treatment [128].

Hussin *et al.* [79] studied the influence of each by-product on space charge and conductivity by soaking LDPE samples. For acetophenone, negative charge accumulation up to 8 C/m^3 is measured at room temperature under an electric field between 30 and 60 kV/mm, which is consistent with the deep trap role of this molecule on electrons. For α -methylstyrene, both negative and positive homocharges accumulation are measured, which is consistent with the deep trap role of this molecule for both electrons and holes. For cumylalcohol, negative heterocharges are measured. Le Roy *et al.* [42] measured heterocharges in LDPE with cumylalcohol for an electric field from 5 kV/mm and 25 kV/mm at 10°C, 25°C and 50°C as shown in Figure 1.33. The presence of heterocharges has been attributed to ions either coming from cumylalcohol dissociation or ionization. Furthermore, current density increases under 10 kV/mm and 15 kV/mm with the presence of cumylalcohol was measured [42] that can be attributed to ionic conductivity of this by-product or to the electric field enhancement due to heterocharge accumulation.

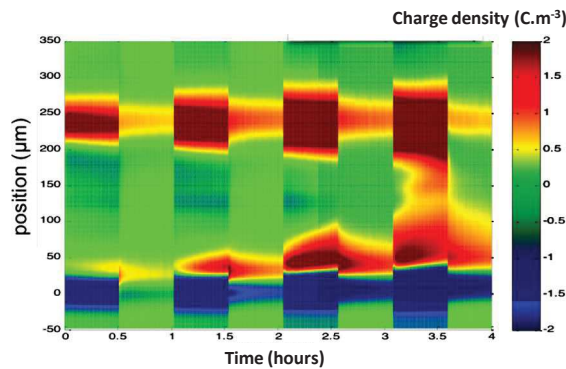


Figure 1.33: Space charge as a function of time and space in LDPE soaked in cumyl alcohol for 4 hours for a protocol of 30 min polarization and 30 min depolarization under electric field of 10, 15, 20 and 25 kV/mm at 25°C [42].

1.5.4 Antioxidants

1.5.4.1 Formation

In addition to peroxide, antioxidants are also added to XLPE to prevent radical degradation both during process and lifetime. Antioxidant is added to prevent oxidation of PE and to improve the heat resistance. Several types of antioxidants are used in polymers such as sulfur antioxidant, phenolic antioxidant and amine antioxidant as shown in Figure 1.34. Phenolic antioxidant is a primary antioxidant that can react with PE radical (alkyl radical) to form phenolic radical [148]. Sulfur-type and amine-type antioxidants are secondary antioxidants that can react with the cumyloxy radical from the DCP [149, 150]. They can also react with cetone, aldehyde, alcohol or acid which are formed within the PE macromolecules during the ageing process [149, 150]. Secondary antioxidants are more efficient against ageing as they inhibit the process of PE radical formation [151]. Sulfur-type and amine-type antioxidants have both an effect on PE crosslinking reaction: Amine-type antioxidant decreases the gel fraction of XLPE and sulfur-type antioxidant appears to delay the crosslinking reaction [144]. Antioxidants may act as center of nucleation impacting the crystallinity as observed by Boudou with a decrease of spherulites size from 40 μm to a few micrometer by adding 0.2% of Bis(4-hydroxy-5-terbutyl-2-lethylephenyl)sulphide [129].

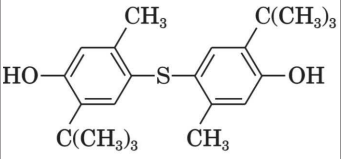
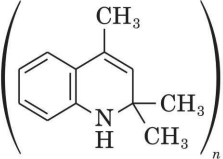

Phenolic antioxidant	Amine antioxidant	Sulfur- and Phosphorous antioxidant
		
4,4'-Thio-bis-(3-methyl-6-tert-butyl phenole)	Polymerized 2,2,4-trimethyl-1,2-dihydroquinoline	Dioctadecyl disulfide

Figure 1.34: Example of antioxidant type.

1.5.4.2 Effect on space charge and conductivity

With phenolic antioxidant, negative homocharges accumulation was measured at 70°C under 70 kV/mm [152]. It shows that phenolic antioxidant probably acts as deep traps for electrons. Conductivity decrease of almost one decade was measured by Goshowaki *et al.* [31] in LDPE with the presence of 0.1% to 0.3% of phenolic antioxidant or sulfuric antioxidant as shown in Figure 1.35. Boudou *et al.* [99] observed contradictory results on phenolic antioxidant at 0.2%

in LDPE with a higher current density for electric field higher than 10 kV/mm. In the first case, antioxidant acts as deep trap explaining the lower conductivity. In the second case, spherulite radius is lower in presence of the antioxidant as observed by Boudou *et al.* [99]. It means lower crystalline/amorphous interface yielding to lower charge trapping and higher conductivity.

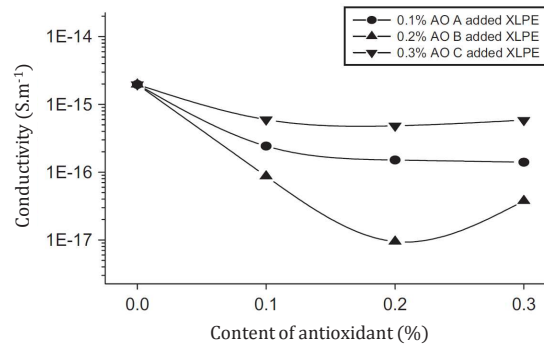


Figure 1.35: Conductivity of fully degassed XLPE under electric field of 30 kV/mm) as a function of content of antioxidant (A and C) phenolic type, (B) sulfuric type [31].

1.5.5 Water content

1.5.5.1 Formation

Water is often present at very low concentration in insulation materials. Firstly, insulation can be in contact with water during the cooling processes of production in CV line. Secondly, the changes in relative humidity of the environment may cause water absorption [153]. Water is also present in XLPE insulation as by-product of the crosslinking reaction coming from the decomposition of cumylalcohol into alpha-methylstyrene and water [154]. Finally, semiconducting layers at the interface of XLPE insulation may contain water as well for the same reasons. Besides, solubility of water is much higher in semiconducting material with fillers compared to non-filled insulation material [154]. However, water molecules may redistribute with time between semiconducting and insulation material according to the temperature history and the solubility characteristics of the materials [154]. At room temperature, the solubility of water in XLPE is close to 100 ppm due to the polar chemical defects present within the macromolecules (carbonyl and hydroxyl) and to the presence of crosslinking by-products. Solubility increases with temperature, typically from 140 ppm to 280 ppm when temperature increases from 70°C to 90°C [155]. However by increasing the temperature, diffusion coefficient of water in XLPE is also increasing, and has to be taken into account to estimate the actual water concentration.

1.5.5.2 Diffusion properties

For water diffusion in LDPE, two diffusion processes were observed by Fourier transform infrared spectroscopy (FTIR) [156]: a fast diffusion process attributed to monomeric water and dimeric water and a slow diffusion process related to cluster water. By taking into account both of these diffusion processes, water diffusion coefficient measured at different temperature is reported in Table 1.3. The related activation energy is 0.31 eV which is close to the hydrogen bond energy for water (0.16 eV) [17].

	Temperature			
	25°C	40°C	60°C	80°C
Diffusion constant (m ² /s)	8.38×10^{-14}	1.69×10^{-13}	2.79×10^{-13}	5.61×10^{-13}

Table 1.3: Diffusion constant of water at different Temperatures [156].

1.5.5.3 Effect on space charge and conductivity

To study influence of water on PE electrical properties, experiments were performed, under controlled relative humidity, in climatic chambers [157, 154, 158]. Low increase of XLPE conductivity was measured with increased of relative humidity for temperatures from 20°C to 80°C under electric field up to 30 kV/mm [154, 157]. Furthermore, with increase of relative humidity, trapped charge increase have been observed, however no effect on the electric onset of space charge was noticed [158]. It is worth noting that in all these measurements, only the value of relative humidity was measured and not real water amount contained in PE.

1.5.6 Oxidation

1.5.6.1 Formation

Thermal aging of XLPE can yield a modification of the chemical composition of its macromolecules. For instance Li *et al.* compared the IR spectra of XLPE aged for 22 years at 60°C under air conditions to unaged XLPE. Thermal oxydation of the polymer was observed by the occurence of IR absorption bands corresponding to ketone, aldehyde, alcohol and carboxylic acid [159]. The formation of these polar groups goes along with PE radicals formation and post crosslinking reaction [160].

In presence of oxygen, thermal decomposition of PE is a reaction with an activation energy of 0.83 - 1.48 eV. The usual oxidation reaction begins by formation of radical sites initiated with temperature but also with UV radiation or presence of peroxide. Oxygen reacts with the radical to form a peroxy-radical. The peroxy-radical abstracts hydrogen to form hydroperoxide and a radical center. The former yields to an alkoxy radical that can abstract a hydrogen to form a hydroxyl group. Intermolecular and intramolecular H-abstractions lead to formation of new radical sites:



Oxidation occurred in the amorphous zone where oxygen can travel easily.

1.5.6.2 Effect on space charge and conductivity

Conduction current increase is observed in LDPE by almost two orders of magnitude for an increase of C=O group absorbance in infrared spectroscopy and is ascribed to localized state formation at the interface due to C=O groups enhancing electron injection [161, 58]. This increase has been also observed in LDPE stressed under 50 kV/mm for 1000 h at various oxygen concentrations (0%, 20%, and 50%) leading to an increasing growth in oxidation product relative to ketone and aldehyde functional groups [162]. Similar carbonyl group increase is observed in PE with thermal aging at 100°C for 15 and 30 days [158] as shown in Figure 1.36. In both studies, space charge measurements on aged LDPE samples showed negative homocharges with a charge accumulation increase with carbonyl group increase as demonstrated in Figure 1.37. Furthermore with aging at 100°C, threshold electric field for charge accumulation decreases from 15 to 11 kV/mm [158]. It is likely that carbonyl groups from PE oxidation introduce deep traps in the volume of the material.

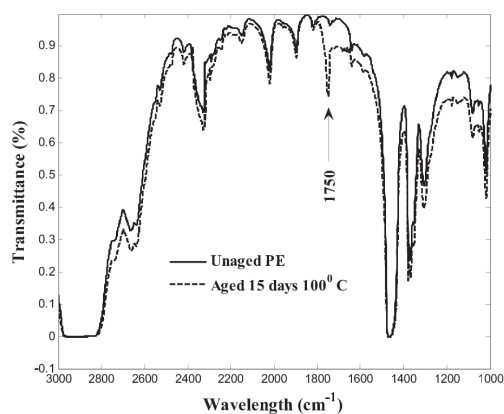


Figure 1.36: Infrared spectroscopy of unaged and thermally aged PE [158].

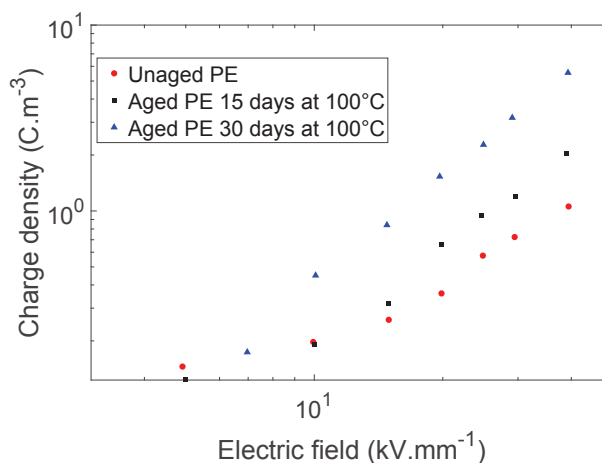


Figure 1.37: Space charge amount as a function of electric field for unaged and aged PE. Adapted from [158].

Summary

Several chemical heterogeneities are present in insulation polymer affecting strongly its electrical properties. The main barrier for preexisting models is to incorporate all these chemical heterogeneities because of their mobile nature as a function of electric field, temperature and time. The aim of the model is to take into account all these heterogeneities and their evolution.

Chapter 2

Experimental approach

This chapter aims at better identifying the respective contributions of polymeric heterogeneities, physical or chemical, on the electrical properties of interest for HVDC applications and their dependence to temperature and electric field. Concerning physical heterogeneities, a focus is made on crystallinity, crosslinking and macromolecular mobility. For that purpose, PET, PP, and PE have been used as material *models*. Concerning chemical heterogeneities, the influence of peroxide decomposition products (PDP) on XLPE electrical properties is studied. Finally influence of interface injection is performed by comparing electrical properties of XLPE in direct contact with brass electrodes and semicon electrodes. In the first section the used material *models* are presented with specific manufacturing process developed to precisely control their microstructure modification. The second section focuses on the physical and chemical analysis of these material *models*. In the last sections are presented the different electrical test benches developed for conductivity and space charge measurements and used on the material *models* to study their electrical properties in addition to dielectric spectroscopy measurements.

2.1 Materials

2.1.1 PE-based material

Several polyethylenes have been chosen as material *models* for studying both physical and chemical heterogeneity impacts on polymer electrical properties.

For crystalline fraction impact, electrical properties of LDPE, HDPE and XLPE are compared. XLPE grade is obtained from LDPE crosslinking with dicumyl peroxide (DCP). Crosslinking is performed under pressure (150 bars) at 190°C for 10 min and then XLPE is degassed for 3 days at 80°C. Melting temperature and crystalline fraction at room temperature measured by Differential Scanning Calorimetry are shown in Figure 2.1.

For leakage current measurements, measurements are performed in thin polymer plates of 350 μm thickness with brass electrodes. For space charge measurements, XLPE based semiconductive electrodes are incorporated inside insulation during sample manufacturing with a final dielectric thickness in the range of 700 μm to 1 mm.

For the influence of PDP, an initial peroxide amount of 1.28wt% is used for PE crosslinking. In this study, the global amount of PDP of fresh XLPE samples is changed by applying degassing

PE-based material	melting peak temperature ($^{\circ}\text{C}$)	χ_c at room temperature
LPDE	110	0.42
HDPE	136	0.80
XLPE	105	0.38

Table 2.1: PE-based materials with melting peak temperature and crystalline fraction χ_c measured by Differential scanning calorimetry.

steps of controlled duration at room temperature. For all insulation systems, the selected amount of chemicals was kept during the whole test duration (up to weeks at 70°C). The PDP wt% of tested XLPE measured by Thermogravimetric analysis is shown in Table 2.2.

XLPE	Degassing time at room temperature (h)	PDP wt%
sample A	0	1.27
sample B	1	0.72
sample C	4	0.56
sample D	6	0.36
sample E	10	0.03
sample F	>12	0

Table 2.2: PDP wt% of tested XLPE samples measured by Thermogravimetric analysis.

Finally, to probe the influence of interface on leakage current measurements, insulation system composed of XLPE insulation with XLPE based semiconductive layers (semicon) are press molded together. Degassed insulation systems are tested and compared to insulation with brass electrodes.

2.1.2 PP-based material

PP-based material is used as material *model* for the study of the influence of the crystallinity as the crystalline fraction of this apolar material can be easily controlled over a broad range. Two grades of PP are used: a grade of PP with a low crystalline fraction, a flexural modulus of 100 MPa and a Melt flow rate (MFR) of 0.8 g/10 min and a grade of PP with a high crystalline fraction, a flexural modulus of 1080 MPa and a MFR of 0.95 g/10 min. PP materials with various crystalline fraction are then obtained by preparing blends of the two references. By varying the relative amounts, a series of samples has been prepared with crystalline fractions ranging from 10% to 40%, as shown in Table 2.3.

PP blends	PP blend A	PP blend B	PP blend C
% of PP 1	100	56	0
% of PP 2	0	44	100
Crystalline fraction at room temperature	0.12	0.27	0.44

Table 2.3: PP blends with crystalline fraction measured by Differential scanning calorimetry.

For leakage current measurement, thin polymer plates ($\sim 350\ \mu\text{m}$) are processed and tested with brass electrodes. For space charge measurements, elastomeric semiconductive electrodes of $500\ \mu\text{m}$ thickness are placed on both sides of the samples plates after processing. Thickness of PP plates are around 1 mm.

2.1.3 PET-based material

PET is used as material *models* for the study of crystallinity influence and for macromolecules relaxation influence on polymer electrical properties. PET samples are press molded at 290°C for 1 min then quenched into cold water to obtain very low crystallinity. The almost amorphous samples (crystallinity is measured lower than 3%) are then further annealed for 10 min at different temperatures in the cold-crystallization temperature range (105°C-130°C). The higher the annealing temperature, the higher the resulting sample crystallinity. The processed PET samples with increased crystalline fraction are shown in Table 2.4.

Annealing temperature (°C)	Annealing time (min)	χ_c at room temperature
Quenched	–	0.03
105	1	0.1
105	10	0.25
115	10	0.33
125	10	0.40
130	10	0.42

Table 2.4: Processed PET samples with increased crystalline fraction χ_c measured by Differential scanning calorimetry.

As for PP samples, elastomeric materials of 500 μm thickness are used for semiconductive electrodes in space charge measurements. Thin plates of 200 to 300 μm thickness are used for dielectric spectroscopy measurements.

2.2 Physical and chemical characterization

2.2.1 Morphological analysis

2.2.1.1 Differential scanning calorimetry (DSC) method

DSC analyses measure physical transformation in material such as phase transitions. By detecting the difference in heat flow as a function of temperature between the sample and a reference at the same temperature, the amount of absorbed or released heat during such transitions is measured. Glass transition corresponds to a step in specific heat ΔC_p whereas polymer melting or crystallization are respectively detected by an endothermic or exothermic peak. DSC measurements are performed using a Q2000 DSC from TA Instruments. The calibration of temperature and heat has been performed using Zinc ($T_{onset}(Zn) = 419.47^\circ\text{C}$, $\Delta H_m(Zn) = 108.37 \text{ J/g}$) and Indium ($T_{onset}(In) = 156.60^\circ\text{C}$, $\Delta H_m(In) = 28.45 \text{ J/g}$) at a rate of 10°C/min. Samples of 5 to 10 mg are placed in an aluminum pan and an empty pan is used as a reference. Two heating scans are carried out by using a heating rate of 3 K/min from -20°C to 220°C for PE and PP based material and from -20°C to 300°C for PET based material. Between the heating scans is performed a cooling scan at a rate of -3 K/min from 220°C to -20°C in PE and PP based materials and from 300°C to -20°C for PET.

2.2.1.2 Analysis on material *models*

DSC is performed on the material *models* to quantify their crystalline fractions and characteristic temperatures. For PE-based material, DSC is performed in LDPE, HDPE and XLPE. The thermogram corresponding to the second heating of PE-based materials is shown in Figure 2.1.

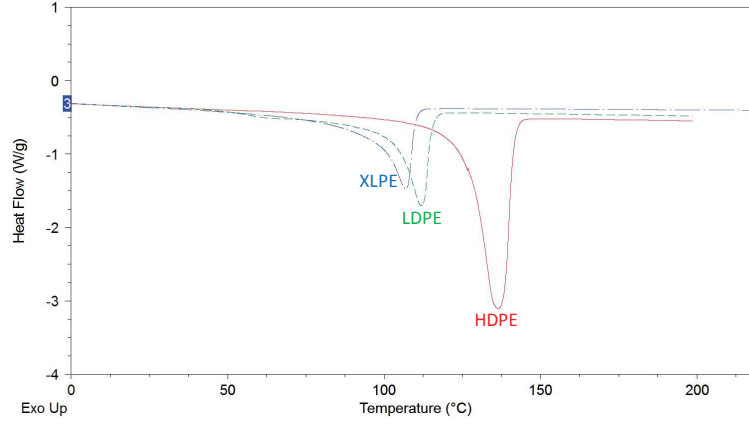


Figure 2.1: DSC measurement of LDPE, HDPE and XLPE.

With increasing temperature, an endothermic peak is observed corresponding to the melting of PE. The onset temperature and peak temperature are the lowest in XLPE and the highest in HDPE. The enthalpy difference ΔH_f due to endothermic peak allows the calculation of the crystalline fraction:

$$\chi_c = \frac{\Delta H_f}{\Delta H_{f0}} \quad (2.2.1)$$

with ΔH_{f0} [J/g] is the theoretical melting enthalpy of the 100% crystallized polymer (290 J/g for PE). HDPE has the highest crystalline fraction with $\chi_c = 0.80$ at room temperature, then LDPE with $\chi_c = 0.42$. The lowest crystalline fraction is obtained in XLPE with $\chi_c = 0.38$. The lower crystalline fraction of XLPE compared to LDPE is due to the polymer chain mobility decrease with the presence of crosslinking bonds [31, 126].

Annealing effect is also investigated in XLPE. DSC of XLPE is performed before and after thermal treatment at 70°C for 5 min. On the thermogram in Figure 2.2 of the two samples during heating at 3 K/min, a difference can be clearly seen in the temperature range of annealing. The correlation from Gibbs-Thomson between the thickness of lamellae and melting temperature demonstrates that the thinnest crystal lamellae melt during annealing and recrystallize into thicker ones [84].

From literature, after 30 min of annealing, no further variation has been observed [99].

For PP based material, crystalline fractions of the processed blends are measured from the melting peak in the second heating and the equation (2.2.1) with $\Delta H_{f0} = 196$ J/g. Measured crystalline fractions are in the range from 0.12 to 0.44.

The thermogram corresponding to the first heating of a quenched PET sample is shown in Figure 2.3. A step in the heat flow corresponding to the glass transition is observed at 70°C. At higher temperature, an exothermic peak is observed corresponding to the cold crystallization of PET [163]. The onset temperature of this crystallization process is observed at 105°C, the peak

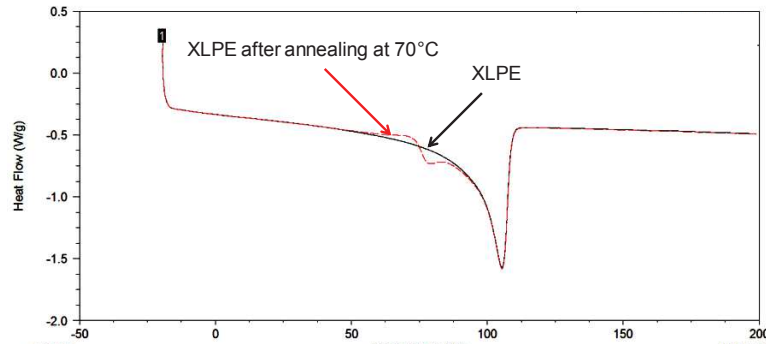


Figure 2.2: DSC measurement of fresh XLPE and XLPE after annealing.

temperature is 130°C. At even higher temperature, the observed endothermic peak corresponds to melting. Its onset temperature is 190°C and the peak temperature is 250°C. The enthalpy difference between cold crystallization and melting (or re-crystallization) allows for calculation of the initial crystalline fraction.

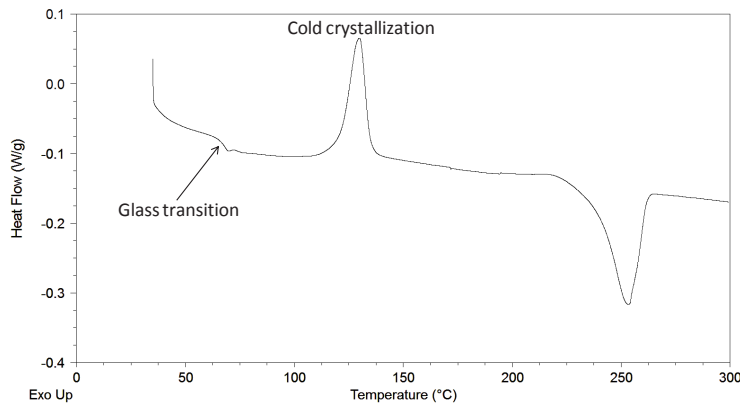


Figure 2.3: DSC measurement of amorphous PET.

2.2.1.3 Crystallinity variation with temperature

From the thermogram corresponding to the first heating measured by DSC, variation of crystalline fraction with temperature is obtained. Figure 2.4 shows crystalline fraction variation with temperature for LDPE, XLPE and HDPE. A high decrease of crystalline fraction with temperature is measured for LDPE and XLPE with a crystalline fraction halved from 30°C to 70°C. Indeed the onset of melting for LDPE and XLPE is around 50°C and partial melting occurs very soon in temperature. For HDPE, onset of melting is around 85°C. Thus crystalline fraction of HDPE is barely affected by temperature increase in the range of 30°C to 90°C with a decrease lower than 0.1%. Figure 2.5 shows crystalline fraction variation with temperature for the three PP blends. For all PP blends, low decrease of crystalline fraction with temperature is measured as their onset of melting is around 100°C. A decrease lower than 0.1% is measured in the temperature range from 30°C to 90°C.

For PET, from 30°C to 90°C, no variation of crystalline fraction is measured with temperature. Figure 2.5 shows crystalline fraction variation with temperature for quenched PET from 90°C to 250°C. From 90°C to 130°C, crystalline fraction is increasing from 0.03% to 0.44% due to the cold crystallization of PET [163]. At higher temperature, crystalline fraction remains stable

until the onset of melting at 190°C. From 190°C to 250°C, crystalline fraction decreases due to polymer melting.

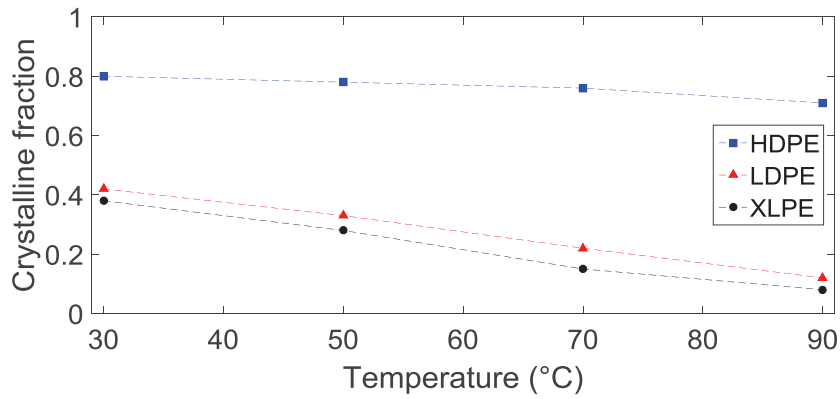


Figure 2.4: Crystalline fraction variation with temperature for LDPE, XLPE and HDPE.

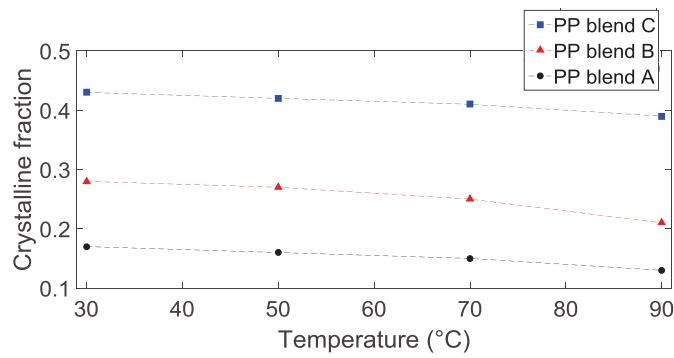


Figure 2.5: Crystalline fraction variation with temperature for PP blend A, PP blend B and PP blend C.

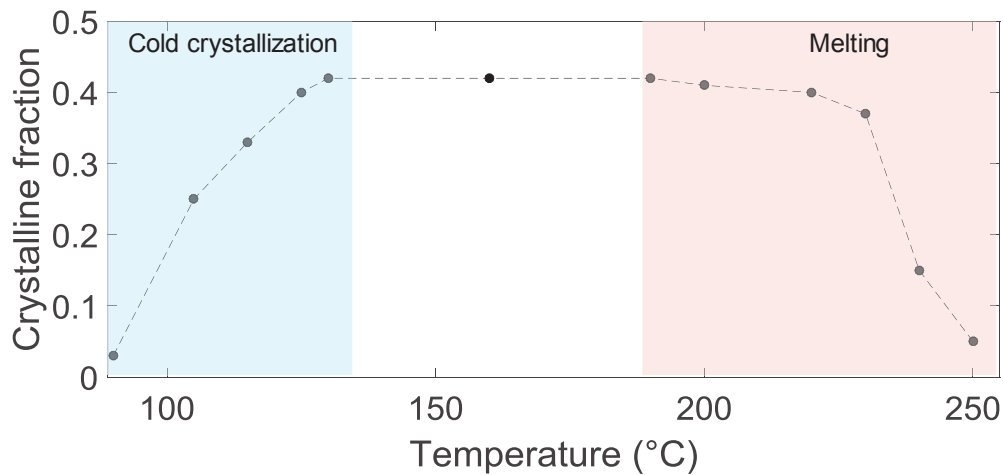


Figure 2.6: Crystalline fraction variation with temperature for PET ($\chi_c = 0.03$ at room temperature).

2.2.2 Chemical composition

2.2.2.1 Methods

Several techniques are used to measure chemical residue concentration: Thermogravimetric (TGA) analysis, Fourier Transform InfraRed spectroscopy (FTIR) and Gas chromatography mass spectrometry (GC-MS).

TGA is a technique that measures the mass change of a material submitted to temperature sweep in a controlled atmosphere. It provides several information related to polymer, such as oxidation kinetic, thermal decomposition or the amount of organic volatile. TGA is done on a TGA Q500 from TAinstruments using ceramic cells of 50 to 200 mg.

TGA allows for obtaining a global appreciation of PDP amounts in the XLPE samples. Freshly crosslinked XLPE samples underwent a temperature sweep from room temperature to 150°C at 40°C/min then an isothermal stay at 150°C for 8 h. The weight loss is in first approach considered to correspond to the global amount of PDP. The mass loss is measured as a function of temperature or time in an inert medium (nitrogen or argon) to avoid oxidation phenomena. The objective here is to observe the XLPE mass variation corresponding to desorption of cross-linking by-products. The obtained information is the global amount of desorbing chemicals.

However ATG does not gives the chemical composition of extracted species and in this case, FTIR and GC-MS appears as more complementary accurate techniques.

Infrared spectroscopy allows identifying molecules by analysis of their constituent bonds. Each chemical bond in a molecule vibrates at a characteristic frequency. A group of atoms in a molecule may have multiple modes of oscillation caused by the stretching and bending motions of the group as a whole. If an oscillation leads to a change in dipole in the molecule then it absorbs a photon that has the same frequency. The vibrational frequencies of most molecules correspond to the frequencies of infrared light. Typically, the technique is used to study organic compounds using light radiation from 4000 to 400 cm^{-1} . The measured spectrum represents the absorbance (or transmittance) *versus* wavenumber. The wavenumbers for which an absorbance is observed are characteristic of the chemical groups present in the sample under analysis. Moreover the intensity of the absorbance peaks is correlated to the concentration of the chemical group responsible for this absorbance [164]. By measuring the area of the characteristic signal, it is possible to dose chemicals. In transmission mode, the measured absorbance is linearly proportional to the sample thickness and its concentration in chemical group of interest. Chemical concentrations is determined from Beer-Lambert's law:

$$A = -\log(T) = \varepsilon \times l \times C \quad (2.2.2)$$

where A is the absorbance, T the transmittance (ratio between intensities of incident and transmitted beams), ε [$\text{L}\cdot\text{mol}^{-1}\cdot\text{cm}^2$] the molar extinction coefficient of the chemical function of interest, l [m] the optical path (sample thickness), and C [mol/L] the concentration in chemical function of interest.

Infrared spectra are obtained in transmission mode. NICOLET 380 FTIR spectrometer operating under dried air is used. Its wavenumber resolution is 4 cm^{-1} . For best signal resolution, 32 scans are accumulated per sample in the 4000 to 500 cm^{-1} range. FTIR analysis is performed

in solutions using an Omni Cell P/N 1800 with potassium bromide (KBr) windows and PTFE spacers of controlled thickness. The calibration consists of obtaining a master curve related to the studied chemical function. Master curve is obtained by measuring the absorbance A of solutions of known concentrations C in chemical of interest. From Beer-Lambert's law, in the linear response domain, the plot of A versus C gives a linear relation which slope corresponds to the product of the molar extinction coefficient ε and sample thickness l . ε value gives a direct information on the sensitivity of FTIR to the chemical function of interest. The higher ε , the higher the sensitivity. Once the molar extinction coefficient determined, concentration C is obtained from the Beer-Lambert's law (2.2.2).

In XLPE, FTIR dosing can be used to measure acetophenone (ACP) concentration thanks to the vibration of its carbonyl group (C=O), which can be observed in the wave-number range of 1820 to 1670 cm^{-1} as shown in Figure 2.7.

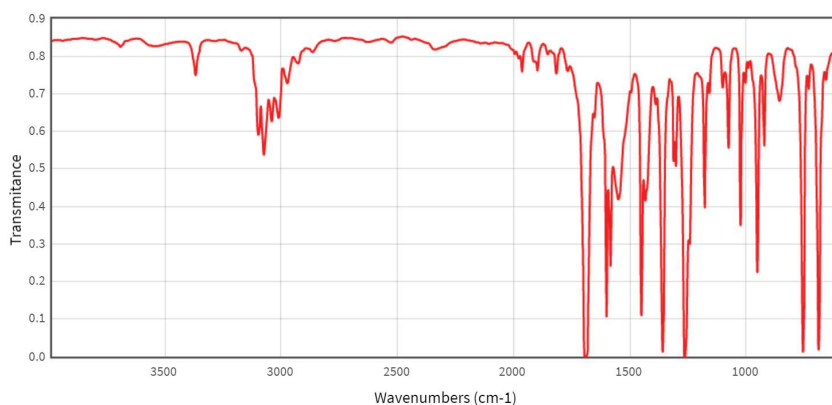


Figure 2.7: FTIR transmittance spectrum of ACP (source NIST).

To perform FTIR analysis of ACP in solutions, samples are placed in extraction solvent for solvation. Master curve is obtained by measuring the absorbance peak area of carbonyl group of known concentration of ACP diluted in the extraction solvent. From this master curve, shown in Figure 2.8, the molar extinction coefficient of carbonyl peak ε is calculated as 168.5 L/(mol cm).

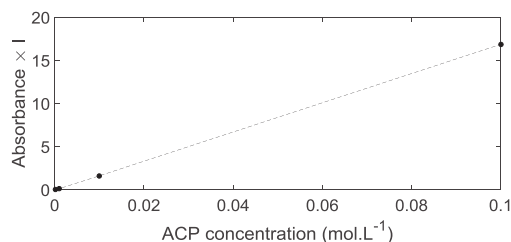


Figure 2.8: Master Curve of ACP Absorbance $\times l$ versus concentration.

An undegassed XLPE sample of weight m is cut into 1 cm^2 pieces and incorporated into an Erlenmeyer containing a volume V of the extraction solvent. The Erlenmeyer is tightly sealed and stirred for 72 h at room temperature to allow the fully solubilisation of PDP. The resulting solution is then submitted to FTIR using a $l = 5.1\text{ mm}$ thick PTFE spacer. The molar concentration C is obtained from absorbance peak area using Beer-Lambert's law (2.2.2). The weight

fraction $wt\%$ of the chemical species is then given by:

$$wt\% = \frac{C M V}{m} \quad (2.2.3)$$

with M [g/mol] the molar mass of the chemicals species, V [m^{-3}] the volume of the solution and m [g] the weight of the sample.

FTIR is a less adapted method to measure α -cumylalcohol (α CA) concentration in XLPE as the free O-H group vibration absorbs at 3592 cm^{-1} , as shown in Figure 2.9, and this zone of the spectra is more difficult to exploit. Indeed, the principle of FTIR is to dose a chemical function. If a chemical function is present in several molecules, the related absorbance peak measured by FTIR will give the global concentration of all molecules having this chemical function. In case of XLPE, both α CA and antioxidant have an alcohol function which make the specific measurement of α CA concentration in XLPE not possible with this technique.

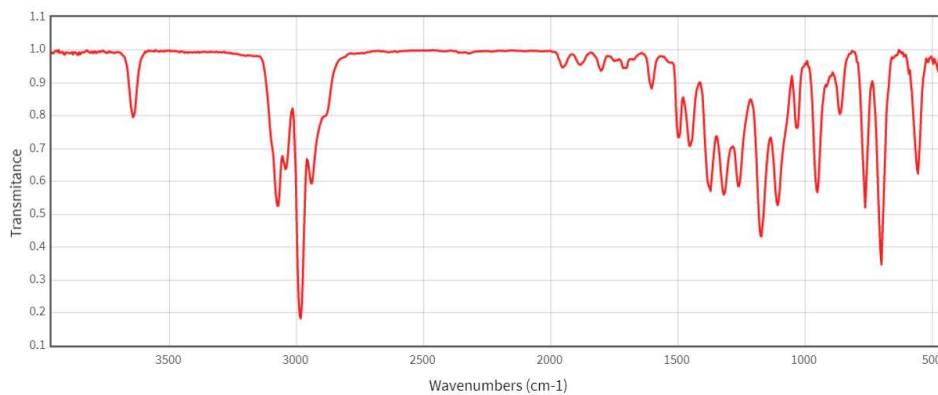


Figure 2.9: FTIR transmittance spectrum of α CA (source NIST).

GC-MS is composed of two parts: the gas chromatograph and the mass spectrometer. The gas chromatograph uses a capillary column in which solution is injected. As the sample travels the length of the column, molecules from the solution are retained by the column and then elute at different retention times. Difference in retention times comes from the difference in chemical properties between molecules of the solution and relative affinity of these molecules for the stationary phase of the column. Then, the mass spectrometer receives, ionizes and detects the ionized molecules separately.

2.2.2.2 Results

ATG, FTIR and GC-MS are used in this experimental study to assess the amount of PDP present in XLPE.

From GC-MS characterizations of undegassed XLPE at 190°C , initial amounts in ACP, α CA and α -methylstyrene are respectively 0.38%, 0.65% and 0.01%. From the chemistry of DCP decomposition, same concentration in methane as acetophenone and same concentration in water as in α -methylstyrene is expected. It gives a total amount of PDP of 1.43%. ATG performed in undegassed XLPE gives a similar value of 1.3%.

In order to study the impact of PDP on XLPE electrical properties, degassing steps have been applied at room temperature in order to obtain samples with varied PDP amounts. In Figure

2.11 is plotted the change of global PDP and ACP amount in XLPE degassed at different duration. Global PDP amount is obtained using TGA, while ACP concentration is measured by FTIR and GC-MS. The change of ACP concentration is compared between FTIR and GC-MS analyses, as shown in Figure 2.10. A maximum difference of 0.02 is measured between the two techniques which is very close to the standard deviation of 0.01 % of the FTIR measurement method.

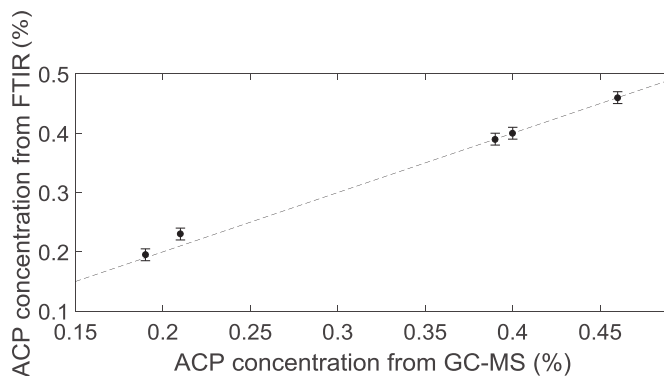


Figure 2.10: ACP concentration measured by FTIR *versus* ACP concentration measured by GC-MS.

A standard deviation of 0.1% is considered for TGA and 0.01% for FTIR. A fair correlation is observed between global PDP amount and ACP concentration as shown in Figure 2.11. These similar values show that the other chemical species such as α CA are diffusing at the same speed as ACP and that the proportion of PDP in XLPE during degassing remains constant.

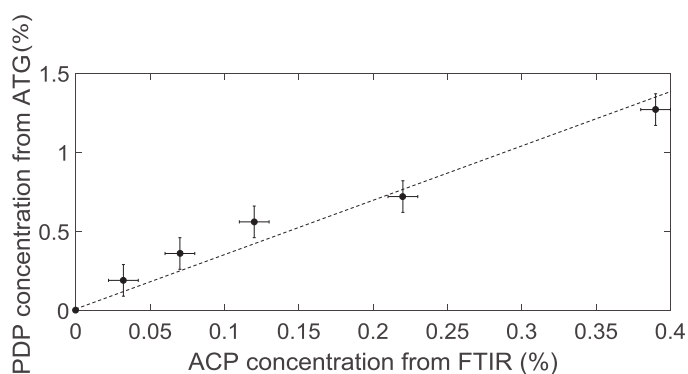


Figure 2.11: PDP concentration ATG as a function of ACP amount from FTIR.

In order to vary the relative amount of ACP and α CA, XLPE is crosslinked at varying crosslinking temperature. Increased crosslinking temperatures are expected to yield increased ACP concentration over α CA. Samples are thus crosslinked at 160°C, 190°C and 220°C in order to increase ACP concentration over α CA. The change of ACP concentration with crosslinking temperature, shown in Figure 5.2, is obtained from FTIR and GC-MS analyses, giving similar values. The observed increase of ACP concentration with increased crosslinking temperature is coherent with the favored β -scission of DCP radicals at elevated temperatures [143]. The change of α CA concentration with crosslinking temperature, obtained from GC-MS analyses is shown in Figure 2.12. α CA concentration is observed to decrease with crosslinking temperature.

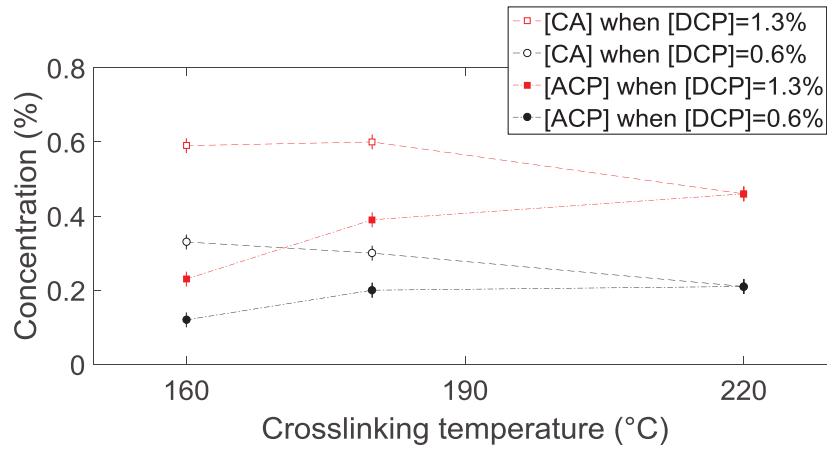


Figure 2.12: Effect of peroxide decomposition temperature on the concentration of ACP and α CA.

2.3 Dielectric spectroscopy measurement

2.3.1 Setup description

Dielectric spectroscopy aims at measuring the dielectric properties of material such as permittivity, AC conductivity and loss tangent as a function of frequency, voltage and temperature.

In amorphous or semi-crystalline polymer, evolution of complex permittivity $\varepsilon^*(\omega)$ either *versus* temperature at a fixed frequency or *versus* frequency ($\nu = \omega/2\pi$) at a fixed temperature allows to probe several processes such as the microscopic fluctuations of molecular dipoles, the displacement of mobile charge carriers or the separation of charge carriers at interfaces (Maxwell/Wagner/Sillars polarization) [1]. Conduction processes are observed at very low frequencies where there is enough time for mobile charges to cross sample thickness within half a cycle of the applied AC field. At even higher frequencies, Maxwell/Wagner/Sillars polarization can be observed where there is enough time for building up at boundaries existing in the bulk of material. At even higher frequencies, charges cannot follow the alternative changes in the electric field and only relaxation processes are observed.

The principle, shown in Figure 2.13, is to measure the alternative current $I(t) = I_0 \cos(\omega t + \varphi)$ in a material submitted to an alternative voltage $U(t) = U_0 \cos(\omega t)$ in order to obtain the complex impedance of this material defined as:

$$Z^*(\omega) = Z' + i Z'' = \frac{U_0}{I^*(\omega)} \quad (2.3.1)$$

with $Z^*[\Omega]$ the Fourier transform of the complex impedance, ω [rad/s] the angular frequency, Z' [Ω] the real part of the impedance, Z'' [Ω] the imaginary part of the impedance, U_0 [V] the amplitude of the applied voltage and I^* [A] the Fourier transform of the alternative current.

From this impedance are deduced the complex permittivity ε^* and the complex conductivity σ^* , defined as:

$$\begin{aligned} \varepsilon^*(\omega) &= \varepsilon' - i \varepsilon'' = -i/(\omega Z^*(\omega) C_0) \\ &\text{and} \\ \sigma^*(\omega) &= \sigma' - i \sigma'' = d/(Z^*(\omega) A) \end{aligned} \quad (2.3.2)$$

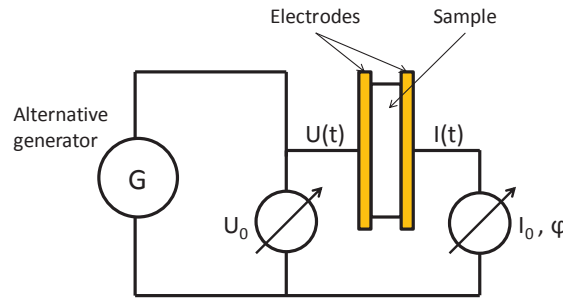


Figure 2.13: Schematic of the dielectric spectroscopy measurement principle.

with C_0 [F] the empty cell capacitance, d [m] the electrode spacing and A [m²] the electrode area. Dielectric spectroscopy measurements are performed using an ‘Alpha-A’ frequency response analyzer from Novocontrol Technologies. Isothermal measurement is performed in the frequency range from 10^{-1} to 10^6 Hz at 1 V.

2.3.2 Morphological impact on permittivity

Broadband dielectric spectroscopy is employed to study the impact of crystalline phase on polymer chain dynamics, charge transport and interfacial polarization. To do so, permittivity in PE, polypropylene (PP) and polyethylene terephthalate (PET) are measured by means of dielectric spectroscopy performed at temperature from 30°C to 90°C at 1 V. In Figure 2.14, Figure 2.15 are represented the relative permittivity change *versus* frequency at temperature from 30°C to 90°C in, respectively, LDPE and PP blend C.

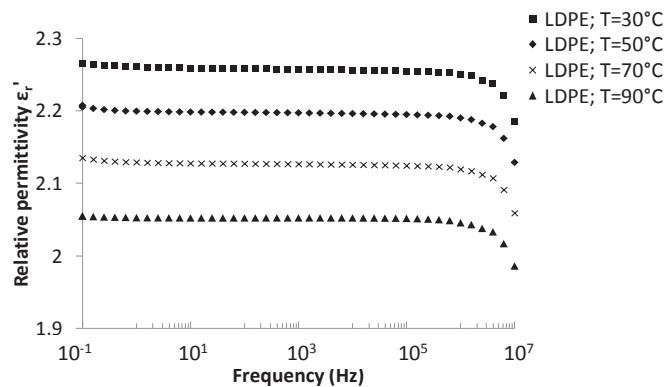


Figure 2.14: Relative permittivity of LDPE *versus* frequency at 30°C, 50°C, 70°C and 90°C.

For PE and PP, no step-like decrease of the relative permittivity with increasing frequency is observed. It means that no relaxation processes is observed at these frequency and temperature ranges. The first reason is that macromolecule relaxations in PE and PP occur at a temperature far below the room temperature [103, 165]. The second reason is that relaxation process cannot be observed in non polar material by dielectric spectroscopy unless polar groups are integrated along the macromolecules. Low increase of permittivity is observed with frequency decrease close to 0.1 Hz . This low increase is related to DC conductivity and interfacial polarization. A decrease of permittivity with temperature is measured. Permittivity of these non-polar materials is mainly related to interfacial polarization between the amorphous and crystalline phases

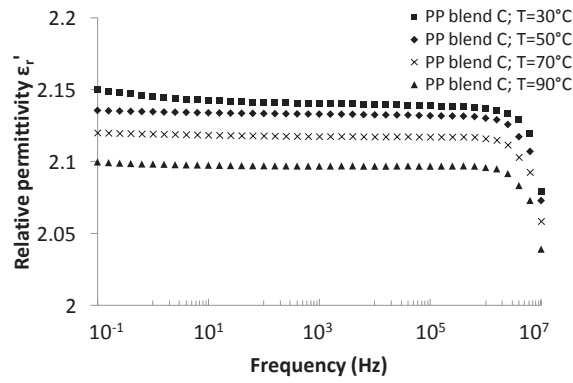


Figure 2.15: Relative permittivity of PP blend C ($\chi_c = 0.44$ at room temperature) *versus* frequency at 30°C, 50°C, 70°C and 90°C.

(Maxwell-Wagner-Sillars polarization). The higher the temperature, the lower the crystallinity and the lower the interface between crystalline and amorphous phase. As a result, interfacial polarization decreases and so does the permittivity. From 30°C to 90°C, the crystalline fraction decrease is around 0.3 in LDPE and around 0.05 in PP blend C. As the crystalline fraction decrease with temperature is lower in PP blend C than in LDPE, relative permittivity decrease is lower.

In Figure 2.16 is represented the relative permittivity change *versus* frequency at temperature from 30°C to 90°C in PET. A step-like decrease of the relative permittivity with increasing fre-

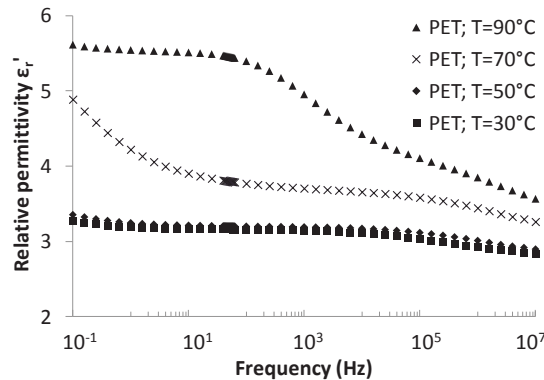


Figure 2.16: Relative permittivity of PET ($\chi_c = 0.1$ at room temperature) *versus* frequency at 30°C, 50°C, 70°C and 90°C.

quency is observed especially at 70°C and 90°C. This step like decrease is due to the α -relaxation process in PET and is also characterized by a peak in the dielectric loss. The α -relaxation corresponds to correlated molecular fluctuations of the chain segments in the amorphous phase and also corresponds to the dynamic glass transition [105]. This relaxation is called α -relaxation and not β -relaxation as only two relaxation are present in PET unlike PE and PP. For PET, an increase of permittivity is measured with temperature. PET is a polar medium and permittivity is related to the orientation of its polar macromolecules. At 0.1 Hz, as the temperature is increasing, a high increase of ϵ_r from 3.4 to 5 is measured when the glass transition at 70°C is reached. Below the glass transition, no global macromolecules movement occurs. Consequently, dipolar orientation is very weak, leading to low dielectric constant. When the glass transition is reached, global molecular relaxation of the macromolecules in the amorphous phase occurs

and polar molecules, acting as dipole, become able to orientate when electrically stressed. This dipole orientation above the glass transition is at the origin of the higher permittivity.

To obtain variation of permittivity with crystalline fraction in PE and PP, dielectric spectroscopy measurements are performed at several temperatures from 30°C to 90°C in LDPE, HDPE and three different blends of PP. Figure 2.17 shows the permittivity variation as a function of the crystalline fraction in these materials when submitted to the different temperatures during measurement. In these non-polar materials, permittivity is increasing with crystalline fraction increase. The higher the crystalline fraction, the higher the interface between crystalline and amorphous phase. As a result, Maxwell-Wagner-Sillars polarization increase and so does the permittivity.

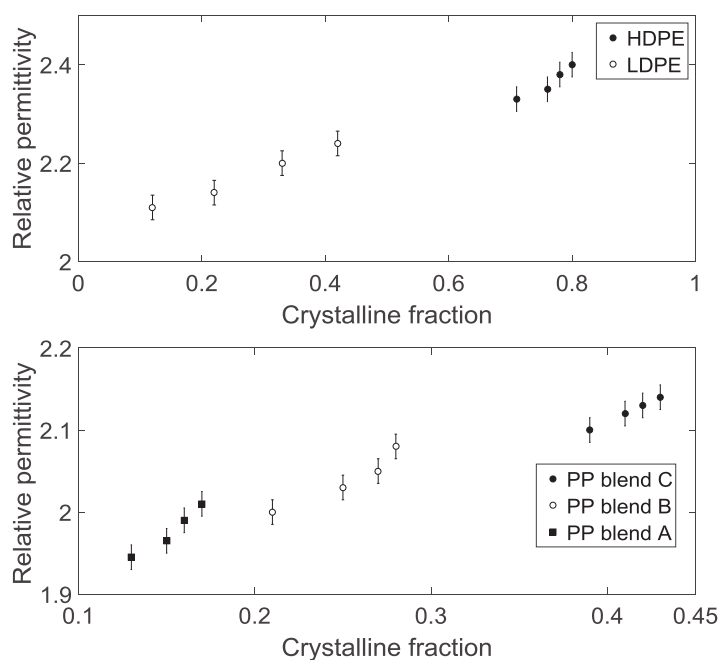


Figure 2.17: Permittivity at 0.1 Hz of PE and PP *versus* crystalline fraction.

Dielectric spectroscopy measurements are performed in PET with various crystalline fraction at 30°C. Isothermal measurement at 30°C of permittivity *versus* frequency for PET with increasing crystalline fraction is shown in Figure 2.18. A decrease of the permittivity with increasing crystallinity is observed. Furthermore permittivity step around the frequency relative to the α -relaxation is less marked when crystallinity increases. When crystallinity increases, movements of macromolecules are more restrained, leading to a decrease of the permittivity with crystallinity.

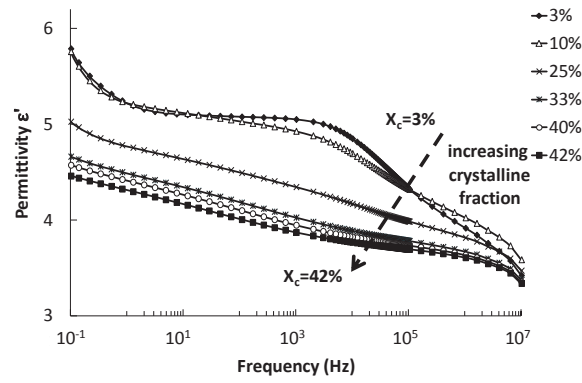


Figure 2.18: Permittivity *versus* frequency at 70°C in PET with various crystalline fraction.

2.3.3 Glass transition and crystalline phase influence on conductivity

To study the influence of macromolecular mobility on the electrical conduction of polar polymer, the change of AC conductivity ($f = 0.1$ Hz) with temperature between 30°C and 90°C in PET samples of various crystalline fractions is measured by dielectric spectroscopy as shown in Figure 2.19. For all tested specimens, conductivity is observed to increase by one order of magnitude from a threshold temperature of 70°C, corresponding to the glass transition temperature.

The onset of global molecular motions assigned to the glass transition is related to electric property changes in semi-crystalline polymer. Below glass transition, charge injection and transport is only assisted by weak local molecule movements, whereas, above the glass transition, global molecular motions assist charge injection and transport. Consequently a step in the conductivity is measured.

Furthermore, from the 0.1 Hz conductivity measurements of Figure 2.19, is observed a decrease of conductivity with crystalline fraction regardless macromolecules mobility. When crystalline fraction increases, electron barrier increases and mechanical activation of charge transport from macromolecule relaxation decreases.

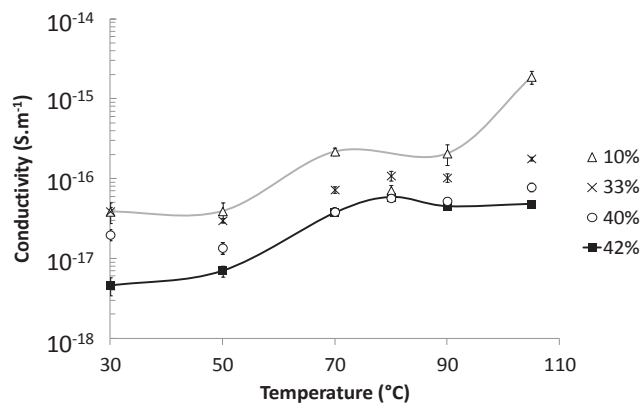


Figure 2.19: Conductivity at 0.1 Hz *versus* temperature for PET of various crystalline fractions.

2.4 Current density measurement

2.4.1 Setup description

A dedicated conductivity measurement bench has been developed and mounted. It is constituted of a ± 12.5 kVDC voltage source that feeds 12 parallel test channels. Its schematic is shown in Figure 2.20. The test cells are placed in ovens to allow a very precise control of the test temperature from room temperature to 90°C . For each test channel, leakage current is measured by means of voltage measurement across a calibrated resistance of $100\text{ M}\Omega$. To prevent hardware failure in case of breakdown, each test channel is equipped with a protection circuit that contains a $1\text{ G}\Omega$ 20 kV protection resistor and a gas sparkler with a trigger voltage of 90 V connected after the protection resistor on one side, and to ground on the other side. Voltage measurement of the 12 test channels is achieved by the use of a multiplexer that physically connects each channel one after the other to a voltmeter. Finally, 12 calibrated temperature probes (K-type thermocouples) are used to measure temperature at the vicinity of each of the tested sample. Table 2.5 summarizes the main features of the conductivity measurement test bench.

Part	Device	Features
Voltage Source	FUG HCP 140-12500	Voltage: $\pm 12.5\text{ kV}$, Low Ripple
Voltmeter	NI PXI 4072	max voltage: 300 V , max current: 1 A
Multiplexer	NI PXIe 2527	64 channel 300 V Multiplexer
Thermocouple input	NI PXI 4353	32 channel thermocouple input
Oven	Shelab	room temperature to 90°C
Computer	Standard PC	/

Table 2.5: Parts of the conductivity measurement test bench.

For low current measurements, the main challenge is to get the highest signal to noise ratio (SNR). A great source of noise is avoided by electromagnetic shielding of all the setup and its wiring. HV, 0V and Earth cables are braided together and put in a grounded metallic mesh. With this setup configuration the noise on current measurement is lower than 10^{-12} A . The minimum conductivity that can be measured is thus 2.10^{-17} S/m .

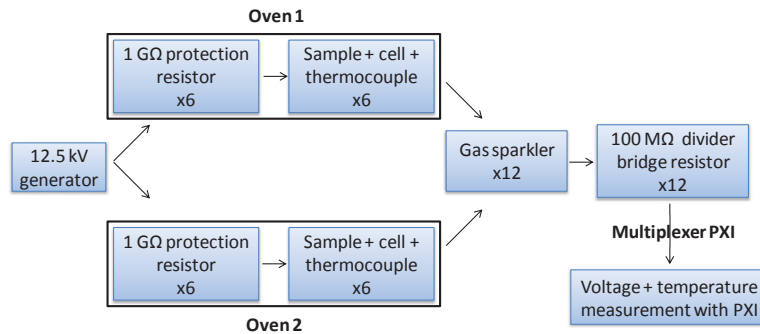


Figure 2.20: Conductivity measurement system schematic.

2.4.2 Test procedures

To assess the change in the dependency to temperature and electric field of sample conductivity, leakage current of plate samples is measured in conditions from IEC60093 or ASTM D257

recommendations [32]. Samples are tested at temperature from 30 to 70°C. Figure 2.21 shows the electric field program. At a given temperature, samples underwent an increasing electric field from 20 to 40 kV/mm. 3 samples are tested per temperature.

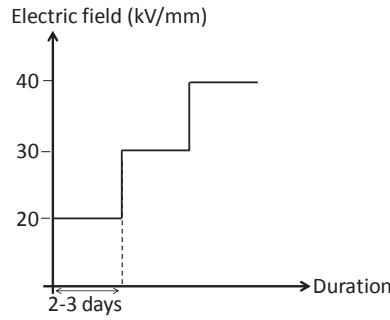


Figure 2.21: Voltage test program.

An example of leakage current measured at $T = 70^\circ\text{C}$ and $E = 30\text{ kV/mm}$ is shown in Figure 2.22.

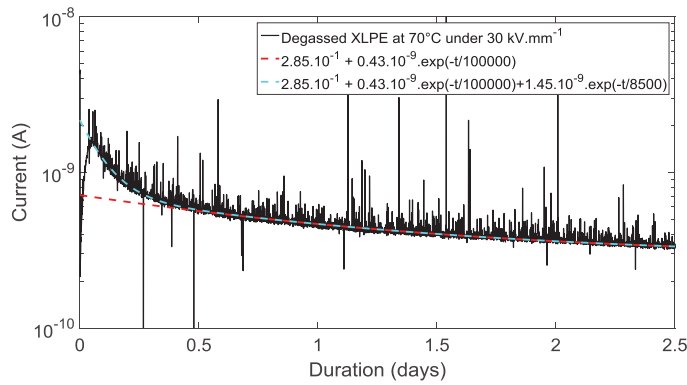


Figure 2.22: Comparison between exponential and double exponential fits of experimental leakage current.

Current decrease with time is following a double exponential law:

$$i = i_{DC} + i_C \exp\left(-\frac{t}{\tau_C}\right) + i_P \exp\left(-\frac{t}{\tau_P}\right) \quad (2.4.1)$$

The first exponential law corresponds to charging current, the second one to polarization current. The time constant of the charging current τ_C is of the order of several hours and that for the polarization current τ_P is several days. From the curve fitting by equation (2.4.1), DC current i_{DC} is obtained. Volume conductivity is further calculated from the sample geometry using Ohm's law:

$$\sigma(E, T) = \frac{i_{DC} e}{U S} \quad (2.4.2)$$

with U [V] the voltage applied, e [m] the sample thickness and S [m²] the surface of the ground electrode. With this approximation, the measured current and calculated conductivity are proportional by a geometric parameter. This means no space charge contribution (*e.g.* space charge limited current) is taken into account for the calculation of the conductivity [166]. The main consequence is that the obtained conductivity is only apparent as the steady state is obtained

after built up and stabilisation of space charge. This calculation is however still of interest as it allows for the identification of so-called *electrical history* by applying increased-decreased step voltage and comparing the measured data. Most of studied samples show this leakage current behavior.

2.4.3 Crystallinity impact on conductivity

To study the impact of crystalline fraction on conductivity of polymer, leakage current measurement is performed in LDPE, HDPE and degassed XLPE whose crystalline fraction at room temperature measured by DSC are respectively $\chi_C = 42\%$, $\chi_C = 80\%$ and $\chi_C = 38\%$. Measurement are performed at 50°C and 70°C under an increasing electric field from 20 kV/mm to 40 kV/mm . Electric field is applied with a ramp up of $0.25\text{ kV}/(\text{mm}\cdot\text{s})$ and for a poling time of $1 \times 10^5\text{ sec}$ at each electric field.

In the measured current at 50°C shown in Figure 2.23, the lowest current density is measured in HDPE with values below the measurement system sensitivity under 20 kV/mm and 30 kV/mm . However, under 40 kV/mm , an unexpected increasing leakage current with time in HDPE is observed.

At 70°C , current increase of HDPE already occurs under 20 kV/mm and becomes higher than current density of LDPE and XLPE as observed in Figure 2.24. The current increase yields to sample breakdown under 30 kV/mm . For 3 tested sample of HDPE, 2 breakdowns have occurred under an electric field of 30 kV/mm and 1 under 40 kV/mm . The increase yielding to breakdown can be due to current displacement due to fast and large charge trapping. Between XLPE and LDPE, higher current density is measured in XLPE under each electric field and at each temperature. It can be attributed to the lower crystalline fraction in XLPE increasing the charge injection although the difference in current densities between the two materials is not significant enough to conclude.

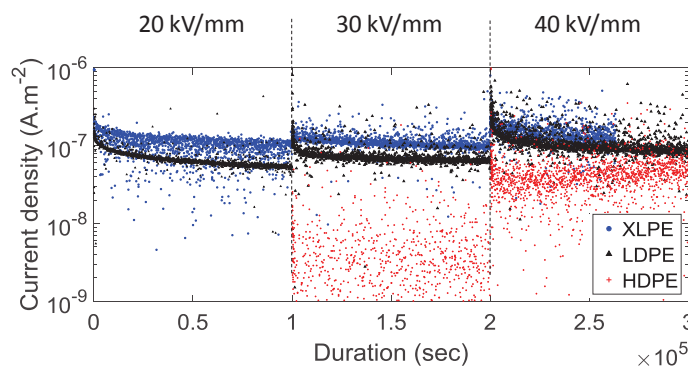


Figure 2.23: Current density *versus* time in LDPE, HDPE and XLPE at 50°C under an electric field from 20 to 40 kV/mm .

To have a better accuracy of the conductivity dependency with crystalline fraction, leakage current measurements are performed in PP and PET whose crystalline fraction can be easily controlled over a broad range by sample processing. PP based materials with crystalline fraction of 0.09 and 0.42 and PET with crystalline fraction of 0.09 and 0.39 are tested at 70°C under increasing electric field steps from 20 to 40 kV/mm . Results dshown in Figure 2.25 for PP

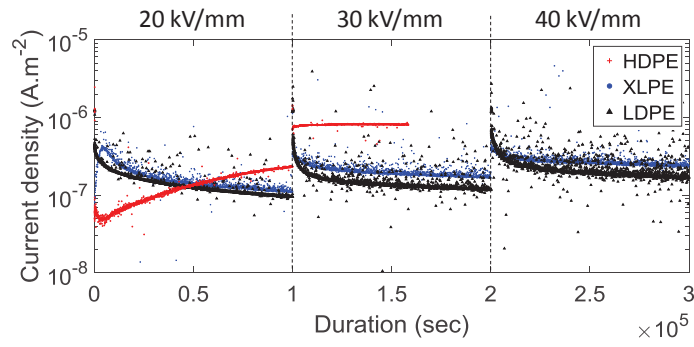


Figure 2.24: Current density *versus* time in LDPE, HDPE and XLPE at 70°C under an electric field from 20 to 40 kV/mm.

and in Figure 2.26 for PET show clearly a decrease of the current with increasing crystallinity. The difference is around 2×10^{-7} A/m² at each electric field for PP and more than one order of magnitude for PET. These results demonstrate that crystallinity acts as barrier for charge injection resulting in a conductivity decrease. This conductivity decrease with crystalline fraction appears as much in polyolefin as in polyester.

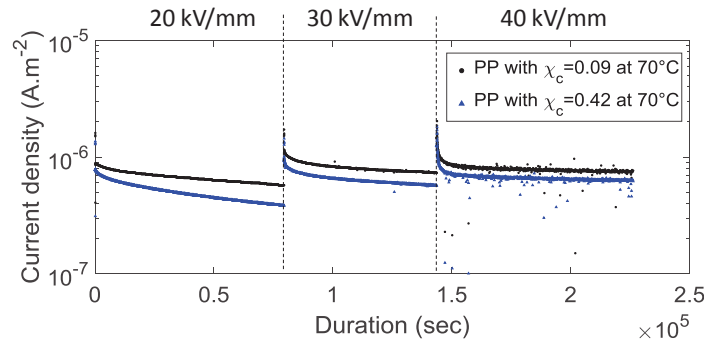


Figure 2.25: Current density *versus* time in low and high crystalline PP at 70°C under an electric field from 20 to 40 kV/mm.

2.4.4 PDP influence on conduction

To study the dependency of current density in XLPE with PDP, leakage current measurement is performed on XLPE with various PDP amounts. In order to experimentally obtain samples with various PDP amounts, degassing step has been applied in freshly crosslinked LDPE at room temperature. Global PDP amount has been measured from weight loss at 150°C using TGA. Samples are tested at 30, 50 and 70°C with steps of increased electric field from 20 to 40 kV/mm as shown in Figure 2.21. For each electric field, current is measured for 2 to 3 days in order to allow samples reaching a steady state. Current density at steady state is obtained from the curve fitting by equation (2.4.1).

In Figure 2.27 is compared current density at steady state in fully degassed XLPE (without PDP) and undegassed XLPE (1.2% of PDP) as a function of temperature under an electric field of 20 kV/mm. An increase of almost one order of magnitude of the current is measured in the presence of PDP and both materials follow a thermal activation law for conductivity. An

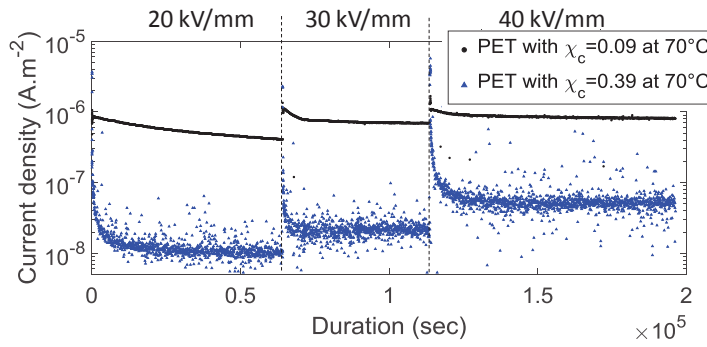


Figure 2.26: Current density *versus* time in low and high crystalline PET at 70°C under an electric field from 20 to 40 kV/mm.

activation energy of 0.35 eV and 0.2 eV are respectively measured in undegassed XLPE and fully degassed XLPE.

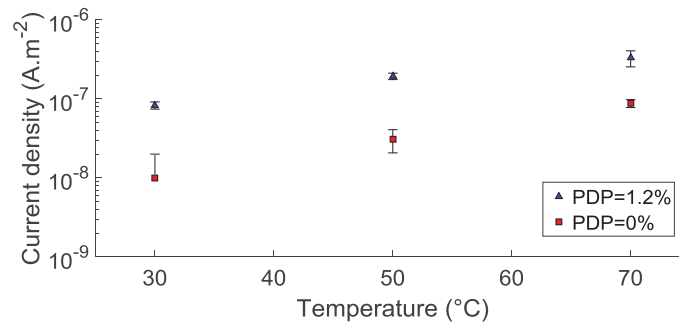


Figure 2.27: Current density *versus* temperature under 20 kV/mm in fully degassed and undegassed XLPE.

In Figure 2.28 is compared current density at steady state in fully degassed XLPE and undegassed XLPE as a function of electric field at 30 °C. A slow increase of the current density with electric field is measured. Linear variations of 3×10^{-9} A/m² and 9×10^{-9} A/m² are respectively obtained in fully degassed and undegassed XLPE. For degassed XLPE, low variation can be explained by homocharge injection, screening the electric field at the interface of these materials. For undegassed material, variation with electric field is higher as heterocharges are present due to the presence of PDP which avoid the screening effect. In Figure 1.6 are plotted the change

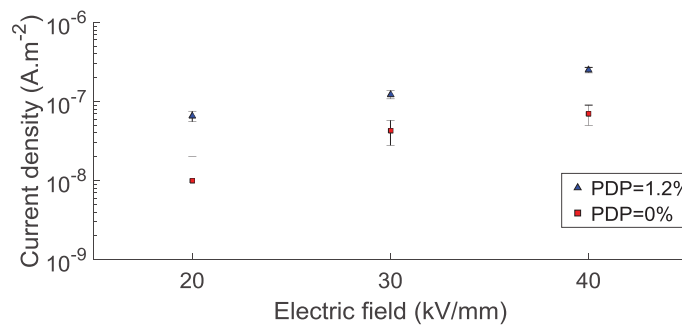


Figure 2.28: Current density *versus* electric field at 30°C in fully degassed and undegassed XLPE.

in current density with increased PDP content in XLPE under an electric field of 20 kV/mm at 30°C, 50°C and 70°C. Each PDP amount corresponds to new series of degassed sample at different controlled duration before being tested. The concentration remains stable during testing. At each temperature, current density is increasing with increasing PDP content. A first current

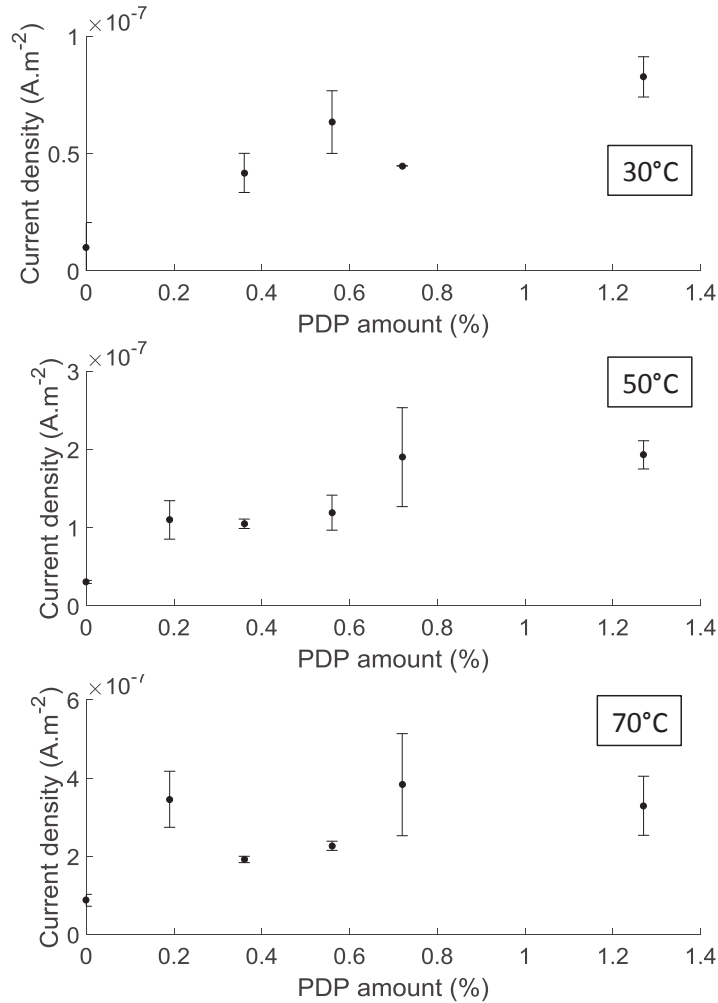


Figure 2.29: Current density in XLPE *versus* PDP amount under 20kV/mm at temperature between 30°C and 70°C.

density increase is observed as soon as a low PDP amount is present (0.2%), showing the strong contribution of such chemicals to conduction processes in XLPE. At 30°C and 50°C, after a high increase of current density between 0% and 0.2% of PDP, a low conductivity increase with PDP is measured at higher PDP amount. At a concentration higher than 0.6%, conductivity reaches a plateau. At 70°C, current density seems to be far less affected by the presence of PDP. It may be due to the increased contribution of thermally assisted conduction process prevailing over the ionic conduction process related to the PDP.

2.4.5 Interface effect

For the interface effect, current density in XLPE is measured with brass electrodes and with semiconductive (SC) electrodes. In order to highlight the influence of interface in insulation current density, measurements are performed in fully degassed XLPE. Experimental measurements are performed at 70°C under an electric field of 30 kV/mm for 10⁵ sec. Current density

variation over time with the two different electrodes is shown in Figure 2.30. A high increase of the current density is measured in presence of the SC electrodes showing the strong influence of the interface on the electrical properties. Larger current density with semiconductive electrodes may be attributed to the presence of localized states at the interface which enhance charge injection. Diffusion of these localized states near the interface are related to the distribution of carbon black (CB) particles at the semicon/insulation interface [9].

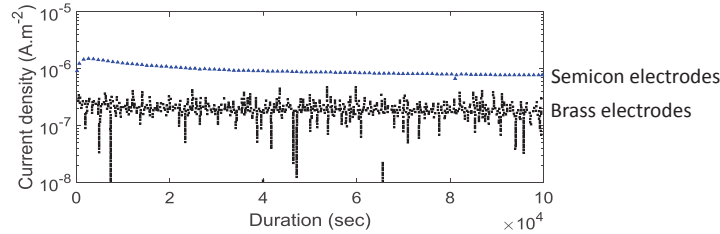


Figure 2.30: Current density variation with time in degassed XLPE with brass electrodes and with SC electrodes.

2.5 Space charge measurement

2.5.1 Setup description

2.5.1.1 Stimulus and measurement systems

A pulsed electro acoustic (PEA) bench has been developed, installed and commissioned. Its schematic is shown in Figure 2.31. The technology is based on voltage steps [167]. The electrical stimulus consists in polarizing the sample to test in a high DC voltage and applying additional voltage steps at a controlled frequency. A low ripple ± 65 kVDC HVDC source is used to achieve sample polarization. A low ripple $\pm 3,5$ kVDC sources connected to a HV switch periodically triggered by a frequency generator generates the voltage step. A protection resistor of $100\text{ M}\Omega$ is used to protect the hardware in case of sample breakdown. The pulse generator is protected from the HVDC source using a high-pass galvanic insulation system. Voltage steps are typically applied at a frequency of 100 Hz.

The mechanical waves resulting from the sample electrical excitation are detected and converted into an electrical signal by a piezoelectric sensor made of $28\text{ }\mu\text{m}$ PVDF film metalized on both sides. This sensor works at temperatures up to 80°C . At higher temperature, the PVDF loses its piezoelectric property and the mechanical wave is not detected anymore [167]. A 40 dB signal amplifier amplifies the electrical signal from the piezoelectric sensor which is then measured by an oscilloscope.

2.5.1.2 Reduction of waves reflections

Wave reflections, a major issue in PEA system, deteriorate the output PEA signal. They originate from multiple reflections of the electrical pulse in cables and from reflection of acoustic

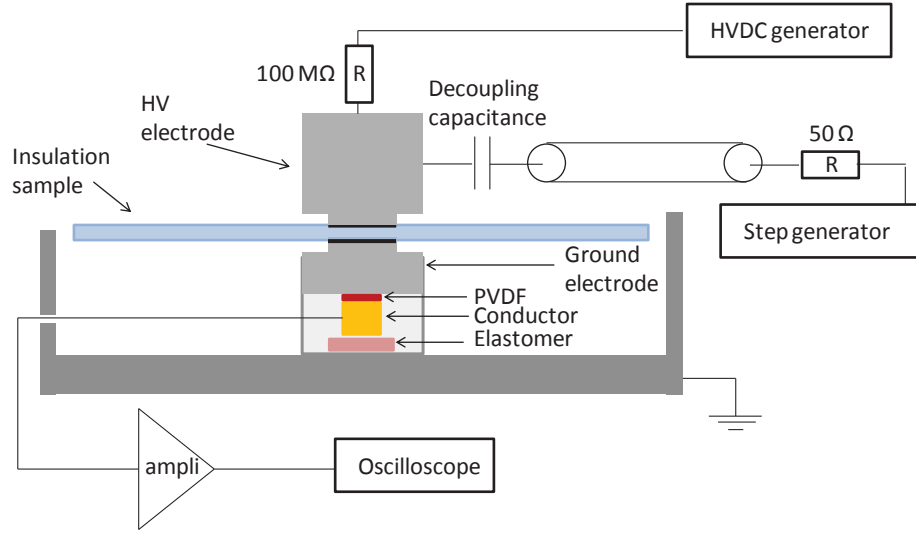


Figure 2.31: PEA system schematic.

waves at the sample/electrode/PVDF interfaces. The former is due to electrical impedance mismatch and the latter to acoustic impedance mismatch. One way to decrease reflections from electrical impedance mismatch is to match the pulse generator to the cable impedance as illustrated in Figure 2.32. The cable impedance depends on the ratio between external electrode radius r_{int} and internal electrode radius r_{ext} as:

$$\frac{1}{2} \sqrt{\frac{\mu}{\epsilon}} \ln\left(\frac{r_{ext}}{r_{int}}\right) \quad (2.5.1)$$

where μ and ϵ are the permeability and permittivity of the cable insulator. For a coaxial cable, this impedance value is usually 50Ω and connecting a 50Ω resistance between HV pulse and coaxial cable is enough to cancel the echo. The only condition is that connection lengths between these different electrical components have to be small enough to remove from the PEA signal, the spurious signals from multiple reflections inside these connections.

The protection resistor, by being placed near the HV electrode, avoids propagation of the electrical pulse in the coaxial cable between HV electrode and $\pm 65 \text{ kVDC}$ HVDC source and thus avoid additional wave reflections.

Reflection coefficient from acoustical impedance mismatch can be estimated from the reflection coefficient of pressure wave:

$$\frac{Z_{Electrode} - Z_{Sample}}{Z_{Electrode} + Z_{Sample}} = \frac{\rho_{Electrode} v_{S,electrode} - \rho_{sample} v_{S,sample}}{\rho_{Electrode} v_{S,electrode} + \rho_{sample} v_{S,sample}} \quad (2.5.2)$$

Where ρ [kg/m^3] is the volume weight and v_S [m/s] is the sound velocity. The choice of electrode material is very crucial to limit reflection and having a proper SNR. Matching material is used at the interfaces, for instance carbon black filled polyethylene or a material similar to the sample. Very thick mismatching electrode is also used to delay the reflection and avoids superimposition of reflections with valuable signal.

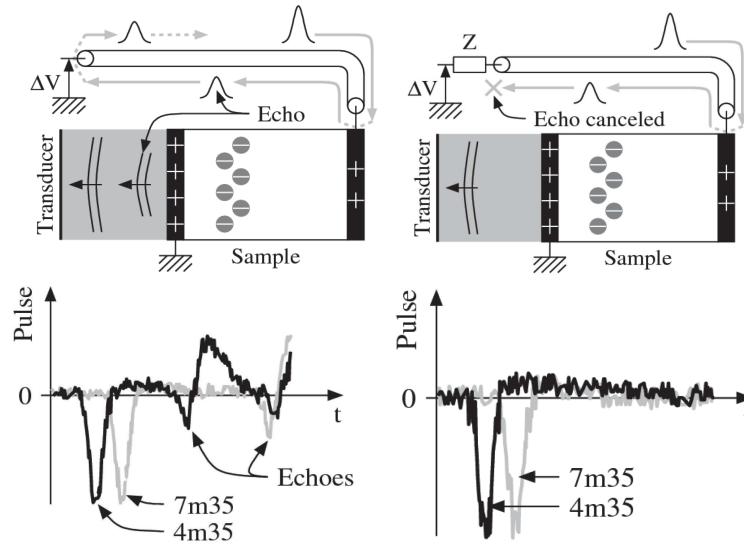


Figure 2.32: (left) Superimposed signals induced by multiple reflections of the electric pulse in the cable; The graph shows the incident pulse and the echo for two cable lengths. (right) Electrical matching of the pulse generator by an impedance Z to avoid electrical reflections; The graph shows the incident pulse but no longer echo for two cable lengths [168].

2.5.1.3 Signal resolution

Two kinds of spatial resolution have to be considered. The first one, illustrated in Figure 2.33, is the positioning resolution. Supposing a signal produced by a charge at the position x_0 and a signal produced by the same charge at the position $x_0 + \delta x_0$. It is possible to tell at which position (x_0 or $x_0 + \delta x_0$) is the charge, only if the difference between the two signals is higher than the noise level. The resolution is given by δx_0 value when the two-signal difference is at the noise level. The positioning resolution in case of voltage step is given by [40]:

$$\frac{0,98.v_s\tau}{SNR} \quad (2.5.3)$$

With v_s [m/s] the speed of the elastic wave inside the sample, τ [s] the step rise time and SNR the signal to noise ratio.

The second spatial resolution is the discerning resolution presented in Figure 2.34. Supposing a signal s_1 produced by two charges at the position $x_0 + \delta x_0/2$ and $x_0 - \delta x_0/2$ and a signal s_2 produced by a charge at the position x_0 with twice the amplitude. It is possible to identify if there is one or two charges only if the difference of the two signals $s_1 - s_2$ is higher than the noise level. The resolution is given by the δx_0 value when the two signals difference is at the noise level. The discerning resolution in case of voltage step is given by [40]:

$$\frac{2.24 v_s \tau}{\sqrt{SNR}} \quad (2.5.4)$$

With the developed PEA setup, the positioning resolution is about $0,5 \mu\text{m}$ and the discerning resolution is about $10 \mu\text{m}$.

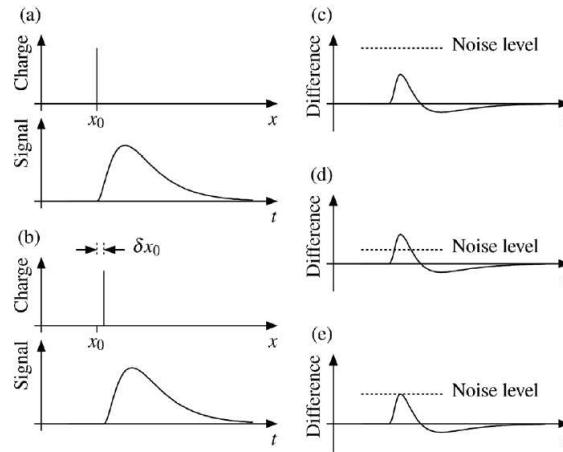


Figure 2.33: Positioning resolution: (a) Signal produced by a charge at the position x_0 . (b) Signal produced by the same charge at the position at the position $x_0 + \delta x_0$. (c) If the difference between the two signals is below the noise level, the position difference is not detected. (d) If the difference between the two signals is above the noise level, the position difference can be detected. (e) The positioning resolution is the value δx_0 at which the difference between the two signals is equal to the the noise level. [40]

2.5.1.4 Data processing

The amplified PEA signal is digitized by a scope triggered by the High Voltage (HV) switch. The time delay between the PEA signal and the voltage step generated by the HV switch corresponds to the electromagnetic wave propagation in the cables and the propagation of the elastic wave inside the ground electrode. As the propagation time inside the cables is negligible compared to the propagation inside the electrode, the time delay is given by:

$$\tau = \frac{d_{gnd\ electrode}}{v_{S,gnd\ electrode}} \quad (2.5.5)$$

with $d_{gnd\ electrode}$ [m] the thickness of the ground electrode and $v_{S,gnd\ electrode}$ [m/s] the sound velocity inside ground electrode (6420 m/s in aluminum). An averaging of 256 signals is applied with the scope, acting as bandpass filter and increasing the SNR . The signal measured is calibrated with a Laplace transform process assuming that the system transfer function is decreasing exponentially. The different steps are as follow (Figure 2.35):

1. (Figure 2.35-1) - For calibration, a PEA signal containing only the two peak signals corresponding to the capacitive charges at the electrodes with no space charge accumulation inside the material is needed. This signal is obtained by applying a sufficiently low electric field (below 10 kV/mm) on fresh sample to prevent injection of charges. If the sample contains already space charge, its electrical response at Volt-on can be used for calibration by subtracting it with its immediate Volt-off response;
2. (Figure 2.35-2-3) - The measured signal is subtracted by an amplitude-adapted delayed copy of this signal:

$$S_{calibrated} = S(t) - A.S(t - \tau) \quad (2.5.6)$$

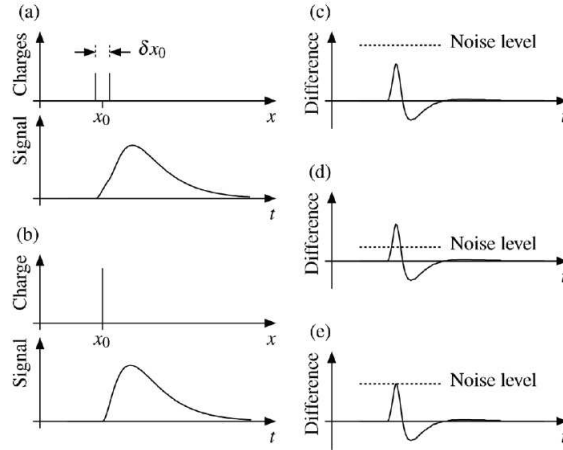


Figure 2.34: Discerning resolution: (a) Signal produced two identical charges at position $x_0 \pm \delta x_0/2$. (b) Signal produced by a charge at position x_0 with twice the amplitude of the charges in (a). (c) If the difference between the two signals is below the noise level, it is not possible to identify if there is one or two charges. (d) If the difference between the two signals is above the noise level, it is possible to identify the presence of two charges. (e) The discerning resolution is the value δx_0 at which the difference between the two signals is equal to the the noise level. [40]

Where A and τ are respectively the coefficients for amplitude and delay. A good choice for τ is the rise time of the signal. A is adjusted so that the tails of $S(t)$ and $A.S(t - \tau)$ are of the same amplitude;

3. (Figure 2.35-4-5) - The electric field is obtained from the integration of the calibrated signal:

$$E(t) = b \int S_{calibrated}(t) dt \quad (2.5.7)$$

The constant b is chosen in order that the local constant electric field value corresponds to the electric field applied in the calibration;

4. (Figure 2.35-6) - The charge density is directly given by the calibrated signal:

$$\rho(t) = \frac{b\epsilon S_{calibrated}(t)}{v_{S,sample}} \quad (2.5.8)$$

With ϵ [F/m] the permittivity and $v_{S,sample}$ [m/s] the sound velocity in sample. Finally elastic wave speed inside sample (~ 2000 m/s for LDPE) is used to switch between temporal and spatial domain. New calibration is necessary for each different temperature and material.

2.5.2 Test procedures

To investigate space charge behavior *versus* electric field and temperature, samples are tested at a temperature from 30 to 70°C in PE and PP samples and from 30°C to 80°C in PET samples. The electric field program is shown in Figure 2.36. At a given temperature, samples underwent an increasing electric field from 20 to 40 kV/mm. Between each application of the electric field,

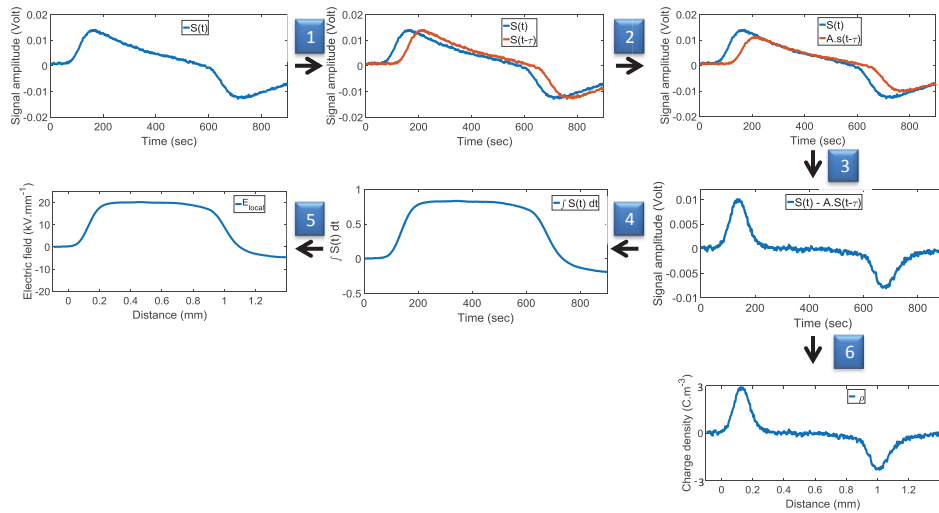


Figure 2.35: Calibration signal processing steps.

depolarization time of 1 min is performed. Space charge evolution with time is recorded both Volt-off and Volt-on.

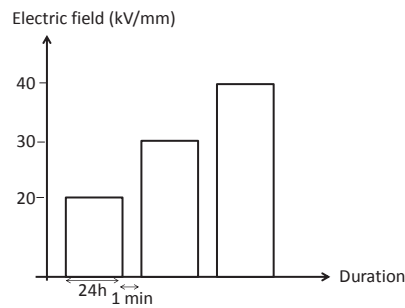


Figure 2.36: Voltage test program for space charge measurements.

2.5.3 Glass transition influence on space charge

To highlight the macromolecules relaxation influence on polymer space charge. PEA measurements are performed in PET below and above glass transition at 70°C . Contrarily to PE and PP, PET is a polar material with carbonyl and hydroxyl terminal group. In addition to charge transport and trapping, polarization of the material may occurs. In Figure 2.37 space charge signal are simulated in case of: *i*) homocharge injection at the anode and cathode which yields at volt off to internal and induced charges with opposite sign. *ii*) Residual polarization which yields at volt off to internal homocharge without the presence of induced charges.

Residual space charge in very low crystalline PET ($\chi_c = 3\%$) is measured at Volt-off after being stressed under 20 kV/mm for 24 h at three temperatures: below T_g (30°C), in the T_g range (70°C) and above T_g (80°C) as demonstrated in Figure 2.38. At 30°C , very low charge density is measured. Residual polarization and charge injection phenomena are not observed at this temperature. At 70°C , negative homocharge density present between $d/d_{max} = 0.8$ and $d/d_{max} = 1$ is observed and corresponds to electron injection. Negative induced charges at the anode demonstrate the presence of positive charge too. There is in this case coexistence of positive and negative charges between $d/d_{max} = 0.6$ and $d/d_{max} = 0.8$ with a slightly higher

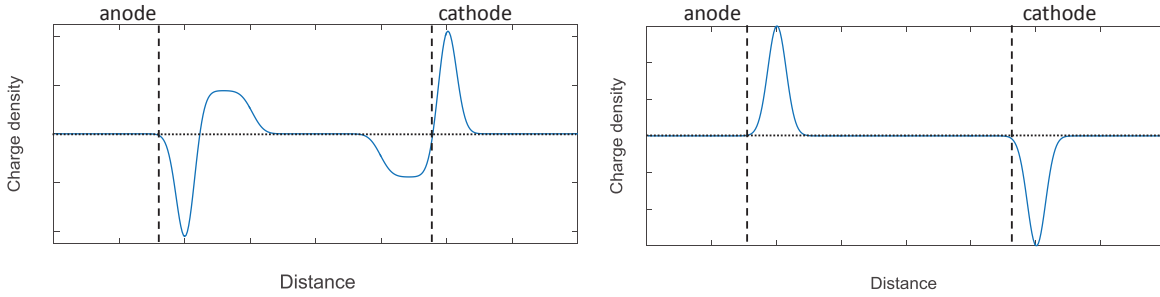


Figure 2.37: Simulated residual space charge in case of: (left) homocharge injection at the anode and cathode. (right) residual polarization.

amount of positive charges. At 80°C , negative homocharge density and positive charge density are present respectively between $d/d_{max} = 0.7$ and $d/d_{max} = 1$ and between $d/d_{max} = 0.4$ and $d/d_{max} = 0.7$. The lower negative induced charges at the anode compared to the positive internal charges nearby demonstrate the presence of residual polarization in addition to charge injection.

Below the glass transition, no global macromolecules movement occurs. Consequently, dipolar orientation is very low and charge injection and transport is only assisted by weak local molecule movements. When the glass transition is reached, global molecular relaxation of the macromolecules in the amorphous phase occurs and polar molecules, acting as dipole, become able to orientate when electrically stressed. It results in a higher positive and negative charge injection and the presence of residual polarization observed in PEA.

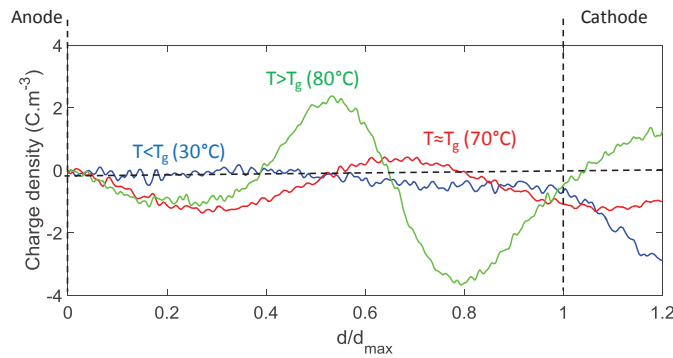


Figure 2.38: Residual space charge measured at Volt-off after stress under 20 kV/mm for 24 h at 30°C , 70°C and 80°C for amorphous PET.

2.5.4 Crystallinity impact on space charge

To investigate the influence of crystallinity on polymer space charge, PEA measurement are performed in PP with two different crystalline fractions: $\chi_C = 0.09$ and $\chi_C = 0.42$. Test procedure shown in Figure 2.36 is applied to PP at 70°C . Space charge measured at Volt-off after poling under the last electric field applied of 40 kV/mm is represented in Figure 2.39. In low crystalline PP, positive charge amount is present in all sample thickness whereas in high crystalline PP, almost no space charge is detected. It demonstrates that crystalline phase acts as a barrier for charge injection.

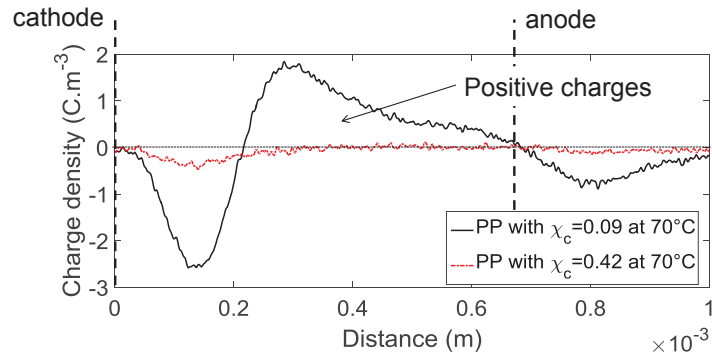


Figure 2.39: Residual space charge measured at Volt-off in low crystalline PP and high crystalline PP after poling at 40 kV/mm and 70°C.

Residual space charge of PET was measured in Volt-off after being stress under 25 kV/mm for 24h at 70°C for 3 different crystalline fractions of PET: 3%, 25% and 40%. Results are shown in Figure 2.40. For PET of very low crystallinity ($\chi_C = 3\%$), negative homocharge density is present near cathode and there is coexistence of positive and negative charges between $d/d_{max} = 0.6$ and $d/d_{max} = 0.8$ with a slightly higher amount of positive charges. For PET with crystalline fraction of $\chi_C = 25\%$, negative and positive homocharges are present with a much higher density for the positive charges. Positive measured charges correspond not only to holes injection but also to residual polarization as demonstrated by the lower negative induced charges at the anode compared to the positive internal charges nearby. With the highest crystalline fraction ($\chi_C = 40\%$), only positive charge amount near anode is observed and correspond to residual polarization.

Crystalline phase acts as a barrier for charge explaining the decrease of charges injection and transport with crystallinity. Furthermore, the presence of residual polarization at high crystallinity results from the restriction of macromolecules movements by the crystalline phase.

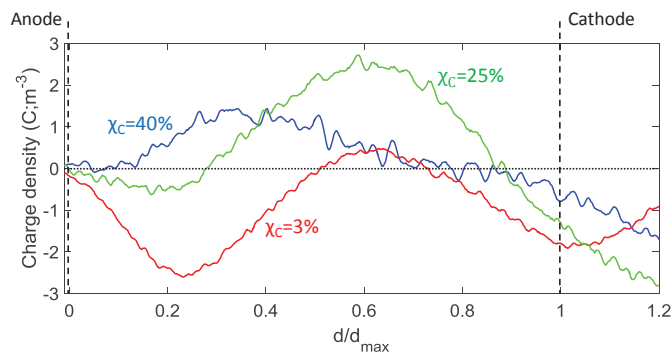


Figure 2.40: Residual space charge measured at Volt-off after stress at 25 kV/mm for 24 h at 70°C for PET of various crystalline fraction.

2.5.5 PDP influence on space charge

To demonstrate the impact of PDP in XLPE space charge, PEA measurement are performed in undegassed (1.2% of PDP) and fully degassed XLPE (0% of PDP) at 30°C and 70°C. At both temperatures, samples underwent an increasing electric field according to the program of Figure

2.36. In Figure 2.41 and Figure 2.42 are shown the residual space charge measured at Volt-off after stress under 40 kV/mm at 30°C and 70°C.

In fully degassed XLPE, positive homocharges are measured at both temperatures. At 30°C, charges are very close to the anode and almost no charges are present in the second half of the material thickness whereas, at 70°C, positive charges are present in all material thickness. No heterocharges are present as there are no chemical residues and no charge packet behavior is occurring.

At 30°C, space charge profile of undegassed XLPE is completely different with the presence of negative heterocharges covering almost all sample thickness. These negative heterocharges may come from the ionization/dissociation of α CA or to its dipolar orientation. At 70°C positive and negative homocharges are present in the material. In this case thermally assisted charge injection is prevailing over the ionic conduction process related to the PDP. Contrary to fully degassed XLPE, negative homocharges are present in undegassed XLPE at 70°C. These negative homocharges may be attributed to the presence of ACP that act as deep trap for electrons.

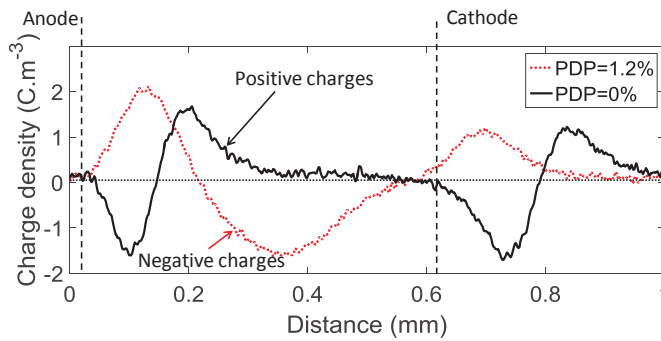


Figure 2.41: Residual space charge measured at Volt-off after stress under 40 kV/mm for 24 h at 30°C for undegassed and fully degassed XLPE.

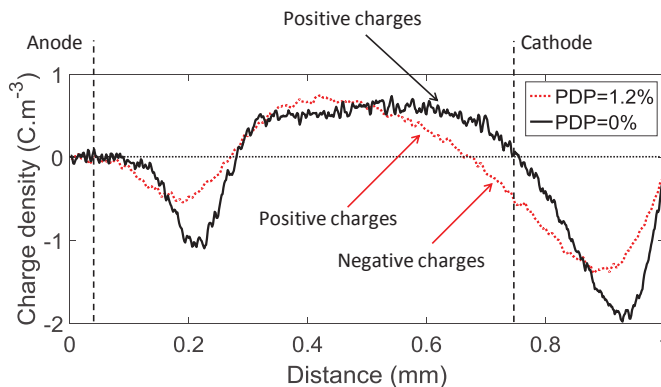


Figure 2.42: Residual space charge measured at Volt-off after stress under 40 kV/mm for 24 h at 70°C for undegassed and fully degassed XLPE.

Discussion

From electrical property variations of the material *models versus* electric field, temperature and time, a qualitative and quantitative impact of the related heterogeneity is obtained. The genetic

algorithm can be developed by establishing the most accurate evolution law to describe both the influence of this heterogeneity on polymer electrical properties and its evolution over time.

Another experimental behavior present in insulation polymer that have to be considered is the correlation between the apparent conductivity and space charge.

According to Poisson's equation, space charge is responsible for electric field distortion, increasing in one part of the insulator with a concomitant decrease elsewhere [169]. The consequence is the current-voltage characteristic becomes governed by space charge accumulation [166]. In the literature, space charge accumulation was indeed observed to be concomitant with the non linearity onset in the current-voltage characteristic [170]. This non-linearity in the current-voltage characteristic is also predicted in the Space Charge Limited Conduction theory (SCLC) [5]. From a critical voltage, the SCLC dominates over the Ohmic component and the field distribution becomes determined by the accumulated space charge.

In order to get correlations, similar electric field program is applied for both conductivity and space charge measurement in XLPE. Aiming at evidencing the effect of electrical history on measured conductivity and space charge in XLPE, steps of increased electric field from 20 to 40 kV/mm are applied followed by steps of decreased electric field from 40 to 20 kV/mm. For each electric field, current is measured for 2 to 3 days in order to allow samples reaching a steady state. For a given electric field, current density at steady state is compared for increased or decreased voltage.

In Figure 2.43 are plotted the change of current density with electric field for degassed XLPE tested at 70°C. For a given electric field, a significant change is observed in the measured steady-state current when considering the increase or decrease of voltage. At same electric field, the difference between the 2 current density values seems to increase with the distance from the maximum electric field that was applied to the sample. In other words, the current-voltage dependence appears increased when the electric program is applied in a decreasing way.

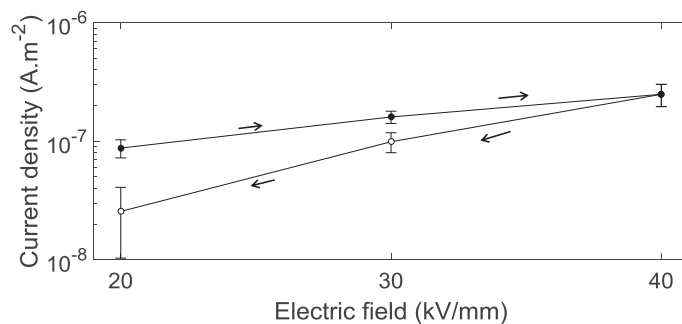


Figure 2.43: Current density *versus* electric field for an increasing and decreasing electric field at 70°C in degassed XLPE.

This behavior comes from the injected charges at high electric field that limit the current at lower fields according to SCLC theory. In fully degassed XLPE, positive homocharges are measured at 70°C with PEA measurements. Due to these homocharges, there is a decrease of local electric field near the injection surface. The mean value of total (positive plus negative) charge density accumulated inside XLPE can be estimated integrating the absolute value of the measured charge

density q_p over insulation thickness d as follows:

$$q = \frac{1}{d} \int_0^d |q_p|(x) dx \quad (2.5.9)$$

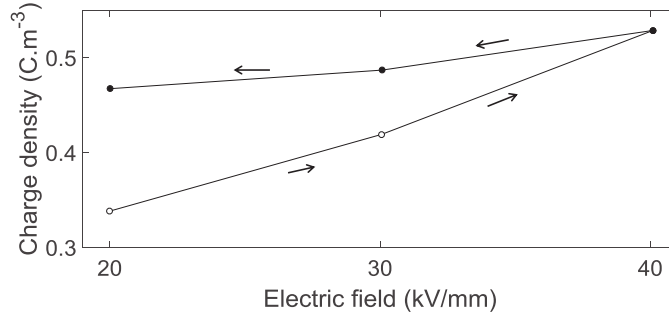


Figure 2.44: Accumulated charge density *versus* electric field for an increasing and decreasing electric field at 70°C in degassed XLPE.

In Figure 2.44 is plotted the mean value of total charge density with electric field in degassed XLPE tested at 70°C.

As for conductivity, a significant change is observed in the measured mean charge density when considering the increase or decrease of voltage. During the voltage decrease, space charge amount is decreasing but this decrease is far weaker than the space charge increase during the voltage increase. This behavior is due to the fact that charges trapped at higher electric field remain trapped in the bulk of XLPE during the voltage decrease.

The lowered conductivity observed after the application of higher electric field are the consequence of the electric field distribution which is directly impacted by the amount of space charge trapped at highest field. Space charge injected and trapped at highest electric field may decrease the local electric field at the interface thus reducing charge injection and conductivity measured for all following electric fields of lower values.

Chapter 3

Genetic model description

The main objective of this work is to develop a model that can simulate the quantitative correlations observed experimentally between microstructure and electrical properties of polymers. In this model, both electrical properties and microstructure evolution with time are taken into account.

The core of this model is based on solid state physics applied to insulation. In this central structure, physics laws such as charge injection, charge extraction and charge trapping are integrated to simulate the electrical behavior of an homogeneous insulation. Then, to take into account influence of polymer microstructure, several simulation *modules* have been developed (see Figure 3.1). Each of these *modules* focus on a specific chemical or physical heterogeneity present in the polymer and integrate the related physics of this heterogeneity. Furthermore this model has multi-scale approach which allows to address the influence of heterogeneity from macroscopic to microscopic scales.

To do so, the polymer of interest is described by a matrix decomposing the material in mesoscopic states. Each state is characterized by a specific local microstructure of polymer. Depending on electric field, temperature and time, each state evolves over time.

The description of the different states composing the insulation structure is determined probabilistically. This description is very well adapted for polymeric materials which generally have a randomly inhomogeneous microstructure. Each state evolves according to probabilistic laws developed from correlations experimentally made between the microstructure and electrical properties of polymer. These laws require a full characterization of the polymer microstructure meaning a very accurate description of all heterogeneities present in polymer and quantitative measurement of the effect of these heterogeneities on dielectric properties of polymer *versus* temperature, electric field and time.

In this chapter, the core of the genetic model developed under MatLab software is described. In a first part, an overall description of the genetic algorithm is made with the electrical properties as state matrices, the evolution laws and the explicit calculation method used in this model. The different calculation methods of electrical properties are shown with the simulation of charge injection, charge extraction and charge trapping in a homogeneous insulation.

In the next two chapters are addressed the *modules* related to the semi-crystalline structure with its characteristic temperatures, the peroxide decomposition products from XLPE and the interface effects.

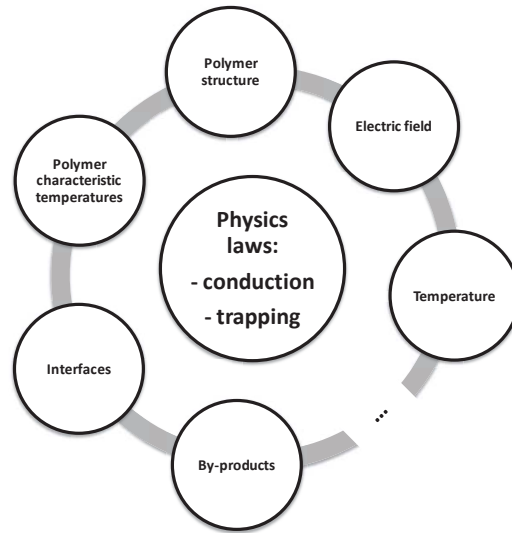


Figure 3.1: Structure of the model.

3.1 Electrical properties output

A 2 dimensions (2D) model is used to describe the polymer insulation. The x -direction is relative to the sample thickness where voltage is applied and the y -direction is relative to the direction orthogonal to the applied macroscopic electric field. A 2D model is chosen instead of 1D model as it allows charge transport in both direction and thus offer the possibility for charges to move around an obstacle (spherulites for instance) in the bulk of insulation. It is assumed that a 3D model increases the simulation time without giving more accurate simulated results than with a 2D model.

The 2D model is decomposed in 100 elements in the x -direction and 20 elements in the y -direction with a length for each element of $10\ \mu\text{m}$ in both directions. Discretisation of $10\ \mu\text{m}$ is relative to the maximum of spherulite diameter found in polymer [80].

Thus, matrix of 100×20 length are ascribed to each heterogeneity and electrical property of polymer. Matrices used to describe main polymer electrical and thermal properties are listed below:

Matrices for polymer electrical properties	
Electric field (kV/mm)	x component of local electric field
	y component of local electric field
	absolute value of local electric field
Charge density (C/m^3)	deep trap electron density
	deep trap hole density
	shallow trap electron density
	shallow trap hole density
	Mobile electron density
	Mobile hole density
Permittivity (F/m)	
Temperature (K)	

Table 3.1: List of matrix used in the model to describe electrical properties of polymer.

Each of these matrices are initialized according to input parameters such as applied voltage and temperature. Electric field calculation method is different from the other electrical outputs as a finite element method (FEM) is used to simulate its distribution.

3.1.1 Electric field

Electric field distribution is obtained by solving Gauss' equation $\vec{\nabla}(\epsilon\vec{\nabla}V) + \rho = 0$ with the finite element method provided by a MatLab function. To apply this method, a discretization of the 100×20 matrix is performed: each square of the matrix is decomposed in two triangles. This discretization allows a very fast solving with an enough accuracy of the electric field distribution. Boundary conditions are applied to the system with Dirichlet's conditions in the x -direction and Neumann's conditions in the y -direction as presented in Figure 3.2. Dirichlet condition is a condition on the amplitude of the potential with $V = V_{applied}$ at one side and $V = 0$ at the other side. Neumann's condition is a condition on the normal component of the electric field at the y -interface, where system is symmetric, which has to be null: $\epsilon\vec{E} \cdot \vec{n} = 0$. To solve the Gauss' equation, points and edges of the mesh, boundary conditions, permittivity and charge density distribution in each element of volume are required.

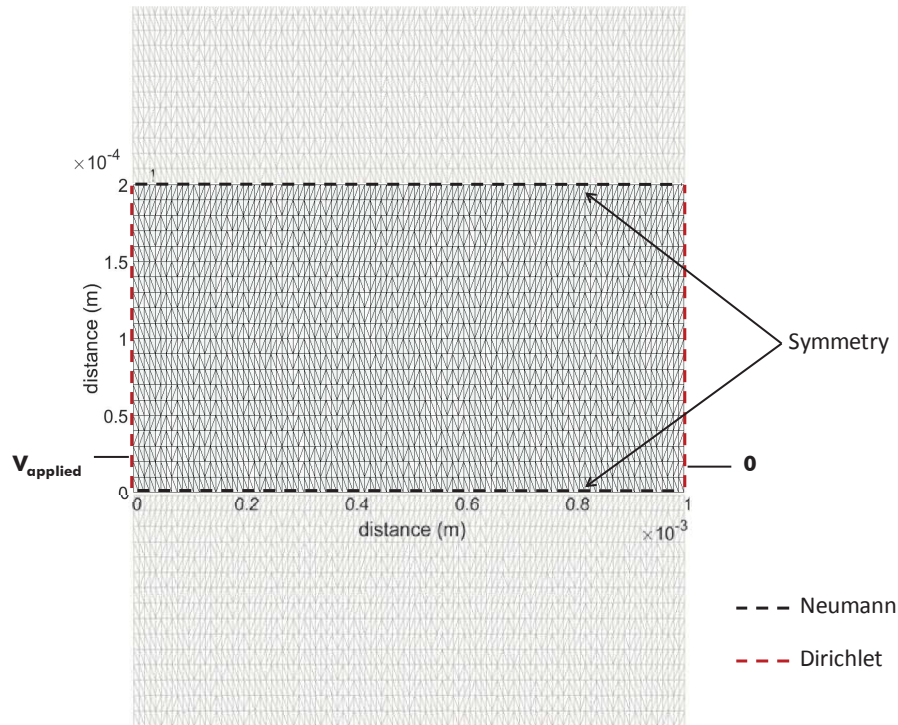


Figure 3.2: Discretization of the matrix and boundary conditions.

The solving function returns the potential at each point of the mesh. Then the x -component and y -component of the electric field in each triangle is calculated from these potential values with the relation: $\vec{E} = -\vec{\nabla}(V)$. Finally, value of electric field in each matrix element corresponds to the mean value of those in the two triangles meshing the related element. The absolute value of electric field is given by:

$$E = \sqrt{E_x^2 + E_y^2} \quad (3.1.1)$$

In Figure 3.3 is shown the simulated distribution of potential and electric field in the x-direction for a material without space charge and with constant permittivity when a voltage of 30 kV is applied. As there is no space charge and as permittivity is constant, an expected decreasing potential from 30 kV to 0 V is observed along the thickness of the material with an expected uniform electric field of 30 kV/mm in the material.

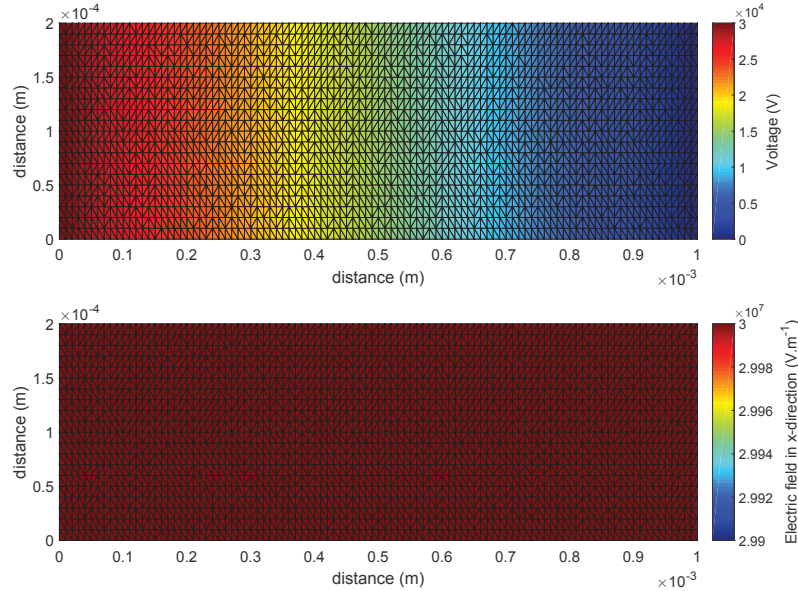


Figure 3.3: (up) Simulated voltage distribution without space charge and with constant permittivity. (down) Simulated electric field in the x-direction distribution without space charge and with constant permittivity.

3.1.2 Charge density

In this model, six matrices are dedicated to the description of electrons and hole behaviors. A 2D bipolar charge transport is considered comprising both electron and hole injection and extraction. Moreover a distinction is made between mobile and trapped charges. For charge trapping, a binary approach is considered with shallow and deep traps. This description is based on the results obtained by Meunier *et al.* [116, 134].

Therefore, two matrices describe the densities of mobile charges (positive and negative). two other matrices are dedicated to the description of the densities of shallowly trapped positive and negative charges. The two last matrices are ascribed to deeply trapped charges.

The net charge density corresponding to the sum of each charge density matrix is used to solve the Gauss' equation and to determine the local electric field. An example is given in Figure 3.4, where a charge density radially decreasing is simulated in the center of the material. The electric field, simulated in presence of this charge density, present an heterogeneous distribution with a higher value on one side of the charge density and a lower value on the other side. The radial electric field increase and decrease on each side of the charge density is directly linked to the radial distribution of the charge density.

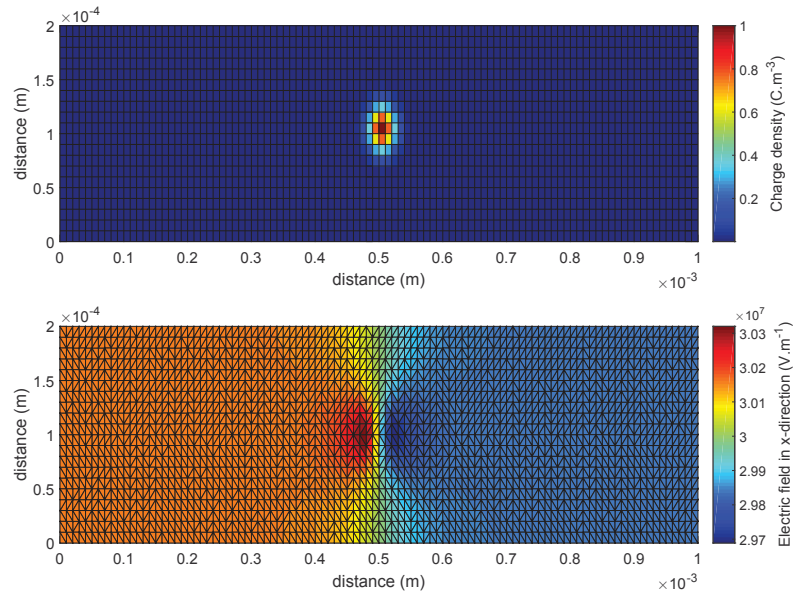


Figure 3.4: (up) Simulated gaussian space charge accumulation in the center of the material. (down) Simulated related local electric field in the x -direction.

3.1.3 Permittivity and temperature

Local permittivity and local temperature are also considered in the model. As XLPE has an heterogeneous microstructure, its permittivity is very likely to have a distribution. Local permittivity matrix has an effect on the electric field distribution from the Gauss' equation. An example of this effect is presented in Figure 3.5, where a permittivity gradient is simulated within the thickness of the material. This permittivity gradient can be present, for instance, in XLPE submitted to a temperature gradient from 30°C to 70°C. The related simulated electric field shows a decreasing electric field while permittivity is increasing.

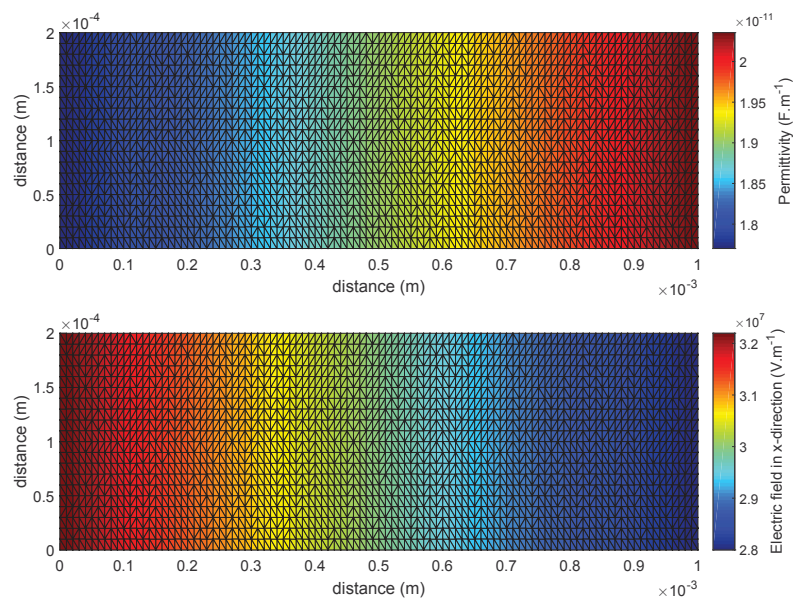


Figure 3.5: (up) Simulated permittivity gradient. (down) Simulated related local electric field in the x -direction.

3.2 Development of evolution laws

First evolution laws developed in this model describe the space charge evolution of an homogeneous insulation system. Injection, transport and extraction laws are developed to describe the behavior of mobile charges. Trapping and detrapping laws are developed and ascribed to the behavior of shallowly and deeply trapped charges. All evolution laws are expressed for a material depth of 1 m.

3.2.1 Charge injection

Law used for charge injection is based on Schottky current injection as it is the most likely mechanism to occur according to the literature [24]:

$$j_{inj} = A. T^2 \exp\left(\frac{e}{k_B T} \sqrt{\frac{eE}{4\pi\epsilon}}\right) \exp\left(-\frac{e.w_{e,h,inj}}{k_B T}\right) \quad (3.2.1)$$

with $A = 4\pi m k_B^2 / \hbar^2$ [A.m⁻²K⁻²] the Richardson constant, T [K] the local temperature, E [V/m] the local electric field and ϵ [F/m] the local permittivity. An evolution law based on this Schottky current density is used for electron injections in states near cathode at each time step:

$$Q_{e,inj} \propto -\delta r \delta t T^2 \exp\left(\frac{e}{k_B T} \sqrt{\frac{eE_{cat}}{4\pi\epsilon}}\right) \exp\left(-\frac{e.w_{e,inj}}{k_B T}\right) \quad (3.2.2)$$

and for holes injection near anode:

$$Q_{h,inj} \propto \delta r \delta t T^2 \exp\left(\frac{e}{k_B T} \sqrt{\frac{eE_{an}}{4\pi\epsilon}}\right) \exp\left(-\frac{e.w_{h,inj}}{k_B T}\right) \quad (3.2.3)$$

with δr [m] the cell length, δt [s] the time step, $w_{e,inj}$ [eV] the energetic barrier for electron injection, $w_{h,inj}$ [eV] the energetic barrier for hole injection, E_{cat} [V/m] the electric field at the cathode and E_{an} [V/m] the electric field at the anode. This injection law depends on the local electric field at the cathode or anode and thus takes into account the space charge accumulation that can occur at the interface. Values used for the activation energy of hole and electron injections in the simulation are shown in Table 3.2. These values were taken from the work of Le Roy [121].

Parameters	signification	unity	value
$w_{e,inj}$	Activation energy of electron injection	eV	27
$w_{h,inj}$	Activation energy of hole injection	eV	1.16

Table 3.2: Parameters chosen for charge injection laws.

3.2.2 Charge transport

For charge transport, a thermo-activated mobility of charge carrier is applied. Current density transport is then expressed as:

$$j_{tr} = \rho_{e/h} \mu_{e/h} \exp\left(-\frac{e\beta_{e/h}}{k_B T}\right) E \quad (3.2.4)$$

with $\rho_{e/h}$ [C/m³] the local charge density of electron and hole, $\mu_{e/h}$ [V.m².s⁻¹] the factor of the local charge mobility of electrons and holes and $\beta_{e/h}$ [eV] the activation energy of electron and hole transport. As a 2D system is addressed in this model, both transport in the x -direction and y -direction is occurring. Evolution laws for electron and hole amounts transported between states at each step time in the x -direction is given by:

$$Q_{e/h,tr,x} = \delta r \delta t \rho_{e/h} \mu_{e/h} \exp\left(-\frac{e\beta_{e/h}}{k_B T}\right) E_x \quad (3.2.5)$$

and in the y -direction:

$$Q_{e/h,tr,y} = \delta r \delta t \rho_{e/h} \mu_{e/h} \exp\left(-\frac{e\beta_{e/h}}{k_B T}\right) E_y \quad (3.2.6)$$

Values used for the activation energy of hole and electron transport and their mobility in the simulation are shown in Table 3.3. An activation energy of charge transport close to the one related to the β -relaxation process in semi-crystalline polymer (0.7 eV) is taken, as it is assumed that macromolecule mobility in the amorphous phase drives the charge transport. Parameters $\mu_{e/h}$ are chosen in order that mobility of electrons and holes in the model at room temperature are close to what is found in the literature for semi-crystalline polymers [121].

Parameters	signification	unity	value
β_e	Activation energy of electron transport	eV	0.65
β_h	Activation energy of hole transport	eV	0.65
μ_e	Mobility of electron	m ² /(V.s)	10 ⁻²
μ_h	Mobility of hole	m ² /(V.s)	2 × 10 ⁻²

Table 3.3: Parameters chosen for charge transport laws.

3.2.3 Charge extraction

Space charge measurements performed in polymers do not show any accumulation of heterocharges coming from the difficulty of extraction of the injected charge carriers after travel through the thickness of the dielectric. Thus no extraction barrier is implemented in this model and current density of charge extraction is given by:

$$j_{ext} = \rho_{e/h} \mu_{e/h} \exp\left(-\frac{e\beta_{e/h}}{k_B T}\right) E \quad (3.2.7)$$

Charge amount extracted for electrons and holes at each step time is given by:

$$Q_{e/h,ext} = \delta r \delta t \rho_{e/h} \mu_{e/h} \exp\left(-\frac{e\beta_{e/h}}{k_B T}\right) E_{an/cat} \quad (3.2.8)$$

3.2.4 Charge trapping and detrapping

For charge trapping, two trap levels are considered with a maximum charge density that can be trapped in each of them. Trapping law corresponds to a probability of trapping that decreases with increased amount of trapped charges. Furthermore trapping law is proportional to the local charge density. Trapping law is expressed as:

$$Q_{trap} = \alpha (\delta r)^2 \rho_{mob} \left(\frac{Q_{trap_{max}} - (\delta r)^2 \rho_{trap}}{Q_{trap_{max}}} \right) \left(\mathcal{P} < \frac{Q_{trap_{max}} - (\delta r)^2 \rho_{trap}}{Q_{trap_{max}}} \right) \quad (3.2.9)$$

with $Q_{trap,max}$ [C] the maximum charge amount that can be trapped in each matrix states, depending on the charge carrier and on the trap level, ρ_{mob} [C/m³] the mobile charge density, ρ_{trap} [C/m³] the trapped charge density, α a parameter inferior to 1 which corresponds to the proportion of charges trapped at each step time and \mathcal{P} a random number between 0 and 1 that corresponds to the probability of trapping depending on the trapped charge amount.

For the detrapping, the law depends on the nature of the trap, either deep or shallow, and on the nature of the charge carrier:

$$Q_{detrapp} = \alpha (\delta r)^2 \rho_{trap} \left(\mathcal{P} < \frac{k_B T}{h} \exp \left(\frac{-e \cdot \xi_a}{k_B T} \right) \right) \quad (3.2.10)$$

with ρ_{trap} [C/m³] the trapped charge density, α a parameter inferior to 1 which corresponds to the proportion of charges detrapped at each step time and ξ_a [eV] the activation energy of detrapping depending on charge carrier and trap depth. Parameter values for trapping and detrapping are shown in Table 3.4. For maximum charge trapping, values are taken from DFT calculation made by Quirke *et al.* [116]. Parameter α is chosen in order that simulated leakage current has a similar exponential decrease as the experimental leakage current measured in insulation polymer. Values for activation energy of shallow traps and deep traps are typical values given in the literature [116, 119].

3.3 Evolution of the system over time

The backbone of the genetic algorithm is shown in Figure 3.6. For each iteration, after determination of the local electric field distribution, the polymer system is modified according to the evolution laws. Then current density is calculated from the system evolution. As an explicit method is used in the genetic algorithm, at each iteration, the step time must be properly chosen to avoid system oscillation.

3.3.1 System evolution from evolution laws

From evolution laws, system evolves at each time step. For the electronic species, electron and hole charge densities of each state of the matrix is modified according to injection, extraction, transport and trapping laws. New values for electron and hole charge densities of each state at $t + dt$ are given by:

$$\rho_{mob}(x, y, t + dt) = \rho_{mob}(x, y, t) + \frac{Q_+(x, y, t)}{(\delta r)^2} - \frac{Q_-(x, y, t)}{(\delta r)^2} \quad (3.3.1)$$

Parameters	signification	unity	value
$Q_{trap_{max,e,deep}}$	maximum trapping for electron in deep trap	C	1.6×10^{-5}
$Q_{trap_{max,e,shallow}}$	maximum trapping for electron in shallow trap	C	1.6×10^{-7}
$Q_{trap_{max,h,deep}}$	maximum trapping for hole in deep trap	C	1.6×10^{-5}
$Q_{trap_{max,h,shallow}}$	maximum trapping for hole in deep trap	C	1.6×10^{-7}
α	proportion of charge trapped/detrapped	/	3×10^{-3}
$\xi_{a,e,deep}$	Activation energy of electron detrapping in deep trap	eV	0.9
$\xi_{a,e,shallow}$	Activation energy of electron detrapping in shallow trap	eV	0.05
$\xi_{a,h,deep}$	Activation energy of hole detrapping in deep trap	eV	0.9
$\xi_{a,h,shallow}$	Activation energy of hole detrapping in shallow trap	eV	0.05

Table 3.4: Parameters chosen for charge trapping and detrapping laws.

where $Q_+(x, y, t)$ [C] corresponds to laws that increase the local charge density of the state such as injection law, transport law from an adjacent state and detrapping law and $Q_-(x, y, t)$ [C] corresponds to laws that decrease the local charge density of the state such as extraction law, transport law in an adjacent state and trapping law.

3.3.2 Current density calculation

Current density is composed of conduction current density and displacement current density. Diffusion current is neglected. Charge conservation law is used to obtain conduction current density from the charge transport occurring in the x -direction:

$$\frac{\partial(Q_x/(\delta r)^2)}{\partial t} + \frac{\partial j_{cond}}{\partial x} = 0 \quad (3.3.2)$$

where Q_x [C] is the charge transport laws in the x -direction, including charge injection and extraction, and j_{cond} [A/m²] is the conduction current density. Displacement current density is given by:

$$j_{displacement} = \frac{\partial \varepsilon E}{\partial t} = \frac{\delta(\varepsilon E)}{\delta t} \quad (3.3.3)$$

where $\delta(\varepsilon E)$ is the variation of product electric field \times permittivity between t and $t + \delta t$.

The Figure 3.7 shows the simulated mean conduction current and mean current displacement over sample surface and the resulting total current density when sample is submitted to a constant electric field of 30 kV/mm under a temperature of 30°C without charge trapping. As both charge transports in the x -direction and y -direction is occurring in this model, conduction current and displacement current signals are noisy. However the resulting total current density is far less noisy. At the beginning, between 0s and 100s, there is no electronic path between

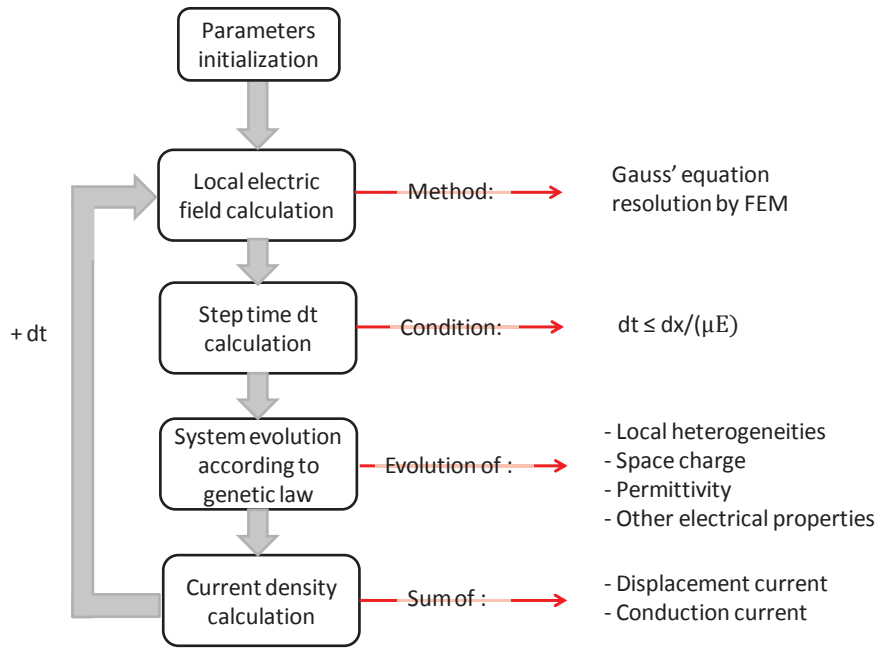


Figure 3.6: Genetic algorithm.

cathode and anode and total current is mostly given by displacement current also called charging current. Then, after 120s, when electronic path between cathode and anode is clearly made, total current is mostly given by conduction current.

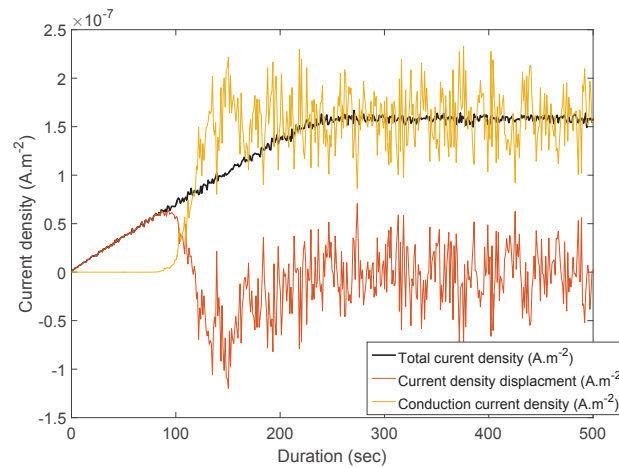


Figure 3.7: Simulation of current displacement density, conduction current density, and total current density with no charge trapping.

3.3.3 Step time calculation

In this model, an explicit method is used for the time evolution. Thus the choice of the time step δt is crucial to avoid oscillation in the simulation. A maximum value for δt is given by the Courant–Friedrichs–Lewy (CFL) condition [171]. The principle behind this condition is that charges cannot cross two matrix units in a single time step δt . By considering the highest

mobility μ_{max} and E_{max} the maximum local electric field, the value of δt has to be lower than:

$$\delta t < \frac{\delta x}{\mu_{max} E_{max}} \quad (3.3.4)$$

It can be seen that the higher the electric field and mobility, the lower the step time. The value of δt can be very low, for instance $\delta t = 0.037$ s with the constants in Table 3.3, a temperature of 70°C and an electric field of 30 kV/mm. Using this low value of δt in all the genetic algorithm is not adapted for the modeling of slow process evolution such as electronic trapping which can take several hours. Indeed, one of the aim of this model is to give a fast solving compared to other models such as FEM. To simulate a material evolution for 1 hour with a step time of 0.037 s requires 1.10^5 iterations. As 100 iterations requires 2s, it will take half an hour to simulate 1 hour experiment time.

The strategy to decrease this simulation time is to make the system evolve accordingly to the evolution laws without calculating the electric field and the current density at each step time. A simulation of 1 hour experiment time in this case lasts less than 5 min. An example is given in Figure 3.8, where the current density is represented as a function of time with slow trapping effect. One of the curve is obtained when the electric field and the current density are calculated at each time step, and the other curve when these values are calculated only every 2000 iterations. Same current is measured in both cases showing that calculation electric field and current density at each iteration during slow process is not necessary. Therefore, simulation time can be dramatically decreased without affecting the simulation results.

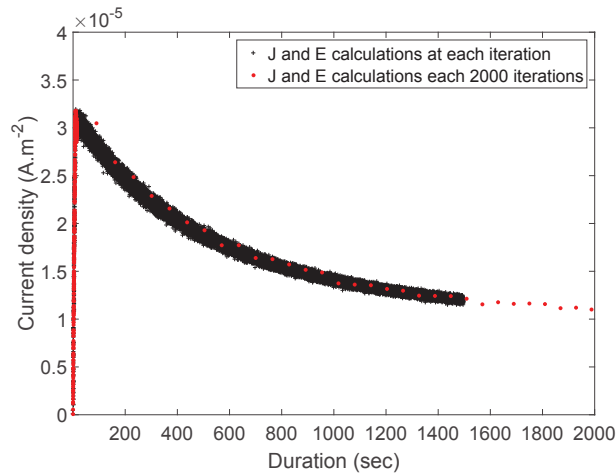


Figure 3.8: Simulated current density with trapping when current density and electric field are calculated at each time step and when they are calculated every 2000 iterations.

3.4 Simulation results

3.4.1 Leakage current and space charge measurements

Leakage current is simulated in a homogeneous insulation at 30°C under steps of increased electric field from 20 to 40 kV/mm. Electric field is applied with ramp up speed of 0.25 kV/(mm.s). For the input parameters of the simulation, the constants relative to electric transport in polymer of Table 3.2, Table 3.3, and Table 3.4 are used.

Results are shown in Figure 3.9 on a log-lin current density *versus* time graph. For each voltage step, an exponential decrease of current is observed. This exponential decrease is related to the charge trapping occurring in the material under electrical stress. As expected, current density at steady state is increasing with electric field.

Simulated space charge at 30°C for electric fields of 20, 30 and 40 kV/mm is simulated as shown in Figure 3.10. In space charge measurements performed with PEA, both internal and induced charges are observed. The latter appear as a positive and negative Gaussians at the interface. Induced charges correspond to charges built up on the electrodes which widths depend on the bandwidth of the measurement system and the interface between the polymer and electrodes. Thus, these induced charges correspond to an experimental artifact that is not present in the simulation, that considers only the charges trapped in the material. Concerning the internal charges, positive and negative homocharges are present.

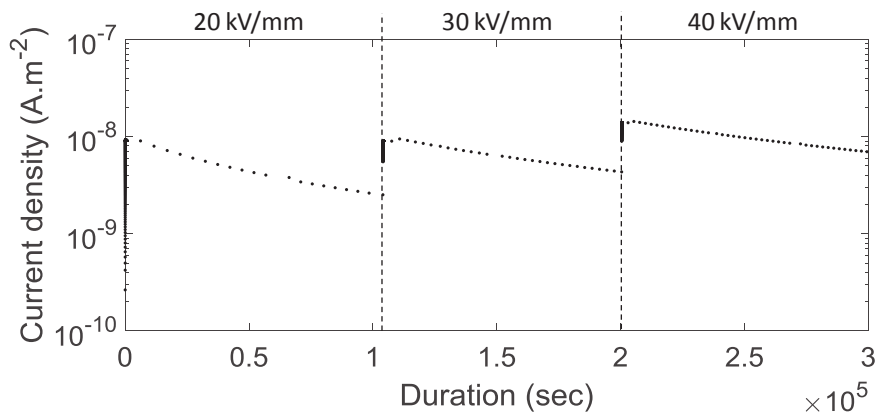


Figure 3.9: Leakage current simulation at 30°C under increasing electric field from 20 to 40 kV/mm

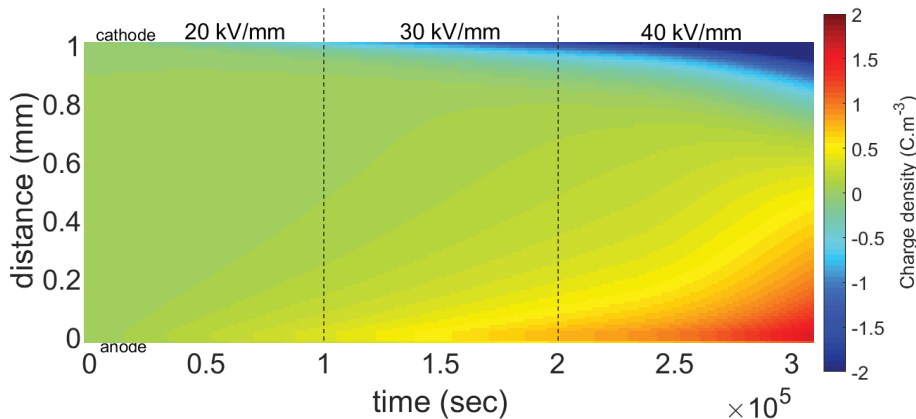


Figure 3.10: Simulation of charge density measured at 30°C under increasing electric field from 20 to 40 kV/mm.

3.4.2 Current density dependency with electric history: space charge effect

Aiming at simulating the effect of electrical history on measured conductivity and space charge in insulation, steps of increased electric field from 20 to 40 kV/mm are applied. Steps of decreased

electric field from 40 to 20 kV/mm are then further applied on the same sample. Each electric field is applied for 10^5 sec.

In Figure 3.11 is plotted simulated current density *versus* time at 70°C . At same electric field, a lower current density is observed after stress at higher electric field. An explanation of this behavior comes from the injected charges at high electric field that limit the current at lower fields according to SCLC theory [5]. Thus, the modeling approach of this work allows for simulating the current limitation from space charge injection. In this homogeneous material, the lowered

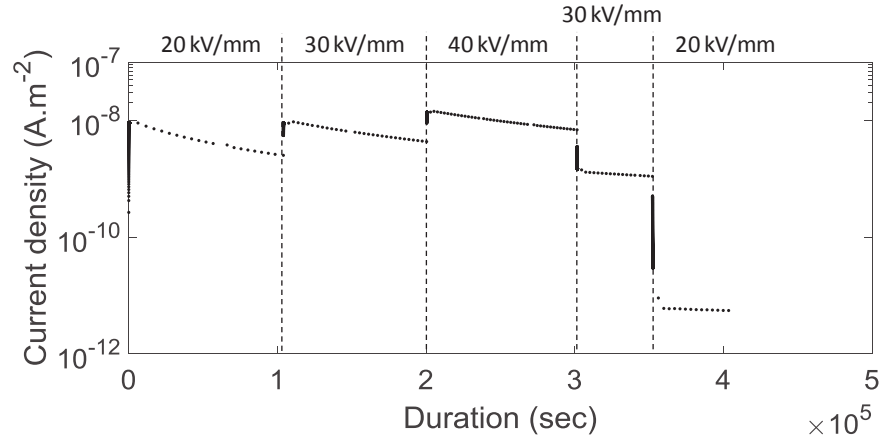


Figure 3.11: Leakage current simulated at 70°C under increasing and decreasing electric field from 20 to 40 kV/mm.

leakage current observed after the application of higher electric field are the consequence of the electric field distribution which is directly impacted by the amount of space charge trapped at highest electric field. Space charges injected and trapped at highest electric field decrease the local electric field at the interface thus reducing charge injection and conductivity for all next lower applied electric fields. Simulation of electric field at 20 and 30 kV/mm in Figure 3.12 demonstrates clearly a lower local electric field at the injection interface after stress at 40 kV/mm.

3.4.3 Electrical properties dependency with electric field: SCLC

In HVDC insulation systems, an electric field threshold value relevant to the stored space charge and steady state leakage current is generally measured [170]. The electric threshold regarding the space charge is obtained by plotting the value of the total accumulated charge density, measured during depolarization time, as a function of the poling electric field. A slow increase of charge density at low fields (values below the resolution of the PEA system) is measured, followed by a higher increase of charge density once the threshold electric field for space-charge accumulation is reached. In log–log plot, linear behavior is generally obtained below and above the threshold, with a higher slope above the threshold.

For leakage current dependency with electric field, according to the SCLC theory, at fields below an electric threshold, the conduction is of Ohmic type, while at fields above the threshold the relation between current density and applied voltage is quadratic [172]. A coincidence between the threshold for space charge measurements and current density measurement has been measured in the literature [54, 173].

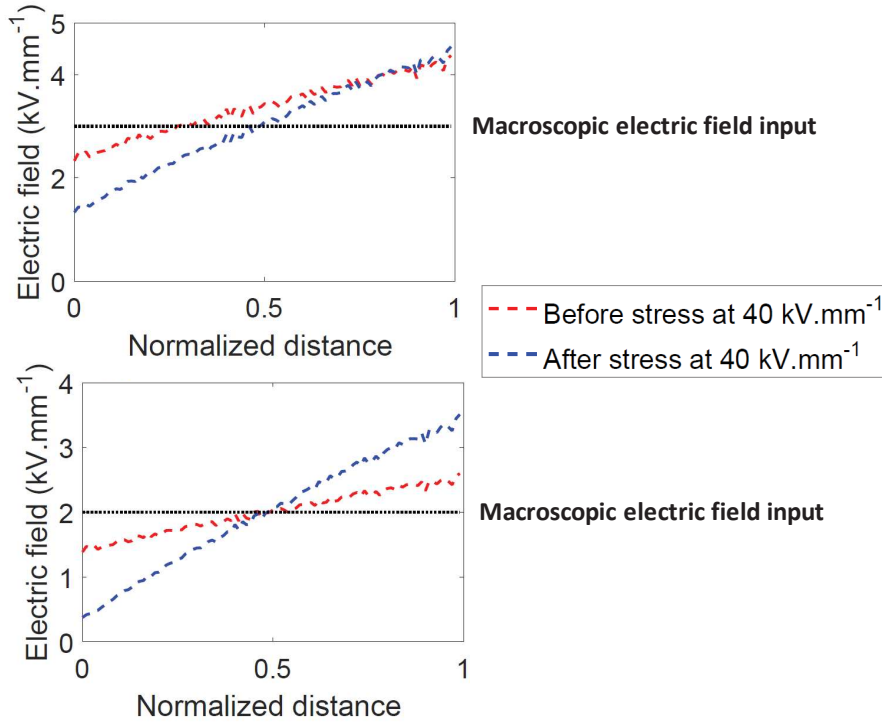


Figure 3.12: Simulated electric field distribution at 70°C under 20 and 30 kV/mm before and after electric stress of 40 kV/mm for 24 h.

Simulated homogeneous insulation system in the genetic model is submitted to increasing electric field from 2 to 210 kV/mm at 30°C . No other input parameters than the applied electric field are varied. Simulated current density *versus* electric field is shown in Figure 3.13. The total accumulated charge density is collected after 24 h of poling at these electric fields and plotted in log-log coordinate *versus* the input macroscopic applied electric field in Figure 3.14.

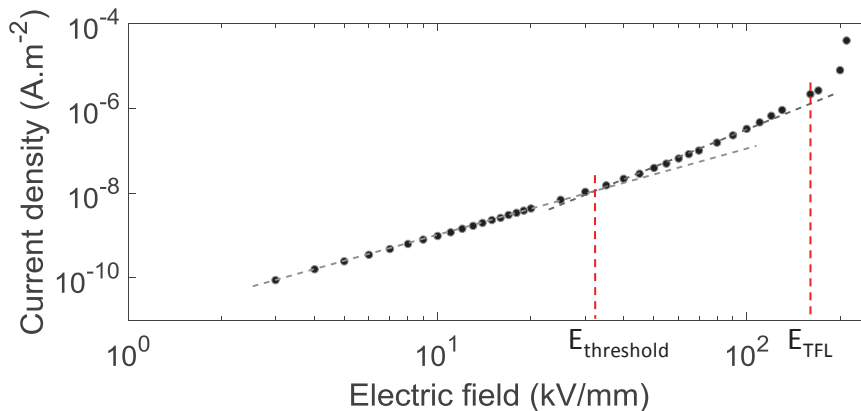


Figure 3.13: Simulated thresholds characteristic of conductivity in log-log plot at 30°C .

The SCLC effect is accurately simulated with the model showing an electric threshold both for charge accumulation and current density with the same value around 30 kV/mm. Furthermore, *trapped filled limit*, which correspond to the electric field limit where all traps are filled, are present in the simulation results with a value around 170 kV/mm. The simulated threshold is at the same order of magnitude of the measured threshold in the literature, between 10 and

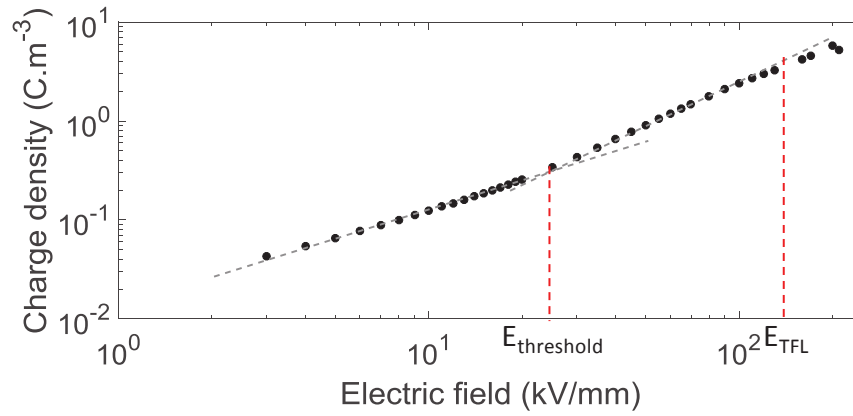


Figure 3.14: Simulated thresholds characteristic of space charge in log–log plot at 30°C.

15 kV/mm, for PE-based material. The difference, around 15 kV/mm, is due to the fact that the specific heterogeneities of PE is not take into account in this simulated SCLC effect. Solving time less than two hours is only needed with the model to obtain current density and charge density values of these 43 electric fields.

Summary

The core of the model is developed in this chapter with the evolution laws describing the charge transport, injection, extraction and trapping. For a given set of input parameters, this model is able to reproduce qualitatively current density variation and space charge profile of homogeneous polymer at several electric fields. Furthermore the simulation of space charge effect on current density and presence of electric field threshold is made possible with this model. Finally all simulation results are obtained with a fast solving time.

Chapter 4

Genetic evolution of semi-crystalline polymer

In this chapter, evolution laws are developed to simulate the impact of the semi-crystalline structure on the electrical properties of polymers. Firstly, morphological analysis is used to create the matrix that describes the polymer microstructure. Then are presented charge transport and trapping in this structure simulated by evolution laws based on experimental results. Secondly, the influence of the model parameters is further assessed and fine tuned to obtain coherent simulated electrical behavior. Finally simulations of several semi-crystalline polymers are compared to experimental data. More particularly, the influences of temperature, electric field, macromolecule relaxations and crystallinity on polymer leakage current and space charge are simulated and compared to experimental data, either from the literature or obtained on purpose.

4.1 Heterogeneous semicrystalline structure simulation

To model the spherulitic semi-crystalline structure of polymers, each state of the matrix related to the material is characterized by a given number of spherulites with various edges and various radii. Furthermore a lamellae thickness distribution is associated to each of these spherulites as described in Figure 4.1.

4.1.1 Distribution of random spherulites in the model

In this model, spherulites are considered as regular polygons containing 3 to 6 faces with a circumradius R equal to the spherulite radius. This description is based on observations of polyethylene (PE) films reported in the literature as shown in Figure 4.2 [89].

Spherulitic distribution within semicrystalline polymers can be characterized by the mean and the standard deviation of spherulite radius. The distribution of spherulite radius is mostly dependent on cooling rate, cooling temperature and presence of defects and can be measured with X-ray analysis. In this work, X-ray data are taken from the work of Banks *et al.* [89] that reports the distribution in spherulite radius in low density polyethylene (LDPE) quenched at different cooling temperatures as shown in Figure 4.3.

List of spherulites present within the matrix

	1	2	3	4	5	6	7	8	9	10	11	12	13	14	15
Spherulite radius	6.2098e-07	5.9806e-07	8.4189e-07	1.1103e-06	6.1591e-07	9.1632e-07	7.9879e-07	9.9377e-07	3.3811e-07	1.5671e-06	1.4537e-06	4.0947e-08	1.0417e-06	2.0307e-06	1.3640e-06
Position in the x-direction		5	12	2	13	15	2	19	1	7	1	20	9	12	7
Position in the y-direction		7	85	4	58	36	76	52	62	15	58	7	20	34	30
Number of faces		6	5	5	3	5	3	6	4	3	3	4	3	3	5
Crystalline surface associated	1.0019e-12	8.5043e-13	1.6852e-12	1.6013e-12	9.0196e-13	1.0907e-12	1.6577e-12	1.9752e-12	1.4851e-13	3.1901e-12	4.2267e-12	2.1780e-15	1.4096e-12	9.8045e-12	4.8338e-12
List of lamellae associated to the spherulite	1.6013e-08	1.5155e-08	1.6837e-08	1.5992e-08	1.3435e-08	1.6973e-08	1.6320e-08	1.8357e-08	1.4334e-08	1.3525e-08	1.5659e-08	1.4384e-08	1.7109e-08	1.5789e-08	1.8430e-08
	1.5349e-08	1.3851e-08	1.5577e-08	1.4263e-08	1.2090e-08	1.2573e-08	1.5090e-08	1.6378e-08	1.3649e-08	1.3142e-08	1.5223e-08	1.1416e-08	1.4081e-08	1.5504e-08	1.7840e-08
	1.4912e-08	1.3849e-08	1.5307e-08	1.2822e-08	1.1762e-08	1.2182e-08	1.4081e-08	1.4709e-08	1.1036e-08	1.2859e-08	1.5050e-08	6.8111e-09	1.2975e-08	1.5356e-08	1.6439e-08
	1.4085e-08	1.3616e-08	1.4852e-08	1.2778e-08	1.1617e-08	1.2142e-08	1.3246e-08	1.4189e-08	1.0962e-08	1.2651e-08	1.4799e-08	6.4787e-09	1.2935e-08	1.5292e-08	1.6368e-08
	1.3310e-08	1.3564e-08	1.3370e-08	1.2667e-08	1.1483e-08	1.1913e-08	1.2827e-08	1.4127e-08	1.0802e-08	1.2630e-08	1.4680e-08	5.0857e-09	1.2803e-08	1.5164e-08	1.5298e-08
	1.3174e-08	1.3326e-08	1.3087e-08	1.2663e-08	1.1265e-08	1.1757e-08	1.2664e-08	1.4084e-08	9.6809e-09	1.2563e-08	1.4552e-08	3.8451e-09	1.2468e-08	1.5063e-08	1.4560e-08
	1.2906e-08	1.2731e-08	1.2668e-08	1.2631e-08	1.1213e-08	1.1579e-08	1.2364e-08	1.3898e-08	9.2428e-09	1.2477e-08	1.3969e-08	3.3339e-09	1.1959e-08	1.5028e-08	1.4425e-08
	1.2844e-08	1.2664e-08	1.2315e-08	1.2214e-08	1.1194e-08	1.1411e-08	1.2184e-08	1.3118e-08	8.9967e-09	1.2449e-08	1.3437e-08	0	1.1989e-08	1.4470e-08	1.3532e-08
	1.2675e-08	1.2602e-08	1.2202e-08	1.2163e-08	1.1076e-08	1.0846e-08	1.2122e-08	1.2764e-08	8.4787e-09	1.2252e-08	1.3387e-08	0	1.1675e-08	1.4932e-08	1.3512e-08
	1.2160e-08	1.2105e-08	1.2191e-08	1.1677e-08	1.1051e-08	1.0797e-08	1.1799e-08	1.2129e-08	8.4211e-09	1.2229e-08	1.3145e-08	0	1.1421e-08	1.3938e-08	1.3278e-08
	1.1908e-08	1.2058e-08	1.2173e-08	1.1574e-08	1.1044e-08	1.0622e-08	1.1778e-08	1.2122e-08	8.3586e-09	1.2029e-08	1.2802e-08	0	1.1182e-08	1.3662e-08	1.3263e-08
	1.1882e-08	1.1951e-08	1.1933e-08	1.1471e-08	1.0731e-08	1.0228e-08	1.1716e-08	1.2013e-08	8.2539e-09	1.1881e-08	1.2787e-08	0	1.1027e-08	1.3613e-08	1.2635e-08
	1.1709e-08	1.1791e-08	1.1799e-08	1.1219e-08	1.0492e-08	9.8665e-09	1.1714e-08	1.1939e-08	8.1364e-09	1.1870e-08	1.2559e-08	0	1.0983e-08	1.3558e-08	1.2520e-08
	1.1695e-08	1.1707e-08	1.1766e-08	1.0781e-08	1.0319e-08	9.6765e-09	1.1435e-08	1.1772e-08	8.0921e-09	1.1818e-08	1.2468e-08	0	1.0745e-08	1.3126e-08	1.2518e-08
	1.1591e-08	1.1663e-08	1.1455e-08	1.0731e-08	1.0141e-08	9.5848e-09	1.1362e-08	1.1695e-08	7.9662e-09	1.1699e-08	1.2344e-08	0	1.0502e-08	1.2924e-08	1.2345e-08
	1.1492e-08	1.1600e-08	1.1273e-08	1.0332e-08	1.0038e-08	9.5363e-09	1.1342e-08	1.1486e-08	7.5373e-09	1.1588e-08	1.2100e-08	0	1.0453e-08	1.2887e-08	1.2245e-08
	1.1437e-08	1.1067e-08	1.1210e-08	1.0080e-08	1.0017e-08	9.4578e-09	1.1323e-08	1.1435e-08	7.4758e-09	1.1352e-08	1.2080e-08	0	1.0120e-08	1.2791e-08	1.2155e-08
	1.1436e-08	1.0806e-08	1.1183e-08	1.0073e-08	9.9983e-09	9.3079e-09	1.1191e-08	1.1201e-08	7.1006e-09	1.1295e-08	1.1849e-08	0	1.0064e-08	1.2662e-08	1.2145e-08
	1.1331e-08	1.0852e-08	1.1104e-08	9.9940e-09	9.7641e-09	9.3373e-09	1.1117e-08	1.1035e-08	7.0318e-09	1.1149e-08	1.1520e-08	0	1.0003e-08	1.2652e-08	1.2131e-08
	1.1325e-08	1.0706e-08	1.0912e-08	9.8511e-09	9.7579e-09	9.0551e-09	1.0928e-08	1.0908e-08	6.9425e-09	1.1066e-08	1.1374e-08	0	9.9724e-09	1.2627e-08	1.2100e-08

Figure 4.1: Characteristics of the spherulites simulated with the radius, the position, the number of faces and the list of related lamella thickness distribution.

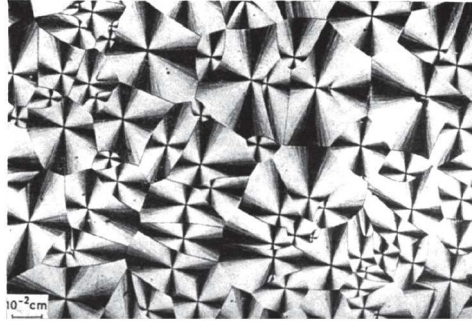


Figure 4.2: Distribution of spherulites in polyethylene in 5 μm thick plate crystallized by cooling at room temperature [89].

According to Banks *et al.* [89], proportion of spherulites radius follows a Gaussian law given by:

$$\frac{1}{\sigma_{\text{spherulite}}\sqrt{2\pi}} \exp\left(-\frac{1}{2}\left(\frac{r - r_{\text{mean}}}{\sigma_{\text{spherulite}}}\right)^2\right) \quad (4.1.1)$$

with a mean radius $r_{\text{spherulite,mean}} = 1,25 \mu\text{m}$ independent of the cooling temperature and a standard deviation depending on the cooling temperature as:

$$\sigma_{\text{spherulite}}(\mu\text{m}) = 0.01 T_{\text{cooling}} + 0.60 \quad (4.1.2)$$

In the model, a list of radius spherulites $[r_1 \dots r_n]$ is randomly selected from this Gaussian distribution. A list of random numbers $[h_1 \dots h_n]$ between 3 and 6 is also drawn to define the geometry of the polygons that symbolize spherulites. Each generated spherulite is assigned to a couple $[r, h]$ and has a surface given by:

$$S = \frac{h}{2} \sin\left(\frac{2\pi}{h}\right) r^2 \quad (4.1.3)$$

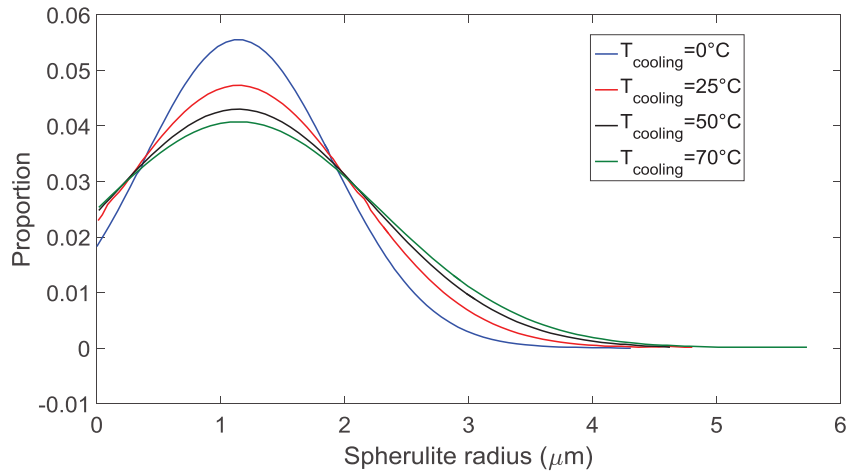


Figure 4.3: Proportion of spherulite radius in PE as a function of the quenching temperature, adapted from [89].

According to the literature, nucleation and growth of spherulites are occurring until they begin to impinge on each other [80]. However a thin layer of amorphous phase is still present at the interface between spherulites, usually called rigid amorphous fraction where macromolecules mobility is lower than in free amorphous phase [174]. From these observations, a compactness coefficient parameter C is used to define this spherulite network. As shown in Figure 4.4, the higher the compactness, the thinner the amorphous phase between spherulites. It means that in our simulation, spherulites have to occupy the ratio C of the matrix surface. Among the list of generated spherulites, a number N is associated to our system in order that the sum of polygon surfaces is equal to the ratio C of the matrix surface:

$$\sum_k^N S_k = C n m \delta r^2 \quad (4.1.4)$$

with n the number of matrix states in the x -direction, m the number of states in the y -direction and δr [m] the state length.

Finally these n spherulites are placed randomly in all the matrix elements. In this random spherulite affectation, the required condition is that the sum of the polygons contained in each matrix element has a surface smaller than the surface of the matrix element δr^2 .

4.1.2 Distribution of random lamellae related to spherulite

Distribution in lamellae is controlled by the chain structure and by crystallization conditions. As the melting temperature of polymer lamellar crystals depends on their thickness, distribution of lamella thickness can be obtained from the stretched melting temperature range in polymer given by Differential Scanning Calorimetry (DSC) measurement as demonstrated for LDPE in Figure 4.5. Heating and cooling rate are 3 K/min.

The correlation between the lamellar thickness and its melting temperature is described by the Gibbs-Thomson equation [84]:

$$T_f = T_{f_0} \left(1 - \frac{2\gamma}{l\Delta H_{f_0}}\right) \quad (4.1.5)$$

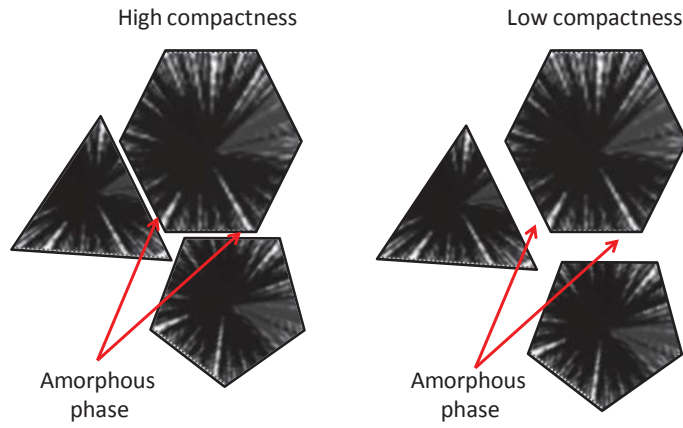


Figure 4.4: Schematic of the compactness principle used in the model.

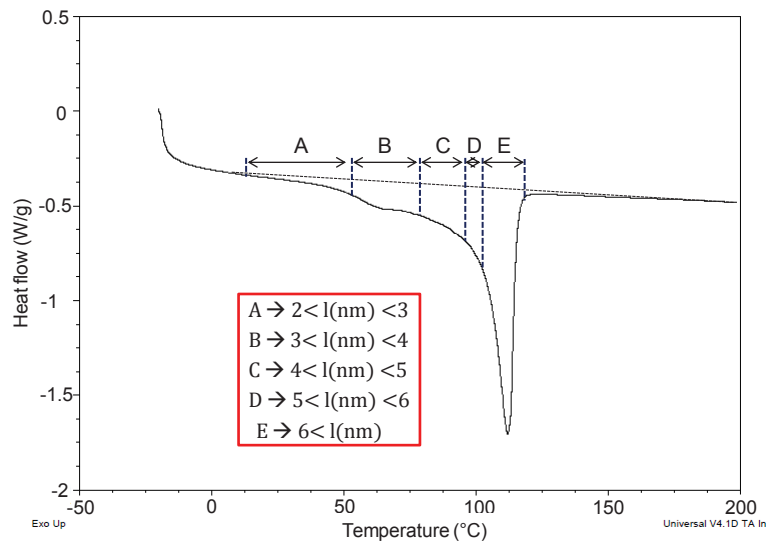


Figure 4.5: DSC measurement of LDPE measured with a heating and cooling rate are 3 K/min with the relation temperature range - lamella thickness range.

where T_{f0} [K] is the theoretical melting temperature of 100% crystallized polymer, ΔH_{f0} [J/m³] is the theoretical melting enthalpy of the 100% crystallized polymer, γ [J/m²] is the surface energy of crystalline lamella and l [m] is the thickness of lamellae. In case of PE-based material, the numerical expression is [86]:

$$l(T) = \frac{263.9}{425.3 - (273.15 + T)} \quad (4.1.6)$$

with l [nm] the lamella thickness and T [°C] the temperature.

The ratio between the heat flow area related to each lamella thickness over the total heat flow area gives the distribution of lamella thicknesses inside the material. Genetic model uses as input this lamellae distribution ranged between l_{min} and l_{max} which respectively correspond to the lamella thickness melting at room temperature (RT) and the lamella thickness melting at the melting temperature peak. A list of lamellae thickness [$l_1 \dots l_n$] is randomly selected in this distribution and a number M of these lamellae are affected to each spherulite of the system. For

each spherulite, the calculated surface is given by:

$$S_k = r_k \sum_1^M l_{k,l}$$

with r_k [m] the radius of the spherulite.

4.1.3 Algorithm for crystalline fraction calculation

From spherulites and lamellae distribution, local crystallinity in each matrix element is calculated as:

$$\chi_{i,j} = \frac{\left(\sum_k^N r_k \sum_l^M l_{k,l} \right)}{dr^2} \quad (4.1.7)$$

with N the number of spherulites in each state and M the number of lamella associated to each spherulite.

The simulated global crystalline fraction of the material is determined as the average value of local crystalline fraction of each matrix element:

$$\chi = \frac{\sum_{i,j}^{n,m} \chi_{i,j}}{n m} \quad (4.1.8)$$

with n the number of matrix states in the x -direction and m the number of states in the y -direction.

To fit with the experimental crystalline fraction at room temperature, either $r_{spherulite,mean}$ and $\sigma_{spherulite}$ or compactness C are modified.

A parametric study is done to assess the influence of these parameters on the resulting local crystallinity on two polymers: LDPE and high density polyethylene (HDPE) with respective crystallinity of 0.42 and 0.80 at room temperature and respective melting temperature of 110 °C and 136°C. Figure 4.6 shows both the simulated crystalline fraction obtained when varying $r_{spherulite,mean}$ with $\sigma_{spherulite} = 1 \mu\text{m}$ and $C = 0.9$ and the simulated crystalline fraction obtained from varying $\sigma_{spherulite}$ with $r_{spherulite,mean} = 1.5 \mu\text{m}$ and $C = 0.9$. For LDPE, simulated crystalline fraction is decreasing as the mean radius and standard deviation are increasing. However a too long solving time of the distribution algorithm is needed to reach the experimental crystalline fraction of LDPE. Furthermore for HDPE, no variation of the simulated crystalline fraction is obtained by acting on $r_{spherulite,mean}$ or $\sigma_{spherulite}$.

Figure 4.7 shows the simulated crystalline fraction obtained when varying C with $r_{spherulite,mean} = 1.5 \mu\text{m}$ and with $\sigma_{spherulite} = 1 \mu\text{m}$. For LDPE and HDPE, both experimental crystalline fraction can be obtained with a very short solving time.

As a result, compactness is used as a varying parameter in the algorithm presented in Figure 4.8 for semicrystalline structure simulation to fit with the global crystalline fraction of the material measured at room temperature.

When a temperature higher than room temperature is applied, all lamellae which are melting at temperatures inferior to the applied temperature are removed from the simulated lamellae

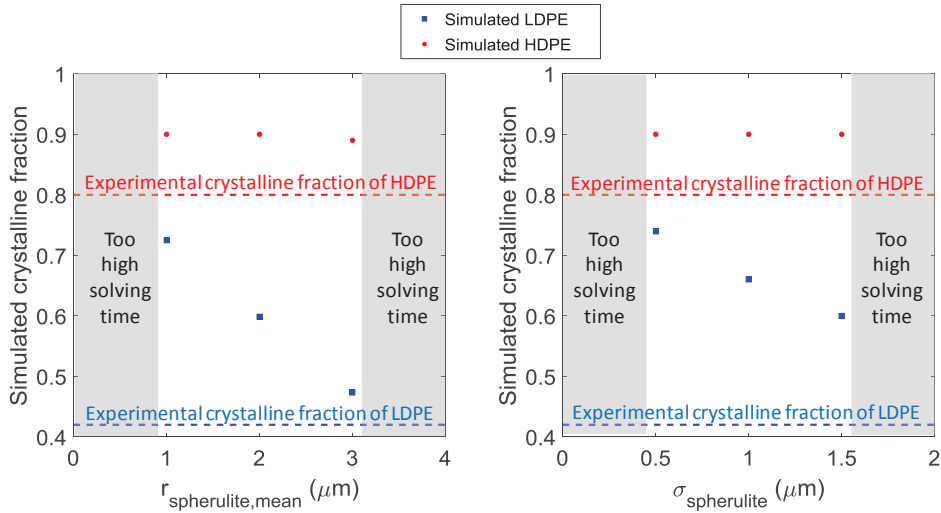


Figure 4.6: Simulated crystalline fraction of LDPE and HDPE as a function of $r_{spherulites,mean}$ and as a function of $\sigma_{spherulite}$.

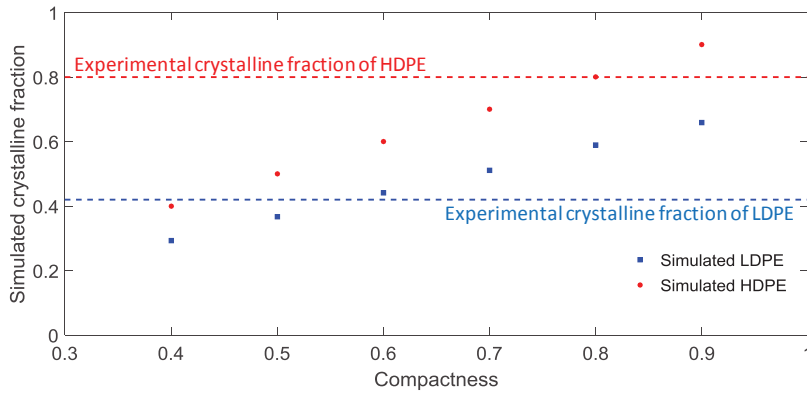


Figure 4.7: Simulated crystalline fraction of LDPE and HDPE as a function of compactness.

distribution. It results in a decrease in the local and global crystalline fraction of the system. In Figure 4.9, the simulated change of crystalline fraction for LDPE and HDPE *versus* temperature are compared to experimental data obtained from DSC measurements. Less than 1% of crystallinity difference is observed between experiment and simulation.

Depending on polymer chemical nature as well as macromolecules morphology (e.g. branching) the crystalline fraction, stretched melting temperature range and melting enthalpy are well known to vary by far from one semicrystalline polymer to the next [174]. For instance, Table 4.1 summarizes the theoretical melting temperature and enthalpy of perfect crystals of PE, PP and PET.

As numerical expression of the Gibbs-Thomson equation depends on theoretical melting temperature and enthalpy of perfect crystals, these difference are taken into consideration in the developed model by changing the values of l_{min} and l_{max} in the lamella thickness distribution according to the polymer. These modifications allow to make the algorithm for crystalline fraction calculation valid regardless of the polymer nature.

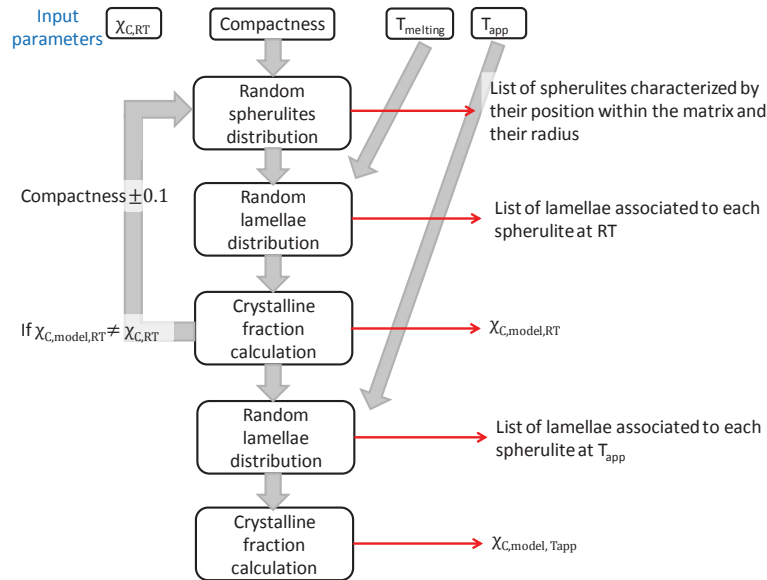


Figure 4.8: Genetic algorithm for spherulite radius and lamellae distribution in the model.

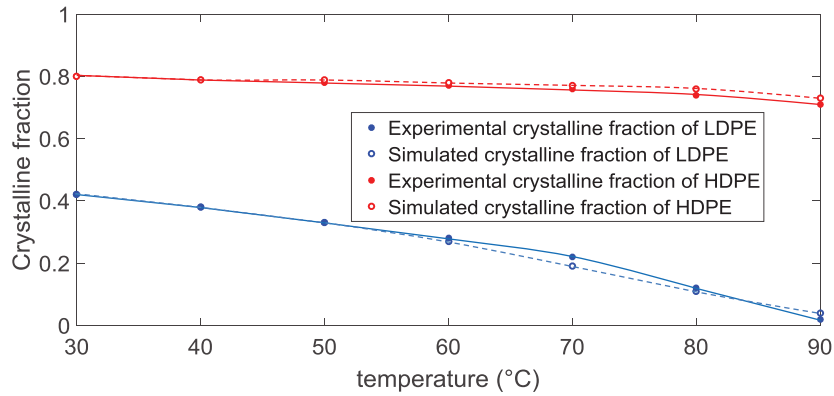


Figure 4.9: Experimental and simulated crystalline fraction of LDPE and HDPE *versus* temperature.

4.1.4 Local permittivity calculation from local crystalline fraction

As related to dipolar orientation, charge transport or interfacial polarization, permittivity is supposed to depend highly on polymer microstructure. The experimental section presented in section 2.3.2 probes the effect of crystallinity on permittivity of polymer by means of dielectric spectroscopy measurements. Experimental results, summarized in the Figure 4.10, demonstrate that:

- In the temperature range between T_g and T_m , and more precisely between the onset and peak temperatures of melting, the permittivity decreases with temperature increase. This is ascribed to partial melting, where the crystalline fraction decreases resulting in a decrease of crystalline/amorphous interface area;
- In the temperature range below T_g up to onset temperature of melting, the permittivity increases with temperature as orientation of polar macromolecules is thermally activated;
- Permittivity in polar materials decreases with crystallinity as crystalline phase restrain the orientation of polar macromolecules. For polar semi-crystalline materials, the permit-

	ΔH_{f0} [J/g]	T_{f0} [K]
PE	290	419
PP	196	461
PET	163	613

Table 4.1: Theoretical melting temperature and enthalpy of 100% crystallized polymer of PE, PP and PET [174].

tivity is driven by orientation of polar macromolecules and Maxwell-Wagner-Sillars effect whereas in non-polar semi-crystalline polymers, Maxwell-Wagner-Sillars effects is the main contributor.

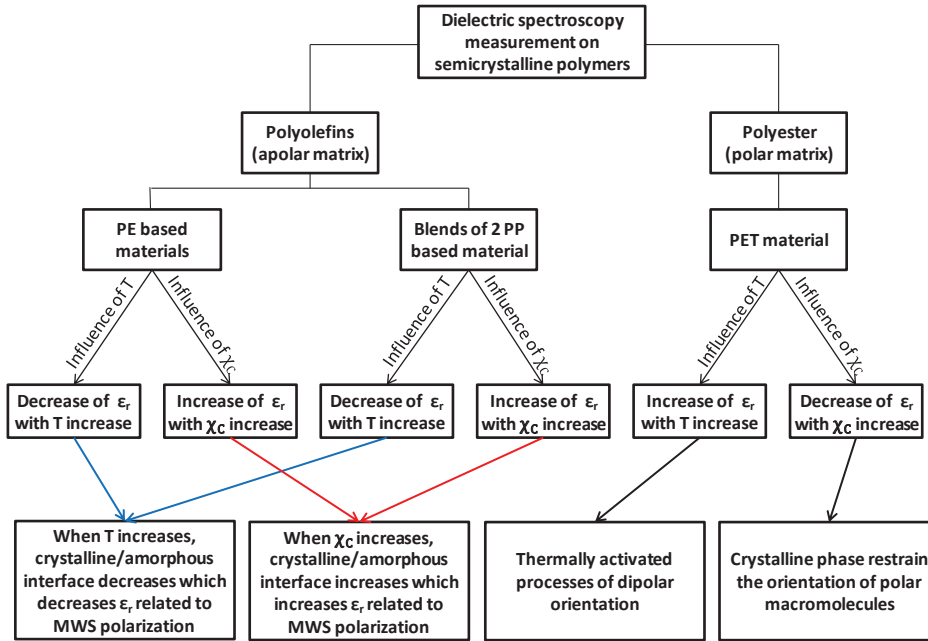


Figure 4.10: Summary of the experimental study about the influence of crystallinity on polymer permittivity.

From permittivity variation as a function of crystalline fraction in PE and PP shown in Figure 4.11, a linear fit of the permittivity with crystalline fraction is considered. An approximation is made with this relation as for a given material, permittivity variation with temperature is not only due to crystalline fraction variation. The following relation between permittivity and crystalline fraction is obtained:

$$\begin{aligned}
 \varepsilon_r &= (2.06 + 0.40 \chi_c) \quad \text{for PE material} \\
 &\quad \text{and} \\
 \varepsilon_r &= (1.89 + 0.56 \chi_c) \quad \text{for PP material}
 \end{aligned}
 \tag{4.1.9}$$

with this linear approximation, only a maximum error of 2% is made compared to the experiment. Then matrix of local permittivity can be determined from the matrix of crystalline fraction in the model.

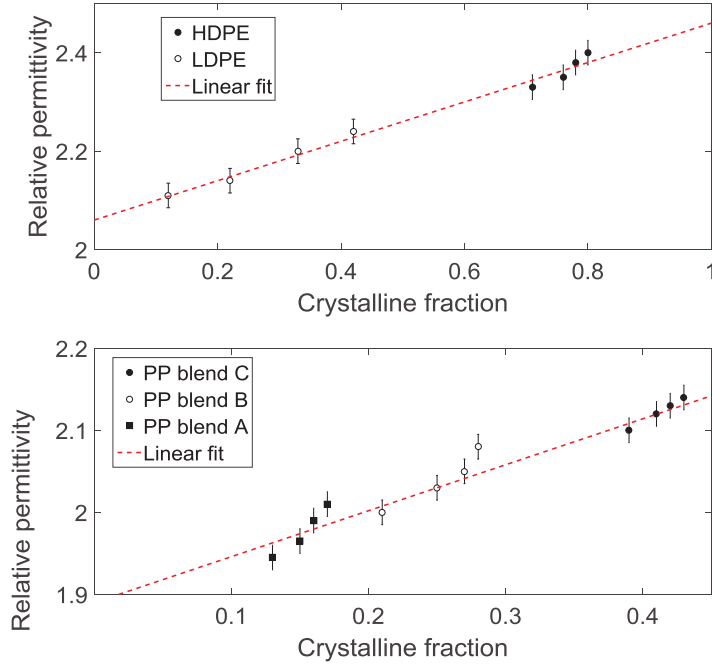


Figure 4.11: Permittivity at 0.1 Hz of LDPE, HDPE and PP blends *versus* crystalline fraction with linear fits.

4.2 Evolution laws development

4.2.1 Charge injection and transport

For homogeneous materials, charge injection obeys a Schottky law [175]. The corresponding evolution law is expressed as:

$$Q_{e/h,inj} \propto T^2 \exp\left(\frac{e}{k_B T} \sqrt{\frac{eE}{4\pi\epsilon}}\right) \exp\left(-\frac{e w_{e/h,inj}}{k_B T}\right) \delta r \delta t \quad (4.2.1)$$

with $w_{e/h,inj}$ [eV] the activation energy for holes and electrons, T [K] the local temperature, E [V/m] the local electric field and ϵ [F/m] the local permittivity.

For semicrystalline polymers, this law has to be adapted to take into consideration the contribution of the local crystalline fraction in each state of the matrix. Crystalline phase is indeed a barrier for hole and electron injection [82]. More precisely, electron injection is known to occur in the free volumes between the macromolecules of the amorphous phase [112]. Holes are injected on in-chain chemical defects [113]. Several experiments confirm this assumption [82, 113]. For instance, Montanari *et al.* measured the leakage current at $T = 20^\circ\text{C}$ under electric field from 10 to 60 kV/mm for LDPE ($\chi_C = 30\%$) and HDPE ($\chi_C = 76\%$) samples [128]. The authors reported a much higher current for the material of lowest crystalline fraction.

In the experimental part presented in chapter 2.4.3, the crystallinity effect on semi-crystalline polymer conductivity is probed. Experimental results, gathered in the Figure 4.13, demonstrate a decrease of the current with increasing crystallinity in PP and PET. In PE based materials, difference between XLPE and LDPE is less significant as their crystalline fractions are close. HDPE behavior is specific with an increase of the current with time leading to breakdown.

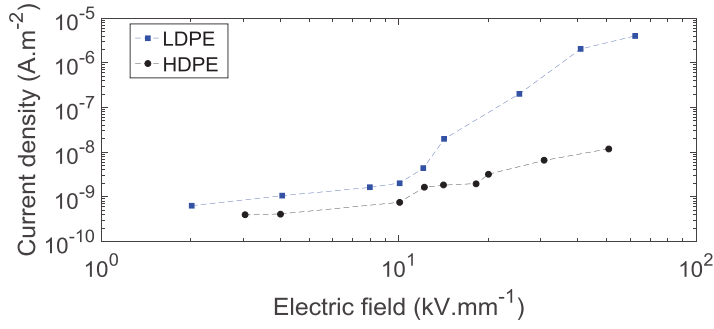


Figure 4.12: Current density at steady state *versus* electric field in LDPE and HDPE at 20°C [128].

These results demonstrate that crystalline phase acts as a barrier for charge injection which yields a conductivity decrease. This behavior is present both in polar and non-polar materials. Thus, an evolution law directly proportional to amorphous phase fraction is used for charge injection:

$$Q_{e/h,inj,X_c} = Q_{e/h,inj} (1 - \chi_C) \quad (4.2.2)$$

with χ_C the local crystallinity.

Evolution laws for charge transport in both x -direction and y -direction for holes and electrons in homogeneous material are defined as:

$$Q_{e/h,tr,x/y} = \delta r \delta t \rho_{e/h} \mu_{e/h} \exp\left(-\frac{e \beta_{e/h}}{k_B T}\right) E_{x/y} \quad (4.2.3)$$

with $\rho_{e/h}$ [C/m³] the local charge density of electron and hole, $\mu_{e/h}$ [m²/(V.s)] the preexponential factor of the local charge mobility of electrons and holes, $\beta_{e/h}$ [eV] the activation energy for electron and hole transport, dr [m] the dimension of the matrix cell and δt [s] the step time.

In heterogeneous semicrystalline polymers, electrons are mostly transported between the chains by a hopping process [112], whereas for holes, transport occurs along the polymer chains with a hopping rate higher in crystalline region than in amorphous region [113].

Evolution law are thus expressed as:

$$\begin{aligned} Q_{e,tr,X_c} &= Q_{h,tr,x/y} (1 - \chi_C) \mathcal{P}_e \\ &\text{and} \\ Q_{h,tr} &= Q_{e,tr,x/y} \chi_C \mathcal{P}_h \end{aligned} \quad (4.2.4)$$

with χ_C the crystalline fraction and \mathcal{P} a probability function whose value is between 0 and 1.

In expression (4.2.4), the higher the local crystallinity, the lower the electron amount transported and the higher the hole amount transported. Furthermore, the probability function \mathcal{P} describes the probability for charges to cross one state to the next one and is directly related to the local crystallinity. For holes, the higher the crystallinity, the higher the probability to be transported. However, in purely amorphous materials, probability for holes transport is not null as holes can still be transported along chain of the amorphous phase with a lower mobility. The case is the opposite for electrons where the transport probability decreases with crystallinity increase. For purely crystalline polymers, this probability is null as the energetic barrier for electrons to cross

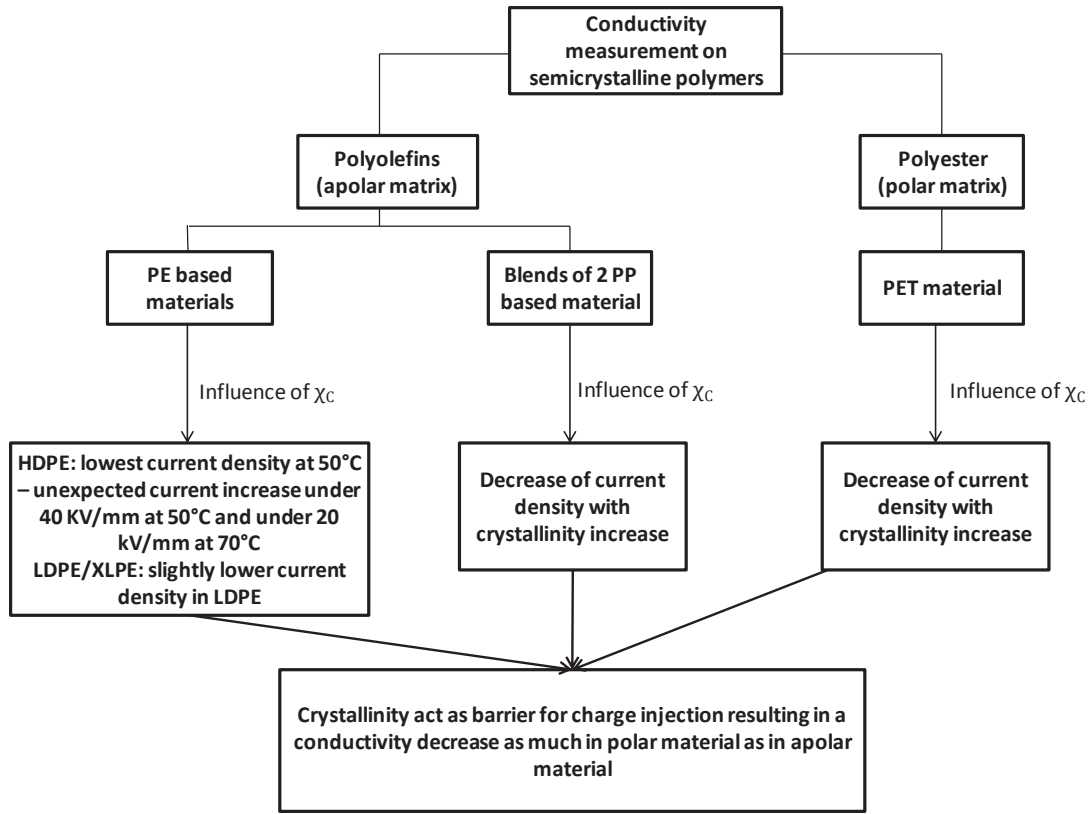


Figure 4.13: Summary of the experimental study about the influence of crystallinity on polymer conductivity.

the crystalline phase is too high [82]. Thus, two different expressions are used depending on the charge carrier nature:

$$\mathcal{P}_e = p > \chi_c \quad \text{for electron} \quad (4.2.5)$$

and

$$\mathcal{P}_h = p < \chi_c + (1 - p/a)(\chi_c < p < \chi_c + a) \quad \text{for hole}$$

with p a random number between 0 and 1, χ_c the local crystallinity, a a constant between 0 and 1 which expresses the difference of hole mobility in amorphous and crystalline phases. The variation of these probability functions \mathcal{P}_e and \mathcal{P}_h as a function of p is shown in Figure 4.14. It can be noticed that for purely amorphous materials, there is a probability of 1 for electrons to be transported, and a probability a for a fraction of holes to be transported.

The onset of global molecular motions assigned to the glass transition is related to electronic property changes in semi-crystalline polymers.

Dielectric spectroscopic measurements performed on PET at low voltage and temperature between 30°C and 90°C and presented in the experimental chapter shows a conductivity increase by one order of magnitude from a threshold temperature of 70°C, corresponding to the glass transition temperature, regardless of the PET crystalline fraction (Figure 2.19).

Below glass transition, charge injection and transport is only assisted by weak local molecule movements, whereas, above the glass transition, global molecular motions assist charge injection and transport. Consequently a step in the conductivity is measured.

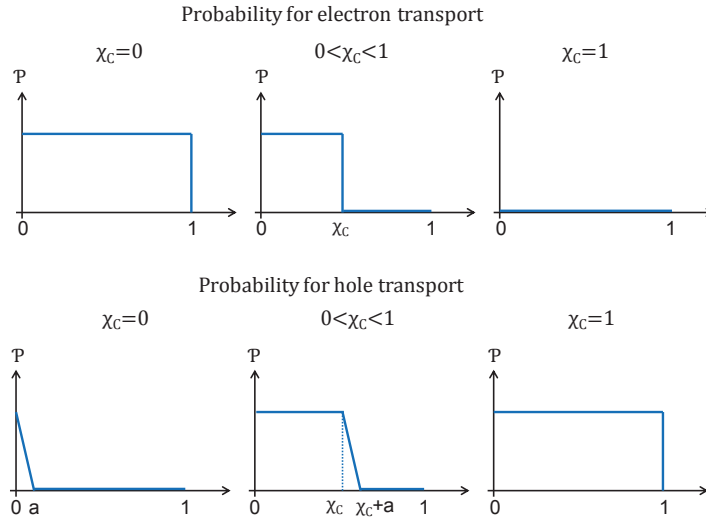


Figure 4.14: Probability functions for charge transport as a function of random number p between 0 and 1.

An evolution law is developed that take into account the T_g -dependency of activation energy for charge transport and injection. Considering an activation energy of 0.6 eV for the charge transport and injection above the glass transition, the influence of glass transition temperature is defined as:

$$w_{e/h,inj}/\beta_{e/h} = \begin{cases} 0.6 \pm 0.05 & \text{if } T > T_g \\ 0.3 \pm 0.05 & \text{if } T < T_g \end{cases} \quad (4.2.6)$$

In case of PE material, the temperature, ranging from 30 to 90°C for power cables, is above the glass transition and below the melting temperature.

4.2.2 Charge trapping

For homogeneous materials, evolution law for charge trapping is given by:

$$Q_{trap} = \alpha (\delta r)^2 \rho_{mob} \left(\frac{Q_{trap,max} - (\delta r)^2 \rho_{trap}}{Q_{trap,max}} \right) \left(p < \frac{Q_{trap,max} - (\delta r)^2 \rho_{trap}}{Q_{trap,max}} \right) \quad (4.2.7)$$

With $Q_{trap,max}$ [C] the maximum charge amount that can be trapped in each matrix state, ρ_{mob} [C/m³] the mobile charge density, ρ_{trap} [C/m³] the trapped charge density, α a parameter lower than 1 which corresponds to the proportion of charges trapped at each time step and p a random number between 0 and 1 that corresponds to the probability of trapping depending on the trapped charge amount.

Among the physical defects related to the heterogenous semi-crystalline structure, nanovoids and conformational disorders both present in the amorphous region create shallow traps for holes and electrons [66, 118]. The maximum shallow trap density is proportional to the local amorphous phase fraction:

$$Q_{shallow\ trap,max} \propto (1 - \chi_C) \quad (4.2.8)$$

Furthermore, the trapping-probability increases with the amorphous phase fraction. The evolution law for shallow trapping is thus given by:

$$Q_{shallow\ trap} = Q_{trap} (1 - \chi_C) \quad (p < (1 - \chi_C)) \quad (4.2.9)$$

The interfacial region between amorphous and crystalline phases was demonstrated from DFT measurement to be a deep electron trap of 1 eV [119]. Thus for polymer materials having a distribution of spherulites, the higher the local crystalline fraction, the higher the deep trap density for electrons:

$$Q_{deep\ trap, max} \propto \chi_C \quad (4.2.10)$$

Moreover the probability of electron trapping increases with the crystalline fraction. Montanari *et al.* indeed observed a high negative charge accumulation in HDPE under 60 kV/mm and at 25°C [54]. The evolution law for deep electron trapping in this case is given by:

$$Q_{deep\ trap, e, X_C} = Q_{trap} \chi_C \quad (p < \chi_C) \quad (4.2.11)$$

Additional space charge measurements are performed in PP and PET to probe crystallinity impact in polymer space charge. Experimental results, described in chapter 2.5.4 and summarized in Figure 4.15, demonstrate that:

- In lowly crystalline polymers, probability of hole deep trapping is increasing with amorphous phase increase. This behavior is consistent with the fact that hole transport occurs along the polymer chains with a hopping rate much lower in amorphous region than in crystalline region.
- In polar materials, residual polarization is increasing with crystallinity increase due to restriction of polar macromolecules orientation by crystalline phase.

Putting together the literature data and experimental results, it can be concluded that the probability of hole deep-trapping is directly proportional to the fraction of amorphous phase. This can be further modeled using an evolution law as:

$$Q_{deep\ trap, h, X_C} = Q_{trap} (1 - \chi_C) \quad (p < (1 - \chi_C)) \quad (4.2.12)$$

Charge detrapping is considered as a thermally activated process. Probability of detrapping depends on temperature and on trap depth ξ_a . For shallow traps, $\xi_a = 0.1$ eV and for deep traps, $\xi_a = 0.9$ eV. The related evolution law is given by:

$$Q_{detrapp} = \alpha (\delta r)^2 \rho_{trap} \left(p < \frac{k_B T}{h} \exp\left(\frac{-e \cdot \xi_a}{k_B T}\right) \right) \quad (4.2.13)$$

with ρ_{trap} [C/m³] the trapped charge density, α which corresponds to the proportion of charges detrapped at each step time and considered as identical to the proportion of charges trapped and ξ_a [eV] the activation energy of detrapping depending on charge carrier and trap depth.

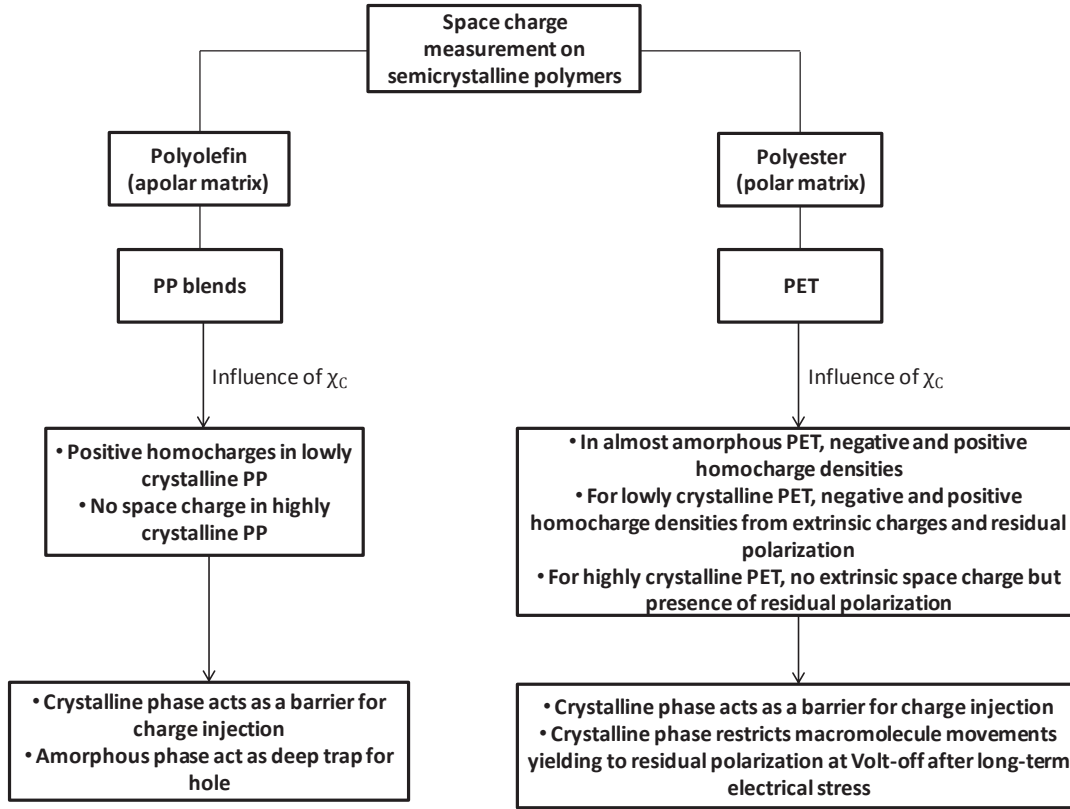


Figure 4.15: Summary of the experimental study about the influence of crystallinity on polymer space charge.

4.2.3 Microstructure modification with temperature: annealing

In the experimental DSC measurements performed on XLPE shown in Figure 2.2 (see part 2.2.1.2), a difference in the thermogram during heating at 3 K/min between fresh sample and sample annealed at 70°C is observed. Gibbs-Thomson correlation between the thickness of lamellae and its melting temperature demonstrates that the difference in thermogram is correlated to thin crystal lamellae recrystallization during cooling into thicker ones after annealing.

It is shown in the literature that lamellae thickness variation occurs always around the annealing temperature and that after 30 min of annealing, no further variation has been observed [99]. To simulate this annealing, it is considered that all lamellae melting at temperature lower than the applied temperature recrystallize, during cooling, with a thickness related to the annealing temperature:

$$l(T < T_{annealing}) \rightarrow l(T_{annealing}) \quad (4.2.14)$$

With l [nm] the lamella thickness and $T_{annealing}$ [°C] the annealing temperature.

4.3 Criticity of model parameters

In this section, the influence of the different parameters on simulated current density and space charge and the sensibility of the evolution laws to these parameters are investigated. The aim is to get to a full understanding of the effects of each parameter and to find their most accurate values to obtain simulated results consistent with experiments. The strength of this model is

that a single set of parameters allows to simulate the electrical behavior of several polymer for an electric field from 10 kV/mm to 60 kV/mm and temperature from 30°C to 90°C. To study these parameters, three polymers with different crystalline fractions are simulated: LDPE with crystalline fraction of 42% and melting temperature of 110°C, HDPE with crystalline fraction of 80% and melting temperature of 136°C and low crystalline PP with crystalline fraction of 12% and melting temperature of 163°C. To simulate the crystalline phase distribution of these three polymers, input parameters reported in Table 4.2 taken from both literature data and DSC measurements are used.

	ΔH_{f0} [J/g]	T_{f0} [K]	T_m [°K]	χ_c at RT
HDPE	290	419	409	0.80
LDPE	290	419	383	0.42
PP	196	461	436	0.12

Table 4.2: Theoretical melting temperature and enthalpy of 100% crystallized polymer of PE, PP and PET [174].

For all results presented in this part, anode is placed in the left side of the matrix and cathode in the right side. First, parameters related to the evolution law of charge injection (equation (4.2.1)) are studied. Then parameters from evolution law of charge transport (equation (4.2.4) and equation (4.2.5)) are addressed. Finally a focus is made on the parameters from the charge trapping evolution law (equation (4.2.7)).

4.3.1 Parameters for charge transport and injection

In the charge injection law (equation (4.2.1)), the studied parameters are the activation energies for hole injection $w_{h,inj}$ and electron injection $w_{e,inj}$. It is considered in this model, that charge injection is driven by the presence of surface states. The related activation energy assumed to be similar in polar and non-polar materials is around 0.6 eV. To study the sensitivity of the evolution law to activation energy of charge injection, current density of the three polymers are simulated for several activation energies of charge injection, comprised between 0.6 eV and 0.7 eV. Figure 4.16 shows the simulated current densities obtained for an electric field of 10 kV/mm at 70°C. As expected, the lower the activation energy for charge injection the higher the current density. The sensitivity of current density to injection activation energy is very strong. An increase of 0.1 eV in injection activation energy results in a two decades decrease of the current density. The activation energy for charge injection does not affect the time to reach the steady state with a maximum of current density obtained at the same time regardless the value of w . By comparing the three polymers, at a given activation energy, current density is the lowest for HDPE as its crystalline fraction is the highest.

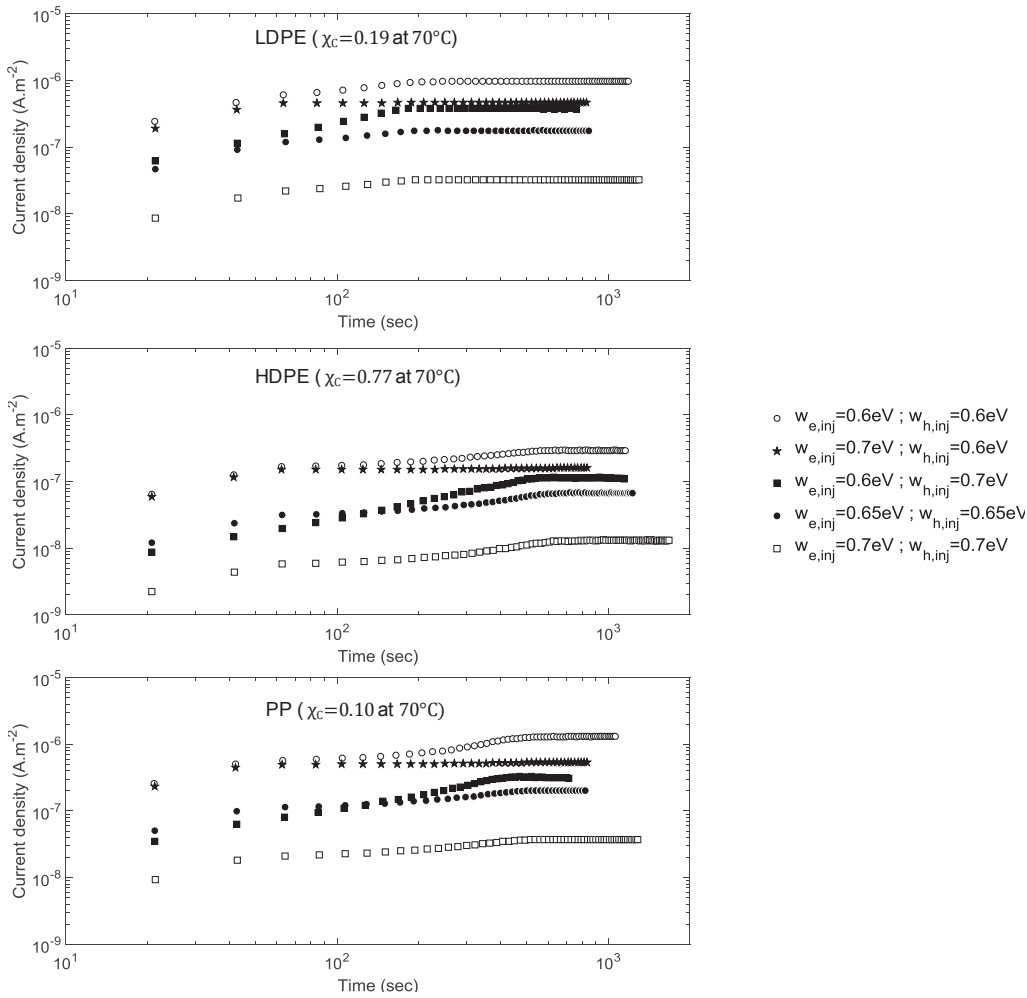


Figure 4.16: (from top to bottom) Simulated current density of LDPE, HDPE and PP at various activation energy of charge injection.

The evolution law for charge transport depends on two parameters: $\beta_{e/h}$ the activation energy of electron and hole transport, and a a constant between 0 and 1 which expresses the difference of hole mobility in amorphous and crystalline phases. It is considered in this model, that charge injection is driven by the global motion of macromolecules in the polymer. The related activation energy of this global motion is assumed to be similar in polar and apolar material with a value around 0.65 eV. With this activation energy, mobility of holes and electrons at room temperature are $1.2 \times 10^{-13} \text{ V}/(\text{m}^2\text{s})$, values close to what is found in the literature [121].

The sensitivity of the evolution law to activation energy of charge transport is assessed by simulating the current density of three polymers with several activation energies of charge transport in the range of 0.65 eV. Figure 4.17 shows the simulated current densities obtained for an electric field of 10 kV/mm at 70°C.

Compared to the injection case, variation of activation energy for charge transport affect much less current density at steady state. However an increase of the activation energy for charge transport increases the time to reach the steady state. For a variation of 0.1 eV for both charge transport, this time can be multiplied by 100. For HDPE, time to steady state is mostly affected by activation energy of electron transport. This behavior can be ascribed to once again the high crystalline fraction, acting as deep trap against electron transport. The higher the activation

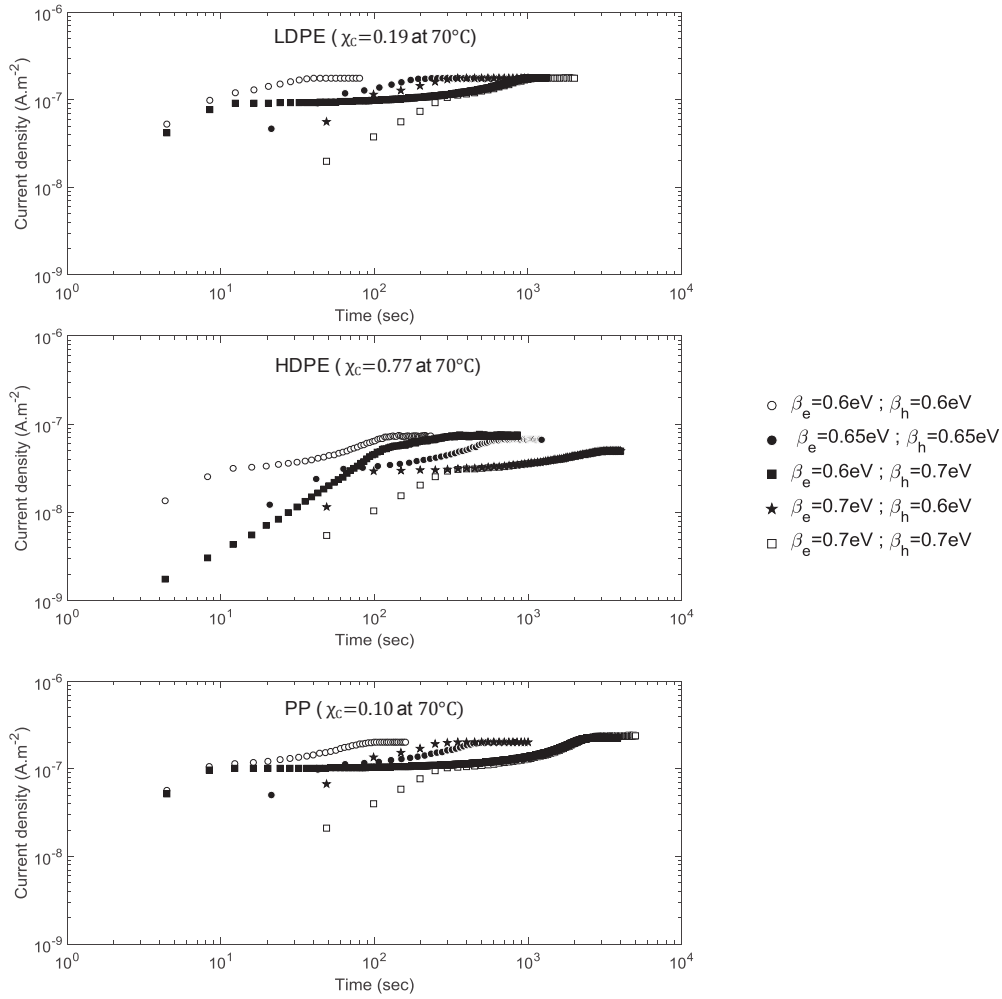


Figure 4.17: Simulated current density of LDPE, HDPE and PP at various activation energy of charge transport.

energy for electron transport, the higher the accumulation of electrons at the interface and the higher the density of trapped electrons. It results in a drop of the electric field at the cathode decreasing the charge transport in the sample and increasing the time to steady state. For LDPE and PP, the opposite behavior is observed, time to steady state is observed as increasing when activation energy for hole transport is 0.7 eV. For these two materials, the large amorphous parts act as barrier for hole transport and a decrease of the electric field is observed near the anode when hole transport is at minimum.

The effect of the probability function \mathcal{P} in the charge transport equation (4.2.5) on current density of LDPE, HDPE and PP with low crystallinity is then investigated with varying values of a which expresses the difference of hole mobility in amorphous and crystalline phase. Figure 4.18 shows the simulated current densities obtained for an electric field of 10 kV/mm at 70°C with value of a of 0, 0.1 and 0.2.

With $a = 0$, the probability of hole transport in amorphous region is zero leading to the highest time to reach the steady state for all materials. For LDPE, as material with low crystallinity, positive charge accumulation near anode occurs. This accumulation is highest when $a = 0$ resulting in a strong decrease of the electric field at the anode interface. However even with $a = 0$, the electric field decrease at the interface is too low to impact charge injection and

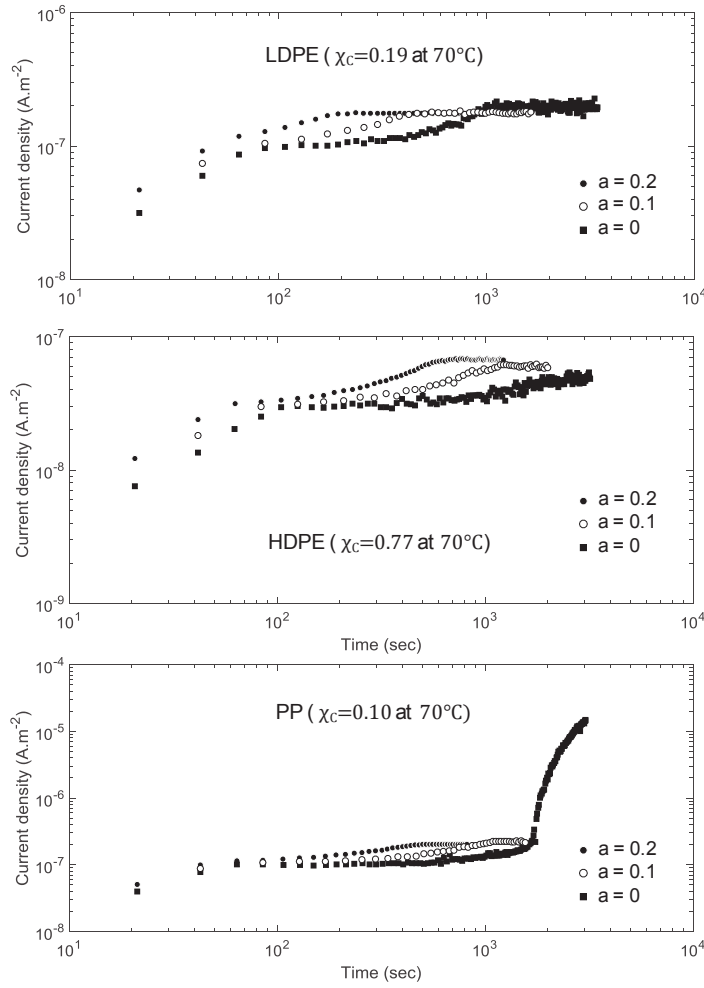


Figure 4.18: Simulated current density in LDPE, HDPE and PP with various a value of the probability function for charge transport.

thus current at steady state is similar. For HDPE, some states of the matrix have a local crystalline fraction higher than 0.95 yielding to negative charge accumulation. Figure 4.19 shows that this accumulation is occurring mostly at the cathode decreasing the local electric field at this interface. Injected holes from the anode and transported to the cathode compensate this negative charge accumulation. With decreasing a , hole mobility is decreasing, and the negative charge accumulation is less and less compensated. Thus electric field is the lowest at the cathode for $a = 0$ as demonstrated in Figure 4.19. For PP with low crystallinity, positive charge accumulation is occurring near anode and is very high with $a = 0$ due to local crystalline fraction close to 0. Figure 4.18 and Figure 4.19 show that in this case electric field is dramatically decreased at the anode, yielding to a current increase due to current displacement.

4.3.2 Parameters for charge trapping

For the evolution law of charge trapping (equation (4.2.7)), the influence of the parameter α corresponding to the proportion of charge trapped at each step time δt is studied. Leakage current variation for 10^5 s is simulated for LDPE, HDPE and PP with low crystallinity at 70°C with an electric field of 20 kV/mm at three values taken for α : $\delta t/500$, $\delta t/50$ and $\delta t/5$. For all materials, the higher the value of α , the higher the decrease of current over time. Current decrease over

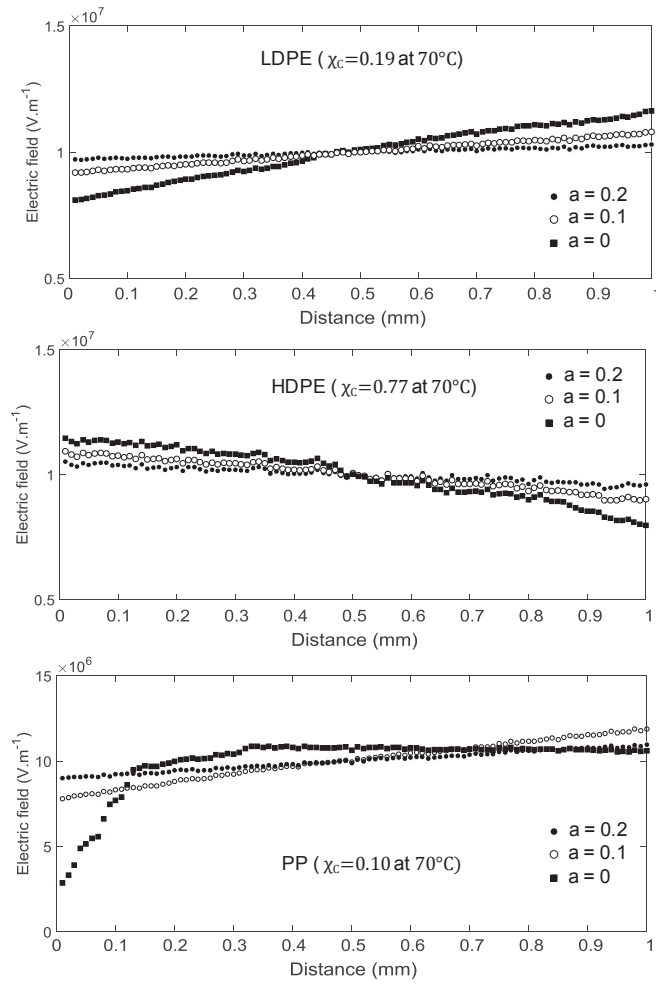


Figure 4.19: Simulated local electric field distribution of LDPE, HDPE and PP with various a value of the probability function for charge transport.

time is indeed related to charge accumulation at the interface reducing the injection. Space charge density of the three materials at the end of poling time is shown in Figure 4.20.

For LDPE, positive charge accumulation is present in the simulation and as expected this amount is increasing with α increase. With $\alpha = \delta t/50$, positive charge accumulation is localized in all sample thickness, whereas for $\alpha = \delta t/5$, positive charge accumulation is more localized near the anode. At the beginning of charge injection, mobile positive charges are near the anode. If fast trapping is occurring at this moment, it consequently gives rise to a larger amount of trapped charge near the injection electrode. Similar observation and conclusion can be made with PP. For HDPE, negative charge near cathode is observed even with low value of α . As crystallinity of HDPE is very high, charge transport of electrons is very low. As a consequence, trapped negative charges are preferentially localized near the anode instead than in the sample thickness, independently of the trapping rate.

Experimentally, for an electric field between 10 and 40 kV/mm and a temperature between 30 and 70°C, current density at steady state is in the range of 1×10^{-10} and 1×10^{-6} A/m² with a time to steady state of around 24 h. Net space charge accumulation measured with PEA is in the range of 1 to 2 C/m³. Finally experimental space charge profiles demonstrate that there is no symmetry between negative and positive charge accumulation meaning different injection

and transport coefficients for holes and electrons. From parameter study and experimental data, universal coefficients for charge injection, transport and trapping used in this model are adjusted and presented in Table 4.3. These universal coefficients are considered as valid regardless the polymer nature.

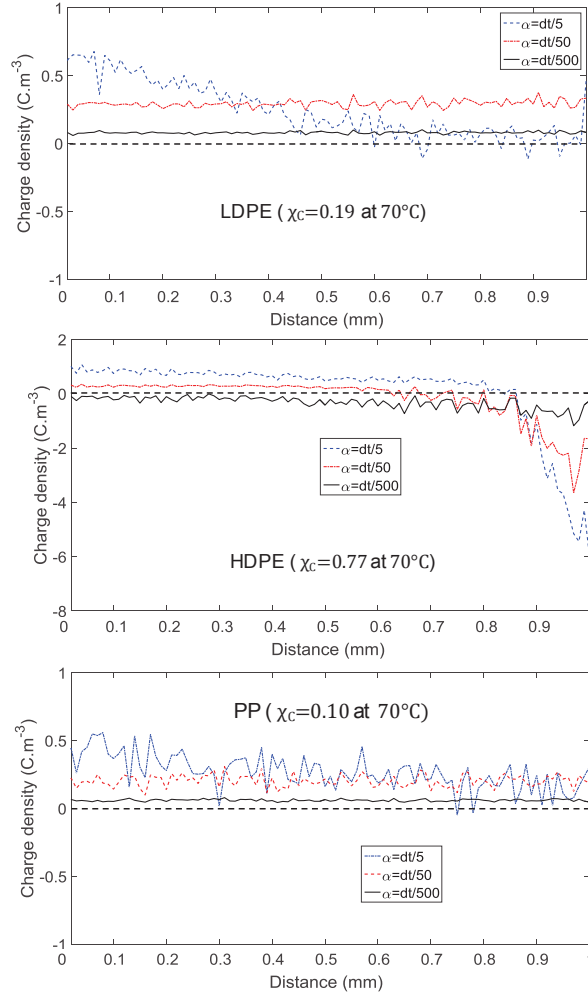


Figure 4.20: Simulated charge density in LDPE, HDPE and PP with various value of α .

Parameters	Unit	Value
$w_{e,inj}$	eV	0.65
$w_{h,inj}$	eV	0.6
β_e	eV	0.64
β_h	eV	0.59
a	/	0.2
α	/	$dt/500$

Table 4.3: Final set of universal parameters.

4.4 Comparison with experiments

4.4.1 Current density behavior

Experimental and simulated leakage currents are compared for LDPE, HDPE and fully degassed XLPE. At 50°C and 70°C, samples are submitted to three increasing electric fields: 20 kV/mm, 30 kV/mm and 40 kV/mm. Both in experiment and simulation, electric field is applied with a ramp up of 0.25 kV/(mm.s). The poling time at steady macroscopic field is 1×10^5 sec. The universal parameters given in Table 4.3 are used as input parameters for the simulations for the three considered PE-based materials. In addition, the input parameters describing the characteristic temperatures, crystalline fraction and specific heat of melting obtained from DSC measurement are presented in Table 4.4.

	ΔH_{f0} [J/g]	T_{f0} [K]	T_m [°K]	χ_c at RT
HDPE	290	419	409	0.80
LDPE	290	419	383	0.42
XLPE	290	419	378	0.38

Table 4.4: Theoretical melting temperature and enthalpy of 100% crystallized polymer, melting temperature and crystalline fraction at room temperature of HDPE, LDPE and XLPE [174].

At 70°C, the simulated crystalline fraction is 0.19 in LDPE, 0.77 in HDPE and 0.12 in XLPE. Figure 4.21 compares the experimental and simulated current densities for LDPE. Similar leakage current densities are obtained between experiment and simulation for all electric field or temperature. The main difference is the absence of the first exponential decrease at each new applied voltage as the electrode charging current is not taken into account in the current density calculation. The differences in current at steady state between experiment and simulation is less than 5×10^{-8} A/m². This difference is similar to the experimental standard deviation (3.5×10^{-8} A/m²) and standard deviation of the model (3.10^{-8} A/m²). For the model, this standard deviation is obtained by simulating the current density at a given electric field and temperature of the same material several times. The resulting dispersion comes from the random semi-crystalline structure of the simulated material and from the random aspect of the evolution laws.

Figure 4.22 shows the experimental and simulated results for HDPE.

For HDPE, at 70 °C, an anomalous behavior is observed where an increase of current density is observed over time at 20 kV/mm and 30 kV/mm , followed by sample breakdown. Simulated current density of HDPE shows as well an increase of current density with time at 30 kV/mm. In the model, current is governed by holes transport as they have a higher mobility. When electric field is applied in simulated HDPE, high negative charges are accumulating near the cathode. This accumulation increases the electric field at the anode, increasing the hole injection and thus the current density. The fact that experimental current increase occurs at a lower electric field than in the simulation may come from an experimental higher trapping rate. Simulation confirms the anomalous experimental behavior and may lead to its comprehension.

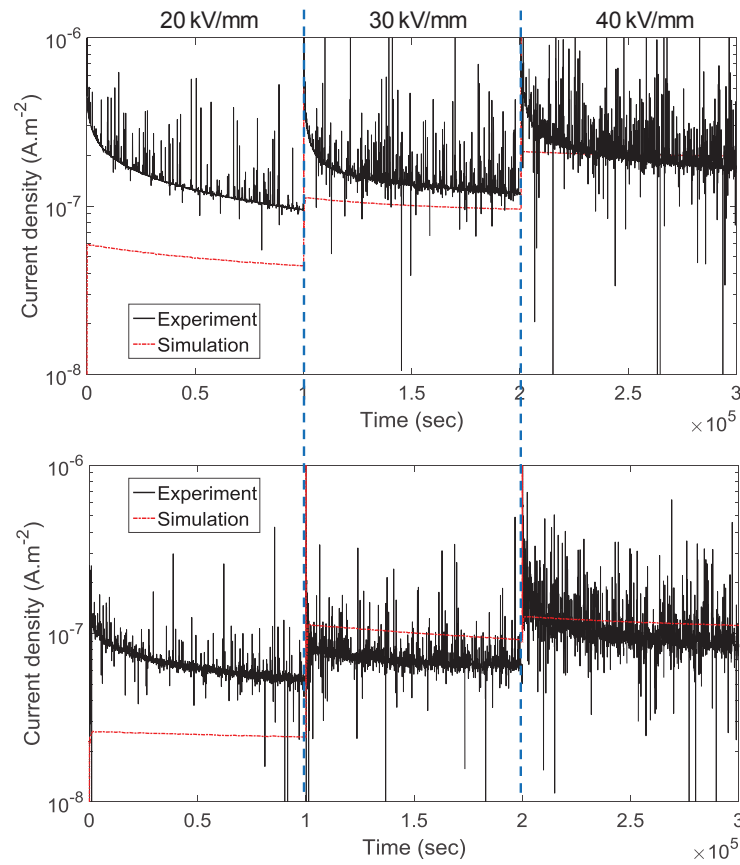


Figure 4.21: Current density of LDPE at 70°C (up) and 50°C (down) with increasing electric field from 20 to 40 kV/mm: experiment and simulation.

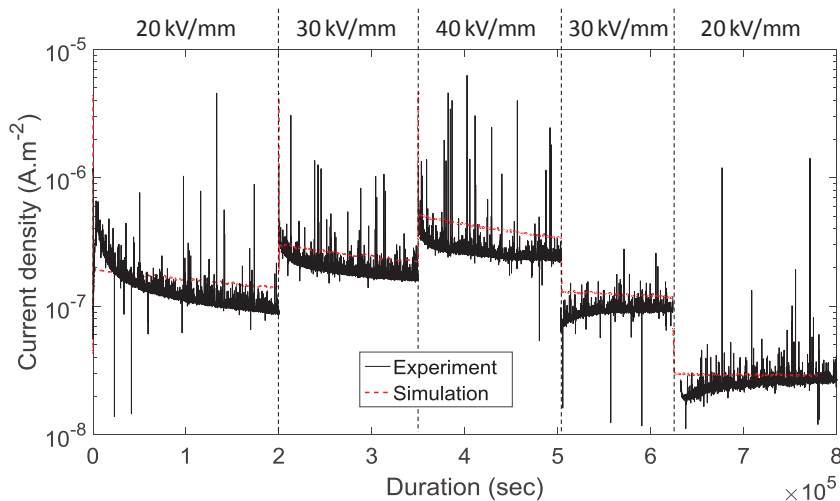


Figure 4.23: Current density of XDPE at 70°C under increasing and decreasing electric field from 20 to 40 kV/mm: experiment and simulation.

Experimental and simulated leakage currents are compared in degassed XLPE at an applied temperature of 70°C. To compare the effect of electrical history on measured and simulated conductivity, steps of increased electric field from 20 to 40 kV/mm are first applied, followed by steps of decreased electric field from 40 to 20 kV/mm. Results are shown in Figure 4.23 with log-lin current density *versus* time graph. Similar leakage current density between experiment and

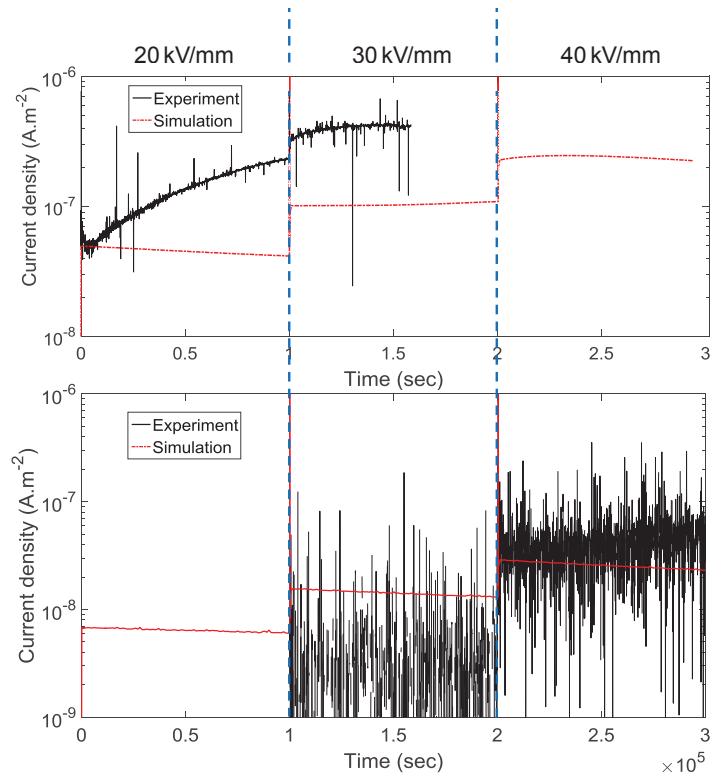


Figure 4.22: Current density of HDPE at 70°C (up) and 50°C (down) at increasing electric field from 20 to 40 kV/mm: experiment and simulation.

simulation is measured at each increasing electric field. At same electric field, a lower current density is measured after stress at higher electric field. An explanation of this behavior comes from the injected charges at high electric field that limit the current at lower fields according to SCLC theory. This behavior is perfectly simulated with the genetic model and very similar to the experiment in terms of values.

Variation of leakage current density with electric field at 30°C is simulated in LDPE and HDPE and compared to measurement performed by Montanari *et al.* [54]. Results are compared in Figure 4.24. Same threshold value of 10 kV/mm is observed for LDPE and HDPE both in experiment and simulation. According to the SCLC theory, at fields below this threshold, the conduction is of Ohmic type, while at fields above the threshold the relation between current density and applied voltage is quadratic [172]. Similar experimental and simulated values are obtained for HDPE expected for electric fields lower than 4 kV/mm where experimental values are higher. It may come from the experimental resolution limit at this very low electric field. For LDPE, a much higher current increase is observed after the threshold in experiment than in simulation. This increase is surprisingly very high and may be assigned to the contribution of other heterogeneities experimentally present in LDPE.

4.4.2 Space charge profile

Simulated and experimental space charge behaviors in LDPE are compared at 50°C and 70°C. At a given temperature, samples underwent an increasing electric field from 20 to 40 kV/mm. Between each electric field step, depolarization time of 1 min is performed. Space charge evolution with time is recorded both during Volt-off and Volt-on. In space charge measurements performed

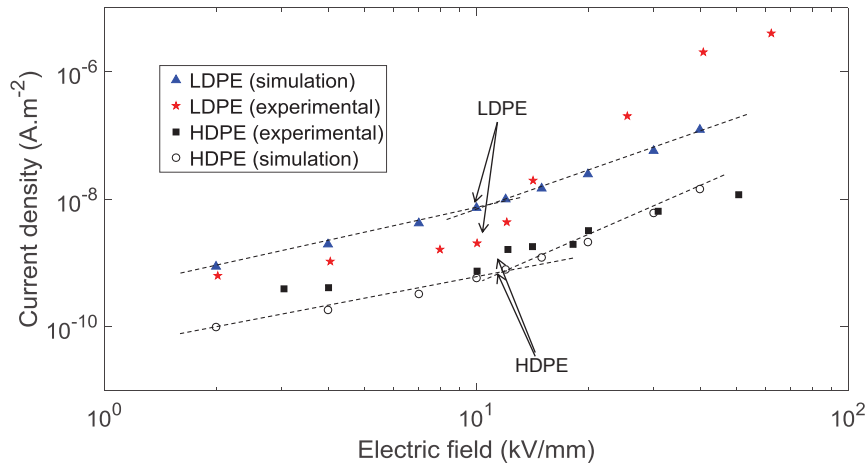


Figure 4.24: Current density *versus* electric field with threshold characteristic on log–log plot for LDPE and HDPE obtained from leakage current measurement by Montanari *et al* [54] and from simulation (the threshold is indicated by arrows).

with PEA, both internal and induced charges are present as observed in Figure 4.25. Induced charges correspond to charges on the electrodes which have a width related to the response time of the measurement system, in particular the voltage rise-time of the pulse, and to the interface with electrodes. Thus, induced charges are neither considered nor represented in the simulations shown in Figure 4.25 as they are not related to charges trapped in the material. Concerning the internal charges, similar charge density profile represented in Figure 4.25 is obtained from PEA measurements and from simulations. In both space charge profiles, positive charges in the bulk are present with a density around 0.4 C/m^3 and a positive charge accumulation near the cathode higher at 70°C than 50°C .

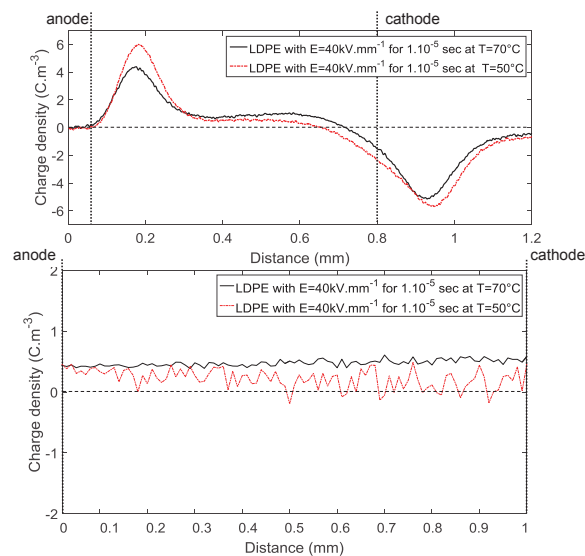


Figure 4.25: Space charge profile of LDPE at 50°C and 70°C in Volt-on after poling at 40 kV/mm for 1.10^5 s obtained from PEA measurement (up) and from simulation (down).

From space charge profile, the electric field distribution within material is obtained. Figure 4.26 compares the experimental and simulated electric field distributions in LDPE at 50°C and 70°C at Volt-on after $1 \times 10^5 \text{ s}$ of poling at increasing electric field from 20 to 40 kV/mm .

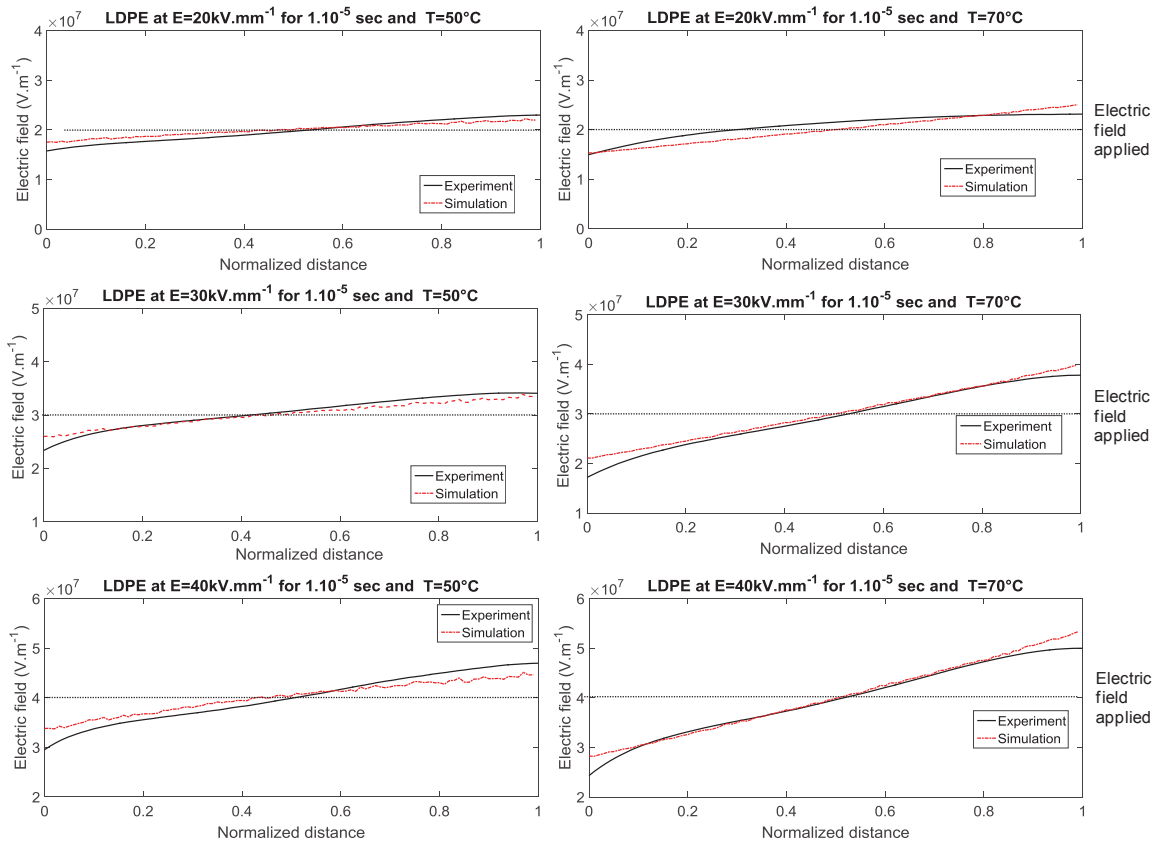


Figure 4.26: Electric field distribution in LDPE at 50°C and 70°C at Volt-on after 1.10^5 s of poling at increasing electric field from 20 to 40 kV/mm obtained from PEA measurement (up) and from simulation (down).

Regardless the temperature and the electric field, electric field distributions obtained in experiment and with simulation are very similar. A difference that may be noticed is near the interfaces, experimental electric field is curved due to the resolution of the space charge measurement method. Concerning LDPE results, decrease of electric field at the anode occurs due to positive charge accumulation. At a given applied electric field, local electric field at the anode is lower at 70°C than at 50°C, due to the higher charge accumulation at the highest temperature. A variation around 30% of the electric field is obtained at the highest electric field and temperature.

Simulation of space charge profile in HDPE is confronted to experimental measurements performed by Montanari *et al.* [54]. Measurement were performed with PEA method in HDPE under 60 kV/mm at $T = 25^\circ\text{C}$. Simulated and experimental space charge profiles of HDPE after 10s of depolarization (Volt-off) are compared in Figure 4.27. Space charge profiles are similar with a high negative charge accumulation observed near cathode. In experiment, negative charges seem to go deeper within the thickness of the material, however thickness of the sample in this experiment is only $205\ \mu\text{m}$. Thus by measuring the depth of the negative charge present within HDPE, simulation and experiment give very close values of penetration depths of respectively $80\ \mu\text{m}$ and $60\ \mu\text{m}$.

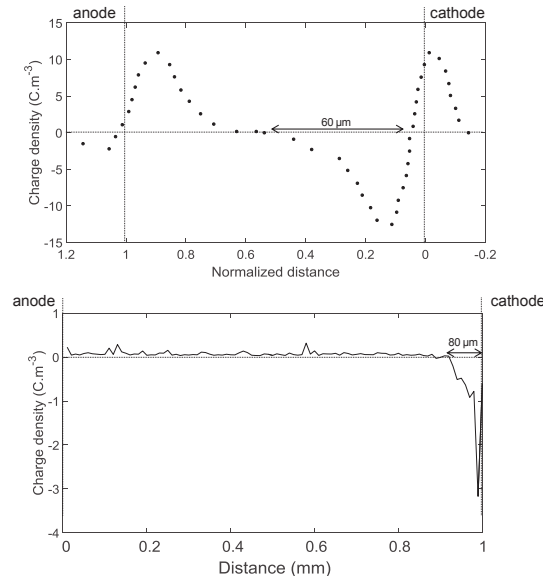


Figure 4.27: Space charge profile of HDPE at 70°C after 10 s of depolarization (Volt-off) following polarization 60 kV/mm for 1.10^4 sec obtained from PEA measurement [54] and from simulation.

From space charge measurements, mean density of total charge q accumulated in the specimen at Volt off, is obtained from the charge density $q_p(x)$ of the space charge profile by applying the expression:

$$q = \frac{1}{d} \int_0^d |q_p|(x) dx \quad (4.4.1)$$

with d [m] the sample thickness.

Variation of this mean charge density with electric field at 30°C is simulated for LDPE and HDPE and compared to measurement performed by Montanari *et al.* [54]. Results are represented in Figure 4.24. Same threshold value of 10 kV/mm is obtained for LDPE and HDPE both in experiment and with simulation. A coincidence between the threshold for space charge measurement and current density measurement is clearly made. In simulation, charge accumulation is much lower in HDPE than in LDPE whereas the contrary is observed experimentally. This difference can be explained by the localization of negative charges in HDPE near anode and not in the whole thickness. Indeed, it has been observed that negative charge in HDPE is present over 80 μm . In this case, the lower the sample thickness, the higher the mean charge density. As sample thickness in the experiment is five times lower than in the model, lower mean charge density is obtained in the simulation. A much lower difference is present for LDPE because space charge is present in the whole thickness.

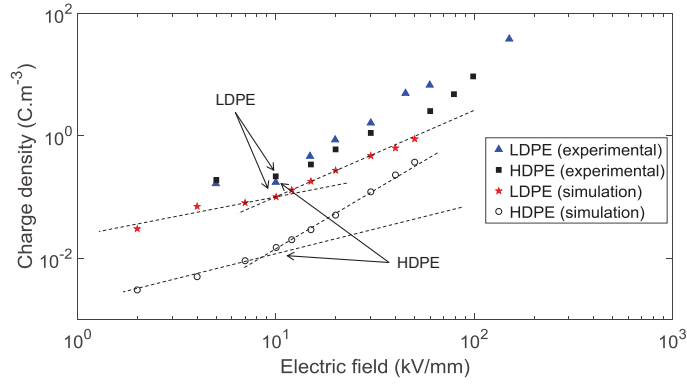


Figure 4.28: Current density *versus* electric field with threshold characteristic on log–log plot for LDPE and HDPE obtained from leakage current measurement by Montanari *et al* [54] and from simulation (the threshold is indicated by arrows).

4.4.3 Dependency with crystallinity

Experimental and simulated leakage currents and space charges are compared in PP blends with three different crystalline fractions: 0.12, 0.24 and 0.39. Both in space charge and leakage current measurements, samples underwent at 70°C under an increasing electric field from 20 to 40 kV/mm. The left part of Figure 4.29 shows current density at steady state at each electric field amplitude. Experimental and simulated values of current density at steady state are very similar regardless crystalline fraction and electric field. Furthermore same decrease of current density with crystalline fraction increase is observed. The highest difference measured between experiment and simulation is 1.5×10^{-7} A/m² for $E = 30$ kV/mm and $\chi_c = 0.12$ which is low and very concluding for the model. From space charge measurements, mean density of accumulated total charge q in the specimen at Volt off, is calculated from the equation (4.4.1). This mean charge density, represented in the right part of Figure 4.29, is measured at Volt off at 70°C after each electric field poling.

In both measurement and simulation, decrease of charge accumulation is observed when increasing crystalline fraction of PP. However, as regarding values, mean charge density for PP with the lowest crystalline fraction is higher in experiment than in simulation. This differences may come from the fact that elastomeric semiconductive electrodes are used in space charge measurement and may allow greater injection in low crystalline polymer than simulated in the model. Indeed, highest injection is generally obtained with semiconductive electrodes than metallic electrodes [61, 62]. Specific activation energy depending on the electrode type, metallic or superconductive electrodes, given as input parameter in the model could reduce the difference. Other explanation is the difference of sample thickness in experiment and in simulation. The difference is reduced by 33% as the difference of experimental and simulated sample thicknesses is about 33%.

4.4.4 Glass transition temperature

For the glass transition effect, current density under 20 kV/mm at temperature from 30°C to 90°C is simulated for a material with two different glass transition temperatures: $T_g = -50^\circ\text{C}$ (LDPE case) and $T_g = 70^\circ\text{C}$ (PET case). As demonstrated in Figure 4.30, from 70°C to 50°C, a

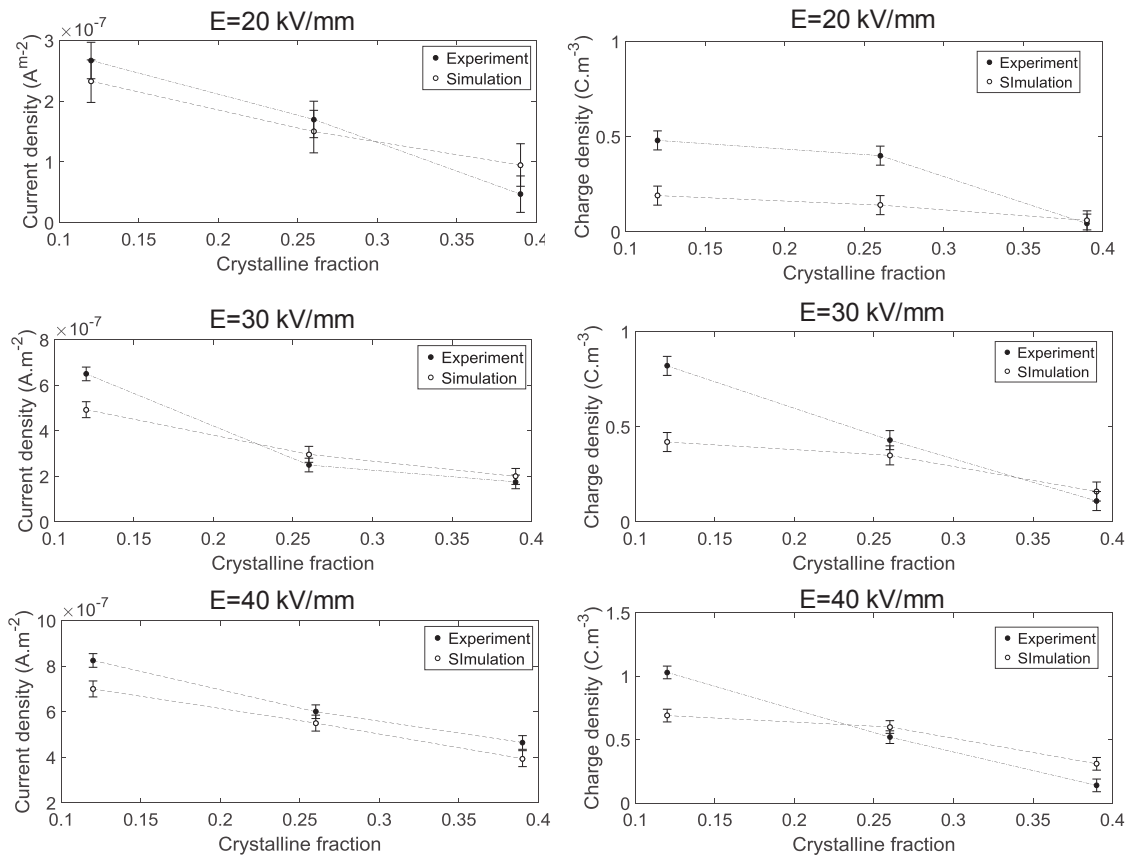


Figure 4.29: Current density at steady state (left) and mean accumulated charge density at Volt off (right) for PP with $\chi_c = 0.12$, 0.27 and 0.39 at 70°C and increasing electric field of 20 kV/mm , 30 kV/mm and 40 kV/mm with 1.10^5 sec of poling time at each electric field.

drop in current density is measured for material whose glass transition is at 70°C . This simulated behavior is similar from the one observed in dielectric spectroscopic measurements performed on PET at low voltage and temperature between 30°C and 90°C . Furthermore, simulated current density values at 70°C and 90°C are close to the experimental current density values measured in PET with $\chi_c = 0.4$ at 70°C and 80°C .

Summary

In this chapter the simulation of electrical properties of semi-crystalline polymer is addressed. For a given set of input parameters, this model simulates the specific physical microstructure of different polymers such as LDPE, HDPE, PP and PET. With the developed evolution laws, the influence of this microstructure on current density and space charge is simulated. This model is then able to calculate current density variation and space charge profile very similar to experimental measurements performed on semicrystalline polymers in this study or taken from the literature. Furthermore, the model succeed in reproducing complex behavior such as electric field thresholds or thermal effect (glass transition, annealing).

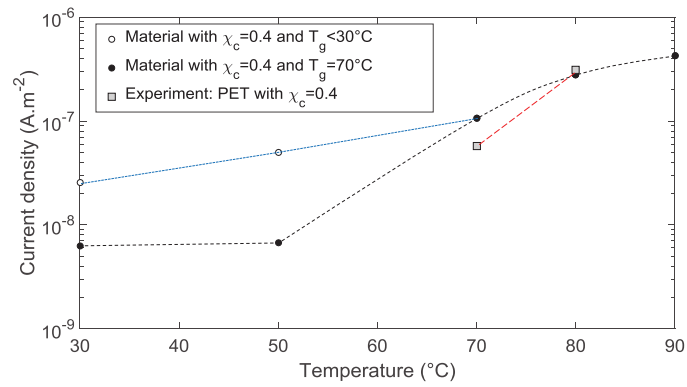


Figure 4.30: Current density at steady state simulated for material with $T_g < 30^\circ\text{C}$ and $T_g = 70^\circ\text{C}$ at 20 kV/mm and temperature from 30°C to 90°C. Experimental values obtained on PET with $\chi_c = 0.4$ at 70°C and 80°C are added.

Chapter 5

Genetic evolution of undegassed insulation system

In this chapter are developed the evolution laws to simulate the electrical properties of undegassed XLPE insulation system. More particularly, the impact of the peroxide decomposition products (PDP) and the interface with electrode are investigated. First, matrices are developed to describe the PDP distribution in XLPE as a function of data from the cross-linking process. Then evolution laws based on experimental results are implemented to simulate the behavior of these PDP under electric field and temperature. Furthermore evolution law are also added to describe the dependency of charge injection to electrode/insulation interface. In a third part, the influence of the different developed parameters on the resulting electrical properties are studied in order to obtain coherent simulated results. Finally results of the model are confronted to experimental results obtained on degassed and undegassed XLPE.

5.1 PDP distribution simulation

Chemical heterogeneities in XLPE can be ranked in two populations: In-chain defects such as double bonds, vinyl groups, carbonyl or hydroxyl randomly present in polyethylene (PE) macromolecules [133] and chemical defects coming from polymer formulation (antioxidants) and crosslinking (crosslinking by-products or PDP). In chain chemical defects create deep traps, in the range of 1.0 to 2.3 eV, and shallow traps in the range of 0.1 to 0.5 eV [133, 134, 135]. These heterogeneities are integrated to the model by considering two trap levels for the charge trapping law.

Chemical residues constitute heterogeneities of high mobility. Among their impact on polymer electrical properties, charge trapping and ionic transport under electric field and temperature are taken into account.

In synthetic crosslinked HVDC systems, when dicumyl peroxide (DCP) is used, the main decomposition products are methane (CH_4), acetophenone (ACP), α -cumyl alcohol (α CA) and α -methylstyrene as shown in Figure 5.1. While small molecules as methane desorb quickly and totally, bigger molecules follow longer diffusion processes and remain trapped within the bulk of insulation layer [176]. The amount and distribution of these PDP depend on the process and

the polymer nature. In this model, a matrix is associated to ACP and α CA. α -methylstyrene is not addressed in this study, as its amount is very low in the studied XLPE (<0.01). However, if needed, a matrix related to α -methylstyrene or other chemical species could further be implemented to the model very easily.

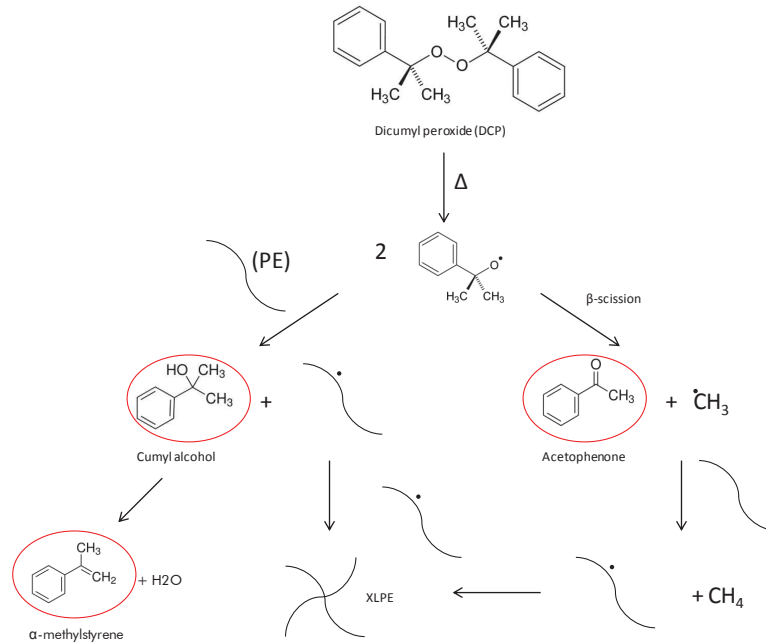


Figure 5.1: Crosslinking reaction of PE with DCP.

5.1.1 Distribution in the polymer

The initial concentration of DCP is given as input parameter. From the initial DCP concentration, concentration of the generated PDP depends especially on process temperature as each of their formation reaction has a specific activation energy. At lower temperature, the formation of α CA is promoted whereas ACP and methane are privileged at higher temperature. In order to measure the α CA and ACP concentrations as a function of crosslinking temperature in PE, LDPE with two different initial amounts of DCP are crosslinked at three different temperatures, 160°C, 190°C and 220°C, with a crosslinking time adjusted according to the processing temperature.

The change of α CA and ACP concentration with crosslinking temperature, obtained from FTIR and GC-MS analyses is shown in Figure 5.2.

From polynomial regression of the concentration variation with temperature, relation between the weight concentration of these PDP and the crosslinking temperature is obtained:

$$\begin{aligned}
 [\text{ACP}] &= \frac{[\text{DCP}]}{1.2} (-4.98 \cdot 10^{-5} T_r^2 + 2.28 \cdot 10^{-2} T_r + 2.143) / 100 \\
 &\text{and} \\
 [\alpha\text{CA}] &= \frac{[\text{DCP}]}{1.2} (-8.33 \cdot 10^{-5} T_r^2 + 2.95 \cdot 10^{-2} T_r + 1.997) / 100
 \end{aligned}
 \tag{5.1.1}$$

with T_r [°C] the crosslinking temperature used as a second input parameter in the model.

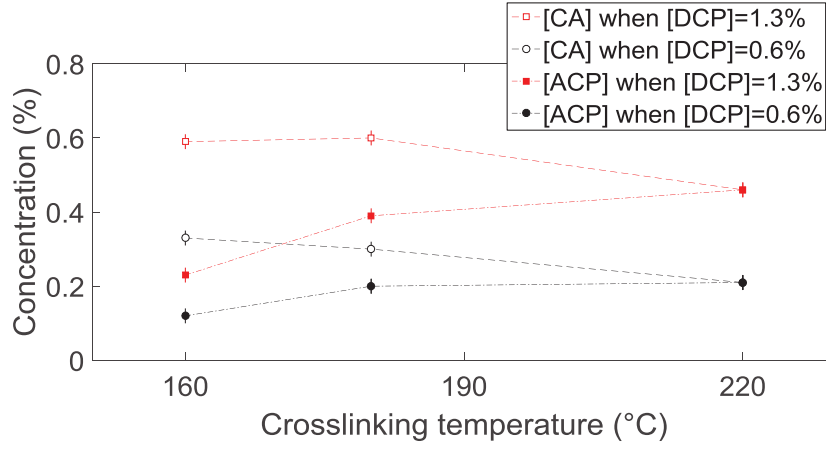


Figure 5.2: Effect of peroxide decomposition temperature on the concentration of ACP and α CA.

The number of moles of these molecules in the simulated polymer matrix which simulate the material is then given by:

$$n_{ACP,tot} = ([ACP] d_{XLPE}) / (M_{ACP} n m dr^2)$$

and

$$n_{\alpha CA,tot} = ([\alpha CA] d_{XLPE}) / (M_{\alpha CA} n m dr^2)$$
(5.1.2)

with M_{ACP} [g/mol] the molar weight of ACP (120.15 g/mol), $M_{\alpha CA}$ [g/mol] the molar weight of CA (136.9 g/mol), d_{XLPE} [kg/m³] the density of the simulated XLPE, and $n m dr^2$ [m²] the surface of the matrix.

All these PDP are localized in the amorphous regions and thus each state (i, j) of the matrix has a given amount of PDP moles according to its local crystallinity:

$$n_{ACP} = (n_{ACP}(1 - \chi_c)) / ((1 - \chi_{c,mean}) n m)$$

and

$$n_{\alpha CA} = (n_{\alpha CA}(1 - \chi_c)) / ((1 - \chi_{c,mean}) n m)$$
(5.1.3)

with χ_c the local crystalline fraction of each state, $\chi_{c,mean}$ the mean crystalline fraction of the matrix, n the number of matrix state in the x -direction and m the number of matrix state in the y -direction.

5.1.2 Impact on local permittivity

The permittivity of PE, around 2.3 at room temperature, may be locally varied in presence of PDP. To take into account the PDP effect, simulated permittivity is assumed to be depending both on the matrix permittivity and on the permittivity of each PDP (given in Table 5.1).

PDP	acetophenone	α -methylstyrene	α cumylalcohol
Relative permittivity (at 28°C)	17	5.6	9.7

Table 5.1: Main physical properties of the PDP [79].

The surface occupied by these molecules in each state is given by:

$$\begin{aligned} S_{ACP} &= n_{ACP} M_{ACP}/d_{ACP} \\ &\text{and} \\ S_{\alpha CA} &= n_{\alpha CA} M_{\alpha CA}/d_{\alpha CA} \end{aligned} \quad (5.1.4)$$

Thus, the value of permittivity according to crystallinity and PDP proportion in each state is:

$$\varepsilon_r = (2.06 + 0.40 \chi_c) \left(1 - (S_{ACP} + S_{\alpha CA})/\delta r^2\right) + (\varepsilon_{r,ACP} S_{ACP} + \varepsilon_{r,\alpha CA} S_{\alpha CA})/\delta r^2 \quad (5.1.5)$$

with χ_c the local crystalline fraction, $\varepsilon_{r,ACP}$ the relative permittivity of ACP and $\varepsilon_{r,\alpha CA}$ the relative permittivity of αCA .

Experimentally, dielectric spectroscopy measurements are performed in fully degassed and undegassed XLPE with a PDP amount of 1.2% at several temperature from 30°C to 90°C. For all temperatures, the difference of relative permittivity between undegassed and degassed XLPE is very low, less than 0.2. The genetic model gives the same low difference of the mean permittivity in XLPE with and without the presence of PDP.

5.1.3 Influence of degassing time

To obtain a relation in the genetic model between PDP concentrations and degassing time, freshly crosslinked XLPE is degassed for different duration at 35°C and quantitative thermogravimetric-analysis (TGA) is performed to obtain a global appreciation of the remaining PDP amount. The weight loss is indeed considered to correspond to the global amount of PDP. Moreover, FTIR analysis are performed to measure the ACP concentration at each degassing time. As shown in Figure 5.3, PDP and ACP amount are plotted as a function of the square root of degassing time. Linear regression of the data demonstrates a Fickian process of diffusion.

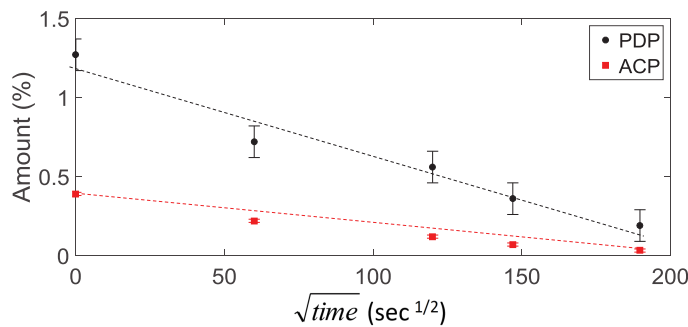


Figure 5.3: PDP and ACP amount as a function of the square root of degassing time.

Assuming a Fickian model of diffusion, the weight loss in this case is:

$$\frac{m_t}{m_{t0}} = \beta \sqrt{t} = \frac{4 \sqrt{D/\pi}}{d} \sqrt{t} \quad (5.1.6)$$

with t [s] the degassing time, m_t [g] the sample weight at t , m_{t0} [g] the sample weight at $t = 0$ s, D [m²/s] the diffusion constant, d [m] the sample thickness, and β the coefficient of the linear fit.

From the equation (5.1.6), a diffusion constant of $5.54 \times 10^{-13} \text{ m}^2/\text{s}$ for ACP is measured and $4.45 \times 10^{-13} \text{ m}^2/\text{s}$ for the global diffusion constant of the PDP. These similar values show that the other chemical species such as αCA are diffusing at similar rate as ACP. From the diffusion constant, the half desorption time $t_{1/2}$ to desorp half of the maximum weight loss is given by:

$$t_{1/2} = 0.04909 \frac{e^2}{D} = \frac{1.37 d^2}{\pi^2 D} \quad (5.1.7)$$

Thus a degassing time can be given in the model as input parameter. Resulting amount present within the matrix is then calculated as a function of the degassing time.

5.2 Evolution law development

5.2.1 Genetic behavior of ACP

5.2.1.1 Diffusion of ACP from concentration gradient

ACP distributed in the free volume of the polymer in the amorphous region [138] may diffuse under concentration or temperature gradient. From the first and second Fick laws, evolution law for ACP transport by diffusion is given by:

$$\delta n_{ACP} = -D_{ACP} \frac{n_{ACP}(x - dx, y, t) - n_{ACP}(x, y, t)}{(\delta r)^2} \delta t \quad (5.2.1)$$

with δn_{ACP} [mol] the variation of mole of ACP during δt , D_{ACP} [m^2/s] the diffusion constant of ACP, δr [m] the length of each state and δt [s] the step time.

From the diffusion constant of ACP at several temperatures from 22°C to 90°C taken from the work by Sayoun *et al.* [176], relation of ACP diffusion constant with temperature is obtained:

$$D_{ACP} = 1.833 \exp(-0.721 e/(k_B T)) \quad (5.2.2)$$

with e [C] the electric charge, k_B [$\text{m}^2.\text{kg}.\text{s}^{-2}.\text{K}^{-1}$] the Boltzmann constant and T [K] the temperature. The direction of the diffusion transport depends on the sign of the concentration difference between neighboring states:

$$\begin{aligned} \text{If } n_{ACP}(x - dx, y, t) < n_{ACP}(x, y, t) \quad & n_{ACP}(x, y, t + 1) = n_{ACP}(x, y, t) + \delta n_{ACP} \\ \text{If } n_{ACP}(x - dx, y, t) > n_{ACP}(x, y, t) \quad & n_{ACP}(x - dx, y, t + 1) = n_{ACP}(x - dx, y, t) + \delta n_{ACP} \end{aligned} \quad (5.2.3)$$

Figure 5.4 shows the simulated variation of ACP concentration with space and time due to diffusion when a concentration of ACP is only at the interface at $t = 0 \text{ s}$ and when electrodes act as barrier to diffusion. As expected, a decrease of concentration at the interface and an increase of concentration in the bulk are observed.

5.2.1.2 Impact on electrical properties: deep traps for electrons

Trap depth for electrons and holes associated to ACP has been determined in the literature by Teyssedre *et al.* with molecular modeling and luminescence techniques [135]. Trap depth

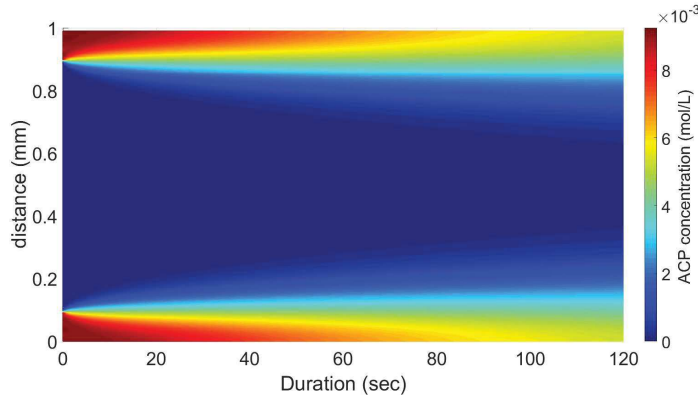


Figure 5.4: Simulated distribution of ACP concentration as a function of space and time when a concentration of ACP is only present at the interface at $t = 0$ s.

values of 0.9 eV for electrons and 0.04 eV for holes demonstrate that ACP is acting as deep trap for electrons and shallow trap for holes. This behavior is further supported by space charge measurements performed by Hussin *et al.* on ACP-soaked LDPE [79]. Hussin *et al.* measured space charge at room temperature and under electric fields from 30 kV/mm to 60 kV/mm. The authors reported negative charge accumulation up to 8 C/m^3 in ACP soaked LDPE and ascribed this behavior to the deep trap role of this molecule on electrons.

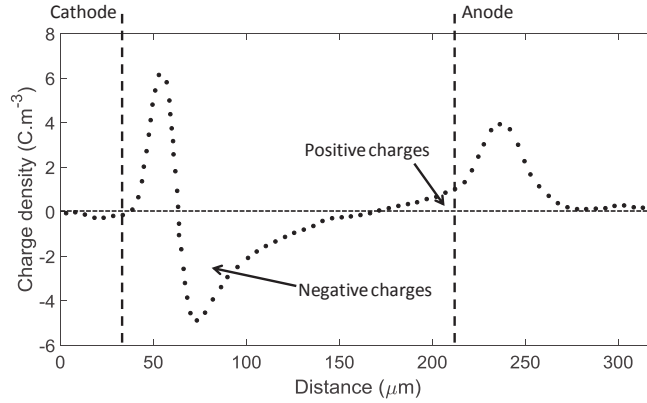


Figure 5.5: Space charge profile of 180- μm thick ACP soaked LDPE stressed at 5 kV ($E \approx 30 \text{ kV/mm}$) and room temperature during Volt off (Adapted from [79]).

An additional trapping law for electron and hole is developed to take into account the ACP contribution to charge trapping in the genetic model:

$$Q_{trap,ACP} = \alpha_{ACP} (\delta r)^2 \rho_{mob} \left(\frac{Q_{trap,max,ACP} - (\delta r)^2 \rho_{trap}}{Q_{trap,max,ACP}} \right) \left(p < \frac{Q_{trap,max,ACP} - (\delta r)^2 \rho_{trap}}{Q_{trap,max,ACP}} \right) \quad (5.2.4)$$

with $Q_{trap,max,ACP}$ [C] the maximum charge amount related to ACP, ρ_{mob} [C/m^3] the mobile charge density, ρ_{trap} [C/m^3] the trapped charge density, α_{ACP} parameter lower than 1 which corresponds to the proportion of trapped charges at each time step and p a random number between 0 and 1 that corresponds to the probability of trapping depending on the amount of trapped charge.

The maximum charge amount $Q_{trap,max,ACP}$ in each state is obtained from the number of mole n_{ACP} present in this state with the relation:

$$Q_{trap,max,ACP} = n_{ACP} e N_a \quad (5.2.5)$$

with N_A [mol^{-1}] the Avogadro number ($6.02 \cdot 10^{-23} \text{mol}^{-1}$) and e [C] the electric charge (1.6×10^{-19} C). In undegassed XLPE, crosslinked with an initial concentration of DCP of 1.2% and a crosslinking temperature of 190°C, each unit of the simulation matrix contains an amount of ACP comprised between 2.89×10^{-9} moles and 3.13×10^{-9} moles. The corresponding charge amount is between 2.78×10^{-4} C and 3.02×10^{-4} C which gives a maximum charge density between 2.78×10^6 C/m³ and 3.02×10^6 C/m³. This high charge density demonstrates that ACP is acting as an infinite reservoir of charges.

For ACP, the trap depth for electrons is $\xi_a = 0.9$ eV and for holes $\xi_a = 0.04$ eV. Charge detrapping from ACP is assumed to be a thermally activated process and the related evolution laws is given by:

$$Q_{detrapp,ACP} = \alpha (\delta r)^2 \rho_{trap} \left(p < \frac{k_B T}{h} \exp\left(\frac{-e \cdot \xi_a}{k_B T}\right) \right) \quad (5.2.6)$$

with ρ_{trap} [C/m³] the trapped charge density, α which corresponds to the proportion of detrapped charges at each step time and considered as identical to the proportion of trapped charges and ξ_a [eV] the activation energy of detrapping.

5.2.2 Genetic behavior of α CA

5.2.2.1 Diffusion of α CA from concentration gradient

Similarly to ACP, evolution law for α CA transport by diffusion is given by:

$$\delta n_{\alpha CA} = -D_{ACP} \frac{n_{\alpha CA}(x - dx, y, t) - n_{\alpha CA}(x, y, t)}{(\delta r)^2} \delta t \quad (5.2.7)$$

with $\delta n_{\alpha CA}$ [mol] the variation of ACP mole during δt , D_{ACP} [m²/s] the diffusion constant of ACP, δr [m] the length of each state and δt [s] the step time.

Variation of the α CA diffusion constant with temperature is obtained from results in the literature [146]:

$$D_{\alpha CA} = 1.833 \exp(-0.721 e / (k_B T)) \quad (5.2.8)$$

However this relation is only valid at temperatures higher than 24°C, corresponding to the melting temperature of α CA. At 22°C, $D_{\alpha CA} = 1.59 \cdot 10^{-13}$ m²/s.

The direction of the diffusion transport is depending on the sign of the concentration difference between neighboring states:

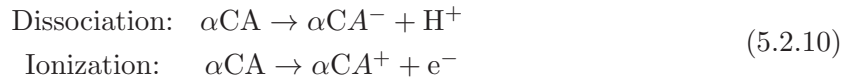
$$\begin{aligned} \text{If } n_{\alpha CA}(x - dx, y, t) < n_{\alpha CA}(x, y, t) \quad & n_{\alpha CA}(x, y, t + 1) = n_{\alpha CA}(x, y, t) + \delta n_{\alpha CA} \\ \text{If } n_{\alpha CA}(x - dx, y, t) > n_{\alpha CA}(x, y, t) \quad & n_{\alpha CA}(x - dx, y, t + 1) = n_{\alpha CA}(x - dx, y, t) + \delta n_{\alpha CA} \end{aligned} \quad (5.2.9)$$

5.2.2.2 Impact on electrical properties: ionic transport

From DFT measurements, α CA constitutes shallow traps for both holes and electrons and does not yield to electronic charge accumulation. Le Roy *et al.* measured space charge at temperatures from 10°C to 50°C and under electric fields from 5 kV/mm to 25 kV/mm on α CA-soaked LDPE. The authors reported negative and positive heterocharges [42].

Heterocharges have been attributed to ions generated from α CA dissociation or ionization. Another possible interpretation is an inhomogeneous distribution of dipoles related to α CA which orientate under electric field. In this study, a focus is made on the ionization/dissociation case.

The dissociation and ionization equations of α CA are :



The nature of ions that are created when introducing α CA in a LDPE matrix are not identified yet in the literature. Thus the general case is addressed in this model by considering the reaction:



with αCA^+ , the resulting positive ionic species and αCA^- , the resulting negative ionic species.

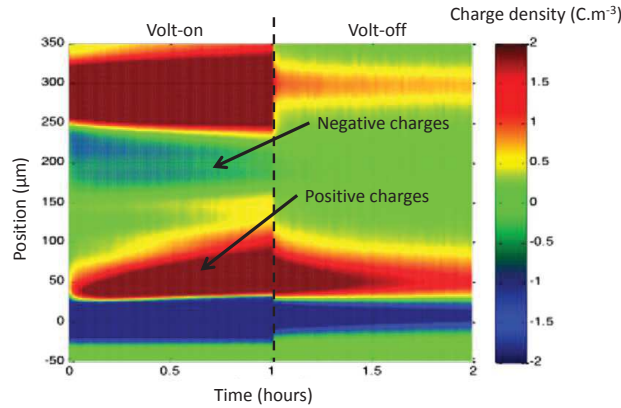


Figure 5.6: Space charge profile of 180 μm α CA soaked LDPE stressed at 5 kV and room temperature during Volt off [42].

In LDPE crosslinked with an initial DCP amount of 1.2% and at a crosslinking temperature of 190°C, if all generated α CA molecules are ionized or dissociated, local ionic charge density is around $4 \times 10^6 \text{ C/m}^3$. This value is far too high compared to the highest values measured experimentally in space charge measurement (10 C/m^3) for α CA soaked LDPE. It means that only a very small fraction of these generated molecules are effectively ionized. Furthermore the very high activation energy related to alcohol dissociation ($\sim 4 \text{ eV}$) or ionization ($\sim 8 \text{ eV}$) is in favor of a low proportion of created ions. Assuming a fraction r of ionized or dissociated

molecules, the amount of formed positive and negative ion densities are:

$$\begin{aligned}\rho_{\alpha CA^+} &= r n_{\alpha CA} N_A e / (\delta r)^2 \\ &\text{and} \\ \rho_{\alpha CA^-} &= -r n_{\alpha CA} N_A e / (\delta r)^2\end{aligned}\tag{5.2.12}$$

with $n_{\alpha CA}$ [mol] the amount of αCA , N_A [mol⁻¹] the Avogadro number (6.02×10^{23} mol⁻¹), e [C] the electric charge (1.6×10^{-19} C) and r the proportion of ionized αCA molecules.

For the evolution laws of this ions transport, assuming a infinite dilute solution due to the low amount of PDP (< 2%) in polymer, Einstein relation is used to obtain mobility of these ions from the diffusion constant:

$$\mu_{\alpha CA} = (D_{\alpha CA} e) / (k_B T)\tag{5.2.13}$$

with $D_{\alpha CA}$ [m²/s] the diffusion constant. However dissociation and ionization of αCA generates two charge carriers with very different mobility. In case of dissociation, the created proton H⁺ has a much higher mobility than the negative counter ions. For ionization, it is the generated electrons which have the highest mobility. Thus, a parameter $\alpha_{ionization}$ is introduced that corresponds to the ratio between positive and negative ion mobilities:

$$\alpha_{ionization} = \mu_{\alpha CA^-} / \mu_{\alpha CA^+}\tag{5.2.14}$$

The evolution law for ion transport is then given by:

$$Q_{\alpha CA} = \delta r \delta t \rho_{\alpha CA} \mu_{\alpha CA} E_{x/y}\tag{5.2.15}$$

When ionic species accumulate at interfaces, they can be transported in the counter-direction by diffusion process as described in section 5.2.2.1. The evolution law for ionic diffusion is given by:

$$Q_{\alpha CA, diff} = D_{\alpha CA} \frac{\delta \rho_{\alpha CA}}{\delta r} \delta r \delta t\tag{5.2.16}$$

When electric field is applied, evolution law for transport due to diffusion is negligible compared to the evolution law for ionic transport. For instance, with an electric field of 5 kV/mm at room temperature and αCA concentration gradient of 0.4 mol/L, $Q_{\alpha CA} \sim 10^{-12}$ C and $Q_{\alpha CA, diff} \sim 10^{-14}$ C. Thus diffusion is likely to impact charge distribution only when no electric field is applied, explaining the experimental decrease of heterocharges observed at Volt-off in space charge measurements.

By neglecting the diffusion current, conduction current in this model is due to both electronic and ionic transport:

$$\frac{\partial(Q_{e/h} / (\delta r)^2)}{\partial t} + \frac{\partial(Q_{\alpha CA} / (\delta r)^2)}{\partial t} + \frac{\partial j_{cond}}{\partial x} = 0\tag{5.2.17}$$

At the interface, it is considered that there is no extraction of these ionic species expected when negative charges are created in case of ionization. After a given duration under electric field, it would yield to an agglomeration of these ions at the interface. However, the similar value of the solubility parameter δ , presented in Table 5.2, between LDPE and αCA show a strong affinity of this molecule with polymer [146]. It is assumed that the created ionic species have a similar

affinity with the polymer which prevents their agglomeration. Consequently, a parameter r_{max} is introduced and is related to the highest αCA amount that can be present in each matrix state according to the equation:

$$n_{\alpha CA} M_{\alpha CA} / d_{\alpha CA} < r_{max} \chi_c dr^2 \quad (5.2.18)$$

with $n_{\alpha CA}$ [mol/m³] the local amount of αCA , αCA^+ and αCA^- , $M_{\alpha CA}$ [g/mol] the molar mass, $d_{\alpha CA}$ the density, χ_c the local crystalline fraction and dr [m] the length of each state of the matrix.

	PE	ACP	αCA
δ (MPA ^{1/2})	17.15	20.2	20.1

Table 5.2: Solubility parameters of ACP, αCA and PE [176].

5.2.3 Effect of macroscopic interfaces

For homogeneous materials, charge injection obeys a Schottky law. The corresponding evolution law is expressed as:

$$Q_{e/h,inj} \propto T^2 \exp\left(\frac{e}{k_B T} \sqrt{\frac{eE}{4\pi\epsilon}}\right) \exp\left(-\frac{e \cdot w_{e/h,inj}}{k_B T}\right) \quad (5.2.19)$$

The properties of the electrode/insulation interface may considerably affect $w_{e/h,inj}$ and, thus, the extent of injected and accumulated electronic charges [59]. Charge injection is highly depending on the metal used as electrode. Taleb *et al.* measured space charge of LDPE using PEA method and leakage current of LDPE with 3 different electrode materials: Silver, Indium and Aluminum [59]. Measurements were performed at room temperature in sample submitted to increasing electric fields from 10 to 90 kV/mm, with 600 s polarization time at each step. Figure 5.7 shows the charge distribution measured at Volt-off after the polarization under 90 kV/mm and Figure 5.8 shows the current at steady state *versus* electric field. The largest charge density amount is measured with silver electrode despite it has the highest work function and may be due to silver diffusion at the interface. Thus to relate the charge injection with the electrode/insulation interface, many other features than metal work function have to be considered such as roughness, presence of chemical residues, oxidation, and so on.

To take into account these surface features in simulation, the presence of surface states are considered. The surface states correspond to localized energy levels in the band gap that can highly promote charge injection from the electrode to the dielectric [20, 21].

Another major difference is when addressing the electrical properties of insulation system with semiconductive electrodes. Indeed, higher hole injection is generally obtained with semiconductive electrodes than metallic electrodes, probably due to the distribution of carbon black particles at the semicon/insulation interface [9, 61, 62].

In the experimental study, leakage current is measured in degassed XLPE with semiconductive electrodes and with brass electrodes at 70°C under 30 kV/mm. Larger current density is measured with semiconductive electrodes than with brass electrodes. It demonstrates that

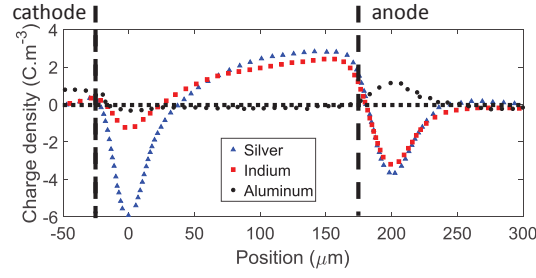


Figure 5.7: (left) Charge density distribution in LDPE with different electrode materials at Volt-off after step increase of field up to 90kV/mm. Adapted from [59].

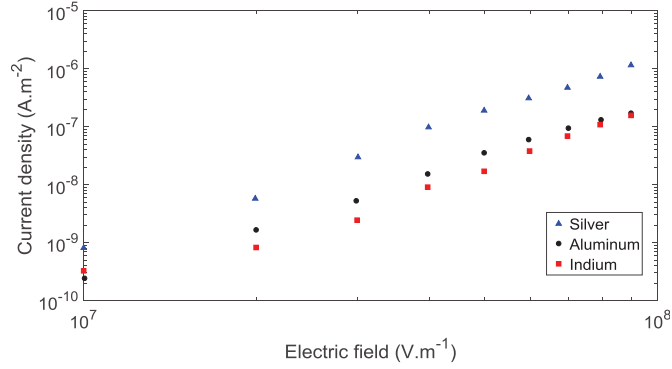


Figure 5.8: Current density at steady state *versus* electric field in LDPE with different electrode materials. Adapted from [59].

semiconductive electrode, compared to brass electrode, enhances charge injection in insulation system. Thus, the energetic barrier in the model for hole injection law is defined as:

$$w_{h,inj} = \begin{cases} 0.6 \text{ eV} & \text{for electrode = brass} \\ 0.55 \text{ eV} & \text{for electrode = semicon} \end{cases} \quad (5.2.20)$$

Furthermore, chemical species such as antioxidants or peroxide decomposition products can increase hole or electron injections. Indeed, charge carriers can be injected in the localized states related to these molecules. For localized states classified as deep traps, charges injected into these states remain near the electrode and do not contribute to conduction. For localized states considered as shallow traps, charges injected in these states are instantaneously detrapped, contributing to conduction. Among the PDP, ACP acts as shallow trap for holes with a depth of 0.04 eV. If ACP molecules are localized near the interface, it is considered in the evolution law that the activation energy for hole injection is reduced by the depth of the ACP shallow trap:

$$w_{h,inj} = \begin{cases} 0.6 \text{ eV} & \text{if } [ACP] = 0 \\ 0.56 \text{ eV} & \text{if } [ACP] \neq 0 \end{cases} \quad (5.2.21)$$

5.3 Criticality of model parameters

In this section, the influence of the different parameters on simulated current density and space charge is investigated. The aim is to get to a full understanding of the different effects of each parameter and to find their best accurate values to obtain simulated results consistent with experiments. Parameters related to the evolution laws describing α CA and ACP electrical behavior are investigated. To study these parameters, XLPE electrical behavior is simulated with different concentrations of the related chemical residue. For all results presented in this part, anode is placed at $x = 0$ and cathode is placed at $x = 1$ mm.

5.3.1 Parameters for α CA genetic behavior

Concerning the genetic behavior of α CA, 3 parameters are investigated: the parameter α which corresponds to the ratio between positive and negative ion mobility, the parameter r which corresponds to the proportion of ionized α CA molecules and r_{max} the parameter which corresponds to the maximum ionic concentration that can be locally present.

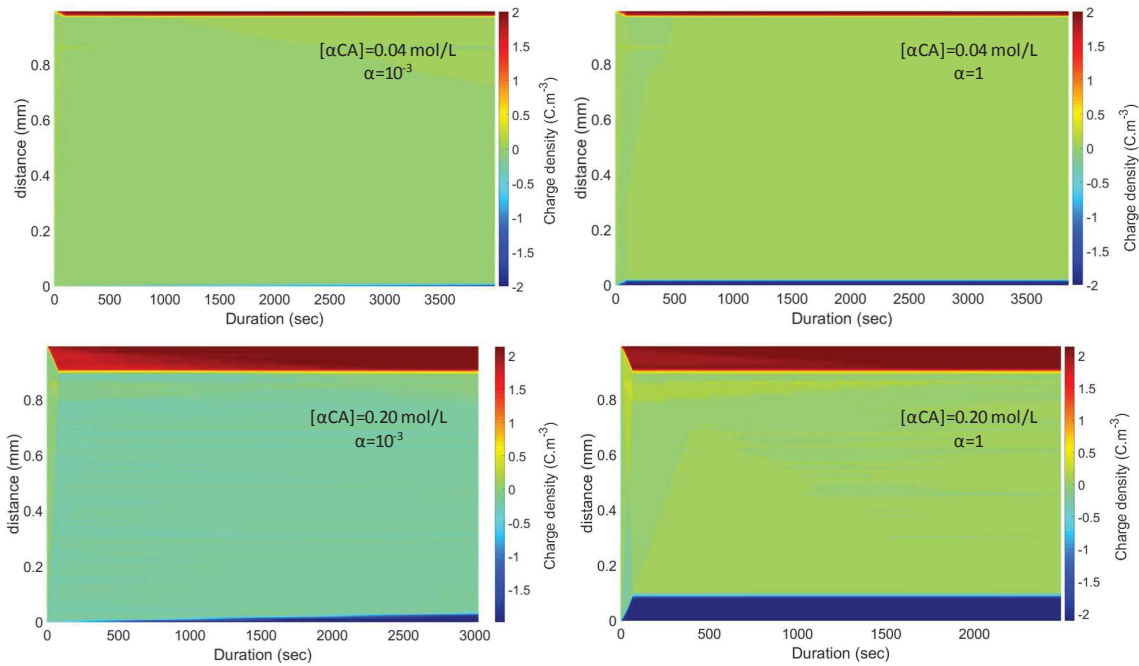


Figure 5.9: Space charge distribution as a function of time and space in LDPE with $[\alpha\text{CA}]=0.04$ mol/L and $[\alpha\text{CA}]=0.2$ mol/L under an electric field of 10 kV/mm and at a temperature of 30°C. Values used for $\alpha = 10^{-3}$ (left) and $\alpha = 1$ (right).

Current density and space charge in XLPE with two different α CA concentrations, 0.04 mol/L and 0.20 mol/L, are simulated under an electric field of 10 kV/mm and at a temperature of 30°C. Different values of α between 10^{-5} and 1 are tested. Figure 5.9 shows the simulated space charge profiles at Volt-on *versus* time and distance for a poling time of 1 h with $\alpha = 10^{-3}$ and $\alpha = 1$. As expected, positive heterocharge near cathode and negative heterocharge near anode are detected due to ionic species. The higher the α CA concentration, the higher the amount of accumulated heterocharges. When $\alpha = 10^{-3}$, positive ions have a much higher mobility than

negative ions resulting in a faster heterocharge accumulation for positive charge carrier than for negative ones. When positive and negative mobilities are the same ($\alpha = 1$), negative and positive charge accumulation are equal.

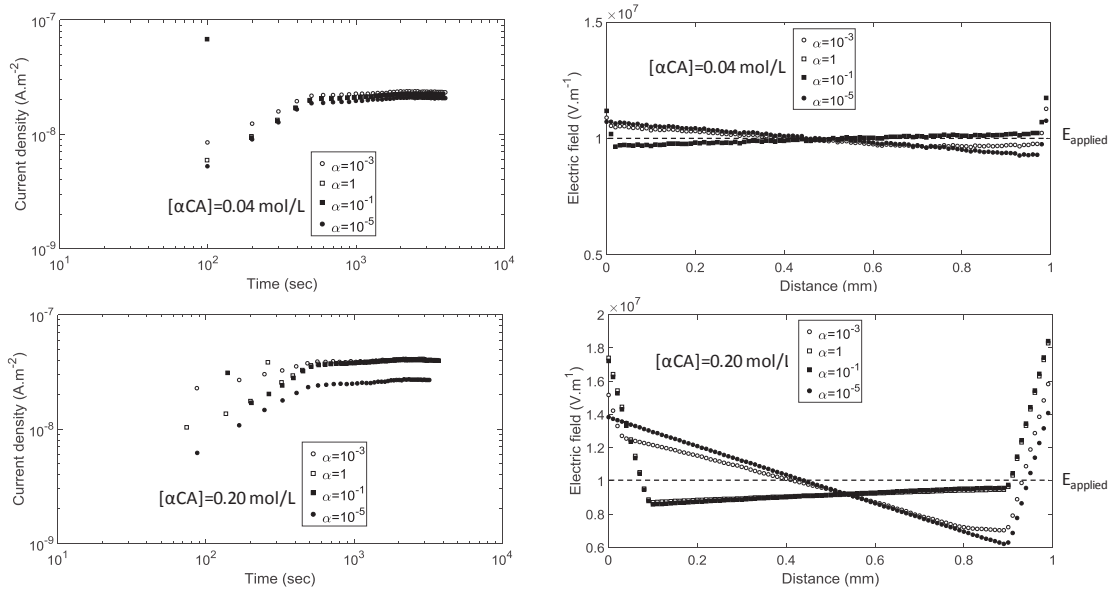


Figure 5.10: Simulated current density (left) and electric field distribution (right) in XLPE with different values for α under an electric field of 10 kV/mm at 30°C .

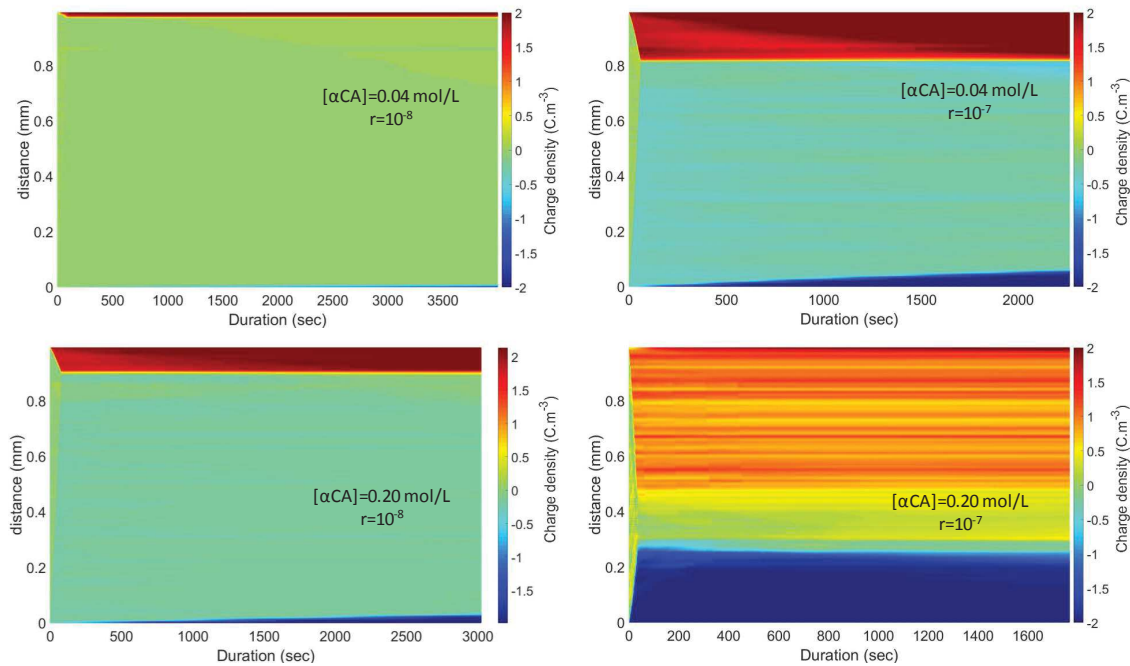


Figure 5.11: Space charge distribution as a function of time and space in XLPE with $[\alpha CA] = 0.04 \text{ mol/L}$ and $[\alpha CA] = 0.2 \text{ mol/L}$ when $r = 10^{-8}$ (left) and $r = 10^{-7}$ (right).

Impact of parameter α on current density and local electric field is shown in Figure 5.10. In XLPE with $[\alpha CA] = 0.04 \text{ mol/L}$, no effect of α in current density is observed. It is because heterocharge amount is low and impact few the local electric field with an increase at the interface lower than 1 kV/mm. In XLPE with $[\alpha CA] = 0.20 \text{ mol/L}$, with the two lowest values

of α , the amount of accumulated heterocharges is higher near cathode than near anode. It results in a higher increase of electric field at the vicinity of the cathode (18 kV/mm). For α close or equal to 1, accumulated heterocharges are similar at both interfaces resulting in the same electric field increase at these interfaces. No effect in current density is observed, expected for $\alpha = 10^{-5}$. At this value, there is almost no negative heterocharge near anode and thus no electric field increase explaining the lower hole injection and lower current density.

Current density and space charge in XLPE with two different αCA concentrations, 0.04 mol/L and 0.20 mol/L, are simulated for an applied electric field of 10 kV/mm, a temperature of 30°C and different values of r . Parameter α is fixed to 10^{-3} and r_{max} to 2. Figure 5.11 represents the space charge profile with two different proportions of ionized αCA : $r = 10^{-8}$ and 10^{-7} . In XLPE with $[\alpha CA] = 0.04$ mol/L, positive heterocharge density is increasing and is present in a thickness 10 times higher when r is increasing. For a higher concentration, when $r = 10^{-7}$, heterocharges are present in all the thickness of the dielectric. In this case, with the imposed parameter r_{max} , the amount of local heterocharges is too high to allow transport from one state to another.

Impact of r on current density and local electric field is shown in Figure 5.12. In XLPE with $[\alpha CA] = 0.04$ mol/L, there is a much higher amount of heterocharges at the highest value of r . It yields to an electric field increase up to 18 kV/mm near cathode and up to 15 kV/mm near anode. With this electric field increase, more holes and electrons are injected resulting in a higher current density at steady state. In XLPE with $[\alpha CA] = 0.20$ mol/L, as there are more heterocharges, electric field increases at the interface is much higher. However for $x < 0.25$ mm, there is a decrease of the electric field that becomes negative and yields to an unstable current density.

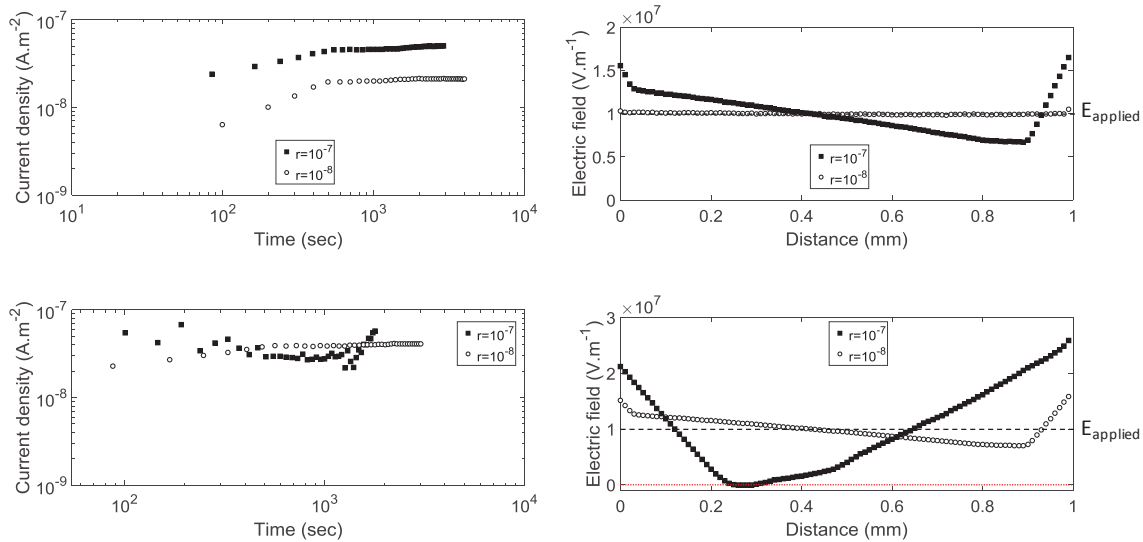


Figure 5.12: Current density (left) and electric field distribution (right) of XLPE with $[\alpha CA] = 0.04$ mol/L and $[\alpha CA] = 0.2$ mol/L at various ratio r of ionized or dissociated αCA .

For the impact of r_{max} , when r_{max} is increasing, heterocharges are present in a thinner thickness at the vicinity of the electrode with a higher density.

In LDPE containing a relative amount of 6% of αCA submitted to an electric field at room temperature, maximal measured heterocharge density with PEA technique is around 4 C/m³.

These heterocharges are present over a thickness of $200 \mu\text{m}$ of the dielectric and a larger amount of positive heterocharges is present compared to the negative ones [79, 42]. From these experimental data, coefficients used for the evolution laws related to αCA are presented in Table 5.3.

Parameters	Unit	Value
α	/	$4/3$
r	/	5×10^{-7}
r_{max}	/	2.6

Table 5.3: Parameters related to αCA used in the model after study of their influence.

5.3.2 Parameters for ACP genetic behavior

Concerning the evolution law related to ACP, the influence of the parameter α_{ACP} corresponding to the proportion of trapped charges by this chemical residue at each time step δt is studied. Space charge in XLPE with a concentration of ACP of 0.15 mol/L is simulated for an electric field of 20 kV/mm , a temperature of 30°C , and three different values taken for α_{ACP} : $\delta t/500$, $\delta t/50$ and $\delta t/5$. Space charge profiles at Volt-on for a poling time of 10^5 s is shown in Figure 5.13.

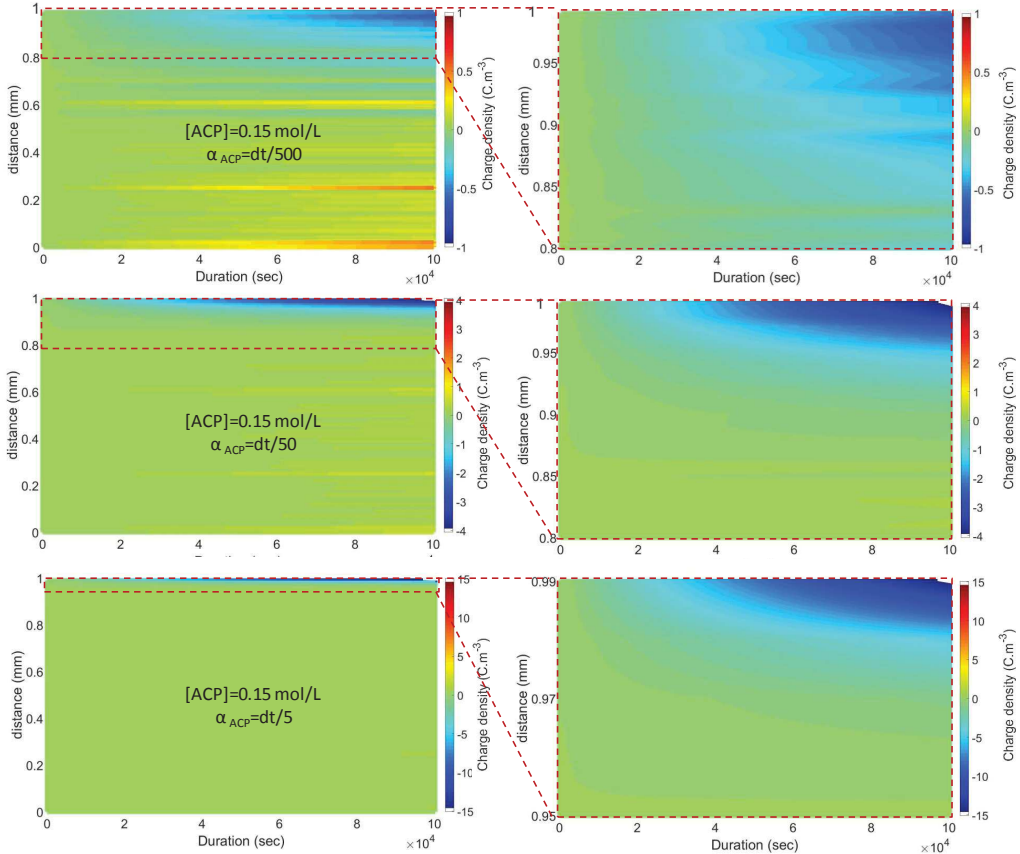


Figure 5.13: Space charge distribution as a function of time and space of XLPE with $[\text{ACP}]=0.15 \text{ mol/L}$ at various α_{ACP} values: (left) Profile in the whole sample thickness. (right) Zoom in the region of negative charge trapping near cathode.

Negative homocharge accumulation is observed near cathode and is related to deep trapping of electrons by ACP. The higher the trapping rate, the higher the density of trapped negative

charge density. With a trapping rate 100 times higher, the maximum trapped charge density is multiplied by 15 showing the high influence of α_{CA} parameter. Furthermore, when the trapping rate is increasing, negative charges are present at the vicinity of the cathode and less spread toward the bulk of the sample.

From these space charge distributions, the related electric field distribution is simulated and illustrated in Figure 5.14.

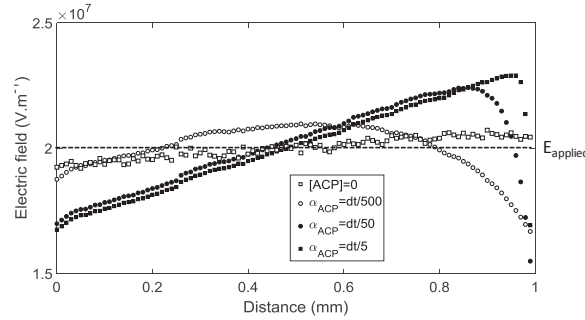


Figure 5.14: Simulation of electric field distribution of fully degassed XLPE and XLPE with $[ACP]=0.15$ mol/L with various α_{ACP} values.

Due to negative homocharge accumulation near the cathode, an electric field decrease down to 15 kV/mm is observed near this interface. For $\alpha = \delta t/50$ and $\alpha = \delta t/5$, this electric field decrease is very sharp and occurs at a distance very closed to the interface. It comes from the fact that negative heterocharges are present on a thickness lower than $100 \mu\text{m}$. In this case, electric field is higher near the cathode just before its decrease. The higher the trapping rate, the higher the electric field maximum. For $\alpha = \delta t/500$, the drop of electric field is less sharp because, with this trapping rate, negative charge density is more spread towards the middle of the dielectric. Maximum of the electric field is localized in the middle of the sample with a value much lower than with $\alpha = \delta t/50$ and $\alpha = \delta t/5$.

5.4 Comparison with experiment

5.4.1 Impact of PDP in space charge distribution of XLPE

5.4.1.1 Effect of α_{CA}

Experimental and simulated space charge distributions are compared for LDPE samples containing several concentrations of α_{CA} . In measurements performed by Le Roy *et al.*[42], LDPE samples have been soaked in α_{CA} at 70°C . Depending on the soaking time, a weight concentration up to 6% has been obtained. Space charge measurements were then performed at 25°C under increasing electric field from 10 to 25 kV/mm with 20 min polarization and 20 min depolarization between each electric field. To compare results of the model with these experiments, simulation is performed in LDPE with different α_{CA} concentrations as input parameter and the same measurement protocol. Constants given in Table 5.3 are used for the evolution laws related to α_{CA} .

First, simulated and experimental space charge distributions are compared in LDPE without α CA as shown in Figure 5.15. Positive charges are observed, coming from the anode and transported along the sample thickness with time. During depolarization, positive charges remain in the material. Positive charge density increases with increased electric field. No negative charges are detected, either because they are not present or because they are hidden by the larger positive charge amount. Simulation reproduces qualitatively this behavior with a positive charge density present within the sample, an increase of this density with electric field and no decrease during depolarization. Quantitatively, charge density amount is similar in the model and in the experiment with a maximum between 0.5 C/m^3 and 0.7 C/m^3 .

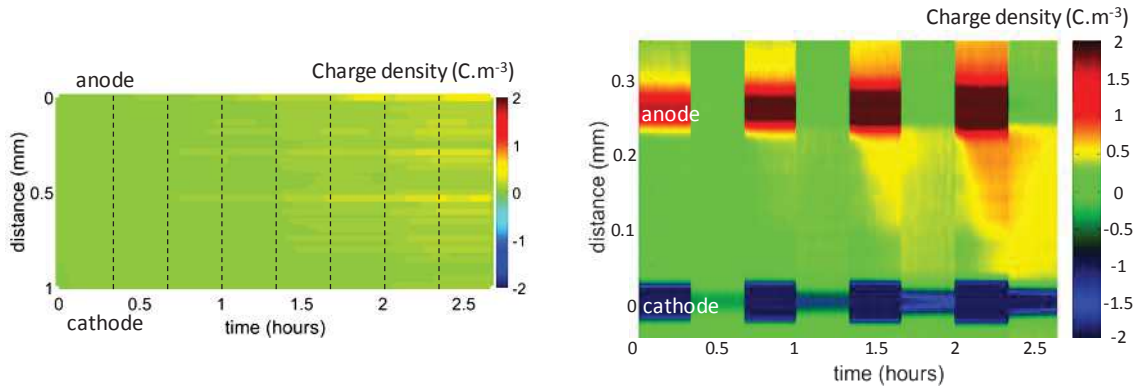


Figure 5.15: Space charge distribution as a function of time and space in LDPE without α CA for a protocol of 20 min polarization and 20 min depolarization, for electric fields of 10, 15, 20 and 25 kV/mm, at 25°C. Results obtained from simulation in the left side and from PEA measurement (adapted from [42]) in the right side.

Then, comparison between simulation and experiment is made for LDPE soaked in α CA. A concentration of 0.35 mol/L is used in the model, similar to the concentration obtained in LDPE samples soaked in α CA for 4 hours at 70°C. Same electrical protocol as for untreated LDPE is used except that the polarization and depolarization durations are 30 min.

In the experimental results represented in the right part of Figure 5.16, negative and positive heterocharges are present at the vicinity of the electrodes as soon as the voltage is applied. The density of positive charges is higher than that of negative charge and positive charge amount is increasing with electric field whereas the amount is decreasing for negative heterocharge. This decrease of negative heterocharges can be attributed to electron extraction. Under 25 kV/mm, this extraction is significant and positive homocharges, coming from the anode, are observed as well as positive heterocharges.

In the simulated results represented in the left part of Figure 5.16, space charge pattern has several similarities with experiment. Positive heterocharge is present at the vicinity of the cathode with similar density in the range of 2 C/m^3 . At 10 kV/mm and 20 kV/mm, these positive heterocharges accumulation is increasing and reach the middle of the dielectric. As in experiment, negative heterocharge are also present at a lower density and a decrease over time is observed. However several discrepancies with experiment can be noticed. Firstly, a higher electron extraction seems to occur in the experiment as positive homocharges near anode are experimentally observed but not simulated. Secondly, a slow decrease of positive heterocharges is measured experimentally during Volt-off. In simulation, even when diffusion is taken into

account, this heterocharge decrease is barely observed. Another process such as recombination, occurring during Volt-off, could simulate this positive heterocharge decrease.

Difference between experiment and simulation can also be explained if another process than ionization/dissociation is occurring. The heterocharge formation can be due to diffusion of permanent dipoles related to α CA. This non-uniform concentration of polarizable species yields to a fast heterocharge build-up at Volt-on. In addition to the inhomogeneous distribution of dipoles, an extraction of electrons may occur resulting in a decrease of negative homocharge amount and an increase of positive charge amount. At Volt-off, only space charge related to electron extraction remains and recombination may occur, thus explaining the positive charge decrease with time.

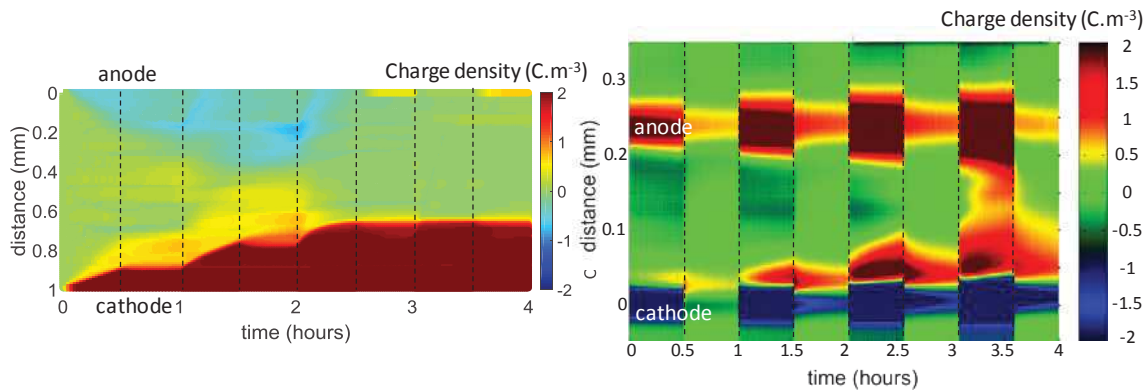


Figure 5.16: Space charge distribution as a function of time and space in LDPE with a concentration of α CA of 0.2 mol/L for a protocol of 30 min polarization and 30 min depolarization, for electric fields of 10, 15, 20 and 25 kV/mm, at 25°C obtained from simulation (left) and from PEA measurement (adapted from [42]) (right).

In order to investigate deeply the impact of the α CA concentration on space charge distribution, different concentrations of α CA in LDPE were experimentally obtained by soaking LDPE sample in α CA at 70°C for 1 h, 2 h and 4 h [42]. These materials were submitted to an electric field of 20 kV/mm at room temperature with a polarization and a depolarization time of 1 h. To compare simulation results to this experimental study, electrical properties in LDPE with three different α CA concentrations are simulated with the same electric program.

Simulated and experimental results are shown in Figure 5.17. For each α CA concentration, distribution of positive heterocharges at Volt-on is similar to the experimental one. With low concentration of α CA, a small amount of positive heterocharge is present at the vicinity of cathode during polarization. With increased concentration, more positive heterocharges are measured in the dielectric. Furthermore this heterocharge amount is increasing with polarization time.

Differences with experiment are, in the simulation, a lower electron extraction at the anode and a lower positive heterocharge decrease at Volt off. With an higher hole injection and by integrating another process such as recombination occurring during Volt-off, the observed differences could be reduced. Another possibility, is an inhomogeneous dipolar orientation related to α CA instead of its dissociation/ionization.

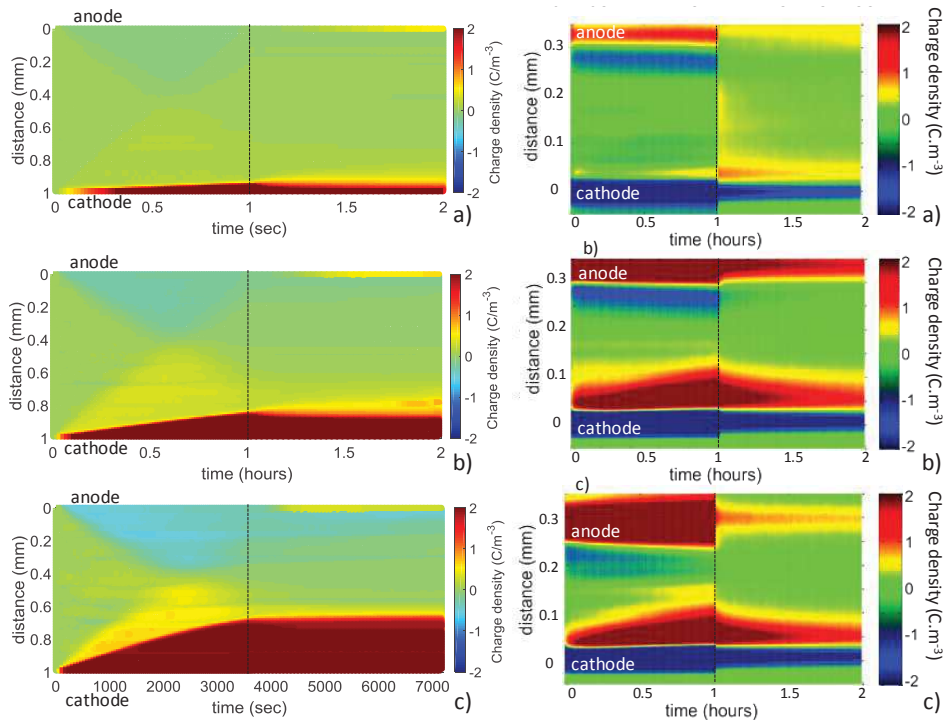


Figure 5.17: Space charge distribution as a function of time and space for a protocol of 1 h polarization and 1 h depolarization at 20 kV/mm and 25°C, for LDPE at three different concentration of α CA. Results obtained from simulation in the left side and from PEA measurement (Adapted from [42]) in the right side.

5.4.1.2 Effect of ACP

Simulation of space charge profile in XLPE in presence of ACP is confronted to experimental measurements performed by Hussin *et al.* [79]. In the work of Hussin *et al.*, space charge measurements were performed with PEA in LDPE soaked for 2 h in ACP. Samples were submitted to an electric field around 30 kV/mm at room temperature for 1 h. Power supply was turned off every 10 min to record signal at Volt-off. SC electrode and aluminum electrode were used as anode and cathode respectively. In the model, space charge are simulated in LDPE with a ACP concentration of 0.15 mol/L which corresponds to the concentration present in the sample experimentally tested and same electrical protocol is applied. Figure 5.18 shows the space charge profile in LDPE with ACP at Volt-off following polarization under 30 kV/mm for 10 min and for 60 min obtained from PEA measurement and from simulation. Similar qualitative space charge profiles in experiment and simulation are obtained with a presence of negative charges near cathode. With polarization time, this negative charge amount is increasing in the bulk of the material. Quantitatively, a high difference is observed between experiment and simulation with a much higher amount measured experimentally. However, if a density of 5 C/m³ was simulated in the model, it would mean the presence of 10⁹ electrons in each state which is physically not possible.

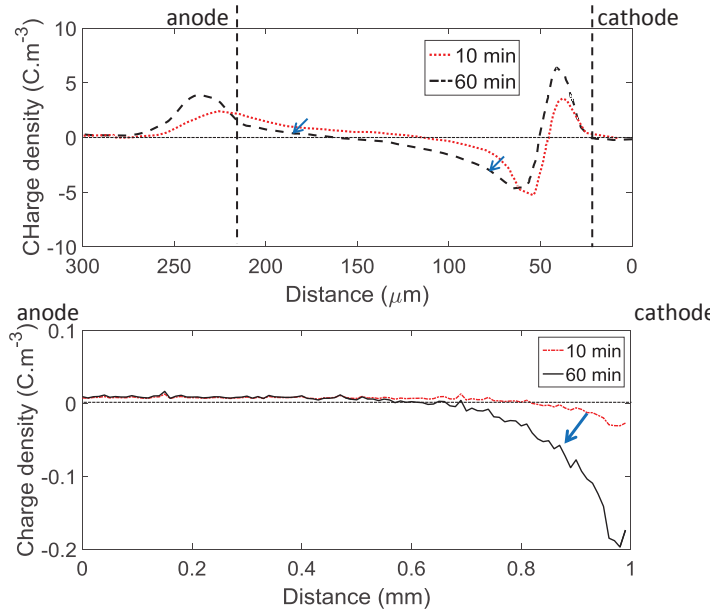


Figure 5.18: Space charge profile of LDPE with 2 ACP at 30°C at Volt-off following polarization under 30 kV/mm for 10 min and for 60 min obtained from PEA measurement (adapted from [79]) in the upper side and from simulation in the down side.

5.4.2 Impact of PDP in current density of XLPE

5.4.2.1 Degassing time

To compare the dependency of leakage current with PDP in experiment and simulation, XLPE is studied with different PDP amount. In order to experimentally obtain XLPE samples with varied PDP amounts, degassing step has been applied at room temperature. Global PDP amount has been measured from weight loss at 150°C using TGA. Samples are tested at 30, 50 and 70°C. At a given temperature, 10 kV/mm steps of increased electric field from 20 to 40 kV/mm are applied. For each electric field step, current is measured for 3 days in order to allow samples reaching a steady state. The input parameters used in the model are presented in Table 5.4.

	XLPE A	XLPE B	XLPE C	XLPE D	XLPE E	XLPE F
T_r (°C)	190					
DCP (wt%)	0	0.03	0.07	0.12	0.22	0.39

Table 5.4: Crosslinking temperature and wt% of DCP used as input parameters in simulation of XLPE.

In Figure 5.19, the current density at steady state is compared in fully degassed XLPE (without PDP) and undegassed XLPE (1.2% of PDP) as a function of temperature under an electric field of 20 kV/mm. Simulated and experimental measurements are similar in values and trends. An increase of almost one order of magnitude is measured in the presence of PDP and all tested and simulated materials follow a thermal activation law for conductivity. Between simulation and experimental measurement, a maximum difference of 3×10^{-8} A/m² is observed in fully degassed XLPE with a difference of activation energy around 0.1 eV and a maximum difference

of $2 \times 10^{-7} \text{ A/m}^2$ in undegassed XLPE is observed with a difference of activation energy around 0.2 eV.

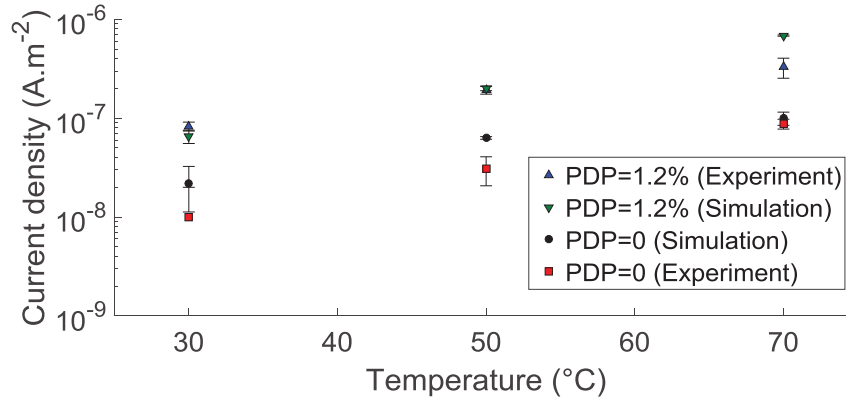


Figure 5.19: Experimental and simulated current densities at steady state *versus* temperature under an electric field of 20 kV/mm in XLPE with no PDP and with 1.2% of PDP.

In Figure 5.20, the current density at steady state is compared in fully degassed XLPE and undegassed XLPE with 1.2% of PDP as a function of electric field at 30 °C. In simulations and in experiments, similar variations are observed with a slow increase of the current density with electric field. For fully degassed XLPE, experiments give a linear slope variation of $3 \times 10^{-9} \text{ A/m}^2$ and simulations give a variation of $6 \times 10^{-9} \text{ A/m}^2$. For undegassed material, linear variations of $9 \times 10^{-9} \text{ A/m}^2$ and $2 \times 10^{-8} \text{ A/m}^2$ are respectively obtained in experiment and in simulation. Low variation can be explained by homocharge injection, screening the electric field at the interface of these materials.

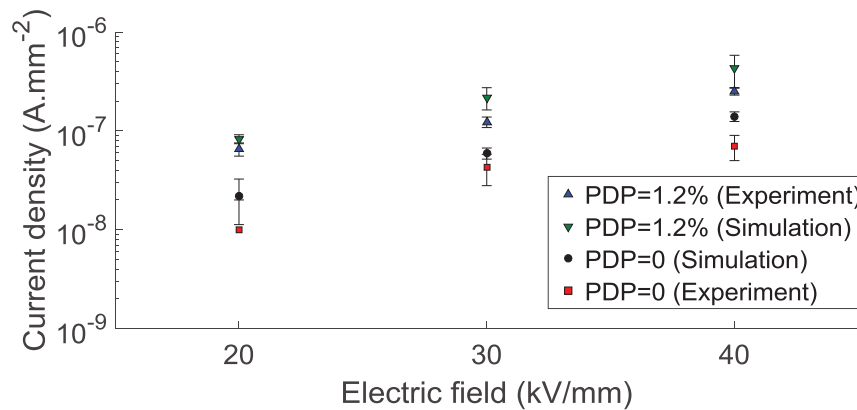


Figure 5.20: Experimental and simulated current densities at steady state *versus* electric field at a temperature of 30 °C in XLPE with no PDP and with 1.2% of PDP.

In Figure 5.21 are plotted the change in current density with increasing PDP content in XLPE under an electric field of 20 kV/mm at 30 °C, 50 °C and 70 °C. Each PDP amount corresponds to new series of samples degassed for different controlled duration before being tested. The concentration remains stable during testing.

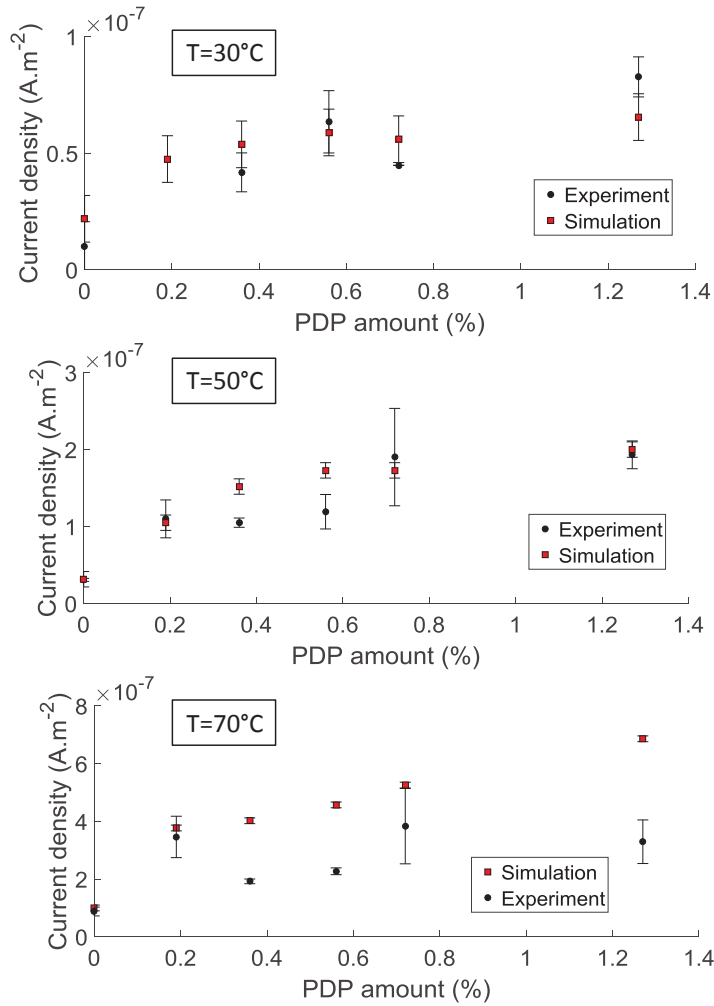


Figure 5.21: Experimental and simulated leakage current *versus* PDP amount under an electric field of 20 kV/mm at a temperature of 30°C, 50°C and 70°C.

At each temperature, current density increases with increasing PDP content. Both in simulation and experiment, a first current density increase is observed as soon as a low PDP amount is present (0.2%), showing the strong contribution of such chemicals to conduction processes in XLPE. This strong influence is simulated by considering the ionization of α CA generating cations and anions that can further migrate by electrophoresis and increase electric field at the interface. Even with low PDP concentration, created amount of ionic charges is enough to impact the electric field. Furthermore, in the model, presence of ACP increases hole injection.

At 30°C and 50°C, simulated and measured current densities are similar for each PDP amount. After a high increase between 0% and 0.2% of PDP, a low conductivity increase with PDP is measured at higher PDP amount. At a concentration higher than 0.6%, conductivity reaches a plateau. In the simulation, at concentration higher than 0.6%, the highest α CA amount that can be present at the vicinity of the electrode is reached. Indeed the solubility parameter δ between LDPE and α CA prevents the agglomeration of the ionic species. Thus at higher PDP amount, same ionic density value is present at the interface but in a thicker distance in the material.

At 70°C, a higher increase of the current density with PDP is measured in the simulation than in the experiment. Experimentally, current density seems to be far less affected by the presence

of PDP. It may be due to the increased contribution of thermally assisted conduction processes prevailing over the ionic conduction process related to the PDP.

5.4.3 Interface effect

For the interface effect, current density of XLPE is measured using brass electrodes and SC electrodes. Measurements are performed on fully degassed XLPE. Indeed, in undegassed system, chemicals from the SC may migrate within the tested dielectric and interfere in the measured values.

Experimental measurement is performed at 70°C under an electric field of 30 kV/mm for 10⁵ s. In the model, electrical properties of degassed XLPE are simulated with different injection laws according to the presence of brass or SC electrodes. Comparison of experimental and simulated current density variations over time is shown in Figure 5.22. Very similar current density variations are obtained experimentally and with the model. A high increase of the current density is measured in presence of the SC electrodes showing the strong influence of the interface on the electrical properties.

To address this interface effect in undegassed insulation system, by-products from the SC have to be taken into account in the model. These by-products can impact the electrical properties of XLPE in the same way as ACP or α CA. From a chemical characterization of these by-products and a study of their impact in polymer electrical properties, evolution laws related to these by-products from the SC could be implemented.

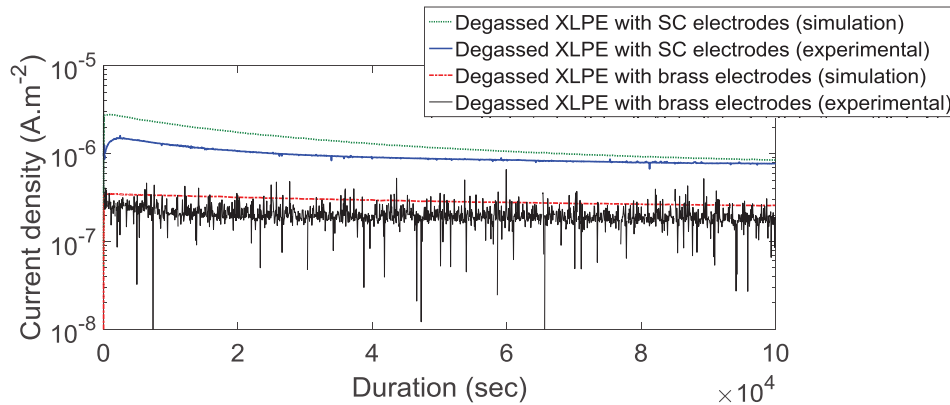


Figure 5.22: Simulated and measured current density variation with time in degassed XLPE with brass electrodes and with SC electrodes.

5.5 Summary

In this chapter, electrical property simulation of XLPE insulation system is addressed. This model describes the distribution of ACP and α CA within the polymer matrix. The impact of these PDP in XLPE electrical properties are taken into account using the developed evolution laws. This model can simulate space charge distribution of PE in presence of each of this PDP and some similar behavior as observed in the literature are obtained. Furthermore, the impact of PDP concentration in XLPE leakage current is accurately reproduced with this model. Finally developed evolution laws integrate the influence of interface in degassed XLPE electrical properties giving conclusive similar results with experiments.

Conclusion

Under DC electric field, polymeric insulation shows propensity to accumulate charges through injection or by internal generation processes. This space charge accumulation is claimed to be the main factor accelerating degradation of polymeric insulation in HVDC conditions. Electrical properties of polymers are directly related to their heterogeneous microstructure. However, none of the existing models in the literature integrates the microstructure evolution of the material with time, temperature and electric field which are the driving forces for conduction mechanisms.

In this context, this work aims at developing a new model able to simulate the modification over time of the microstructure in insulation polymers under electric field and temperature as well as the subsequent impacts on electrical properties and durability.

To develop this model, it is necessary to have a comprehensive understanding of the influence of physical and chemical heterogeneities on electrical properties of polymer. Such correlations between microstructure and electrical properties are of essential importance for the simulation of electrical properties and lifetime of polymer under temperature and electric field.

From the literature review, physical heterogeneity is related to the semi-crystalline structure of insulation polymer. This structure depends on the polymer matrix nature, processing and electrical and thermal stresses. Sources of chemical heterogeneities are chemical defects from the chemistry of PE and chemical species present in polymer which come from polymer formulation (antioxidants), crosslinking (crosslinking by-products), aging (oxidation), and conditioning (water). These heterogeneities are present at several scales and can affect strongly polymer electrical properties.

To do so, matrices are used in the model to describe each heterogeneity distribution in semi-crystalline polymer. From this microstructure distribution, matrices of electrical properties, such as space charge, local permittivity or current density values, are simulated for a given electric field and temperature. When stressed under electric field and at temperature, matrices of microstructure evolve from implemented evolution laws. This simulated microstructure evolution yields to the simulation of electrical property changes over time at transient and steady state.

The core of this model is based on solid states physics applied to insulation based on literature study. Evolution laws are developed to describe charge transport, injection, extraction and trapping processes. To take into account influence of polymer microstructure, *modules* are developed to focus on a specific chemical or physical heterogeneity present in the polymer and integrate the related physics of this heterogeneity. To find the appropriate evolution laws related to the *modules*, experimental studies have been performed in order to obtain a quantitative correlation of each kind of polymeric heterogeneity with its electrical properties.

In order to assess the impact of crystallinity and chain relaxation in polymer electrical property, PE, PP and PET are selected as material *models*. Experimental results obtained in these materials demonstrate that charge injection and transport are promoted by macromolecules mobility and by decrease of crystallinity. Then, the impact of peroxide decomposition products in electrical properties in XLPE is investigated. Experimental results highlight the strong influence of PDP in conductivity increase and show the presence of heterocharges with the presence of PDP. Finally, high increase of the measured current density in presence of semiconductive electrodes demonstrate the impact of interface on polymer electrical properties.

From these experimental results, simulation *modules* related to the semi-crystalline structure are developed. For a given set of input parameters, specific physical microstructure of several polymers such as PE, PP and PET is simulated. Developed evolution laws simulate the influence of this microstructure on current density and space charge which allow to obtain similar simulated results with experiments. Then, simulation *modules* related to XLPE in presence of PDP and semiconductive electrodes are developed. From the distribution of ACP and α CA within the matrices of the model, space charge distribution and leakage current are simulated and give similar experimental electrical behavior. Furthermore, simulated current density is adapted according to the use of semiconductive or brass electrodes.

Based on these genetic evolution laws, this modeling approach allows to simulate DC electrical behavior of polymers only from their physical and chemical characterizations as shown in Figure 5.23. Matrices of microstructure are generated from these physical and chemical characterizations. Evolution laws related to solid states physics are then adapted according to these matrices of microstructure.

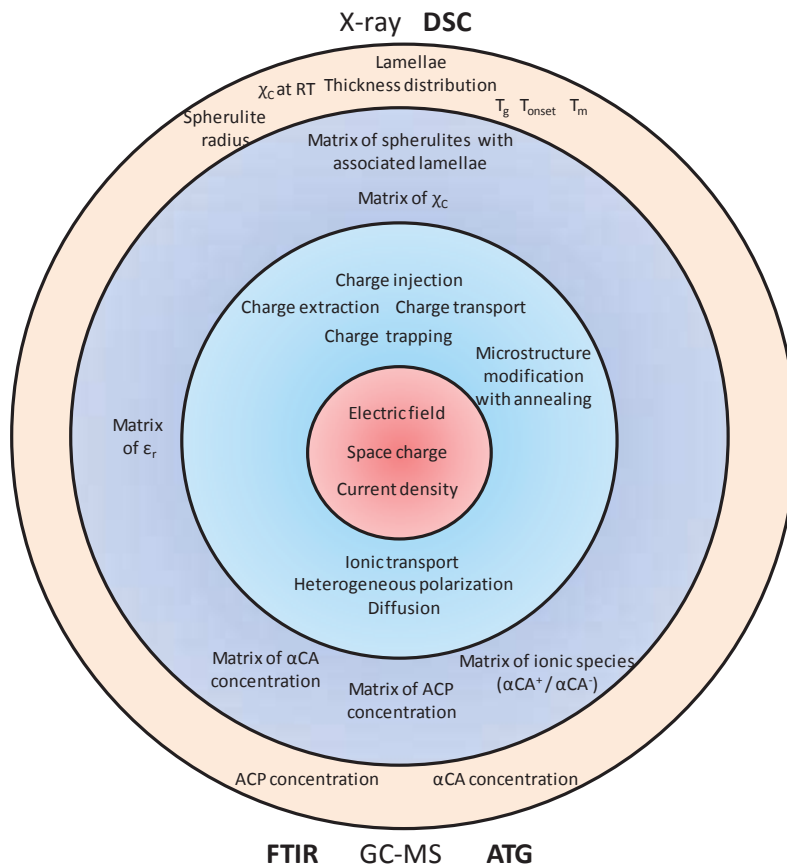


Figure 5.23: Principle of the genetic model.

Among the strengths of the developed model, it has the ability to cover the behavior of several semi-crystalline polymers and to integrate several physics such as diffusion, ionic transport, electronic transport. Thus, contrary to other models, the genetic model is not restricted to a single polymer simulation with a single physical process. Furthermore, this model is very adaptive and can integrate additional heterogeneity present at different scale without changing its structure. Moreover, the use of evolution laws allow this model to adapt its simulation to ageing processes. Concerning simulation efficiency, with the use of simple laws to make evolve the system, a faster solving time compared to other simulation method is obtained.

The perspective of this model will consist of adding other *modules* related to other heterogeneities and physical behaviors present in polymer. Among them, there is the presence of antioxidant that can act as deep trap for charge and the diffusion of additional by-products from the undegassed semiconductive electrode to the insulation. Dipolar orientation, due to the polymeric matrix or from chemical residues, is another process that could be taken into account. Furthermore ageing effect can also be addressed by this model with, for instance, the modification of the semicrystalline structure with high electric field, polymer melting by joule effect or impact of voids on electrical properties. Finally, interface effect can be deeper investigated by addressing the effect of other metal electrodes.

Bibliography

- [1] C. Duke, *Tunneling in solids*. Academic press, 1969.
- [2] D. Lamb, *Electrical conduction mechanisms in thin insulating films*. Methuen, 1967.
- [3] “Economic and environmental advantages.” <http://new.abb.com/systems/hvdc/why-hvdc/economic-and-environmental-advantages>. Accessed: 2017-12-13.
- [4] M. Ieda, “Electrical Conduction and Carrier Traps in Polymeric Materials,” *IEEE Transactions on Electrical Insulation*, vol. EI-19, no. 3, pp. 162–178, 1984.
- [5] A. Rose, “Space-Charge-Limited Currents in Solids,” *Physical Review*, vol. 97, no. 6, pp. 1538–1544, 1955.
- [6] P. Fischer and P. Röhl, “Thermally stimulated and isothermal depolarization currents in low-density polyethylene,” *Journal of Polymer Science: Polymer Physics Edition*, vol. 14, no. 3, pp. 531–542, 1976.
- [7] R. T. Tung, “The physics and chemistry of the Schottky barrier height,” *Applied Physics Reviews*, vol. 1, no. 1, p. 011304, 2014.
- [8] K. Kircher, *Chemical reactions in plastics processing*. Oxford University Press, 1988.
- [9] G. Marzinotto, M. Mazzanti, “Main Principles of HVDC Extruded Cable Design,” in *Extruded Cables For High-Voltage Direct-Current Transmission*, pp. 41–98, John Wiley & Sons, Inc., 2013.
- [10] L. Dissado, G. Mazzanti, and G. Montanari, “The role of trapped space charges in the electrical aging of insulating materials,” *IEEE Transactions on Dielectrics and Electrical Insulation*, vol. 4, no. 5, pp. 496–506, 1997.
- [11] J.-M. André and G. Leroy, “All-electrons band structure of polyethylene in the nearest cell approximation,” *Chemical Physics Letters*, vol. 5, no. 2, pp. 71–74, 1970.
- [12] J. Jones, J. Llewellyn, and T. Lewis, “The contribution of Field-induced morphological change to the electrical aging and breakdown of polyethylene,” *IEEE Transactions on Dielectrics and Electrical Insulation*, vol. 12, no. 5, pp. 951–966, 2005.
- [13] D. Foata and A. Fuchs, *Processus stochastiques : Processus de Poisson, chaînes de Markov et martingales : Cours et exercices corrigés*. Dunod, 2006.
- [14] W. Thue, ed., *Electrical Power Cable Engineering*. CRC Press, 1998.

- [15] S. Kirkpatrick, "Percolation and Conduction," *Reviews of Modern Physics*, vol. 45, no. 4, pp. 574–588, 1973.
- [16] F. Lux, "Models proposed to explain the electrical conductivity of mixtures made of conductive and insulating materials," *Journal of Materials Science*, vol. 28, no. 2, pp. 285–301, 1993.
- [17] L. Flandin, T. Prasse, R. Schueler, K. Schulte, W. Bauhofer, and J.-Y. Cavaille, "Anomalous percolation transition in carbon-black-epoxy composite materials," *Physical Review B*, vol. 59, no. 22, pp. 14349–14355, 1999.
- [18] M. Jeroense, M. Saltzer, and H. Ghorbani, "Technical challenges linked to HVDC cable development," *REE. Revue de l'électricité et de l'électronique*, no. 4, 2014.
- [19] "Interconnexion électrique france-espagne par le golfe de gascogne." https://www.inelfe.eu/sites/default/files/2017-09/RTE_V2_pp.pdf. Accessed: 2017-12-15.
- [20] L. Zehong, G. Liying, W. Zuli, Y. Jun, Z. Jin, and L. Licheng, "R&D progress of ± 1100 kV UHVDC technology," *B4-201-2012, CIGRE Session*, 2012.
- [21] B. Sanden, J. Matallana, J. Parpal, A. Macphail, D. Wald, T. Kvarts, L. Benard, E. Zacccone, S. Hirano, J. Kim, *et al.*, "Recommendations for testing dc extruded cable systems for power transmission at a rated voltage up to 500 kv," in *CIGRE Colloquium on HVDC and Power Electronic Systems*, 2012.
- [22] J. A. Anta, G. Marcelli, M. Meunier, and N. Quirke, "Models of electron trapping and transport in polyethylene: Current voltage characteristics," *Journal of Applied Physics*, vol. 92, no. 2, pp. 1002–1008, 2002.
- [23] F. Boufayed, G. Teyssède, C. Laurent, S. Le Roy, L. A. Dissado, P. Ségur, and G. C. Montanari, "Models of bipolar charge transport in polyethylene," *Journal of Applied Physics*, vol. 100, no. 10, p. 104105, 2006.
- [24] L. Dissado and J. Fothergill, *Electrical degradation and breakdown in polymers*. IET, 1992.
- [25] T. Lewis, "Polyethylene under electrical stress," *IEEE Transactions on Dielectrics and Electrical Insulation*, vol. 9, no. 5, pp. 717–729, 2002.
- [26] S. Hole, T. Ditchi, and J. Lewiner, "Non-destructive methods for space charge distribution measurements: what are the differences?," *IEEE Transactions on Dielectrics and Electrical Insulation*, vol. 10, no. 4, pp. 670–677, 2003.
- [27] Ying Li, M. Yasuda, and T. Takada, "Pulsed electroacoustic method for measurement of charge accumulation in solid dielectrics," *IEEE Transactions on Dielectrics and Electrical Insulation*, vol. 1, no. 2, pp. 188–195, 1994.
- [28] P. Notingham, S. Agnel, and A. Toureille, "Thermal step method for space charge measurements under applied dc field," *IEEE Transactions on Dielectrics and Electrical Insulation*, vol. 8, no. 6, pp. 985–994, 2001.

- [29] T. Mizutani, "Space charge measurement techniques and space charge in polyethylene," *IEEE Transactions on Dielectrics and Electrical Insulation*, vol. 1, no. 5, pp. 923–933, 1994.
- [30] B. Qiao, G. Teyssedre, C. Laurent, and N. Shimizu, "The significance of electroluminescence in polyolefins," in *2016 IEEE International Conference on Dielectrics (ICD)*, 2016.
- [31] M. Goshwami, I. Endoh, K. Noguchi, U. Kawabe, and Y. Sekii, "Influence of antioxidants on electrical conduction in LDPE and XLPE," *Journal of Electrostatics*, vol. 65, no. 9, pp. 551–554, 2007.
- [32] Standard and A. D257-07, "Standard Test Methods for DC Resistance or Conductance of Insulating Materials," vol. i, no. C, pp. 1–18, 2007.
- [33] L. W. Meng and J. Pang, "The dangers of DC High Voltage test for XLPE cables at site," in *The Singapore Engineer*, pp. 18–20, 2011.
- [34] H. Ghorbani, T. Christen, and H. Edin, "Role of thermal and electrical relaxations for the long-term conduction current in polyethylene," in *2016 IEEE International Conference on Dielectrics (ICD)*, pp. 1106–1109, 2016.
- [35] N. Ahmed and N. Srinivas, "Review of space charge measurements in dielectrics," *IEEE Transactions on Dielectrics and Electrical Insulation*, vol. 4, no. 5, pp. 644–656, 1997.
- [36] T. Takada, "Acoustic and optical methods for measuring electric charge distributions in dielectrics," in *1999 Annual Report Conference on Electrical Insulation and Dielectric Phenomena*, pp. 1–14, IEEE, 1999.
- [37] M. Marzinotto and G. Mazzanti, "A procedure for space charge measurements in full-size HVDC extruded cables in order to access the electric field in the insulation wall," in *CIGRE Session*, pp. 1–6, CIGRE, 2012.
- [38] T. Takada, T. Maeno, and H. Kushibe, "An Electric Stress-Pulse Technique for The Measurement of Charges in A Plastic Plate Irradiated by an Electron Beam," *IEEE Transactions on Electrical Insulation*, vol. EI-22, no. 4, pp. 497–501, 1987.
- [39] O. Gallot-Lavallée, V. Griseri, G. Teyssedre, and C. Laurent, "The pulsed electro-acoustic technique in research on dielectrics for electrical engineering. Today's achievements and perspectives for the future," *Revue internationale de génie électrique*, vol. 8, no. 5-6, pp. 749–772, 2005.
- [40] S. Holé, "Resolution of direct space charge distribution measurement methods," *IEEE Transactions on Dielectrics and Electrical Insulation*, vol. 15, no. 3, pp. 861–871, 2008.
- [41] S. Holé, V. Griseri, L. a. Dissado, and J. C. Fothergill, "Improvement of PEA signal analysis using simulations for complex geometry samples," *Journal of Physics D: Applied Physics*, vol. 35, no. 1, pp. 19–24, 2002.
- [42] S. Le Roy and G. Teyssedre, "Ion generation and transport in low density polyethylene under electric stress," in *2015 IEEE Conference on Electrical Insulation and Dielectric Phenomena (CEIDP)*, pp. 63–66, IEEE, 2015.

- [43] P. Fischer, "Electrical conduction in polyolefins," *Journal of Electrostatics*, vol. 4, no. 2, pp. 149–173, 1978.
- [44] T. Mizutani, H. Semi, and K. Kaneko, "Space charge behavior in low-density polyethylene," *IEEE Transactions on Dielectrics and Electrical Insulation*, vol. 7, no. 4, pp. 503–508, 2000.
- [45] L. Dissado, C. Laurent, G. Montanari, and P. Morshuis, "Demonstrating a threshold for trapped space charge accumulation in solid dielectrics under dc field," *IEEE Transactions on Dielectrics and Electrical Insulation*, vol. 12, no. 3, pp. 612–620, 2005.
- [46] G. Montanari, I. Ghinello, F. Peruzzotti, and M. Albertini, "Behavior of voltage-current characteristics and threshold indications for XLPE-based materials," in *1998 Annual Report Conference on Electrical Insulation and Dielectric Phenomena*, pp. 128–131, IEEE, 1998.
- [47] M. Taleb, G. Teyssedre, and S. Le Roy, "Role of the interface on charge build-up in a low-density polyethylene: Surface roughness and nature of the electrode," in *2009 IEEE Conference on Electrical Insulation and Dielectric Phenomena*, pp. 112–115, IEEE, 2009.
- [48] Y. Chong, G. Chen, and Y. Ho, "Temperature effect on space charge dynamics in XLPE insulation," *IEEE Transactions on Dielectrics and Electrical Insulation*, vol. 14, no. 1, pp. 65–76, 2007.
- [49] S. Das and N. Gupta, "Space charge accumulation in epoxy resin and polyethylene," in *2012 IEEE 10th International Conference on the Properties and Applications of Dielectric Materials*, pp. 1–4, IEEE, 2012.
- [50] C. Kittel, *Physique de l'Etat solide*. Dunod, 1983.
- [51] N. Mott and R. Gurney, *Electronic processes in ionic crystals*. Clarendon Press, 1940.
- [52] M. Lampert and P. Mark, *Current injection in solids*. Academic press, 1970.
- [53] R. Bodega, G. Montanari, and P. Morshuis, "Conduction current measurements on XLPE and EPR insulation," in *2004 IEEE Annual Report Conference on Electrical Insulation and Dielectric Phenomena (CEIDP)*, pp. 101–105, IEEE, 2004.
- [54] G. C. Montanari, G. Mazzanti, F. Palmieri, A. Motori, G. Perego, and S. Serra, "Space-charge trapping and conduction in LDPE, HDPE and XLPE," *Journal of Physics D: Applied Physics*, vol. 34, no. 18, pp. 2902–2911, 2001.
- [55] N. Mott and E. Davis, *Electronic Processes in Non-Crystalline Materials*. OUP Oxford, 2012.
- [56] R. Fowler and L. Nordheim, "Electron Emission in Intense Electric Fields," *Proceedings of the Royal Society of London*, vol. 119, no. 781, pp. 173–181, 1928.
- [57] D. M. Taylor and T. J. Lewis, "Electrical conduction in polyethylene terephthalate and polyethylene films," *Journal of Physics D: Applied Physics*, vol. 4, no. 9, p. 315, 1971.

- [58] T. Mizutani, "Behavior of charge carriers near metal/polymer interface," in *2005 IEEE Proceedings of 2005 International Symposium on Electrical Insulating Materials (ISEIM)*, pp. 1–6, IEEE, 2005.
- [59] M. Taleb, G. Teyssedre, S. Le Roy, and C. Laurent, "Modeling of charge injection and extraction in a metal/polymer interface through an exponential distribution of surface states," *IEEE Transactions on Dielectrics and Electrical Insulation*, vol. 20, no. 1, pp. 311–320, 2013.
- [60] J. Viertel, L. Petersson, A. Friberg, G. Dominguez, and C. Tornkvist, "Electrode influence on DC conductivity measurements of low density poly ethylene," in *2013 IEEE International Conference on Solid Dielectrics (ICSD)*, pp. 1048–1051, IEEE, 2013.
- [61] G. Chen, T. Tay, A. Davies, Y. Tanaka, and T. Takada, "Electrodes and charge injection in low-density polyethylene using the pulsed electroacoustic technique," *IEEE Transactions on Dielectrics and Electrical Insulation*, vol. 8, no. 6, pp. 867–873, 2001.
- [62] M. Hao, A. Fazal, A. S. Vaughan, G. Chen, J. Cao, and H. Wang, "The effect of electrode material and semicon bonding on space charge dynamics of XLPE," in *2016 IEEE International Conference on Dielectrics (ICD)*, pp. 200–203, IEEE, 2016.
- [63] C. Xiao, Y. Zhang, F. Zheng, W. Wei, H. Xuan, and Z. An, "Space charge injection in LLDPE from electrode influenced by the interface state of material," in *2009 IEEE 9th International Conference on the Properties and Applications of Dielectric Materials (ICPADM)*, pp. 899–902, IEEE, 2009.
- [64] C. Laurent, F. Massines, and C. Mayoux, "Optical emission due to space charge effects in electrically stressed polymers," *IEEE Transactions on Dielectrics and Electrical Insulation*, vol. 4, no. 5, pp. 585–603, 1997.
- [65] G. Blaise, "Space charge physics and the breakdown process," *Journal of Applied Physics*, vol. 77, no. 7, pp. 2916–2927, 1995.
- [66] G. Blaise and W. Sarjeant, "Space charge in dielectrics. Energy storage and transfer dynamics from atomistic to macroscopic scale," *IEEE Transactions on Dielectrics and Electrical Insulation*, vol. 5, no. 5, pp. 779–808, 1998.
- [67] P. Conner, J. Jones, J. Llewellyn, and T. Lewis, "A mechanical origin for electrical ageing and breakdown in polymeric insulation," in *1998 IEEE 6th International Conference on Conduction and Breakdown in Solid Dielectrics (ICSD)*, pp. 434–438, IEEE, 1998.
- [68] L. C. E. Struik, *Physical aging in amorphous polymers and other materials*. Citeseer, 1977.
- [69] C. Reddy and T. Ramu, "On the intrinsic thermal stability in HVDC cables," *IEEE Transactions on Dielectrics and Electrical Insulation*, vol. 14, no. 6, pp. 1509–1515, 2007.
- [70] G. Montanari and L. Simoni, "Aging phenomenology and modeling," *IEEE Transactions on Electrical Insulation*, vol. 28, no. 5, pp. 755–776, 1993.

- [71] H. A. Alghamdi, G. Chen, and A. S. Vaughan, "Comparison of two schools of polymeric ageing models: Causes and effects of space charge," in *2012 Annual Report Conference on Electrical Insulation and Dielectric Phenomena (CEIDP)*, pp. 827–830, IEEE, 2012.
- [72] L. Dissado, G. Mazzanti, and G. Montanari, "The incorporation of space charge degradation in the life model for electrical insulating materials," *IEEE Transactions on Dielectrics and Electrical Insulation*, vol. 2, no. 6, pp. 1147–1158, 1995.
- [73] J. Crine, J. Parpal, and G. Lessard, "A model of aging of dielectric extruded cables," in *1989 IEEE Proceedings of the 3rd International Conference on Conduction and Breakdown in Solid Dielectrics*, pp. 347–351, IEEE, 1989.
- [74] D. Kececioglu and J. A. Jacks, "The Arrhenius, Eyring, inverse power law and combination models in accelerated life testing," *Reliability Engineering*, vol. 8, no. 1, pp. 1–9, 1984.
- [75] L. Simoni, "A General Approach to the Endurance of Electrical Insulation under Temperature and Voltage," *IEEE Transactions on Electrical Insulation*, vol. EI-16, no. 4, pp. 277–289, 1981.
- [76] D. H. Kim and S. C. Kim, "Dicumyl Peroxide-Initiated Crosslinking Reaction of Low Density Polyethylene," *Polymer Society of Korea*, vol. 8, pp. 44–52, 1984.
- [77] A. Smedberg, J. O. Boström, D. Wald, and R. Peters, "Comparison of Different Analytical Test Methods to Monitor Crosslinking By-Products in XLPE Insulated Cables," in *2007 IEEE 7th International Conference on Insulated Power Cables (Jicable)*, p. 6, IEEE, 2007.
- [78] Xu Zhang, F. Zhou, Zhimin Yan, Mengjia Liu, Huan Li, and J. Li, "Effect of dicumyl peroxide on space charge accumulation characteristics of cross-linked polyethylene," in *2016 IEEE International Conference on Dielectrics (ICD)*, pp. 196–199, IEEE, 2016.
- [79] N. Hussin and G. Chen, "Space charge accumulation and conductivity of crosslinking byproducts soaked LDPE," in *2010 IEEE Annual Report Conference on Electrical Insulation and Dielectric Phenomena (CEIDP)*, pp. 1–4, IEEE, 2010.
- [80] W. Banks, M. Gordon, R.-J. Roe, and A. Sharples, "The crystallization of polyethylene I," *Polymer*, vol. 4, pp. 61–74, 1963.
- [81] P. Combette and I. Ernoult, *Physique des polymères. Tome I, Structure, Fabrication et emploi*. Hermann, 2000.
- [82] S. Serra, E. Tosatti, S. Iarlori, S. Scandolo, G. Santoro, and M. Albertini, "Interchain states and the negative electron affinity of polyethylene," in *1998 IEEE Annual Report Conference on Electrical Insulation and Dielectric Phenomena (CEIDP)*, pp. 19–22, IEEE, 1998.
- [83] T. J. Lewis and J. P. Llewellyn, "Electrical conduction in polyethylene: The role of positive charge and the formation of positive packets," *Journal of Applied Physics*, vol. 113, no. 22, p. 223705, 2013.
- [84] G. Teyssedre, *Caractérisation des polymères par analyse thermique*. Techniques de l'ingénieur, 1997.

- [85] B. Wunderlich, "Thermodynamics and kinetics of crystallization of flexible molecules," *Journal of Polymer Science: Polymer Physics Edition*, vol. 46, no. 24, pp. 2647–2659, 2008.
- [86] K. Illers and H. Hendus, "Melting Point and Crystal Size in Polyethylenes Crystallized from Melts and Solution," *Makromolekulare chemie-macromolecular chemistry and physics*, vol. 113, no. APR, p. 1, 1968.
- [87] A. M. Cunha and S. Fakirov, *Structure development during polymer processing*. Springer Netherlands, 2000.
- [88] A. Sharples, "The formation of nuclei in crystallizing polymers," *Polymer*, vol. 3, no. 110, pp. 250–252, 1962.
- [89] W. Banks, M. Gordon, R.-J. Roe, and A. Sharples, "The crystallization of polyethylene I," *Polymer*, vol. 4, no. 5, pp. 61–74, 1963.
- [90] M. Avrami, "Kinetics of Phase Change. I General Theory," *The Journal of Chemical Physics*, vol. 7, no. 12, pp. 1103–1112, 1939.
- [91] H. D. Keith, F. J. Padden, and R. G. Vadimsky, "Intercrystalline Links in Polyethylene Crystallized from the Melt," *Journal of Polymer Science Part B: Polymer Physics*, vol. 4, no. 2, pp. 267–281, 1966.
- [92] N. Hannay, *Treatise on Solid State Chemistry: Volume 3 Crystalline and Noncrystalline Solids*. Springer Science & Business Media, 2012.
- [93] H. Zhao, F. Zheng, and Y. Zhang, "Packet-like Space Charge Dynamics in Polyethylene with Various Crystallinity," in *2009 IEEE Proceedings of the 9th International Conference on Properties and Applications of Dielectric Materials (ICPADM)*, pp. 879–882, IEEE, 2009.
- [94] Y. Zhou, W. Yunshan, M. Zahn, W. Ninghua, S. Qinghua, L. Xidong, and G. Zhichen, "Morphology Effects on Space Charge Characteristics of Low Density Polyethylene," *Japanese Journal of Applied Physics*, vol. 50, no. 1R, p. 017101, 2011.
- [95] R. H. Boyd, "Relaxation processes in crystalline polymers: experimental behaviour- a review," *Polymer*, vol. 26, no. 3, pp. 323–347, 1985.
- [96] J. Muccigrosso and P. Phillips, "The Morphology of Cross-Linked Polyethylene Insulation," *IEEE Transactions on Electrical Insulation*, vol. EI-13, no. 3, pp. 172–178, 1978.
- [97] A. Ajji and M. M. Dumoulin, "Biaxially oriented polypropylene (BOPP) processes," in *Polypropylene*, pp. 60–67, Springer, 1999.
- [98] M. Mackey, L. Flandin, A. Hiltner, and E. Baer, "Confined crystallization of PVDF and a PVDF-TFE copolymer in nanolayered films," *Journal of Polymer Science Part B: Polymer Physics*, vol. 49, no. 24, pp. 1750–1761, 2011.
- [99] L. Boudou, *Influence des paramètres de mise en oeuvre sur la morphologie et la conductivité électrique d'un polyethylene destiné à la fabrication des cables*. PhD thesis, Université Paul Sabatier-Toulouse 3, 2001.

- [100] O. L. Hestad, F. Mauseth, and R. H. Kyte, "Electrical conductivity of medium voltage XLPE insulated cables," in *2012 IEEE International Symposium on Electrical Insulation (ISEI)*, pp. 376–380, IEEE, 2012.
- [101] T. G. Aakre, O. L. Hestad, J. Holto, and S. Hvidsten, "The effect of temperature cycling on mechanical and electrical properties of syndiotactic polypropylene," in *2016 IEEE International Conference on Dielectrics (ICD)*, pp. 1093–1096, IEEE, 2016.
- [102] R. H. Boyd, "Strengths of the Mechanical alpha-, Beta-, and Gamma-Relaxation Processes in Linear Polyethylene," *Macromolecules*, vol. 17, no. 4, pp. 903–911, 1984.
- [103] Y. P. Khanna, E. A. Turi, T. J. Taylor, V. V. Vickroy, and R. F. Abbott, "Dynamic mechanical relaxations in polyethylene," *Macromolecules*, vol. 18, no. 6, pp. 1302–1309, 1985.
- [104] B. Wunderlich, "Motion in Polyethylene. III. The Amorphous Polymer," *The Journal of Chemical Physics*, vol. 37, no. 10, p. 2429, 1962.
- [105] R. H. Boyd, "Relaxation processes in crystalline polymers: molecular interpretation - a review," *Polymer*, vol. 26, no. 8, pp. 1123–1133, 1985.
- [106] P. R. Mamy, J. Martinez-Vega, J. C. Dupre, and N. Bretagne, "Quantification of mechanical deformations induced by an electric field in a semicrystalline organic insulator," *Journal of Applied Polymer Science*, vol. 93, no. 5, pp. 2313–2321, 2004.
- [107] Y. M. Shkel and D. J. Klingenberg, "Electrostriction of polarizable materials : Comparison of models with experimental data," *Journal of Applied Physics*, vol. 83, no. 12, pp. 415–424, 1998.
- [108] I. Diaconu and D. Dorohoi, "Properties of polyurethane thin films," *Journal of Optoelectronics and Advanced Materials*, vol. 7, no. 2, pp. 921–924, 2005.
- [109] Q. M. Zhang, J. Su, C. H. Kim, R. Ting, and R. Capps, "An experimental investigation of electromechanical responses in a polyurethane elastomer," *Journal of Applied Physics*, vol. 81, no. 6, p. 2770, 1997.
- [110] T. Demin, Y. Yi, W. Xuan, and F. Yong, "Space charge distribution, TSC and TSL spectra in polyethylene aged by electrical stress," in *2000 IEEE Proceedings of the 6th International Conference on Properties and Applications of Dielectric Materials*, pp. 46–50, IEEE, 2000.
- [111] R. Hoffmann, C. Janiak, and C. Kollmar, "A chemical approach to the orbitals of organic polymers," *Macromolecules*, vol. 24, no. 13, pp. 3725–3746, 1991.
- [112] S. Serra, E. Tosatti, S. Iarlori, S. Scandolo, and G. Santoro, "Interchain electron states in polyethylene," *Physical Review B*, vol. 62, no. 7, pp. 4389–4393, 2000.
- [113] M. Sato, A. Kumada, K. Hidaka, T. Hirano, and F. Sato, "Determination of hole mobility in polyethylene: First principle calculation based on Marcus theory," in *2015 IEEE Conference on Electrical Insulation and Dielectric Phenomena (CEIDP)*, pp. 10–13, IEEE, 2015.

- [114] T. Tanaka, "Optical absorption and electrical conduction in polyethylene," *Journal of Applied Physics*, vol. 44, no. 5, pp. 2430–2432, 1973.
- [115] D. K. Davies, "Carrier transport in polythene," *Journal of Physics D: Applied Physics*, vol. 5, no. 1, p. 322, 1972.
- [116] M. Meunier and N. Quirke, "Molecular modeling of electron trapping in polymer insulators," *The Journal of Chemical Physics*, vol. 113, no. 1, p. 369, 2000.
- [117] G. Teyssedre and C. Laurent, "Charge transport modeling in insulating polymers: From molecular to macroscopic scale," *IEEE Transactions on Dielectrics and Electrical Insulation*, vol. 12, no. 5, pp. 857–874, 2005.
- [118] S. Serra, S. Iarlori, E. Tosatti, S. Scandolo, M. C. Righi, and G. E. Santoro, "Self-trapping vs. non-trapping of electrons and holes in organic insulators: Polyethylene," *Chemical Physics Letters*, vol. 360, no. 5-6, pp. 487–493, 2002.
- [119] D. Cubero, N. Quirke, and D. F. Coker, "Electronic states for excess electrons in polyethylene compared to long-chain alkanes," *Chemical Physics Letters*, vol. 370, no. 1-2, pp. 21–25, 2003.
- [120] S. Le Roy, G. Teyssède, and C. Laurent, "Modelling space charge in a cable geometry," *IEEE Transactions on Dielectrics and Electrical Insulation*, vol. 23, no. 4, pp. 2361–2367, 2016.
- [121] S. Le Roy, *Modélisation numérique des phénomènes de transport électrique dans un isolant polyéthylène sous contrainte électrique*. PhD thesis, Université Paul Sabatier-Toulouse 3, 2004.
- [122] S. Le Roy, G. Teyssedre, and C. Laurent, "Numerical methods in the simulation of charge transport in solid dielectrics," *IEEE Transactions on Dielectrics and Electrical Insulation*, vol. 13, no. 2, pp. 239–246, 2006.
- [123] J. P. Runt and J. J. Fitzgerald, *Dielectric Spectroscopy of Polymeric Materials*. American Chemical Society, 1997.
- [124] Y. Ping, "Influence of crystallinity on DC conduction in polyethylene," in *1998 IEEE Proceedings of 1998 International Symposium on Electrical Insulating Materials (ISEIM)*, pp. 191–194, IEEE, 1998.
- [125] S. Kolesov, "The Influence of Morphology on the Electric Strength of Polymer Insulation," *IEEE Transactions on Electrical Insulation*, vol. EI-15, no. 5, pp. 382–388, 1980.
- [126] Y. Sekii, "Influence of antioxidants and crosslinking on the crystallinity of XLPE dielectrics," in *2007 IEEE Conference on Electrical Insulation and Dielectric Phenomena (CEIDP)*, pp. 719–722, IEEE, 2007.
- [127] U. U. H. Nilsson, R. C. R. Dammert, A. Campus, A. Sneck, and Jakosuo-Jansson, "Morphology of polyethylene for power cable insulation: effects of antioxidant and crosslinking," in *1998 IEEE Proceedings of the 6th International Conference on Conduction and Breakdown in Solid Dielectrics (ICSD)*, pp. 365–367, IEEE, 1998.

- [128] G. Montanari, C. Laurent, G. Teysse, A. Campus, and U. Nilsson, "From LDPE to XLPE: investigating the change of electrical properties. Part I. space charge, conduction and lifetime," *IEEE Transactions on Dielectrics and Electrical Insulation*, vol. 12, no. 3, pp. 438–446, 2005.
- [129] L. Boudou, J. Guastavino, N. Zouzou, and J. M. Vega, "Conductivity of polyethylene - role of antioxidant and crosslinking by-products," in *2001 IEEE Proceedings of the 7th International Conference on Solid Dielectrics (ICSD)*, pp. 245–247, IEEE, 2001.
- [130] E. Nakane, K. Kaneko, T. Mizutani, H. Takino, and M. Ishioka, "Comparison of Space Charge behavior between Polypropylene and Polyethylene," in *2005 IEEE Proceedings of 2005 International Symposium on Electrical Insulating Materials (ISEIM)*, pp. 42–45, IEEE, 2000.
- [131] X. Li, Q. Du, J. Kang, and D. Tu, "Influence of microstructure on space charges of polypropylene," *Journal of Polymer Science, Part B: Polymer Physics*, vol. 40, no. 4, pp. 365–374, 2002.
- [132] Borealis, "Borlink™ Supercure based high voltage cable insulation." <https://www.distrupol.com/Borealis-compounds-for-high-voltage-cables.pdf>, 2013. Accessed: 2017-02-07.
- [133] A. Huzayyin, S. Boggs, and R. Ramprasad, "An overview of impurity states and the basis for hole mobility in polyethylene," *IEEE Electrical Insulation Magazine*, vol. 28, no. 6, pp. 23–29, 2012.
- [134] M. Meunier, N. Quirke, and A. Aslanides, "Molecular modeling of electron traps in polymer insulators: Chemical defects and impurities," *The Journal of Chemical Physics*, vol. 115, no. 6, p. 2876, 2001.
- [135] G. Teysse, C. Laurent, A. Aslanides, N. Quirke, L. Dissado, G. Montanari, A. Campus, and L. Martinotto, "Deep trapping centers in crosslinked polyethylene investigated by molecular modeling and luminescence techniques," *IEEE Transactions on Dielectrics and Electrical Insulation*, vol. 8, no. 5, pp. 744–752, 2001.
- [136] A. Smedberg and D. Wald, "Determination of diffusion constants for peroxide byproducts formed during the crosslinking of polyethylene," pp. 586–590, IEEE, 2008.
- [137] M. Nagao, I. Konba, T. Tsurimoto, Y. Mizuno, and M. Kosaki, "Effect of acetophenone on carrier injection into polyethylene," in *1992 IEEE Conference on Electrical Insulation and Dielectric Phenomena (CEIDP)*, pp. 148–153, IEEE, 1992.
- [138] A. Wutzler, H. Radusch, and K. Gehrman, "Diffusion of Acetophenone in Peroxide Cross-Linked Cable Compounds," *Journal of Macromolecular Science Physics*, vol. 38, no. 5-6, pp. 1095–1099, 1999.
- [139] H. Flynn, "A collection of kinetic data for the diffusion of organic compounds in polyolefins," *Polymer*, vol. 23, no. 9, pp. 1325–1344, 1982.

- [140] M. Saleem, A.-F. a. Asfour, D. De Kee, and B. Harrison, "Diffusion of organic penetrants through low density polyethylene (LDPE) films: Effect of size and shape of the penetrant molecules," *Journal of Applied Polymer Science*, vol. 37, no. 3, pp. 617–625, 1989.
- [141] K. Friedrich, G. Boiteux, and G. Seytre, "Physicochemical changes in epoxy-amine systems studied by ionic conductivity and ionic carriers mobility measurements," *Polymer*, vol. 51, no. 9, pp. 648–655, 2006.
- [142] T. Miyamoto and K. Shibayama, "Free-volume model for ionic conductivity in polymers," *Journal of Applied Physics*, vol. 44, no. 12, pp. 5372–5376, 1973.
- [143] Y. Sekii and T. Maeno, "Generation and Dissipation of Negative Heterocharges in XLPE and EPR," *IEEE Transactions on Dielectrics and Electrical Insulation*, vol. 16, no. 3, pp. 668–675, 2009.
- [144] Y. Sekii, Y. Idei, and K. Asakawa, "Influence of antioxidants on polyethylene chemical crosslinking reaction," in *2001 IEEE Conference on Electrical Insulation and Dielectric Phenomena (CEIDP)*, pp. 83–87, 2001.
- [145] M. Fu, G. Chen, and J. C. Fothergill, "The influence of residue on space charge accumulation in purposely modified thick plaque XLPE sample for DC application," in *2005 IEEE XIVth International Symposium on High Voltage Engineering (ISH)*, pp. 1–6, IEEE, 2005.
- [146] J. Sahyoun, A. Crepet, F. Gouanve, L. Keromnes, and E. Espuche, "Diffusion mechanism of byproducts resulting from the peroxide crosslinking of polyethylene," *Journal of Applied Polymer Science*, vol. 134, no. 9, p. 56, 2017.
- [147] M. Fu, G. Chen, L. a. Dissado, and J. C. Fothergill, "Influence of thermal treatment and residues on space charge accumulation in XLPE for DC power cable application," *IEEE Transactions on Dielectrics and Electrical Insulation*, vol. 14, no. 1, pp. 53–64, 2007.
- [148] T. Yamazaki and T. Seguchi, "ESR Study on Chemical Crosslinking Reaction Mechanisms of Polyethylene Using a Chemical Agent - II . The Effect of Phenolic Antioxidants," *Journal of Polymer Science Part A: Polymer Chemistry*, vol. 35, no. 12, pp. 2431–2439, 1997.
- [149] T. Yamazaki and T. Seguchi, "ESR Study on Chemical Crosslinking Reaction Mechanisms of Polyethylene Using a Chemical Agent . III . Effect of amine type antioxidants," *Journal of Polymer Science Part A: Polymer Chemistry*, vol. 37, no. 3, pp. 349–356, 1999.
- [150] T. Yamazaki and T. Seguchi, "ESR Study on Chemical Crosslinking Reaction Mechanisms of Polyethylene Using a Chemical Agent . IV . Effect of sulfur-and phosphorous-type antioxidants," *Journal of Polymer Science Part A: Polymer Chemistry*, vol. 38, no. 17, pp. 3092–3099, 2000.
- [151] Y. Rolland, "Antioxydants naturels végétaux," *Oléagineux, Corps gras, Lipides*, vol. 11, no. 6, pp. 419–424, 2004.
- [152] F. Oldervoll and E. Ildstad, "Space charge, oxidation and morphology changes in low density polyethylene during high voltage DC ageing," in *2000 IEEE Conference Record of the 2000 IEEE International Symposium on Electrical Insulation*, pp. 477–480, IEEE, 2000.

- [153] A. Aragonese, I. Tamayo, A. Lebrato, J. Cañadas, J. Diego, D. Arencón, and J. Belana, "Effect of humidity in charge formation and transport in LDPE," *Journal of Electrostatics*, vol. 71, no. 4, pp. 611–617, 2013.
- [154] C.-O. Olsson, B. Kallstrand, and H. Ghorbani, "Conductivity of crosslinked polyethylene influenced by water," in *2014 IEEE Conference on Electrical Insulation and Dielectric Phenomena (CEIDP)*, pp. 832–835, IEEE, 2014.
- [155] C.-O. Olsson, "Diffusion in polymers with temperature dependent properties," in *International Heat Transfer Conference 13*, Begel House Inc., 2006.
- [156] M. Wang, P. Wu, S. S. Sengupta, B. I. Chadhary, M. Cogen, and B. Li, "Investigation of Water Diffusion in Low-Density Polyethylene by Attenuated Total Reflectance Fourier Transform Infrared Spectroscopy and Two-Dimensional Correlation Analysis," *American Chemical society*, vol. 50, no. 10, pp. 6447–6454, 2011.
- [157] T. A. Ve, F. Mauseh, and E. Ildstad, "Effect of water content on the conductivity of XLPE insulation," in *2012 IEEE Conference on Electrical Insulation and Dielectric Phenomena (CEIDP)*, pp. 649–653, IEEE, 2012.
- [158] S. Das and N. Gupta, "Charge trapping and transport phenomenon in aged and unaged epoxy resin and polyethylene," *Iranian Journal of Science and Technology - Transactions of Electrical Engineering*, vol. 36, no. E1, pp. 51–66, 2012.
- [159] W. Li, J. Li, X. Wang, S. Li, G. Chen, J. Zhao, and B. Ouyang, "Physicochemical origin of space charge dynamics for aged XLPE cable insulation," *IEEE Transactions on Dielectrics and Electrical Insulation*, vol. 21, no. 2, pp. 809–820, 2014.
- [160] A. Boubakeur, Y. Mecheri, and M. Boumerzou, "Comportement diélectrique et mécanique du polyéthylène réticulé chimiquement soumis a un vieillissement thermique continu," *Annales de Chimie Science des Matériaux*, vol. 25, no. 6, pp. 457–470, 2000.
- [161] C. Banmongkol, T. Mori, T. Mizutani, and M. Ishiokal, "Effects of Oxidation on Electrical Conduction and Breakdown of LDPE Films with Different Densities," in *1997 IEEE Conference on Electrical Insulation and Dielectric Phenomena (CEIDP)*, pp. 28–31, IEEE, 1997.
- [162] L. Zhang, Y. Zhou, J. Huang, J. Tian, Y. Wang, and Y. Sha, "Influence of oxidation on space charge dynamics in DC aged low-density polyethylene," *Journal of Electrostatics*, vol. 71, no. 3, pp. 403–406, 2013.
- [163] J. Belana, M. Pujal, P. Colomer, and S. Montserrat, "Cold crystallization effect on α and ρ amorphous poly(ethylene terephthalate) relaxations by thermally stimulated discharge currents," *Polymer*, vol. 29, no. 10, pp. 1738–1744, 1988.
- [164] G. Socrates, *Infrared and raman characteristic group frequencies : tables and charts*. John Wiley & Sons, 2007.
- [165] B. Read, "Mechanical relaxation in isotactic polypropylene," *Polymer*, vol. 30, no. 8, pp. 1439–1445, 1989.

- [166] C. Laurent, “Charge dynamics in polymeric materials and its relation to electrical ageing,” in *2012 IEEE Conference on Electrical Insulation and Dielectric Phenomena (CEIDP)*, pp. 1–20, IEEE, 2012.
- [167] E. Motyl, “Comparison between step and pulsed electroacoustic techniques using both PVDF and LiNbO transducers,” *Journal of Electrostatics*, vol. 51, pp. 530–537, 2001.
- [168] S. Holé, “Behind space charge distribution measurements,” *IEEE Transactions on Dielectrics and Electrical Insulation*, vol. 19, no. 4, pp. 1208–1214, 2012.
- [169] J. C. Fothergill, “Space charge in dielectrics: old theories and new measurements,” *IET*, 2000.
- [170] G. Montanari, “The electrical degradation threshold of polyethylene investigated by space charge and conduction current measurements,” *IEEE Transactions on Dielectrics and Electrical Insulation*, vol. 7, no. 3, pp. 309–315, 2000.
- [171] R. Courant, K. Friedrichs, and H. Lewy, “Über die partiellen Differenzgleichungen der mathematischen Physik,” *Mathematische Annalen*, vol. 100, no. 1, pp. 32–74, 1928.
- [172] Y. Segui, “Diélectriques, Courants de conduction,” *Techniques de l'ingénieur, D2301-5*, pp. 1–12, 2000.
- [173] G. C. Montanari, “The Electrical Degradation Threshold of and Conduction Current Measurements,” *IEEE Transactions on Dielectrics and Electrical Insulation*, vol. 7, no. 3, pp. 309–3015, 2000.
- [174] T. L. Nguyen, *Approche multi-échelles dans les matériaux polymères : de la caractérisation nanométrique aux effets d'échelles*. PhD thesis, Compiègne, 2014.
- [175] D. Fabiani, G. Montanari, C. Laurent, G. Teyssedre, P. Morshuis, R. Bodega, L. Dissado, A. Campus, and U. Nilsson, “Polymeric HVDC Cable Design and Space Charge Accumulation. Part 1: Insulation/Semicon Interface,” *IEEE Electrical Insulation Magazine*, vol. 23, no. 6, pp. 11–19, 2007.
- [176] J. Sahyoun, A. Crepet, F. Gouanve, L. Keromnes, and E. Espuche, “Diffusion mechanism of byproducts resulting from the peroxide crosslinking of polyethylene,” *Journal of Applied Polymer Science*, vol. 134, no. 9, pp. 1–11, 2017.

Annex: Final set of universal parameters used in the model

Parameters	Name	Unit	Value
$w_{e,inj}$	barrier for electron injection	eV	0.65
$w_{h,inj}$	barrier for hole injection	eV	0.6
β_e	activation energy for electron transport	eV	0.64
β_h	activation energy for hole transport	eV	0.59
a	hole mobility difference in amorphous and crystalline phase	/	0.2
α	proportion of trapped charges at each step time δt	/	$\delta t/500$
α_{ion}	ratio between positive and negative ion mobilities	/	4/3
r	proportion of ionized αCA molecules	/	$5 \cdot 10^{-7}$
r_{max}	highest αCA volume ratio present in each matrix state	/	$2.6 \times \chi_C$

Table 5.5: Final set of universal parameters.